AIX-MARSEILLE UNIVERSITÉ
Institut de Recherche sur les Phénomènes Hors Équilibre

THÈSE

présentée pour obtenir le grade de

DOCTEUR DE L'UNIVERSITÉ DE PROVENCE

Spécialité : Mécanique, Physique des Fluides

École doctorale : Sciences pour l'ingénieur : Mécanique, Physique, Micro et Nanoélectronique

par **Romain LAGRANGE**

le 09 décembre 2009

Dynamique d'un fluide dans un cylindre en précession

Directeur de thèse : **M. Patrice MEUNIER**
Co-directeur de thèse : **M. Christophe ELOY**

JURY :

M. Philippe CARDIN	*Rapporteur*
M. Uwe EHRENSTEIN	
M. Christophe ELOY	*Co-directeur*
M. Patrice MEUNIER	*Directeur*
M. François NADAL	*Responsable CEA*
M. Maurice ROSSI	
M. Denis SIPP	*Rapporteur*
M. Andréas TILGNER	

AIX-MARSEILLE UNIVERSITÉ
Institut de Recherche sur les Phénomènes Hors Équilibre

THÈSE

présentée pour obtenir le grade de

DOCTEUR DE L'UNIVERSITÉ DE PROVENCE

Spécialité : Mécanique, Physique des Fluides

École doctorale : Sciences pour l'ingénieur : Mécanique, Physique, Micro et Nanoélectronique

par **Romain LAGRANGE**

le 09 décembre 2009

Dynamique d'un fluide dans un cylindre en précession

Directeur de thèse : **M. Patrice MEUNIER**
Co-directeur de thèse : **M. Christophe ELOY**

JURY :

M. Philippe CARDIN	*Rapporteur*
M. Uwe EHRENSTEIN	
M. Christophe ELOY	*Co-directeur*
M. Patrice MEUNIER	*Directeur*
M. François NADAL	*Responsable CEA*
M. Maurice ROSSI	
M. Denis SIPP	*Rapporteur*
M. Andréas TILGNER	

REMERCIEMENTS

Mes premiers remerciements s'adressent à mes directeurs de thèse : Patrice Meunier et Christophe Eloy, pour leur très grande disponibilité, leur gentillesse et leur dynamisme pendant ces trois années. Au delà de leurs qualités humaines rares et très appréciables, ils ont su me placer dans les conditions idéales pour réaliser ma thèse. Travailler avec eux fut un véritable plaisir. Je remercie également François Nadal, d'une part pour son très bon accueil lors de mes déplacements au CEA, d'autre part pour l'intérêt qu'il a montré envers mon travail en se tenant constamment informé de mes avancées.

Cette thèse n'aurait évidemment pas été possible sans le soutien financier du CEA et du CNRS. A ce titre je les remercie pour la confiance qu'ils m'ont accordé.

Je remercie les rapporteurs : Philippe Cardin et Denis Sipp ainsi que les membres du jury : Uwe Ehrenstein, Maurice Rossi et Andréas Tilgner pour avoir accepté d'examiner mon travail de thèse.

Au sein de l'IRPHE je remercie l'ensemble des chercheurs avec qui j'ai pu interagir durant ces trois années de thèse et qui m'ont aidé d'une façon ou d'une autre. Je pense en particulier aux membres suivants de l'équipe Écoulements Tournants et Géophysiques : Patrice Le Gal, Michael Le Bars et Stéphane Le Dizès.

Je voudrais également remercier parmi les chercheurs de l'IRPHE Lionel Schouveiler et Laurence Pietri qui m'ont donné la chance d'effectuer mes premiers pas dans l'enseignement en tant que vacataire à l'IUT de Marseille Saint Jérôme.

Je n'oublie pas dans ces remerciements les membres de l'équipe technique : Eric Portal, Hubert Ekongolo N'Kake, Eric Golubic, Mathieu Roy, Raymond Vaudo et Patrice Joly qui m'ont permis de résoudre rapidement de nombreux problèmes expérimentaux.

Je remercie également Lucienne Bazzali, Delphine Lignon et Sophie Mebkhout qui assurent le bon fonctionnement administratif du laboratoire.

Je pense aussi aux doctorants qui ont partagé mon quotidien pendant ces trois années de thèse, en particulier mes collègues de bureau qui se sont succédés : Christophe Almarcha et Pierre Yves Passaggia.

"Last but not least", je remercie mes parents qui depuis le début de mes études ont toujours fait tout leur possible pour que je puisse bénéficier des meilleures conditions de travail pour réussir.

TABLE DES MATIÈRES

1. INTRODUCTION

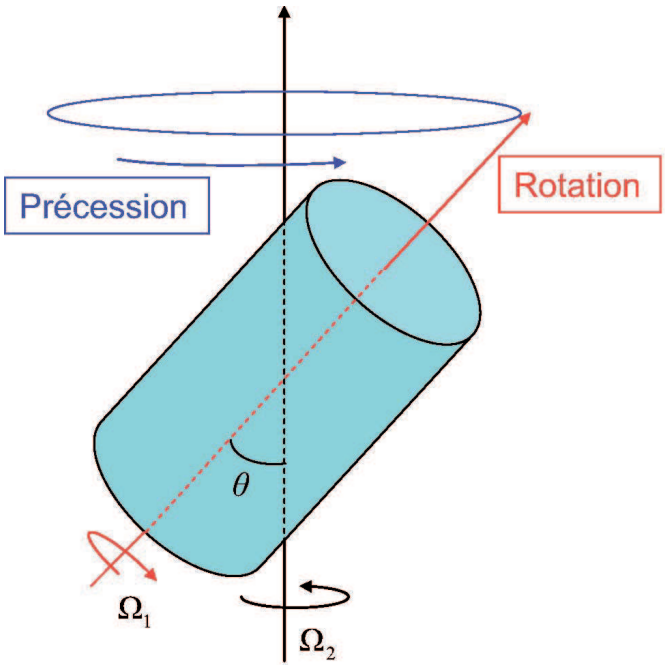

Figure 1.1: Schéma d'un cylindre en précession. Le cylindre tourne autour de son axe de révolution à la vitesse angulaire Ω_1. Cet axe tourne lui même autour d'un second axe incliné par rapport au premier à la vitesse angulaire Ω_2. L'angle entre les deux axes de rotation est l'angle de précession θ.

Le mouvement d'un fluide dans un cylindre en rotation autour de son axe est stable et correspond à une simple rotation solide. Son étude ne présente donc pas un grand intérêt scientifique. Lorsque l'axe de rotation du cylindre est lui-même en rotation autour d'un second axe incliné par rapport au premier (voir la figure 1.1) on parle de précession et l'écoulement devient plus complexe et est assez mal connu à l'heure actuelle. C'est cet écoulement que nous allons étudier d'un point de vue expérimental et théorique. Outre son intérêt fondamental cet écoulement de précession se retrouve dans de nombreuses applications ; ce qui motive en grande partie cette étude.

1.1 Applications

1.1.1 En aéronautique

Le premier grand domaine d'application de cette étude concerne l'aéronautique. En effet, un moyen couramment utilisé pour stabiliser les trajectoires d'objets volants tels que les satellites ou les fusées consiste à leur donner une composante de rotation propre. Cette composante est représentée sur la figure 1.2 par un vecteur rotation $\mathbf{\Omega}_1$. La plupart du temps les objets volants contiennent un carburant liquide qui est alors entrainé en rotation par frottement sur les parois du réservoir. En l'absence de perturbation externe ce carburant liquide est en rotation solide, c'est-à-dire qu'il tourne en bloc avec son contenant. Pour diverses raisons, par exemple une asymétrie

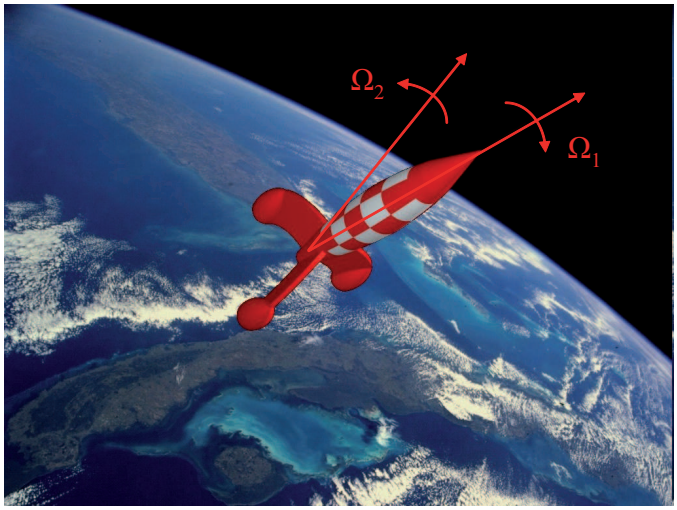

Figure 1.2: Objet volant en précession. L'objet a une rotation propre autour de l'axe $\mathbf{\Omega}_1$. Cet axe tourne lui-même autour d'un second axe incliné par rapport au premier à la vitesse angulaire Ω_2.

au niveau de la géométrie de l'objet volant, un petit angle de précession peut apparaitre et entrainer un changement de direction de l'axe de rotation propre $\mathbf{\Omega}_1$. Cet axe peut alors se retrouver en rotation autour d'un axe noté $\mathbf{\Omega}_2$ sur la figure 1.2. Dans ce cas, vu dans un référentiel Galiléen l'objet volant a un mouvement de précession. Si l'écoulement du fluide carburant est résonnant l'angle de précession initial peut croître et cela peut conduire à une modification majeure de la stabilité de l'objet volant. Ce genre de processus a conduit à un certain nombre d'études aussi bien théoriques, expérimentales que numériques (voir Stewartson, 1958; Karpov, 1965; Gans, 1984; Garg *et al.*, 1986; Herbert, 1986; Pocha, 1987; Agrawal, 1993; Bao & Pascal, 1997; Lambelin *et al.*, 2009).

1.1.2 Les phénomènes atmosphériques

De nombreux phénomènes atmosphériques tels que les cyclones et les tornades ont un lien direct avec les problèmes de mécanique des fluides tournants. La dynamique de ces phénomènes est étroitement liée à une force omniprésente dans les fluides en rotation : la force de Coriolis. Cette force agit perpendiculairement à la vitese d'un corps en déplacement dans un un référentiel en rotation et doit son nom à l'ingénieur français Gaspard-Gustave Coriolis.

Un cyclone (i.e. une dépression) localisé dans l'hémisphère nord est montré sur la figure 1.3. La structure en spirale observée correspond à un écoulement fluide à la surface de la Terre et qui a une composante verticale de mouvement beaucoup plus faible que la composante horizontale. Cette couche de fluide est très mince relativement au rayon de la Terre. D'un point de vue météorologique on parle alors de flux à grande échelle (échelle synoptique) de l'atmosphère terrestre. Classiquement, la dynamique des cyclones est alors

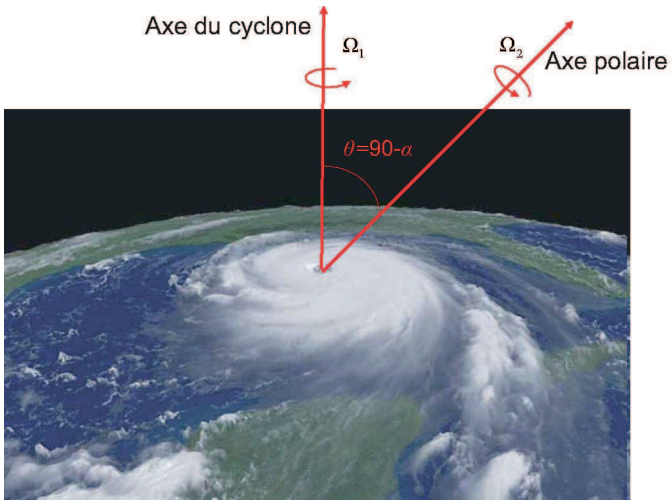

Figure 1.3: Cyclone en précession. Le cyclone tourne autour de l'axe vertical (axe du cyclone) à la vitesse angulaire Ω_1. Cet axe tourne lui même autour de l'axe polaire à la vitesse angulaire Ω_2. L'angle entre les deux axes de rotation est l'angle de précession et vaut $90 - \alpha$ degrés, où α est la latitude du cyclone.

prédite par des modèles numériques qui résolvent les équations primitives atmosphériques. Ces équations sont une version simplifiée des équations de Navier-Stokes. Pour cela on considère notamment que le cyclone est en rotation autour de la verticale locale à la vitesse angulaire $\Omega_1 = \Omega_2 \sin\alpha$; Ω_2 étant la vitesse de rotation de la Terre et α la latitude du cyclone. Dans ces équations l'axe de rotation $\mathbf{\Omega}_1$ du cylone est supposé de direction constante. Pourtant cet axe est lui-même en rotation autour de l'axe polaire et précesse donc à la vitesse angulaire Ω_2. Ce mouvement de précession s'effectue alors avec un angle $\theta = 90 - \alpha$ degrés. La question que l'on peut se poser est : quelle est l'influence de la précession sur la dynamique de ce cyclone ?

1.1.3 En géophysique

Le troisième grand domaine d'application de notre étude concerne la géophysique interne. La forme de la Terre est modélisée par un ellipsoïde, une forme ronde légèrement aplatie aux pôles, et plus précisément par le géoïde dont le diamètre approximatif de référence est de 12 742 km. La Terre tourne autour de l'axe polaire (axe nord sud) avec une période d'environ 23h56' (jour sidéral). Cette rotation est représentée sur la figure 1.4 par une vitesse angulaire Ω_1. La rotation de la Terre tend à éloigner par force centrifuge la matière de l'axe de rotation et cela d'autant plus que cette matière en est éloignée. Cela forme une sorte de "bourrelet" sur l'équateur qui fait en sorte que le diamètre à l'équateur est 43 km plus long que le diamètre polaire. Les forces qui s'exercent sur le bourrelet équatorial par de gros corps comme la Lune et le Soleil tendent à faire incliner l'axe polaire d'un angle de 23° par rapport à un axe perpendiculaire au plan de l'écliptique (plan géométrique qui contient l'orbite de la Terre autour du Soleil), ce qui produit l'alternance des saisons sur la surface du globe. Au mouvement de rotation propre de la

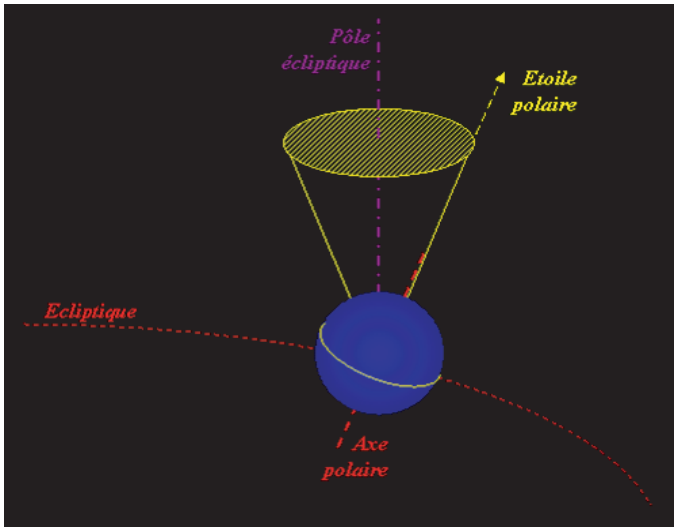

Figure 1.4: Précession terrestre. La Terre tourne autour de l'axe polaire avec une période d'environ 24h. Cet axe de rotation tourne lui même autour d'un second axe appelé le pôle de l'écliptique avec une période d'environ 26000 ans. L'angle entre les deux axes de rotation est d'environ 23°.

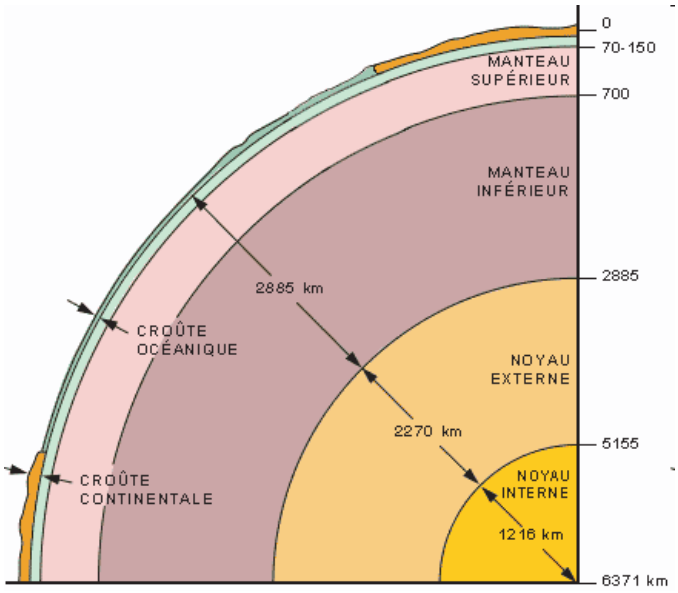

Figure 1.5: Structure interne de la Terre. Le noyau externe de la Terre est liquide et composé à 80% de fer.

Terre s'ajoute alors un mouvement de précession de l'axe polaire : cet axe tourne autour de la direction perpendiculaire au plan de l'écliptique avec une période égale à 25 800 ans. La Terre a donc un mouvement de précession par rapport à un référentiel Galiléen.

La figure 1.5 est une coupe schématique représentant la structure interne de la Terre. La Terre est constituée de plusieurs couches internes identifiables à peu près concentriques : la croûte terrestre (océanique ou continentale), le manteau supérieur, le manteau inférieur, le noyau externe et interne. Cette structure est connue au moyen de l'étude de la propagation des ondes sismiques (tomographie sismique) entre une source et différents points de la surface terrestre. Certaines ondes arrivent rapidement : ce sont les ondes P (comme Premières) ; d'autres sont retardées et sont enregistrées plus tard : ce sont les ondes S (comme Secondes). Les ondes P sont des vibrations qui agissent en compression : les particules se déplacent dans le sens de propagation de l'onde, un peu comme dans un ressort ou une onde sonore. Ces ondes de compression se propagent dans les solides, les liquides et les gaz. Les ondes S sont des ondes de cisaillement : les particules se déplacent perpendiculairement au sens de propagation de l'onde, un peu comme une oscillation sur une corde. Ces ondes de cisaillement se propagent dans les solides mais pas dans les milieux liquides ou gazeux. En utilisant cette propriété Harold Jeffreys découvre en 1926 que le noyau externe de la Terre est liquide. Il est essentiellement composé de fer (environ 80 %) et de nickel plus quelques éléments plus légers. Sa viscosité est proche de celle de l'eau, sa température moyenne atteint 4000 °C et sa densité 10. Cette énorme quantité de métal en fusion (fluide conducteur d'électricité) est forcée par le mouvement de précession Terrestre (mais aussi par des effets de convection thermique (voir Grote *et al.*, 1999, 2000; Grote & Busse, 2001), de convection chimique ou encore par des effets de marées) qui induit une certaine dynamique du noyau. Nous savons que des écoulements de fer liquide peuvent y engendrer des courants électriques qui donnent naissance à des champs magnétiques qui renforcent les courants créant ainsi un effet dynamo en s'entretenant les uns les autres. Le noyau liquide est donc à l'origine du champ magnétique terrestre (voir Bullard, 1949). La question que l'on se pose alors est : la précession peut elle engendrer une géodynamo ? D'après Rochester *et al.* (1975) et Loper (1975) le forçage de précession n'est pas assez important pour instaurer un mécanisme de géodynamo. Ce forçage peut néanmoins être suffisant dans le cas où l'écoulement induit par la précession est turbulent (voir Roberts & Gubbins, 1987; Kerswell, 1996). En ce qui concerne les expériences, Gans (1970*a*) a essayé de montrer un effet dynamo avec du sodium dans un cylindre en précession. Malheureusement cette expérience n'a pas donné le résultat escompté. Pourtant, Tilgner (2005) a démontré numériquement qu'un fluide en précession dans une cavité sphérique peut engendrer un effet dynamo. De plus il avance que cet effet dynamo peut être observé pour des nombres de Reynolds magnétiques comparables à ceux d'autres écoulements considérés dans des expériences en laboratoire (voir Tilgner, 2000*b*; Gailitis *et al.*, 2002). Dans tous les cas il apparaît primordial de connaître précisément l'influence du mouvement de précession sur la dynamique du noyau externe liquide si nous voulons déterminer le rôle d'un tel mouvement dans le processus de

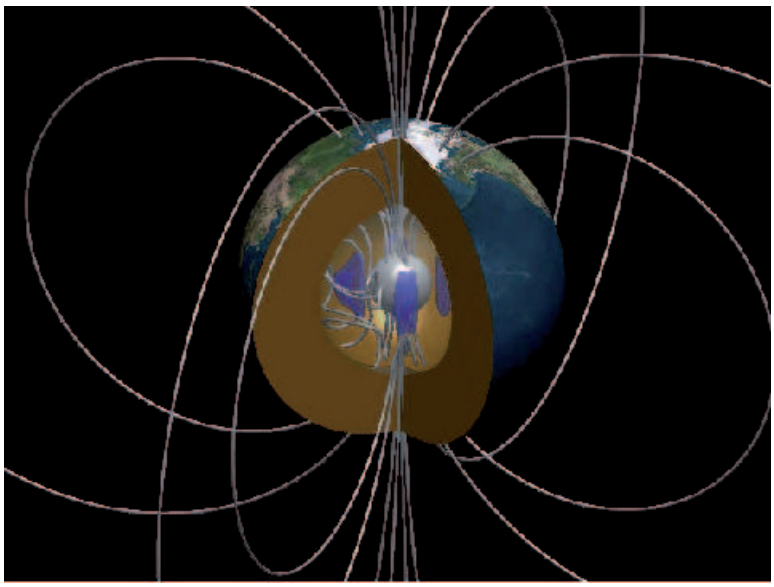

Figure 1.6: Vue écorchée de l'intérieur de la Terre. Les mouvements de fluide conducteur (structures tourbillonnaires en bleu) étirent les lignes du champ magnétique, leur donnant de l'énergie. Figure de J. Aubert de l'IPGP.

génération du champ magnétique terrestre.

En recherchant des effets non-linéaires dûs à la précession on pourrait également espérer expliquer quelques phénomènes exotiques telle que l'inversion du champ magnétique, représentée sur la figure 1.7.

1.2 Description mathématique d'un fluide en rotation

1.2.1 Formulation

Dans cette section nous établissons l'équation de mouvement d'un fluide dans un référentiel en rotation. Une introduction plus complète à la dynamique des fluides tournants pourra être trouvée dans les ouvrages de Greenspan (1968), de Pedlosky (1987), de Rieutord (1997) ou encore de Guyon *et al.* (2001).

Nous notons ρ la masse volumique de ce fluide (considéré comme incompressible), ν sa viscosité cinématique et $\mathbf{\Omega}(T)$ le vecteur rotation, dependant du temps T. Le vecteur position est noté $\mathbf{R}$. Enfin nous notons $\mathbf{U}_a$ la vitesse du fluide dans un repère Galiléen (repère absolu représenté par un indice a) et $\mathbf{U}$ sa vitesse dans le repère en rotation (représenté par un indice r). Les variations temporelles dans le repère Galiléen et dans le repère tournant pour un champ de vecteur $\mathbf{A}$ quelconque sont reliées par la relation

$$\left(\frac{d\mathbf{A}}{dT}\right)_a = \left(\frac{d\mathbf{A}}{dT}\right)_r + \mathbf{\Omega} \times \mathbf{A}, \tag{1.1}$$

où $\left(\frac{d\mathbf{A}}{dT}\right)$ représente une dérivée lagrangienne. Appliquons tout d'abord l'équation (1.1) au vecteur position $\mathbf{R}$ dont les dérivées temporelles sont les vitesses

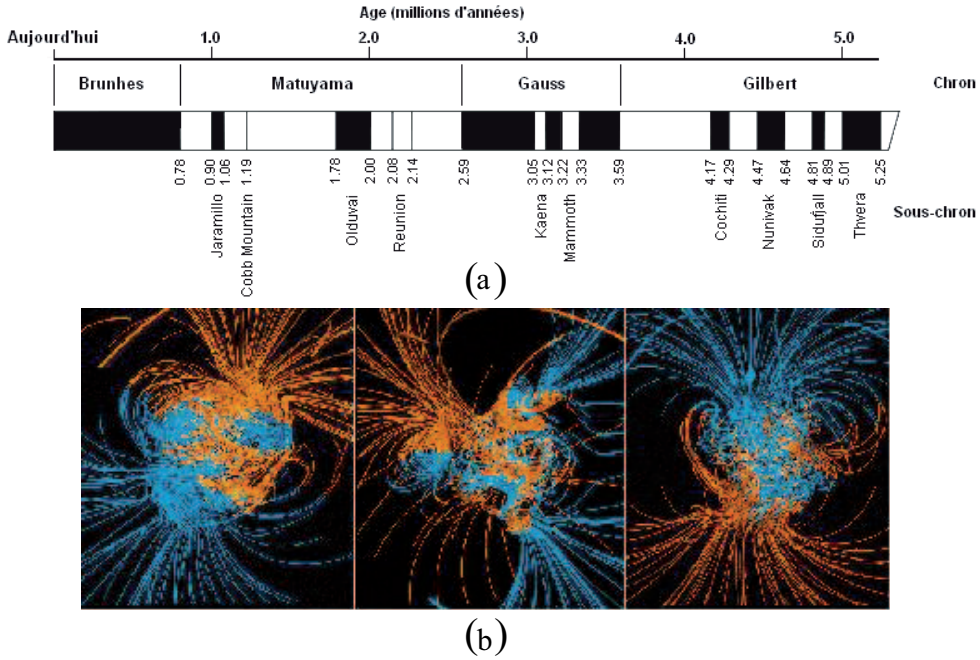

Figure 1.7: (a) Époques et évènements d'inversion du champ magnétique terrestre. Les époques correspondent à de longues périodes d'inversion moyenne. Les évènements sont des inversions courtes dans une époque. En noir : même polarité que celle actuelle. Il y a eu au moins 170 inversions au cours des 100 derniers millions d'années. (b) Simulation de l'inversion du champ géomagnétique réalisée en 1995 par Glatzmaier et Roberts au Pittsburgh Supercomputing Center (PSC) de Los Alamos (voir Glatzmaier & Roberts, 1996). La zone de transition (centre) dure environ 1000 ans.

$\mathbf{U}_a$ et $\mathbf{U}$. On obtient

$$\mathbf{U}_a = \mathbf{U} + \mathbf{\Omega} \times \mathbf{R}. \tag{1.2}$$

En appliquant de nouveau l'équation (1.1) à l'expression précédente on obtient

$$\left(\frac{d\mathbf{U}_a}{dT}\right)_a = \left(\frac{d\mathbf{U}_a}{dT}\right)_r + \mathbf{\Omega} \times \mathbf{U}_a = \left(\frac{d\mathbf{U}}{dT}\right)_r + 2\mathbf{\Omega} \times \mathbf{U} + \mathbf{\Omega} \times (\mathbf{\Omega} \times \mathbf{R}) + \left(\frac{d\mathbf{\Omega}}{dT}\right)_a \times \mathbf{R}. \tag{1.3}$$

L'équation de Navier–Stokes dans un repère Galiléen s'écrit

$$\left(\frac{d\mathbf{U}_a}{dT}\right)_a = \frac{\partial \mathbf{U}_a}{\partial T} + (\mathbf{U}_a \cdot \nabla)\,\mathbf{U}_a = \frac{-1}{\rho}\nabla P + \nu \Delta \mathbf{U}_a + \nabla \phi, \tag{1.4}$$

où ϕ représente le potentiel des forces en volume par unité de masse tel que $\phi = gz$ pour la gravité. En combinant (1.2), (1.3) et (1.4) on obtient alors l'équation de Navier–Stokes dans le référentiel tournant

$$\frac{\partial \mathbf{U}}{\partial T} + (\mathbf{U} \cdot \nabla)\,\mathbf{U} = -\nabla\left(\frac{P}{\rho} + \phi\right) - 2\mathbf{\Omega} \times \mathbf{U} - \mathbf{\Omega} \times (\mathbf{\Omega} \times \mathbf{R}) - \left(\frac{d\mathbf{\Omega}}{dT}\right)_a \times \mathbf{R} + \nu \Delta \mathbf{U}. \tag{1.5}$$

Dans cette équation le terme $\mathbf{\Omega} \times (\mathbf{\Omega} \times \mathbf{R})$ correspond à la force centrifuge. On peut démontrer que ce terme est potentiel puisque $\mathbf{\Omega} \times (\mathbf{\Omega} \times \mathbf{R}) = -\frac{1}{2}\nabla\,(\mathbf{\Omega} \times \mathbf{R})^2$.

La composante $2\mathbf{\Omega} \times \mathbf{U}$ est appelée force de Coriolis et est normale au mouvement des particules de fluide. C'est cette même force qui explique la déviation vers l'est des corps en chute libre. Le terme $\left(\frac{d\mathbf{\Omega}}{dT}\right)_a \times \mathbf{R}$ correspond à l'accélération du repère tournant par rapport au repère absolu et est appélé accélération de Poincaré. Nous verrons que ce terme est essentiel dans un mouvement de précession car il représente un terme de forçage spécifique sur le fluide.

Définissons R l'échelle caractéristique des longueurs de l'écoulement et Ω^{-1} l'échelle caractéristique du temps. Cela nous donne $R\Omega$ comme échelle de vitesse et fait apparaitre naturellement le nombre de Rossby

$$Ro = \frac{U}{\Omega R}, \tag{1.6}$$

comme unité de vitesse.

Le nombre de Rossby représente le rapport entre les ordres de grandeurs du terme de transport convectif de l'équation de mouvement et du terme de force de Coriolis. Les écoulements à faible nombre de Rossby sont ceux pour lesquels les effets de rotation et de force de Coriolis sont dominants. En géophysique le nombre de Rossby ne devient faible pour des vitesses d'écoulement typiques uniquement à grande échelle. Ainsi, pour un écoulement atmosphérique $\Omega \sim 10^{-4}$ s^{-1}, $U \sim 10$ m/s et $L \sim 10^3$ km on trouve

$Ro \sim 10^{-1}$. Cela explique pourquoi la rotation terrestre influence le sens des mouvements cycloniques, qui sont de grandes échelles : ils sont d'un sens différent dans les hémisphères nord et sud. Ce n'est plus le cas pour un typhon où avec une vitesse de 100 m/s et une échelle de 10 km on a $Ro = 10^2$.

Le remplacement des variables $\mathbf{R}$, T, $\mathbf{U}$, $\mathbf{\Omega}$, P par $R\mathbf{r}$, $\Omega^{-1}t$, $R\Omega\mathbf{u}$, $\Omega\mathbf{u}_z$ et $\rho\Omega URp$ permet de réduire l'équation (1.5) sous la forme adimensionnée

$$\frac{\partial \mathbf{u}}{\partial t} + (\mathbf{u}\cdot\nabla)\,\mathbf{u} + 2\mathbf{u}_z \times \mathbf{u} = -\nabla p - \left(\frac{d\mathbf{u}_z}{dt}\right)_a \times \mathbf{r} + Ek\Delta\mathbf{u}. \tag{1.7}$$

Notez que dans cette équation la pression a été redéfinie et inclut tous les termes potentiels.

Le nombre d'Ekman Ek est défini par

$$Ek = \frac{\nu}{\Omega L^2}. \tag{1.8}$$

Il représente le rapport entre les ordres de grandeur du terme visqueux de l'équation de mouvement et du terme de Coriolis. Ce nombre interviendra principalement dans l'étude des écoulements près du fond d'un récipient ou d'une paroi en rotation. Dans la suite de l'étude nous utiliserons plutôt le nombre de Reynolds $Re = Ek^{-1}$.

Le rotationnel de l'équation (1.7) donne alors l'équation adimensionnée pour la vorticité $\zeta = \nabla \times \mathbf{u}$ de l'écoulement

$$\frac{\partial \zeta}{\partial t} + (\mathbf{u}\cdot\nabla)\,\zeta - [(\zeta + 2\mathbf{u}_z)\cdot\nabla]\,\mathbf{u} = Ek\Delta\zeta. \tag{1.9}$$

La seule différence entre cette équation et celle obtenue en l'absence de rotation est la présence du terme de vorticité planétaire $2\mathbf{u}_z$ à côté du terme de vorticité ζ. La somme de ces deux termes $\zeta + 2\mathbf{u}_z$ est appelée vorticité absolue. En l'absence de rotation le terme $(\zeta\cdot\nabla)\,\mathbf{u}$ représente les variations de vorticité accompagnant celles de longueur ou d'orientation des tubes de vorticité. La rotation ajoute une contribution supplémentaire du même type qui peut être dominante pour des vitesses de rotation élevées.

1.2.2 Écoulement de rotation solide

Si on suppose que le vecteur rotation $\mathbf{\Omega}$ est indépendant du temps une solution triviale de l'équation (1.7) est $\mathbf{u} = \mathbf{0}$ et $p = constante$. Cela signifie que le fluide n'a pas de mouvement par rapport au référentiel tournant. On parle alors de rotation solide. Expérimentalement cette rotation solide peut être facilement observée. Prenons le cas par exemple d'un cylindre transparent entièrement rempli d'eau et mis en rotation grâce à une plateforme tournante sur laquelle il a été fixé. Dans ce cylindre rempli d'eau nous ajoutons de la poudre d'aluminium préalablement diluée dans un mélange d'eau et de savon. Eclairons maintenant le cylindre sur un coté grâce à une nappe de lumière verticale et regardons dans une direction perpendiculaire à l'éclairement ce qu'il se passe. Le résultat de cette expérience est montré sur la figure 1.8. Une structure fluide localisée au niveau de l'axe de rotation du cylindre est observée. Un très léger mouvement de cisaillement dans n'importe

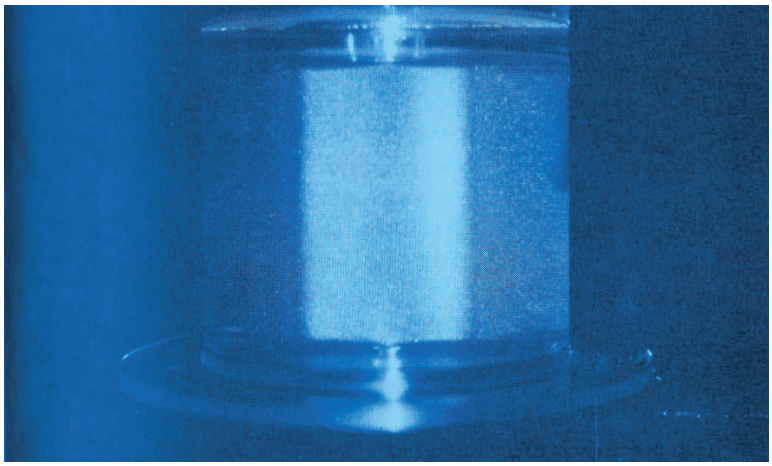

Figure 1.8: Écoulement de rotation solide. A la fin de la phase de spin-up le fluide tourne en bloc avec le cylindre. L'axe de rotation est observé grâce à des particules réfléchissantes introduites dans le cylindre et éclairées par un plan lumière vertical.

quelle section du cylindre est suffisant pour aligner les particules métalliques et ainsi changer l'intensité lumineuse reçue par l'observateur. Cette méthode de visualisation est très simple et permet de marquer les structures de l'écoulement (voir Goldsmith & Mason, 1962; Gauthier *et al.*, 1998). Dans cette expérience la structure observée correspond à l'axe de rotation du fluide. Cet axe est le même que l'axe de rotation du cylindre. Vu d'un référentiel Galiléen le fluide tourne en bloc avec le cylindre et sa vitesse adimensionnée est $\mathbf{u}_z \times \mathbf{r}$. Le mouvement de rotation solide est la principale réponse d'un fluide soumis à une rotation. A cet écoulement primaire des écoulements de plus faibles amplitudes peuvent se superposer. Ces écoulements secondaires sont d'une importance cruciale lorsqu'on étudie la dynamique d'un fluide tournant. En effet, ils sont bien souvent à l'origine de la transition d'un écoulement laminaire à un écoulement turbulent. Nous commençons par les écoulements secondaires dit géostrophiques.

1.2.3 Les écoulements géostrophiques

En plus de la solution de rotation solide, l'équation (1.7) admet d'autres solutions, beaucoup moins triviales. Certaines peuvent être trouvées en faisant plusieurs hypothèses. Les écoulements géostrophiques sont des solutions de (1.7) avec $\mathbf{u}_z$ et $\mathbf{u}$ indépendants du temps (ou quasi-stationnaires) et obtenues en supposant que le nombre de Rossby et d'Ekman sont petits devant 1. Ces hypothèses permettent de négliger les termes de transport convectif ainsi que les forces de viscosité. De plus on suppose l'écoulement incompressible, c'est-à -dire tel que

$$\nabla \cdot \mathbf{u} = 0. \tag{1.10}$$

Dans ces conditions les équations (1.7) et (1.9) donnent

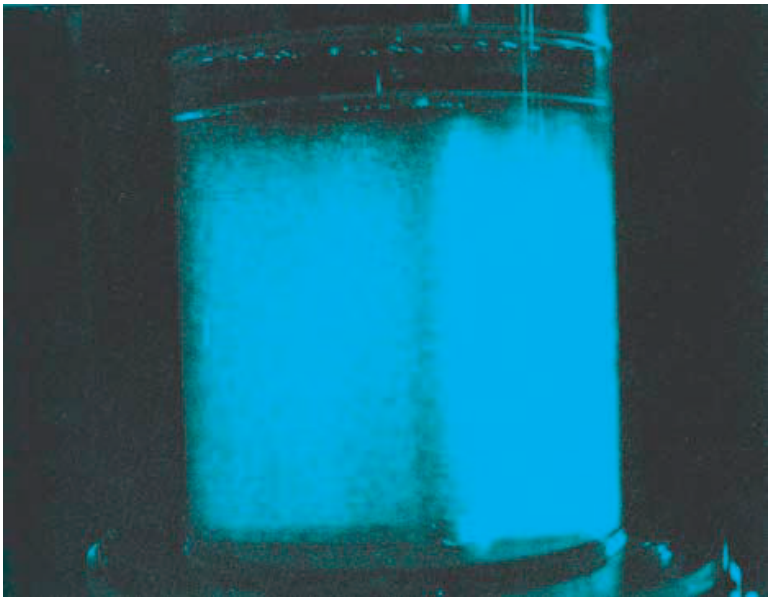

Figure 1.9: Colonne de Taylor–Proudman au dessus d'un petit objet solidement fixé sur le fond d'un cylindre en rotation. L'écoulement dans cette colonne de fluide est bidimensionnel.

$$\nabla p = -2\mathbf{u}_z \times \mathbf{u}, \tag{1.11}$$

et

$$\frac{\partial \mathbf{u}}{\partial z} = 0. \tag{1.12}$$

On en déduit alors qu'un écoulement géostrophique a les trois caractéristiques suivantes :

1. l'écoulement est normal au gradient de pression : les lignes de courant coïncident donc avec les isobares,
2. la vitesse $\mathbf{u} = (u, v, w)$ de l'écoulement est indépendante de la coordonnée définie le long de l'axe de rotation, notée z,
3. la section d'une courbe plane normale à $\mathbf{\Omega}$ qui suit le mouvement du fluide reste constante.

Ces trois caractéristiques représentent le théorème de Taylor–Proudman.

Expérimentalement pour observer un écoulement géostrophique, fixons sur la paroie inférieure d'un cylindre un petit objet et mettons l'ensemble en rotation solide. Une fois cet état de rotation solide atteint, changeons sensiblement la vitesse de rotation du cylindre de telle façon qu'il existe une rotation différentielle faible entre le cylindre et le fluide. Regardons sur la figure 1.9 le résultat de cette expérience. On observe un écoulement particulier au dessus de notre objet fixé sur la paroie inférieure du cylindre. Cet écoulement s'étend sur toute la hauteur du cylindre car il est indépendant de z ; il forme alors une colonne de fluide. En fait, tout se passe comme si l'intérieur de cette colonne de fluide était séparé de l'extérieur. A l'extérieur de la

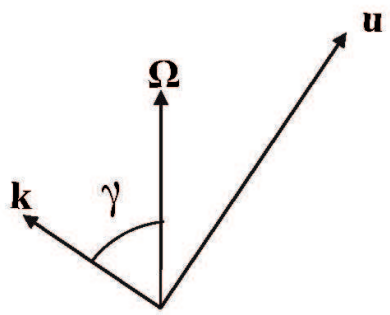

Figure 1.10: Une onde inertielle est transverse et a une fréquence adimensionnée comprise entre $-2 \leq \omega \leq 2$. La vitesse de groupe d'une onde inertielle est perpendiculaire au vecteur d'onde.

colonne on a alors le même écoulement que si on avait un fluide parfait en rotation s'écoulant autour d'un cylindre solide vertical. Cette colonne de fluide a été prédite théoriquement par Proudman et confirmée expérimentalement par Taylor. On parle alors de colonne de Taylor–Proudman.

1.2.4 Les ondes inertielles

Reprenons maintenant l'équation (1.7) en supposant toujours les nombres de Rossby et d'Ekman petits devant 1 et le vecteur rotation indépendant du temps. L'équation (1.7) s'écrit alors en régime instationnaire

$$\frac{\partial \mathbf{u}}{\partial t} + 2\mathbf{u}_z \times \mathbf{u} = -\nabla p. \tag{1.13}$$

En prenant deux fois le rotationnel de l'équation (1.13) on obtient avec la condition d'incompressibilité (1.10) que la vitesse $\mathbf{u}$ vérifie

$$\frac{\partial^2}{\partial t^2}(\Delta \mathbf{u}) + 4\frac{\partial^2}{\partial z^2}\mathbf{u} = 0. \tag{1.14}$$

Les solutions de l'équation (1.14) forment une famille que l'on appelle les ondes inertielles. Cette famille est un sous ensemble des ondes planes (i.e. modes normaux, (voir Waleffe, 1990)). Ainsi une solution de (1.14) peut être recherchée sous la forme complexe (voir Greenspan, 1968)

$$\mathbf{u}(\mathbf{r}) = \mathbf{u}_0 e^{\mathrm{i}(\omega t + \mathbf{k}\cdot\mathbf{r})}, \tag{1.15}$$

où ω est la pulsation de l'onde et $\mathbf{k}$ son vecteur d'onde.

En introduisant cette forme dans l'équation (1.14) on obtient la relation de dispersion des ondes inertielles

$$\omega = 2\cos\gamma, \tag{1.16}$$

où γ est l'angle entre le vecteur d'onde $\mathbf{k}$ et le vecteur rotation $\mathbf{\Omega}$ (voir figure 1.10). La relation de dispersion ne dépend donc pas du module du vecteur d'onde mais seulement de son orientation. De plus, les ondes inertielles ont

une fréquence adimensionnée telle que $-2 \leq \omega \leq 2$. Enfin, la fréquence est d'autant plus grande que le vecteur $\mathbf{k}$ se rapproche de l'axe de rotation. Pour la petite histoire, notons l'analogie qui peut être faite entre les ondes inertielles et les ondes dites internes dûes à la stratification du milieu et dont la relation de dispersion est $\omega = N \sin\gamma$ lorsque la stratification principale se fait selon la même direction que l'axe de rotation. Ici N est la fréquence de Brünt–Vaisälä et est définie par $N = \sqrt{\frac{-g}{\rho_0}\frac{\partial \rho}{\partial z}}$; ρ_0 étant la moyenne sur z de la masse volumique ρ et g la gravité.

A partir de l'équation de continuité (1.10) on montre que les ondes inertielles sont transverses, c'est-à-dire telles que $\mathbf{k} \cdot \mathbf{u} = 0$ (voir figure 1.10). La vitesse selon $\mathbf{k}$ pour laquelle la phase $\omega t + \mathbf{k} \cdot \mathbf{r}$ de l'onde inertielle reste constante est appelée vitesse de phase et est donnée par

$$\mathbf{v}_p = \pm 2 \frac{\mathbf{u}_z \cdot \mathbf{u}_k}{|\mathbf{k}|} \mathbf{u}_k, \tag{1.17}$$

où $\mathbf{u}_k$ est le vecteur unitaire orienté selon $\mathbf{k}$. La vitesse de phase dépendant de ω, deux ondes inertielles ayant des fréquences différentes ont des phases qui se propagent à des vitesses différentes. On dit alors que le phénomène de propagation des ondes inertielles est dispersif.

La vitesse de propagation d'énergie associée à une onde inertielle est appelée vitesse de groupe et est donnée par

$$\mathbf{v}_g = \frac{\partial \omega}{\partial \mathbf{k}} = \pm 2 \frac{\mathbf{u}_k \times (\mathbf{u}_z \times \mathbf{u}_k)}{|\mathbf{k}|}. \tag{1.18}$$

Cette vitesse est perpendiculaire au vecteur d'onde. Lorsque $\cos\gamma = 0$ (i.e. le vecteur d'onde est perpendiculaire au vecteur rotation) la relation de dispersion donne $\omega = 0$. Dans ce cas la vitesse de phase est nulle et la vitesse de groupe vaut $\mathbf{v}_g = \pm 2 |\mathbf{k}|^{-1} \mathbf{u}_z$ et nous retrouvons alors les écoulements géostrophiques résultant de l'équilibre entre force de pression et force de Coriolis.

D'autre part, le caractère hyperbolique de l'équation (1.14) implique l'existence de discontinuités de vitesse et de pression dans le fluide au niveau de surfaces caractéristiques. Ces surfaces sont des cônes dont l'angle au sommet dépend de la fréquence adimensionnée ω. Pour illustrer cette propriété, Görtler (1944, 1957) a mené des expériences dans un cylindre rempli d'eau et en rotation rapide autour de son axe de révolution à la vitesse angulaire Ω (voir figure 1.11). Grâce à un disque horizontal de faible rayon par rapport au rayon du cylindre et animé dans le référentiel tournant d'un mouvement oscillant de translation verticale de fréquence adimensionnée ω et d'amplitude très faible par rapport aux dimensions du cylindre Görtler (1944, 1957) a perturbé le système en rotation solide. Il a visualisé avec des paillettes réfléchissantes éclairées par un plan de lumière vertical les structures de l'écoulement perturbé. Pour $\omega < 2$ la perturbation se propage sur les surfaces caractéristiques qui sont des cônes dont l'angle au sommet augmente avec ω. Pour $\omega = 2$ ces surfaces caractéristiques deviennent des plans horizontaux. Notez que les colonnes de Taylor–Proudman présentées précédemment correspondent à des surfaces caractéristiques telles que $\omega = 0$. L'étude des surfaces caractéristiques dans les fluides en rotation a donné

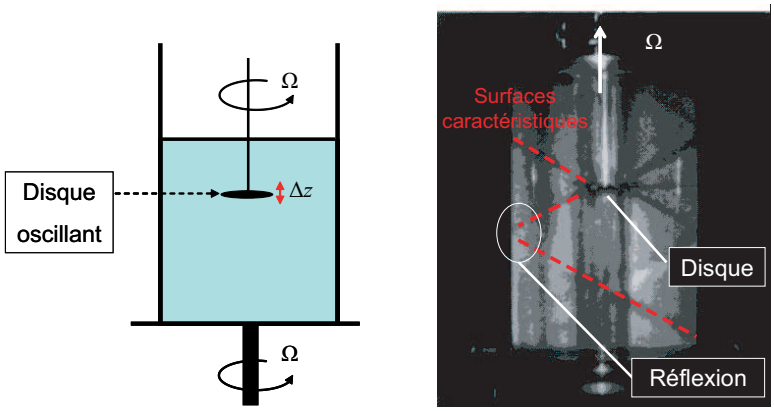

Figure 1.11: (a) Schéma de l'expérience de Görtler (1957). (b) Surfaces caractéristiques des ondes inertielles d'un fluide dans un cylindre en rotation. Le fluide est excité par un disque ayant un mouvement oscillant vertical de faible amplitude Δz et de fréquence adimensionnée ω. L'angle entre les surfaces caractéristiques et la verticale augmente avec ω.

lieu a de nombreux papiers experimentaux (voir Oser, 1958; Beardsley, 1970; McEwan, 1970), analytiques (voir Walton, 1975; Kerswell & Barenghi, 1995; Tilgner, 2000*a*) et numériques (voir Hollerbach & Kerswell, 1995; Rieutord & Valdetarro, 1997; Tilgner, 1999*a*,*b*,*c*; Fotheringham & Hollerbach, 1998) afin de déterminer leur influence sur la stabilité des écoulements en rotation.

1.2.5 Les modes de Kelvin

D'un point de vue mathématique l'équation (1.14) est de type hyperbolique. En règle générale (géométrie du problème quelconque) il n'est pas possible de trouver des solutions d'une telle équation vérifiant des conditions limites. Pour des géométries simples comme celle d'un cylindre la détermination exacte de ces solutions est néanmoins possible (ce qui n'est pas le cas pour une géométrie conique par exemple (voir l'étude expérimentale de Beardsley, 1970, et numérique de Henderson & Aldridge (1992))). Ces solutions sont appelées modes de Kelvin et ont un profil radial correspondant à une fonction de Bessel. En coordonnées cylindriques (r, φ, z) un mode de Kelvin s'écrit

$$\mathbf{u} = \mathbf{u}_0\,(r)\,e^{i(\omega t + m\varphi + kz)}, \tag{1.19}$$

avec m le nombre d'onde azimutal et k le nombre d'onde axial du mode. La fréquence ω vérifie toujours la relation $-2 \leq \omega \leq 2$ et est reliée aux nombres d'onde m et k par une relation de dispersion obtenue via la condition limite en $r = 1$. Waleffe (1990) a montré qu'un mode de Kelvin correspond à une somme d'ondes inertielles de même angle $\gamma = \arccos(\omega/2)$. Les modes de Kelvin seront définis plus en détail dans la section 2.3. Nous utiliserons ces modes tout au long du manuscrit car ils forment une base orthogonale

permettant de décomposer le champ de vitesse.

1.2.6 Les couches d'Ekman

Les relations sur les écoulements géostrophiques et les ondes inertielles étudiées précédemment ont été obtenues en négligeant le terme visqueux de l'équation de Navier–Stokes (1.7). Un moyen classique de prendre en compte la viscosité est de considérer que cette dernière agit essentiellement près des parois et que son influence en volume est négligeable devant la force de Coriolis. L'écoulement peut alors être considéré comme non visqueux loin des parois et visqueux lorsqu'on s'en approche. La transition entre ces deux écoulements s'effectue alors à une distance caractéristique δ_{Ek} de la paroi qui correspond à l'état d'équilibre entre force de Coriolis et force visqueuse. La couche de fluide située entre la paroi et la limite δ_{Ek} est appelée couche d'Ekman. Sa taille caractéristique est $\delta_{Ek} \sim Ek^{1/2}$. Les couches d'Ekman ont la particularité d'aspirer ou de rejeter du fluide : c'est le pompage d'Ekman, noté $\mathbf{u}_p$. Ainsi, ces couches limites exercent une influence sur l'écoulement en volume et le pompage d'Ekman peut être vu comme un écoulement secondaire proportionnel à $Ek^{1/2}$. Dans le cas simple d'une paroi perpendiculaire à l'axe de rotation $\mathbf{\Omega}$ et de normale sortante $\mathbf{n} = \pm\mathbf{u}_z$ une expression du pompage d'Ekman est

$$\mathbf{u}_p \cdot \mathbf{n} = -\frac{1}{2} Ek^{1/2} \zeta \cdot \mathbf{u}_z. \tag{1.20}$$

On en déduit que si $\zeta \cdot \mathbf{u}_z > 0$ (resp. $\zeta \cdot \mathbf{u}_z < 0$) la couche d'Ekman éjecte du fluide (resp. aspire du fluide).

1.3 Stabilité d'un fluide en rotation

Nous venons de voir dans les sections précédentes que l'écoulement d'un fluide en rotation est à l'ordre dominant une rotation solide à laquelle se superposent des écoulements de plus faibles amplitudes : les écoulements secondaires. Ces écoulements sont des solutions de l'équation de Navier–Stokes (1.7). La question est de savoir si ces solutions sont stables vis à vis d'une perturbation extérieure. En d'autres termes, comment vont se comporter les ondes inertielles en présence d'une rotation différentielle ? d'un champ de cisaillement externe ? d'un changement continu de la direction de l'axe de rotation ? Nous allons brièvement répondre aux deux premières questions en introduisant les notions d'instabilité centrifuge et d'instabilité elliptique. La solution à la dernière question, qui fait référence à la précession, sera évidemment développée dans tout le reste de cette étude.

1.3.1 L'instabilité centrifuge

L'instabilité centrifuge (également appelée instabilité de Taylor–Couette est discutée en détail dans de nombreux ouvrages, en particulier dans Chandrasekhar (1961) et Drazin & Reid (1981). En ce qui concerne les aspects non linéaires il est conseillé de se reporter à des ouvrages plus spécialisés tels que ceux de Chossat & Iooss (1994) et Koschmieder (1993). Nous nous limitons

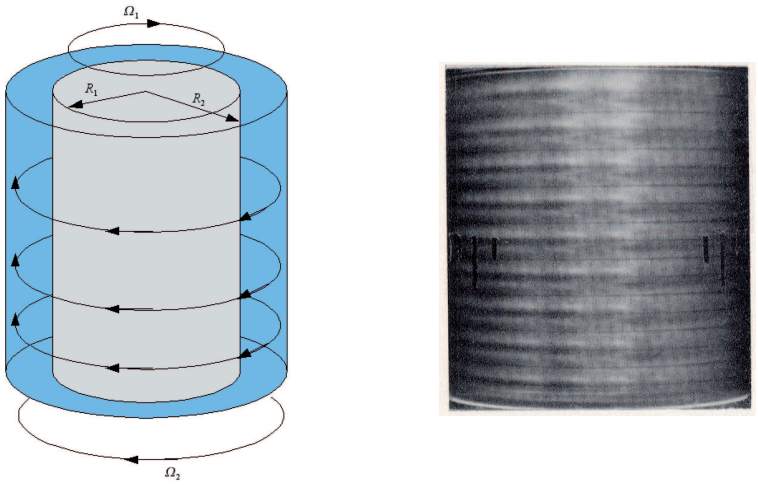

Figure 1.12: (a) Schéma de l'écoulement de Taylor–Couette entre deux cylindres emboités et rotatifs. (b) Développement de l'instabilité centrifuge et visualisation des rouleaux de Taylor (visualisation issue de Fenstermacher *et al.*, 1979).

ici aux éléments essentiel concernant l'instabilité centrifuge afin d'insister sur son mécansime physique.

Nous avons vu dans la section 1.2.1 qu'un fluide en rotation est soumis à la force centrifuge. Cette force qui dérive d'un potentiel tend à expulser les particules fluides le plus loin possible de l'axe de rotation. A cette force s'oppose un gradient de pression permettant de la contrebalancer. En coordonnées cylindres cet état d'équilibre s'écrit

$$\frac{u_\varphi(r)^2}{r} = \frac{1}{\rho}\frac{\partial p}{\partial r}, \tag{1.21}$$

où u_φ est la composante orthoradiale de la vitesse, p la pression et ρ la masse volumique du fluide. Dans certaines conditions (i.e. pour certains profils de vitesse $u_\varphi(r)$) cet état d'équilibre peut être rompu et une instabilité (dite centrifuge) prend naissance. Le premier à avoir établi une condition nécessaire de stabilité fut Rayleigh (1916) qui énnonca : pour être en situation instable il faut que le moment cinétique $r^2 u_\varphi(r)^2$ de l'écoulement soit une fonction décroissante de r. Ce critère fut redémontré plus rigoureusement que ne l'avait fait Rayleigh (1916) par Synge (1933). Ce dernier a de plus prouvé qu'en régime non visqueux la croissance monotone du carré du moment cinétique en fonction de la distance r est une condition nécessaire et suffisante de stabilité. L'étude visqueuse entreprise par Taylor (1923) a quant à elle montré que le rôle de la viscosité est uniquement de retarder l'apparition de l'instabilité centrifuge.

D'un point de vue expérimental l'instabilité centrifuge peut se développer dans tout écoulement dévié par une paroi créant un gradient de pression normal aux lignes de courant. Un exemple célèbre consiste à considérer l'écoulement entre deux cylindres coaxiaux et tournant chacun avec des vitesses

Ω_1 et Ω_2 (voir figure 1.12(a)). En fonction des deux nombres de Reynolds construits sur ces vitesses angulaires et du rapport des rayons des cylindres un écoulement stationnaire et spatiallement structuré apparait. Cette structure est constituée de rouleaux toriques contra-rotatifs et est périodique dans la direction axiale (voir figure 1.12(b)). Son apparition est dûe à l'instabilité centrifuge. Nous reparlerons de ce type d'instabilité dans notre étude afin de savoir si elle est possible dans le cas d'un cylindre en précession.

1.3.2 L'instabilité elliptique

L'instabilité elliptique (ou instabilité de marées) correspond à la déstabilisation tridimensionnelle d'écoulements tournants bidimensionnels dont les lignes de courant sont elliptiques (voir Kerswell, 2002, pour une revue). C'est une instabilité générique qui intervient dans de nombreux systèmes naturels, dans lesquels l'ellipticité est générée par exemple par des interactions entre tourbillons ou par des effets de marées. Sa présence est ainsi suggérée dans les sillages d'avion (voir Leweke & Williamson, 1998*b*), les tourbillons atmosphériques et océaniques (voir Afanasyev, 2002), les noyaux liquides des planètes (voir Kerswell & Malkus, 1998), les étoiles doubles et disques d'accrétion (voir Lubow *et al.*, 1993), et plus généralement dans les écoulements turbulents présentant des structures cohérentes elliptiques (voir Pierrehumbert, 1986; Bayly, 1986).

L'instabilité elliptique a été découverte par Widnall *et al.* (1974) en étudiant la dynamique d'anneaux tourbillonnaires. Moore & Saffman (1975) ont étendu ce cas particulier en effectuant une analyse linéaire de stabilité d'un tourbillon bidimensionnel dans un champ d'étirement uniforme. En reprenant le vortex de Moore & Saffman (1971, 1975) plongé dans un champ d'étirement extérieur supposé d'extension spatiale infinie, Tsai & Widnall (1976) ont démontré que l'écoulement de base peut se coupler avec des modes de Kelvin de nombres d'onde azimutaux $m = -1$ et $m = 1$. Ce couplage peut alors conduire à l'instabilité de l'écoulement de base si les modes de Kelvin ont la même fréquence et la même longueur d'onde (voir Eloy & Le Dizès, 1999). Cette condition est appelée condition de résonance triadique entre l'écoulement de base et les modes de Kelvin. Ce couplage de mode s'effectue alors par le terme non-linéaire de l'équation de Navier–Stokes. Le taux de croissance de l'instabilité est alors proportionnel au champ d'étirement. Cette propriété reste vraie même lorsque le champ d'étirement a une extension spatiale finie (voir l'étude numérique de Robinson & Saffman, 1984). Une expression analytique du taux de croissance pour le vortex de Moore & Saffman (1971, 1975) est donnée par Tsai & Widnall (1976) en considérant une résonance triadique faisant intervenir des modes de Kelvin stationnaires. Dans le cas d'un vortex de Lamb–Oseen une expression simple du taux de croissance n'est plus possible et il faut se contenter d'une équation faisant intervenir des produits scalaires entre les modes instables et l'écoulement de base (voir Moore & Saffman, 1975; Eloy & Le Dizès, 1999; Eloy, 2000). L'instabilité elliptique a ensuite été redécouverte en utilisant des méthodes mathématiques dites locales (voir Bayly, 1986; Lifschitz & Hameiri, 1991). Ces méthodes consistent à étudier la stabilité d'un écoulement de base ellip-

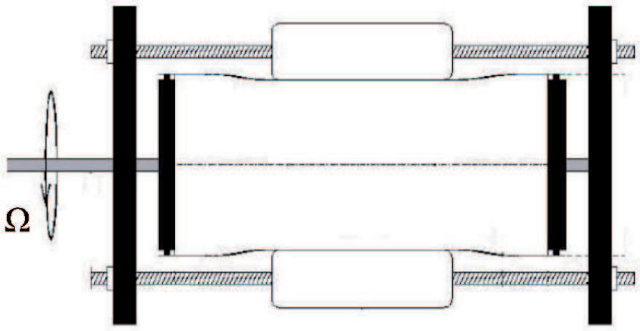

Figure 1.13: Un cylindre en rotation autour de son axe de révolution est déformé elliptiquement par deux rouleaux situés de chaque coté du cylindre, (figure issue de Eloy *et al.*, 2003).

tique vis à vis de perturbations de la forme (voir Craik & Criminale, 1986)

$$\mathbf{v}\left(\mathbf{r},t\right)=\mathbf{v}_0\left(t\right)e^{\mathrm{i}\mathbf{k}(t)\cdot\mathbf{r}}, \tag{1.22}$$

où $\mathbf{r}$ est le vecteur position et $\mathbf{k}(t)$ le vecteur d'onde de la perturbation et qui dépend du temps. La condition d'incompressibilité donne $\mathbf{k}\cdot\mathbf{v}=0$ (voir Sipp & Jacquin, 1998) et les évolutions temporelles de $\mathbf{k}$ et de $\mathbf{v}_0$ sont indépendantes. Bayly (1986) a montré que $\mathbf{v}_0$ vérifie alors une équation paramétrique faisant intervenir un couplage entre l'ellipticité des lignes de courant et la perturbation. En fonction de l'ellipticité des lignes de courant et de l'angle γ minimum que fait le vecteur d'onde avec l'axe du vortex les ondes de (1.22) peuvent être instables. Le taux de croissance ne dépend alors que de ces deux paramètres. Pour des ellipticités faibles, les ondes instables sont celles pour lesquelles $\gamma=\pi/3$ (voir Bayly, 1986). Pour des ellipticités finies, les ondes sont instables pour un certain intervalle d'angle γ. Waleffe (1990) a alors montré que le maximum du taux de croissance de l'instabilité elliptique pour un champ d'étirement ε est

$$\sigma=\frac{9}{16}\varepsilon. \tag{1.23}$$

Waleffe (1990) et Gledzer & Ponomarev (1992) ont unifié l'approche globale par modes de Kelvin et l'approche locale en démontrant qu'un mode de Kelvin correspond à une somme d'ondes inertielles de même angle γ.

D'un point de vue expérimental l'instabilité elliptique a été mise en évidence par Malkus (1989); Thomas & Auerbach (1994); Leweke & Williamson (1998*a*) et numériquement par Laporte & Corjon (2000). L'expérience de Malkus (1989) est représentée sur la figure 1.13. Un cylindre rempli d'eau et en rotation autour de son axe de révolution est déformé elliptiquement par deux rouleaux situés de chaque côté du cylindre. L'axe de rotation du fluide est visualisé par la technique classique consistant à introduire dans le cylindre des particules réfléchissantes éclairées par une source de lumière. La figure 1.14 montre alors que lorsque le cylindre en rotation est déformé l'axe de rotation du fluide est déformé sinusoïdalement par l'instabilité elliptique. Pour certains régimes particuliers de rotation et de déformation du

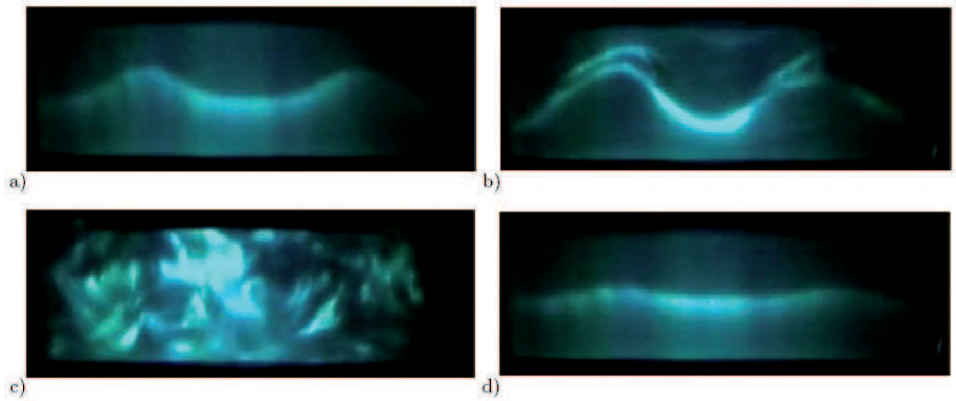

Figure 1.14: Clichés successifs des cycles intermittents de l'instabilité elliptique dans un cylindre. (a) Apparition de l'instabilité elliptique, (b) état fortement non-linéaire, (c) écoulement turbulent, (d) relaminarisation, (figure issue de Eloy *et al.*, 2003).

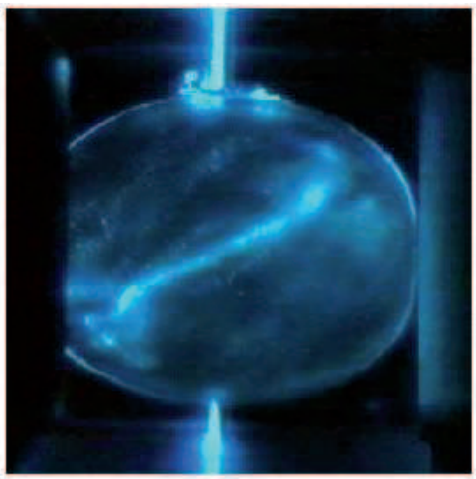

Figure 1.15: Mode de retournement produit par l'instabilité elliptique dans une sphère en rotation et légèrement déformée par deux rouleaux visibles de chaque côté de la figure (voir Lacaze *et al.*, 2004).

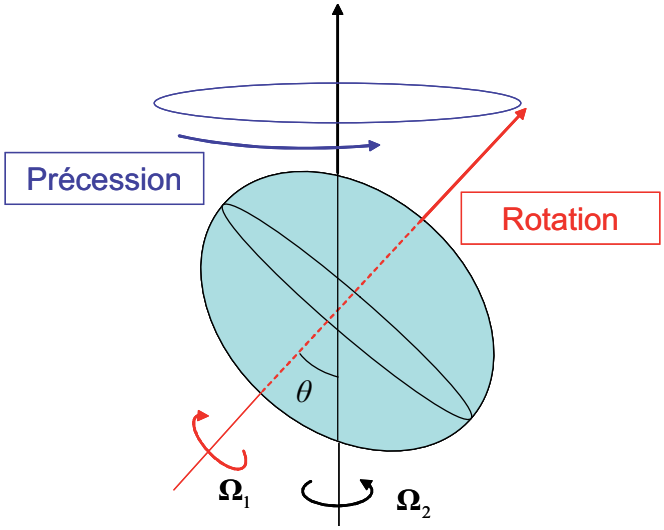

Figure 1.16: Schéma de principe d'un sphéroïde en précession. Le sphéroïde tourne autour d'un axe à la vitesse angulaire Ω_1. Cet axe tourne lui même autour d'un second axe incliné par rapport au premier à la vitesse angulaire Ω_2. L'angle entre les deux axes de rotation est l'angle de précession θ.

cylindre Malkus (1989) a également observé qu'après l'apparition de l'instabilité elliptique se succèdent une phase fortement non linéaire, puis une phase correspondant à un écoulement turbulent et finalement une phase de relaminarisation. Nous verrons que ce genre de phénomène intervient dans le cas de l'instabilité de précession. Le même genre d'expérience avec une sphère en rotation déformée elliptiquement à été réalisé par Lacaze *et al.* (2004). Le résultat de cette expérience est montré sur la figure 1.15. On observe l'apparition d'un mode instable dit de "spin-over", qui force le fluide à tourner suivant un axe perpendiculaire à l'axe d'entraînement (axe vertical sur la figure 1.15).

1.4 Écoulement de précession

Dans cette section nous allons nous intéresser au forçage des ondes inertielles par la précession. Dans ce cas le forçage est dû à l'instationnarité du vecteur rotation $\mathbf{\Omega}$ qui dans un référentiel fixe a une orientation qui change au cours du temps. Au niveau de l'équation (1.7) cela se traduit par le fait que le terme d'accélération de Poincaré $\left(\frac{d\mathbf{u}_z}{dt}\right)_a \times \mathbf{r}$ n'est pas nul. Avant de commencer notre analyse sur la dynamique d'un fluide dans un cylindre en précession nous allons rappeler les résultats obtenus dans le cas d'un sphéroïde.

1.4.1 Dans une cavité sphéroïdale

Le schéma de principe d'un sphéroïde en précession est représenté sur la figure 1.16.

Écoulement de base

En négligeant les forces de viscosité, Sloudsky (1895) et Poincaré (1910) ont démontré que le mouvement d'un fluide dans un sphéroïde en précession est une rotation solide autour d'un axe fixe dans le référentiel de précession et appartenant au plan ($\mathbf{\Omega}_1$, $\mathbf{\Omega}_2$). A cette rotation solide s'ajoute un écoulement irrotationnel permettant d'assurer la condition de non pénétration aux bords (voir Malkus, 1994). La théorie non visqueuse ne permet cependant pas de déterminer exactement le vecteur rotation du fluide. En introduisant les effets de couche limite Busse (1968) a alors complété la théorie non-visqueuse et donné une expression analytique de l'axe de rotation du fluide.

La première tentative expérimentale de visualisation directe de l'axe de rotation du fluide a été réalisée par Vanyo (1991); Vanyo *et al.* (1995) dans un conteneur d'ellipticité 1/100. Les résultats obtenus ne semblant pas rendre compte de la prédiction de Busse (voir Pais, 1999) des simulations numériques ont été réalisées pour étudier ce problème. Pour un conteneur sphérique, Noir *et al.* (2001*b*) a montré que la prédiction de Busse (1968) était numériquement correcte dans la limite des faibles nombre d'Ekman. La validation de la prédiction de Busse (1968) pour un conteneur sphéroïdal a finalement été obtenue numériquement par Lorenzani & Tilgner (2001).

Noir *et al.* (2003) a alors réalisé de nouvelles expériences dans un conteneur d'ellipticité 1/25 mis en précession. Ces expériences lui ont permi de valider la prédiction de Busse (1968) concernant l'axe de rotation solide du fluide.

Écoulement secondaire

L'écoulement secondaire se superposant à la rotation solide de Poincaré dans une cavité sphéroidale a été pour la première fois étudié expérimentalement (par visualisation directe) par Malkus (1968). En faisant varier la vitesse angulaire de précession d'un sphéroïde d'ellipticité 1/25, il a alors observé trois régimes d'écoulement secondaire (voir figure 1.17) :

1. un régime d'écoulement géostrophique laminaire,
2. un régime d'écoulement turbulent bidimensionnel,
3. un régime d'écoulement turbulent développé.

Ces différents régimes ont été confirmés expérimentalement par Vanyo & Likins (1971); Vanyo (1991); Vanyo *et al.* (1995); Noir (2000) (voir figure 1.17).

Le premier régime qui est observé pour des faibles vitesses angulaires de précession fait apparaitre des cylindres géostrophiques orientés suivant l'axe de rotation solide du fluide. Ces cylindres représentent des zones de cisaillement de l'écoulement en volume. Plusieurs études se sont alors penchées sur l'influence des couches limites afin d'expliquer l'apparition de ces zones de cisaillement. Ces couches limites dans le cas d'un sphéroïde en précession ont une épaisseur d'ordre $Ek^{1/2}$ partout, sauf pour certaines latitudes critiques où l'épaisseur devient d'ordre $Ek^{2/5}$. Ainsi, en plus du pompage d'Ekman traditionnel en $Ek^{1/2}$ il en résulte alors un nouveau pompage d'orde $Ek^{1/5}$

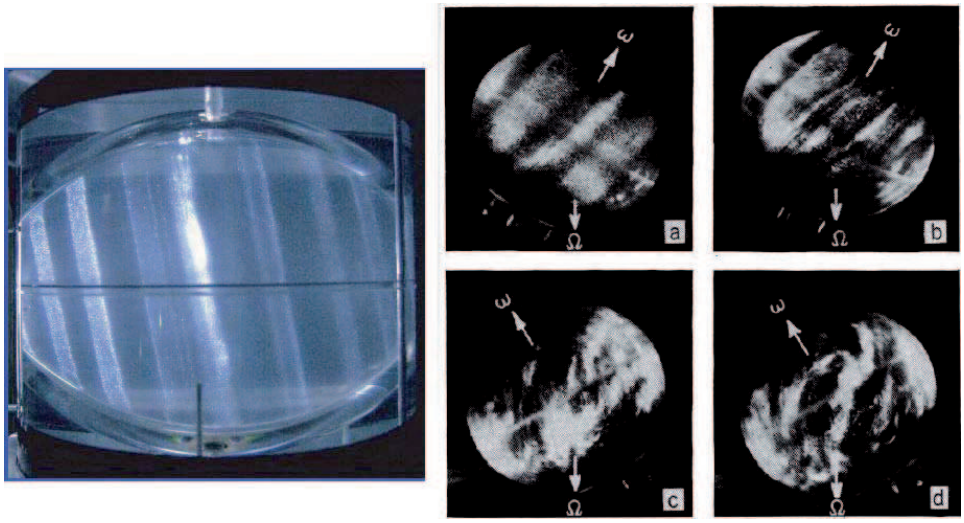

Figure 1.17: A gauche : cylindres géostrophiques dans un sphéroïde d'ellipticité 1/25 observés par Noir (2000). A droite : visualisation de l'écoulement secondaire dans un sphéroïde d'ellipticité 1/25 en rotation à la vitesse angulaire $\Omega_1 = 60$ tr/min et en précession autour de l'axe $\mathbf{\Omega}_2$. (a) $\Omega_2 = -0.75$ tr/min régime d'écoulement géostrophique laminaire, (b) $\Omega_2 = -1$ tr/min régime turbulent bidimensionnel, (c) et (d) $\Omega_2 = -1.33$ tr/min régime turbulent développé, (voir Malkus, 1968).

(voir Stewartson & Roberts, 1963; Noir, 2000) appelé éruption de couche limite.

Bondi (1953) a alors proposé que l'éruption de couche limite puisse se propager en volume en restant localisée sur des surfaces caractéristiques. Walton (1975) et Kerswell (1995) ont confirmé la possibilité d'un tel mécanisme et Tilgner (1999*b*,*c*) l'a vérifié numériquement. Tilgner (2000*a*) a montré que ces zones de cisaillement peuvent être décrites comme des paquets d'ondes inertielles localisées dans l'espace, et dont les réflexions successives induisent une diminution de leurs amplitudes (voir Phillips, 1953). Une étude numérique menée par Noir *et al.* (2001*b*) visant à déterminer la taille des zones de cisaillement ainsi que l'amplitude du champ de vitesse à l'intérieur de ces zones a validé le processus de génération non-linéaire des mouvements géostrophiques dans la couche limite.

Néanmoins le mécanisme physique à l'origine de l'instabilité conduisant à l'apparition de la turbulence reste inconnu. Des études numériques (voir Tilgner & Busse, 2001; Lorenzani & Tilgner, 2001, 2003) sur les instabilités hydrodynamiques dans une cavité ellipsoïdale en precession ont confirmé l'existence d'une instabilité inertielle (les ondes inertielles ayant été observées expérimentalement par Noir *et al.* (2001*a*)) déja prédite par Kerswell & Barenghi (1995) et ont montré que d'autres mécanismes d'instabilité étaient possibles.

A notre connaissance aucun mécanisme physique n'a été identifié pour expliquer l'instabilité d'un fluide dans un sphéroïde en précession ; le problème reste donc ouvert.

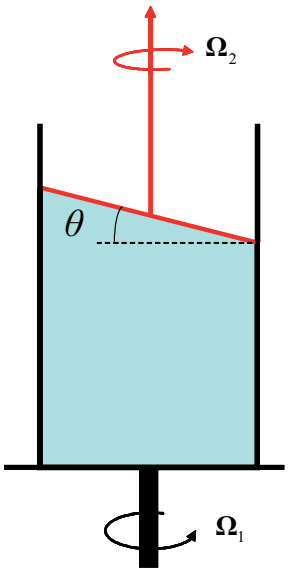

Figure 1.18: Expérience de McEwan (1970). Le cylindre tourne à la vitesse angulaire Ω_1 (par rapport à un référentiel fixe) autour de son axe de révolution. Son couvercle supérieur est incliné par rapport à l'horizontale d'un angle θ et tourne à la vitesse Ω_2 par rapport au cylindre. Ce système est équivalent à un forçage par précession.

1.4.2 Dans un cylindre

Le schéma de principe d'un cylindre en précession est représenté sur la figure 1.1.

Écoulement de base

Les premiers travaux expérimentaux dans un cylindre ont été obtenus par McEwan (1970). Son expérience est représentée sur la figure 1.18. Elle consiste à exciter un fluide placé dans un cylindre en rotation propre tournant à une vitesse angulaire Ω_1 dans un référentiel fixe, grâce à un couvercle incliné par rapport à l'axe du cylindre, et tournant à une vitesse Ω_2 dans le référentiel du cylindre. Une théorie linéaire montre que ce type de forçage est équivalent à un forçage par précession. Cette étude pionnière a montré qu'à la rotation solide du fluide se superposent des modes sinusoïdaux correspondant aux ondes inertielles (aussi appelées modes de Kelvin en géométrie cylindrique), dont la longueur d'onde axiale dépend des fréquences Ω_1 et Ω_2. Ces modes sont bien visibles sur la figure 1.19 issue des travaux de McEwan (1970). Pour certains rapports de fréquences Ω_2/Ω_1 dépendants du rapport d'aspect h du cylindre la période d'oscillation d'un mode peut diverger. On dit alors que le cylindre est résonnant. Pour observer les résonances des modes, McEwan (1970) a fixé un rapport de fréquences et a fait varier le rapport d'aspect de son cylindre en positionnant le couvercle incliné à différentes hauteurs. Il a montré que la prédiction de la position de ces résonances par Kelvin (1880) était en très bon accord avec les expériences (voir figure 1.20). Grâce à une sonde thermique positionnée dans

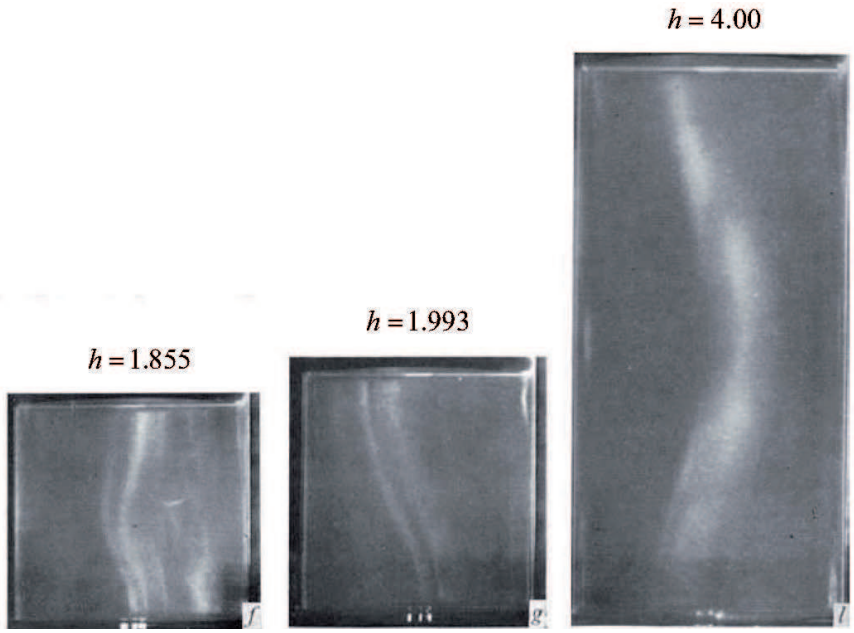

Figure 1.19: Visualisations des modes de Kelvin excités dans un cylindre en rotation par un couvercle incliné en faible rotation, obtenues par McEwan (1970) pour différents rapports d'aspect h.

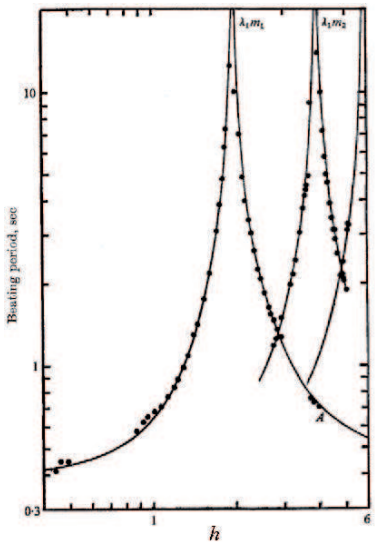

Figure 1.20: Période d'oscillation du premier mode de Kelvin (mode ayant la structure la plus simple) en fonction du rapport d'aspect $h = hauteur/rayon$. $\Omega_1 = 16.9$ rad/s, $\Omega_2 = -16.9$ rad/s, $\theta = 1.96°$. La théorie linéaire est représentée par la courbe en trait continu et les expériences de McEwan (1970) sont représentées par des points. Un mode est résonnant quand sa période d'oscillation diverge.

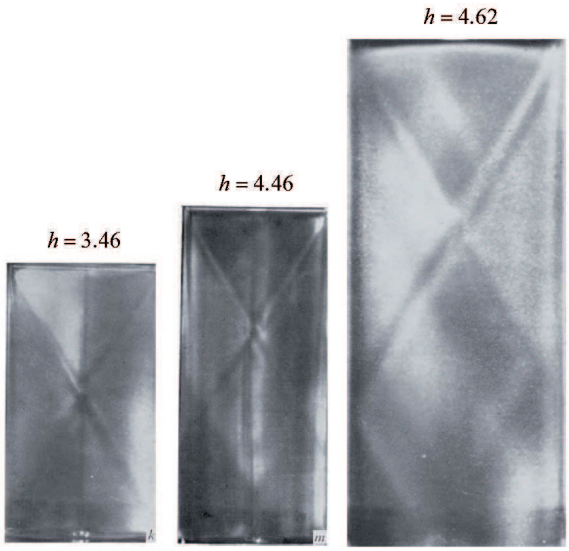

Figure 1.21: Surfaces caractéristiques observées par McEwan (1970). Les surfaces caractéristiques se propagent depuis les coins supérieurs du cylindre et s'atténuent après une réflexion sur une paroi.

l'écoulement McEwan (1970) a également pû mesurer l'amplitude des modes de Kelvin. Ses mesures ont montré que l'amplitude du mode forcé est bien prédite par la théorie linéaire non-visqueuse lorsque l'on est autour des résonances et que cette amplitude est $O(\theta)$. A une résonance, cette théorie ne permet plus de prédire la saturation en amplitude du mode forcé. Il est alors nécessaire d'inclure les effets visqueux et non-linéaires pour sa détermination. La prise en compte des effets visqueux par Kudlick (1966), Greenspan (1968) et Gans (1970*b*) a montré que la saturation en amplitude est $O(Re^{1/2})$; cela a été vérifié expérimentalement par Fultz (1959); McEwan (1970); Kobine (1995) et numériquement par Kerswell & Barenghi (1995). La détermination analytique de l'amplitude de saturation avec effets visqueux et non-linéaires est l'objet du chapitre 2 de cette étude.

Notons que pour certains rapports d'aspect, McEwan (1970) a observé (en appliquant un champ électrique de 1 kV/cm entre le bas et le haut du cylindre) des surfaces caractéristiques issues des coins supérieurs du cylindre (voir figure 1.21). Il a mesuré la largeur de ces bandes caractéristiques grâce à un micro-densimètre et a montré une dépendance en $Re^{-1/3}$, comme prédit par Wood (1965, 1966). Il a de plus observé que le cosinus de l'angle entre les surfaces caractéristiques et le vecteur rotation $\mathbf{\Omega}_1$ (i.e. angle γ des ondes inertielles fixé par l'équation (1.16)) évolue linéairement avec la fréquence d'excitation $\omega = (\Omega_1 - \Omega_2)/\Omega_1$. Ces surfaces caractéristiques n'ont jamais été observées dans nos expériences de précession. Nous pensons donc qu'elles sont dues à un cisaillement entre la paroi latérale du cylindre et le couvercle incliné ; ce cisaillement se propage alors en volume en restant localisé sur des surfaces caractéristiques.

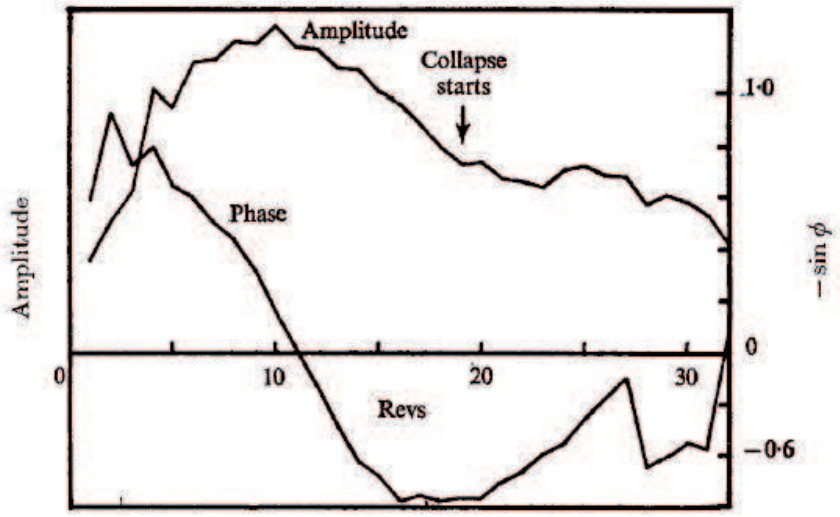

Figure 1.22: Évolution de l'amplitude et de la phase du mode de base en fonction du nombre de révolutions du cylindre. Le phénomène de décroissance soudaine de l'amplitude a été appelé phénomène de "resonant collapse" par McEwan (1970) et est lié à l'apparition de l'instabilité dans le cylindre.

Écoulement instable

McEwan (1970) a montré que l'écoulement de base (i.e. mode de Kelvin résonnant) devient instable lorsque le nombre de Reynolds augmente, menant à un écoulement très désordonné, et possédant de petites structures comparé à la taille du cylindre. L'apparition relativement brutale de ce désordre a suggéré à McEwan (1970) de nommer ce phénomène le "resonant collapse". Il se traduit par une violente chute de l'amplitude du mode de base comme on peut le voir sur la figure 1.22 et par l'apparition d'un écoulement purement azimutal.

Pour vérifier que les observations de McEwan (1970) dans un cylindre avec un couvercle incliné se retrouvent dans un cylindre en précession, Manasseh (1992, 1994, 1996) a construit un dipositif expérimental de précession. Dans ses expériences, le cylindre possède une rotation propre Ω_1 et précesse à la vitesse angulaire Ω_2 avec un angle de précession inférieur à 10°. Comme McEwan (1970), il a observé l'écoulement de manière qualitative en injectant des particules réfléchissantes dans le cylindre, marquant ainsi les structures de l'écoulement. Manasseh a d'abord confirmé que la théorie linéaire était correcte : les modes de Kelvin sont toujours présents et leur amplitude devient infinie aux rapports de fréquence prédits théoriquement. Il a ensuite étudié comment cet écoulement de base se déstabilise (ce qu'il a appelé explosion turbulente de l'écoulement au lieu de "resonant collapse"). Il a suggéré qu'en fonction du rapport Ω_2/Ω_1 et du rapport d'aspect du cylindre il existe de nombreux scénarios menant à l'explosion de l'écoulement de base. Il a identifié (visuellement) 7 scénarios possibles qu'il a nommés par une lettre allant de A à G. Le développement temporel du "breakdown" de type A est représenté sur la figure 1.23. Il semble que l'écoulement principal excite des

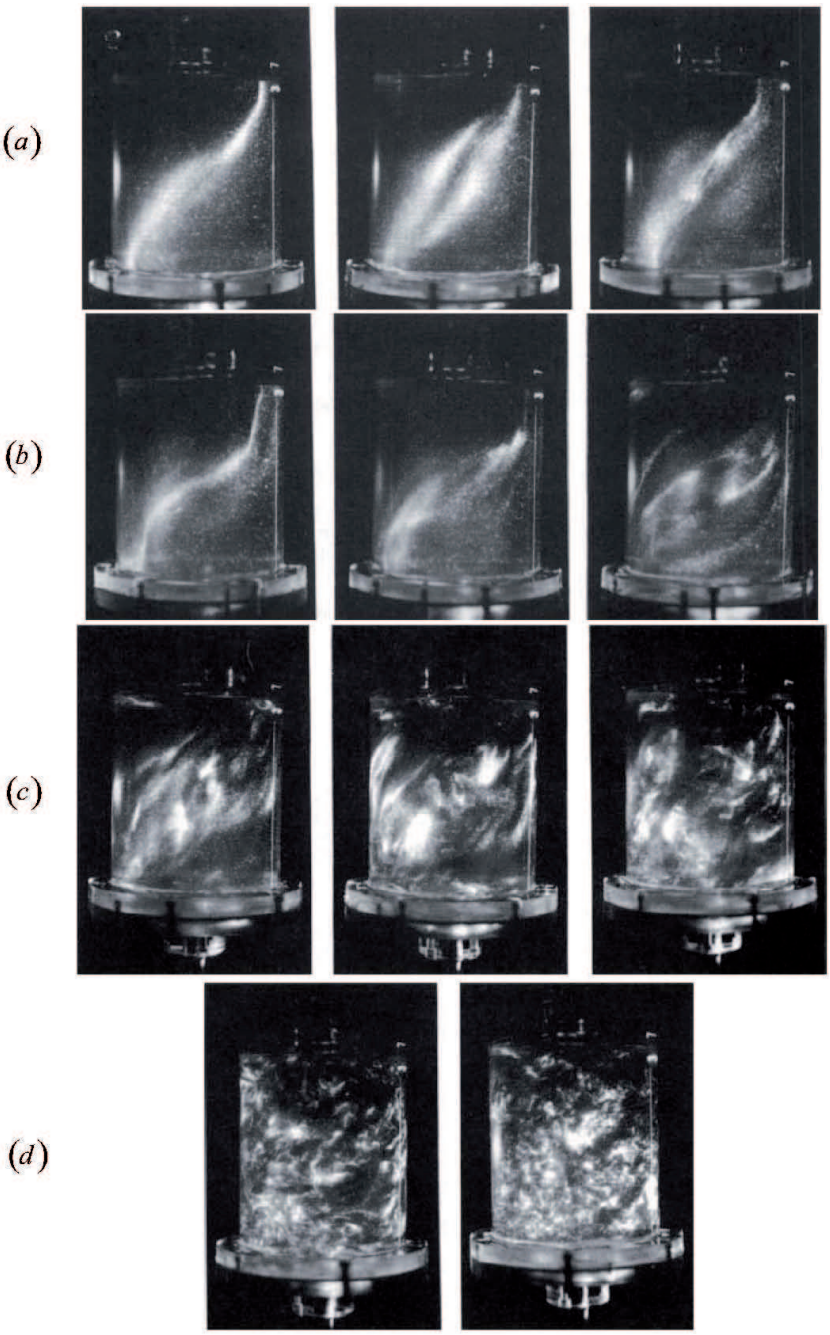

Figure 1.23: Visualisation par particules réfléchissantes et en fonction du temps de l'instabilité d'un fluide dans un cylindre en précession par Manasseh (1992). (a) Écoulement de base : mode de Kelvin forcé, (b) développement de l'instabilité, (c-d) écoulement turbulent. "Breakdown" de type A selon la classification de Manasseh (1992).

modes avec des longeuurs d'onde plus faible, ce qui crée des petites échelles de longueur qui dégénèrent en un écoulement turbulent. Manasseh a aussi découvert des régimes dans lesquels l'écoulement se déstabilise vers un écoulement turbulent puis se relaminarise, puis se redéstabilise, etc. ; comme cela a été observé par Malkus (1968) dans le cas d'un sphéroïde en précession ou encore par Eloy *et al.* (2000) dans le cas de l'instabilité elliptique. Dans la suite de notre étude nous parlerons d'un phénomène d'intermittence.

Comme les mesures de Manasseh étaient uniquement qualitatives, Kobine (1995, 1996) a repris un dispositif expérimental similaire et a mis en place un système de mesures de vitesse ponctuel par de la Vélocimétrie Laser Doppler. Ces résultats ont permis de valider une fois de plus la théorie linéaire. Kobine a aussi montré que la viscosité a un effet très faible en dehors des résonances, mais que la viscosité crée des couches de cisaillement lorsque le cylindre est résonnant, comme prédit théoriquement. Il a enfin mesuré la vitesse de l'écoulement azimuthal (déjà observé par McEwan (1970)) qui apparaît proche des résonances à cause d'effets non-linéaires et qui se manifeste lors de l'apparition de l'instabilité. Kobine a alors proposé que l'écoulement géostrophique puisse être déstabilisé par instabilité centrifuge. D'autres scénarios ont été proposés, notamment par McEwan (1970) qui explique qu'un mode de Kelvin peut participer à un mécanisme de résonance triadique avec deux autres modes (comme cela est le cas pour l'instabilité elliptique) pour aboutir à une instabilité. Une succession de déstabilisations par résonance triadique entre modes de Kelvin pourrait alors expliquer la transition vers la turbulence. De telles instabilités secondaires par résonance triadique entre modes de Kelvin ont été vérifiées numériquement par Kerswell (1999) en considérant des faibles nombres d'Ekman ($Ek < 10^{-4}$). Il démontre que si A est l'amplitude d'un mode de Kelvin, le taux de croissance de l'instabilité est proportionnel à A. Si l'amplitude A est inférieure (resp. supérieure) à une amplitude critique, l'écoulement est stable (resp. instable). La difficulté réside alors dans la détermination de cette amplitude critique qui dépend notamment des effets visqueux de couche limite. Ceci sera l'objet du chapitre 4 de notre étude. Dans le cas particulier d'un mode forcé par précession Kerswell (1999) a aussi démontré que l'apparition du mode géostrophique visualisé par McEwan, Manasseh et Kobine intervient après l'apparition de l'instabilité, sauf dans le cas limite non-visqueux.

Un autre mécanisme d'instabilité a été proposé par Mahalov (1993). Ce dernier explique que le cisaillement présent dans un écoulement enfermé dans un cylindre en précession peut se coupler avec deux modes de Kelvin pour donner un mécanisme d'instabilité par résonance triadique. En considérant un cylindre infini, Mahalov (1993) montre que l'intéraction triadique entre le cisaillement et des modes ayant des nombres d'ondes azimutaux $m = 0$ et $m = 1$ peut conduire à une instabilité. Nous reviendrons sur ce résultat dans le chapitre 6 de cette étude.

En conclusion, il existe assez peu de données expérimentales sur l'écoulement dans un cylindre en précession. De plus la plupart des données sont qualitatives (visualisations directe) ou, dans le meilleur des cas, sont des mesures ponctuelles de vitesse. Enfin il semble que les récentes études ex-

périmentales de Manasseh et Kobine n'aient pas débouché sur des modèles théoriques pour expliquer le phénomène d'instabilité.

1.5 Plan de l'étude

Le but de cette étude est de comprendre la dynamique d'un fluide dans un cylindre en précession. Cette étude est une résolution d'un problème fondamental de forçage d'un écoulement tournant et doit permettre de comprendre la transition vers la turbulence que l'on observe dans de tels écoulements. Nous espérons également que cette étude permettra de mieux comprendre l'instabilité d'un fluide dans un sphéroïde en précession, qui a notre connaissance n'est pas encore expliquée. A long terme, cette étude devrait permettre d'apporter des éléments de réponse sur la stabilité des objets volants en précession, l'influence de la précession sur la dynamique du noyau liquide terrestre ou encore sur la dynamique des cyclones.

L'écoulement de base (i.e. l'écoulement avant l'apparition de l'instabilité) d'un fluide dans un cylindre en précession est étudié théoriquement et les résultats sont comparés aux expériences dans le chapitre 2.

Dans le chapitre 3 l'instabilité de précession est étudiée d'un point de vue expérimental grâce à des mesures de Vélocimétrie par Images de Particules.

Dans le chapitre 4 une analyse linéaire de stabilité est développée afin de prédire les caractéristiques de l'instablité. Les résultats issus de cette analyse sont confrontés aux données expérimentales. Une analyse faiblement non-linéaire est également présentée dans ce chapitre afin de prédire la dynamique de l'écoulement instable.

Le chapitre 5 s'intéresse à l'instabilité de précession lorsque l'écoulement de base correspond à un mode de Kelvin différent de celui étudié dans les chapitres 3 et 4. Les prédictions théoriques issues de l'analyse linéaire de stabilité du chapitre 4 sont comparées avec des résultats expérimentaux.

Le chapitre 6 revient sur l'étude théorique non-visqueuse de Mahalov (1993) qui s'est intéressé à la stabilité de l'écoulement de cisaillement vertical dans un cylindre en précession. Nous étendons son étude obtenue dans le cas d'un cylindre infini au cas d'un cylindre de dimension finie et nous comparons les prédictions théoriques avec les résultats expérimentaux.

Nous concluons et donnons les perspectives de l'étude de la dynamique d'un fluide dans un cylindre en précession dans le chapitre 7.

2. ÉCOULEMENT DE BASE D'UN FLUIDE DANS UN CYLINDRE EN PRÉCESSION

Ce chapitre est consacré à une étude théorique et expérimentale de l'écoulement de base d'un fluide dans un cylindre en précession. Ce chapitre reprend une publication parue dans la revue *Journal of Fluid Mechanics* sous le titre "A rotating fluid cylinder subject to weak precession". Dans ce papier le nombre de Rossby est noté ε. Cependant, afin d'unifier les notations dans le manuscrit de thèse, nous le noterons Ro, comme dans tous les autres chapitres de cette étude.

Abstract

In this paper, we report experimental and theoretical results on the flow inside a precessing and rotating cylinder. Particle Image Velocimetry measurements have revealed the instantaneous structure of the flow and confirmed that it is the sum of forced inertial (Kelvin) modes, as predicted by the classical linear inviscid theory. But this theory predicts also that the amplitude of a mode diverges when its natural frequency equals the precession frequency. A viscous and weakly nonlinear theory has therefore been developed at the resonance. This theory has been compared to the experimental results and shows a good quantitative agreement. For low Reynolds numbers, the mode amplitude scales as the square root of the Reynolds number due to the presence of Ekman layers on the cylinder walls. When the Reynolds number is increased, the amplitude saturates at a value which scales as the precession angle power one third for a given resonance. The nonlinear theory also predicts the forcing of a geostrophic (axisymmetric) mode which has been observed and measured in the experiments. These results allow to fully characterise the flow inside a precessing cylinder in all regimes as long as there is no instability.

2.1 Introduction

In the field of aerospace, the stability of spinning spacecrafts containing propellant liquids is still a topical question. For instance, the attitude of spinning satellites (see Stewartson, 1958; Gans, 1984; Garg *et al.*, 1986; Agrawal, 1993; Bao & Pascal, 1997) is likely to be disrupted by the hydrodynamics of the inside fluid. Consequently, a good understanding of the behaviour of such a fluid–structure coupled system requires a precise knowledge of the dynamics of the rotating contained fluid. Moreover, rotating fluid dynamics lies far beyond the scope of aerospace : a lot of atmospheric phenomena (hurricanes, tornadoes), are closely connected to this class of problems, due to the predominant role played by the Coriolis force at low Rossby numbers (Vanyo, 1993).

First experimental and theoretical studies on rotating fluids date from the end of the 19th century. Lord Kelvin (1880) suggested that the flow of a disturbed rotating fluid could be decomposed into a sum of so-called normal Kelvin modes (i.e. inertia waves), each of them corresponding to a well defined frequency which is always less than twice the basic rotation frequency. The inviscid approach of Kelvin can be extended in the limit of large Reynolds numbers by taking into account viscous boundary layers on the walls of the container as shown by Kudlick (1966) and Greenspan (1968). A large set of experimental and numerical studies in the case of a completely filled cylinder (see Fultz, 1959; McEwan, 1970; Kobine, 1995; Kerswell & Barenghi, 1995) has confirmed the values of the frequencies and viscous decay rates predicted by these theories.

An important aspect of these rotating flows is that Kelvin modes have been shown to become unstable for large Reynolds numbers. McEwan (1970) first showed that when a rotating fluid cylinder is forced at a given frequency

on one of its ends, Kelvin modes are forced. One of these Kelvin modes can become resonant if its wavelength matches the height of the cylinder. This leads to a *resonant collapse* (i.e. a breakdown of the initial mode) degenerating into a fine-scale disordered flow. In some cases, this very disordered flow can relaminarise into solid body rotation again leading to a cycle of instability, breakdown and relaminarisation. These behaviours have also been reported when the Kelvin modes are forced in a partly filled and tilted cylinder (Thompson, 1970) or in completely filled cylinder in precession (Manasseh, 1992; Mahalov, 1993) or when they are the natural modes of an instability such as the elliptic instability (Malkus, 1989; Eloy *et al.*, 2000; Kerswell, 2002; Eloy *et al.*, 2003). The physical mechanism leading to the breakdown is still unclear but several scenarios have been proposed. Kerswell (1999) proposed that a given Kelvin mode can trigger a triad resonance with two other Kelvin modes leading to an instability (this mechanism bears similarity with the mechanism of the elliptic instability). The triggered modes can themselves be unstable leading to a secondary instability and eventually to a tertiary instability, and so on. This cascade of bifurcation may explain the transition to turbulence observed in these flows. When nonlinear effects are important, another aspect of these rotating flows is the generation of a geostrophic motion which slows down the main solid body rotation and modifies its radial profile. Kobine (1995, 1996) has proposed that, due to this geostrophic motion, the main flow can be modified enough to cause a centrifugal instability responsible of the breakdown. Finally the observed breakdown could also be due to a boundary layer instability near the wall of the container. So far, there is no clear experimental evidence to support one of these scenarios.

The picture is different for an ellipsoidal container since there are no corners to prevent the azimuthal circulation. For an inviscid fluid, Poincaré (1910) showed that there exists a class of solution with uniform vorticity whose direction rotates around the precession axis. In a real fluid, the presence of viscous boundary layers selects a unique solution in which the viscous and pressure torques balance the precessional torque (Lorenzani & Tilgner, 2001). However, some (conical) inertial waves are still generated by the breakdown of the Ekman layer at a critical latitude (Noir *et al.*, 2001*b*). It can lead to an instability consisting of cylindrical waves propagating around the axis of rotation of the fluid (Lorenzani & Tilgner, 2001) and generates a strong turbulent flow (Goto *et al.*, 2007). It is thus unclear if this flow will be unstable through local destabilisation of the Ekman layers or through a global instability (such as a triadic resonance) for large Reynolds numbers.

In this paper, we address the basic laminar flow in the case of a precessing cylinder full of water. This flow can be decomposed into a sum of Kelvin modes which are resonant if their wavelength is equal to $2H$, $2H/3$, $2H/5$, etc (where H is the cylinder height). By performing Particle Image Velocimetry (PIV) measurements in the precessing frame, we investigate the primary inertial flow in both situations : far from a resonance, where the linear inviscid theory is valid, then close to a resonance, where viscous and nonlinear effects determine the amplitude of the resonant Kelvin mode. Gans (1970*b*) first gave a theoretical interpretation of the amplitude saturation close to the

resonance by taking into account the viscous effects only. In this paper, the derivation of the amplitude equations is performed by considering both viscous and nonlinear terms. We have distinguished two different regimes of saturation. At low Reynolds numbers, the main mode amplitude is saturated by viscosity (which is consistent with Gans' results (Gans, 1970*b*), whereas the nonlinear effects prevail at higher Reynolds numbers (Wood, 1965). Such nonlinear couplings of Kelvin modes have been largely studied in the context of the elliptic instability (Waleffe, 1989; Eloy *et al.*, 2003; Mason & Kerswell, 1999).

The paper is organized as follows. Section 2.2 is dedicated to the general problem formulation. The equations governing the fluid motion are first introduced then the whole experimental setup is presented in details in §2.2.2. In §2.3, the linear inviscid theory is presented to express the Kelvin mode amplitudes when the flow is non-resonant. Experimental flow fields are then shown and compared to these theoretical predictions. In §2.4 the viscous and nonlinear amplitude equations are derived and compared to the PIV velocity fields measured at the resonance. Finally our results are discussed in §2.5.

2.2 Presentation of the problem

2.2.1 Formulation

We address the equations governing the flow inside a precessing cylinder full of fluid of density ρ and kinematic viscosity ν. This problem is illustrated in figure 2.1(a). In the laboratory reference frame (O, $\hat{\mathbf{x}}$, $\hat{\mathbf{y}}$, $\hat{\mathbf{z}}$), we consider a turntable rotating at constant angular frequency $\Omega_2 = \dot{\psi}$ around the axis $(O, \hat{\mathbf{z}})$. In the reference frame of this turntable, a cylinder of radius R_c and height H rotates around its own axis $(O', \hat{\mathbf{k}})$ at the angular frequency $\Omega_1 = \dot{\phi}$. The angle between these two axes of rotation is the nutation angle θ. As shown in figure 2.1(a), the angles (ψ, θ, ϕ) are the classical Euler coordinates of the cylinder.

In the reference frame of the cylinder (O', $\hat{\mathbf{i}}$, $\hat{\mathbf{j}}$, $\hat{\mathbf{k}}$), the radius vector $\mathbf{R}$ is located by its cylindrical coordinates (R, φ, Z) as shown in figure 2.1(b). The time-dependent rotation vector of the cylinder in the laboratory frame is

$$\boldsymbol{\Omega} = \Omega_1 \hat{\mathbf{k}} + \Omega_2 \hat{\mathbf{z}}. \tag{2.1}$$

Since the cylinder frame is non galilean, the Navier–Stokes equations satisfied by the velocity field $\mathbf{U}(\mathbf{R}, T)$ and the pressure field $P(\mathbf{R}, T)$ take the following form

$$\frac{\partial \mathbf{U}}{\partial T} + (\mathbf{U}\cdot\boldsymbol{\nabla})\,\mathbf{U} + 2\,\boldsymbol{\Omega}\times\mathbf{U} + \boldsymbol{\Omega}\times(\boldsymbol{\Omega}\times\mathbf{R}) + \frac{\mathrm{d}\,\boldsymbol{\Omega}}{\mathrm{d}\,T}\times\mathbf{R} + \boldsymbol{\Gamma}_{O'} = -\frac{1}{\rho}\boldsymbol{\nabla}P + \nu\Delta\mathbf{U}, \tag{2.2a}$$

and

$$\boldsymbol{\nabla}\cdot\mathbf{U} = 0, \tag{2.2b}$$

with the boundary condition $\mathbf{U} = \mathbf{0}$ on the cylinder walls.

In the Navier–Stokes equation (2.2a), the first two terms are the usual inertial terms, the third and the fourth terms are the Coriolis and centrifugal acceleration respectively, the fifth term is due to the acceleration of

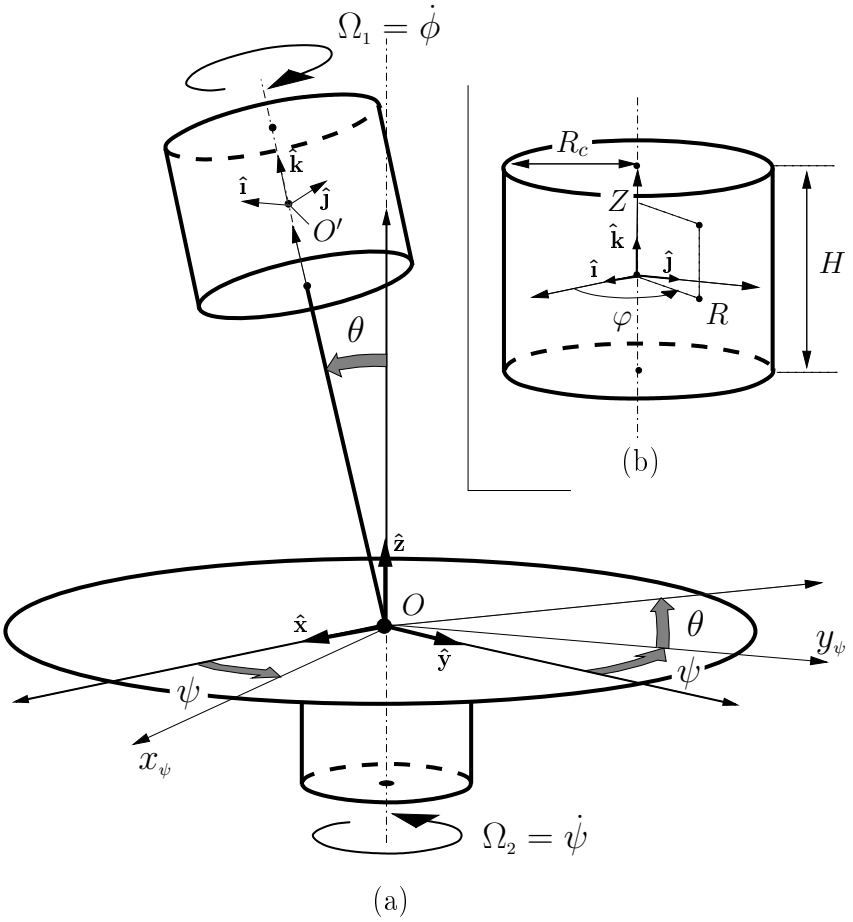

Figure 2.1: Sketch of the problem. (a) The cylinder of radius R_c and height H rotates about its axis at fixed angular frequency Ω_1. The precession rate Ω_2 and the nutation angle θ are also fixed. (b) Polar coordinates (R, φ, Z) defined in the cylinder rotating frame.

the rotation vector and $\mathbf{\Gamma}_{O'}$ refers to the acceleration of the centroid O' of the cylinder. Note that this latter term is potential and corresponds to a hydrostatic pressure $\mathbf{\Gamma}_{O'} \cdot \mathbf{R}$.

The previous equations are made dimensionless by using R_c and Ω^{-1} as characteristic length and time, where

$$\Omega = \mathbf{\Omega} \cdot \hat{\mathbf{k}} = \Omega_1 + \Omega_2 \cos\theta. \tag{2.3}$$

By using lowercase letters for the dimensionless quantities, the Navier–Stokes equations for the dimensionless velocity field $\mathbf{u}(\mathbf{r}, t)$ become

$$\begin{aligned} \frac{\partial \mathbf{u}}{\partial t} + 2\,\hat{\mathbf{k}} \times \mathbf{u} + \boldsymbol{\nabla} p &= -2Ro\zeta\omega r \cos(\omega t + \varphi)\,\hat{\mathbf{k}} \\ &+ \mathbf{u} \times (\boldsymbol{\nabla} \times \mathbf{u}) - 2Ro\zeta\,\boldsymbol{\delta} \times \mathbf{u} + \frac{1}{Re}\Delta\mathbf{u}, \end{aligned} \tag{2.4a}$$

and

$$\boldsymbol{\nabla} \cdot \mathbf{u} = 0, \tag{2.4b}$$

with

$$\omega = \frac{\Omega_1}{\Omega},\ Ro = \left|\frac{\Omega_2 \sin\theta}{\Omega}\right|,\ \zeta = \operatorname{sgn}\left(\frac{\Omega_2 \sin\theta}{\Omega}\right),\ \boldsymbol{\delta} = \cos\omega t\,\hat{\mathbf{i}} - \sin\omega t\,\hat{\mathbf{j}}, \tag{2.5 a–d}$$

and $Re = \Omega R_c^2/\nu$ the Reynolds number. In this dimensionless form, $h = H/R_c$ is the aspect ratio of the cylinder. The dimensionless pressure field $p(\mathbf{r}, t)$ is constructed to include all the potential terms

$$\begin{aligned} p = \frac{P}{\rho\Omega^2 R_c^2} - \frac{1}{2}r^2 &+ Ro\,|1-\omega|\,rz\cos(\omega t + \varphi) \\ &+ \boldsymbol{\gamma}_{O'} \cdot \mathbf{r} - \frac{1}{2}Ro^2[z^2 + r^2\sin^2(\omega t + \varphi)] + \frac{1}{2}\,\mathbf{u}^2, \end{aligned} \tag{2.6}$$

where $\boldsymbol{\gamma}_{O'} = \mathbf{\Gamma}_{O'}/R_c\Omega^2$ is the dimensionless acceleration of the cylinder centroid. The boundary condition of the velocity field is

$$\mathbf{u} = \mathbf{0} \quad \text{at the walls } (r = 1 \text{ or } z = \pm h/2). \tag{2.7}$$

The Navier–Stokes equations (2.4 *a, b*) with the boundary condition (2.7) govern the flow inside a precessing cylinder. This set of equations has been obtained without any approximation and is thus valid for any value of the experimental parameters. It is clear from these equations that the problem is entirely governed by four dimensionless parameters : the forcing amplitude Ro ; the forcing frequency ω ; the Reynolds number Re ; and the cylinder aspect ratio h. However, these equations cannot be solved easily in the general case and we will limit ourselves hereinafter to the case of asymptotically small amplitude Ro and large Reynolds number Re. This is the relevant limit if one is interested in the flow forced by the precession before it becomes unstable or at the onset of instability.

For the sake of clarity and brevity, a four-component formulation for the complex velocity-pressure field $\mathbf{v} = (\mathbf{u}, p)$ expressed in cylindrical coordinates will be used. With this formulation the Navier–Stokes equations (2.4 *a, b*) take the following form

$$\left(\frac{\partial}{\partial t}\mathcal{I} + \mathcal{M}\right)\mathbf{v} + \text{c.c.} = Ro\zeta\,\mathbf{F}_0 \mathrm{e}^{\mathrm{i}(\omega t+\varphi)} + \mathbf{N}(\mathbf{v},\mathbf{v}) + \left(Ro\zeta\,\mathcal{D}\,\mathrm{e}^{\mathrm{i}(\omega t+\varphi)} + \text{c.c.}\right)\mathbf{v} + \frac{\mathcal{L}\,\mathbf{v}}{Re} + \text{c.c.}, \quad (2.8)$$

where the operators $\mathcal{I}$, $\mathcal{M}$, $\mathcal{D}$, $\mathcal{L}$, the forcing vector $\mathbf{F}_0$ and the bilinear function $\mathbf{N}$ are defined in appendix 2.6.1. The symbol c.c. stands for the complex conjugate and the real velocity-pressure field is given by $\mathbf{v} + \text{c.c.}$

We will solve a linearised version of the above equation in §2.3.1 and the weakly nonlinear and viscous solution corresponding to the saturated resonant flow will be given in §2.4.1.

2.2.2 Experimental setup

The experimental setup is sketched in figure 2.2. It corresponds exactly to the configuration depicted in figure 2.1. A right-circular PMMA cylinder, filled with distilled water, rotates at the angular velocity Ω_1 around its axis and is mounted on a rotating platform. The cylinder axis is tilted relative to the axis of the platform with an angle θ. The platform, that ensures the precessing component of the motion, also rotates at a velocity Ω_2. The platform is mounted on a wide vertical axis in order to limit the vibrations of the structure at high precession velocities.

The angular frequency Ω_1 can be increased up to $60\,\mathrm{rad\,s^{-1}}$ and is measured with an accuracy of 0.1%. The precession frequency Ω_2 is limited to $6\,\mathrm{rad\,s^{-1}}$ and is measured with an accuracy of 0.2 % when the precession frequency is larger than $0.2\,\mathrm{rad\,s^{-1}}$. Each axis having its own driving motor, the angular velocities can be varied independently so that the dimensionless frequency ω can be varied over the whole range $[-2, 2]$. We used three different cylinders : a cylinder of aspect ratio $h = H/R_c = 1.989 \pm 0.3\%$ ($H = 9.14\,\mathrm{cm}$) has been used at first, but its principal resonance was found for a vanishing precessing frequency ($\omega \approx 1$). A second cylinder with aspect ratio $h = 1.8 \pm 0.7\%$ ($H = 8.27\,\mathrm{cm}$) has been thus designed to study this resonance. Finally, a third cylinder with the same aspect ratio 1.8 but smaller dimensions ($H = 2.7\,\mathrm{cm}$) has also been used to obtain data at smaller Reynolds numbers (by a factor almost 10). The thickness of the cylinder walls is extremely large (2 cm) in order to avoid shade areas in the light sheet (because of refraction on the cylindrical wall).

The acquisition computer is located on the rotating platform to limit the number of rotating electrical contacts and improve the quality of the data. The power is brought up to the platform by a rotating collector through the vertical axis and is used to supply the cylinder motor, the video camera and the electromagnet of the release device. The rotating collector also conveys back the signal from the video camera to an auxiliary screen, which is used for observation and optical adjustment of the PIV system.

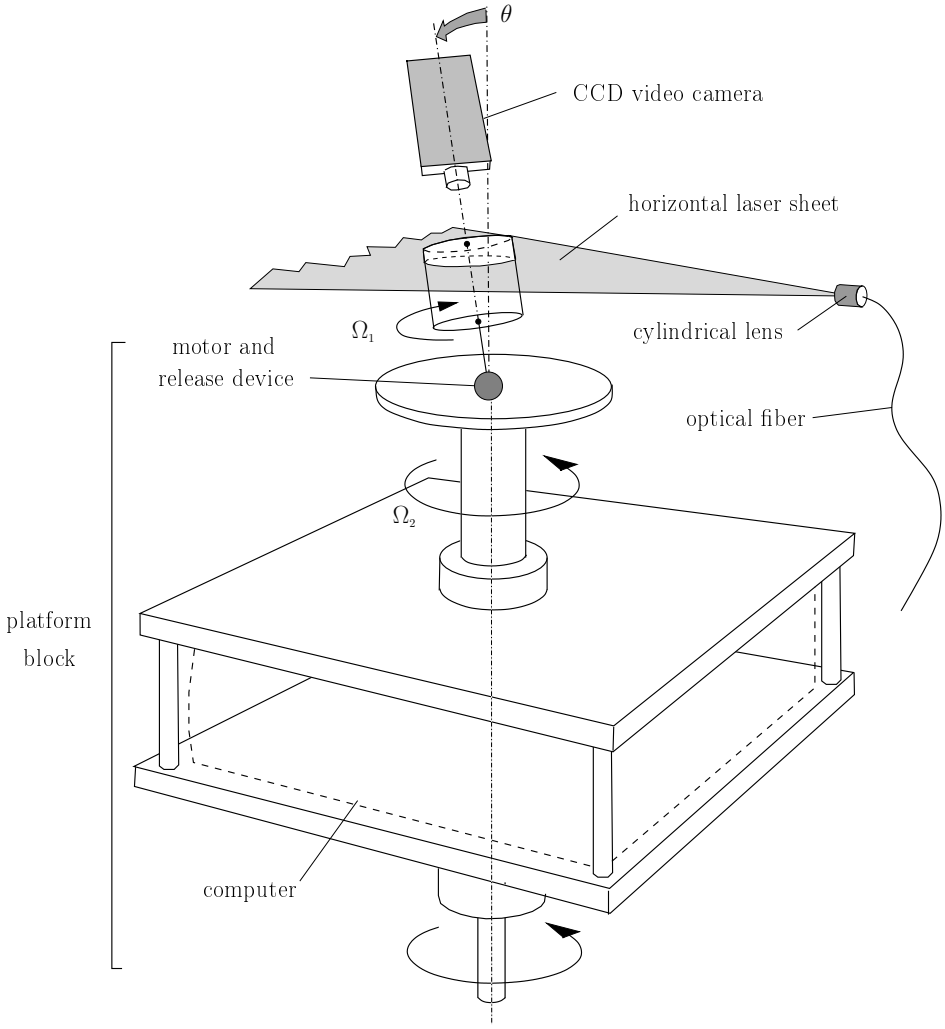

Figure 2.2: Sketch of the experimental setup. The cylinder is directly mounted on the axis of the motor which is located on the rotating platform, and can be tilted during the rotation of the platform. The camera, located above the cylinder is fixed in the platform frame of reference. The whole platform block, including the computer, rotates at angular frequency Ω_2.

A release device is mounted on the platform and is controlled externally, so that the cylinder can be tilted during the rotation of the platform. It allows the observation of the transient stage during which the observed Kelvin modes grow. The release device is composed of an electromagnet designed to keep the cylinder in a vertical position during the spin-up phase. Once the electromagnet is turned off, a drawback spring pulls the cylinder into its tilted position. The electromagnet is then turned on again to ensure the stability of the nutation angle θ during the experiment. This angle can be varied from 0 to 15 degrees. Due to the spring strength, we consider that the swing of the axis happens in a duration (about half a second) much smaller than the duration of the transient stage (varying from 3 to 50 seconds).

The PIV measurement system is schematically presented in figure 2.2. The fluid is seeded with small reflecting particles (Optimage Ltd.) of mean diameter 50μm and density $1000 \pm 20\,\mathrm{kg\,m^{-3}}$. They are illuminated with a light sheet of thickness 2 mm, created either by a Yag pulsed laser for large velocities or by an Argon Ion continuous laser (through an optical fiber) for small velocities. The laser beam goes through a cylindrical lens to provide the laser sheet. None of the lighting system is rotating so the laser sheet is fixed relative to the laboratory frame. As far as the tilt angle θ is not too large (smaller than 5 degrees), the laser sheet, due to its thickness, can be considered normal to the cylinder axis. This might introduce a bias at larger nutation angles and the laser sheet should then be created on the rotating platform with a set of mirrors. The altitude of the laser sheet can be varied along the height of the cylinder and was chosen in a subtle way, depending on the type of experiments that was done. First, to look at the dependence of the amplitude with the frequency ω, we had to take a sheet close to the center of the cylinder (in order to not be at a node of the Kelvin mode) : a good compromise was taken as $z = 0.12h$. Then, to study the first (resp. second) resonance of a Kelvin mode, we took $z = h/4$ (resp. $z = h/6$) in order to measure a maximum transverse velocity.

The images of particles are recorded by a PIV camera (Kodak Megaplus ES 1.0, 1008×1018 pixels) mounted on the rotating platform and aligned with the axis of the cylinder. The time interval between two successive images is relatively large (from 5 ms to 1 s) such that the cylinder rotates of approximately 20 degrees between the two images. This creates large displacements of the particles at the periphery of the cylinder (150 pixels), but the two images are rotated around the center of the cylinder in order to remove the solid body rotation of the particles. The PIV thus gives directly the velocity field in the cylinder reference frame. This procedure allows to measure very small velocities down to 1% of the velocity of the cylinder wall. Such measurements would not have been possible without the image rotation. The pairs of images are then treated by a cross-correlation algorithm detailed in Meunier & Leweke (2003) which gives velocity fields with 60×60 vectors.

To perform the acquisition of a PIV field, we proceed as follows. First the cylinder is kept vertical and rotates at Ω_1. The platform rotates at Ω_2 so that the angular velocity of the cylinder relative to the laboratory frame is $(\Omega_1 + \Omega_2)\,\hat{\mathbf{z}}$. Once the spin-up stage is completed, the cylinder is released to its tilted position. This allows to study the transient and the spin-up phase

independently.

Some preliminary visualisations were also performed with Kalliroscope particles, in order to check that the resonances were in good agreement with the linear inviscid theory, and to validate our set-up by comparison of these visualisations with those from the literature (Manasseh, 1992; Kobine, 1995). However, no quantitative new results were obtained and we will not present any of these visualisations in this paper.

2.3 Flow inside a non-resonant cylinder

2.3.1 Linear inviscid theory

We assume an asymptotically small forcing amplitude Ro and asymptotically large Reynolds number Re. In this limit, the velocity-pressure field $\mathbf{v}$ is $O(Ro)$ and the Navier–Stokes equation (2.8) becomes at first order in Ro

$$\left(\frac{\partial}{\partial t}\mathcal{I} + \mathcal{M}\right)\mathbf{v} = Ro\zeta\,\mathbf{F}_0 \mathrm{e}^{\mathrm{i}(\omega t+\varphi)}. \tag{2.9}$$

For an inviscid fluid, the no-slip boundary condition (2.7) becomes a condition of no outward flow

$$\mathbf{u}\cdot\mathbf{n} = 0 \quad \text{at the walls } (r=1 \text{ or } z=\pm h/2), \tag{2.10}$$

where $\mathbf{n}$ is an unitary vector normal to the wall.

Equations (2.9) and (2.10) form a linear system for the vector $\mathbf{v} = (\mathbf{u},\, p)$, with a forcing term. It admits a particular solution of the form

$$\mathbf{v}_{\text{part.}} = (0,\, 0,\, Ro\,\zeta\,\mathrm{i}\,r\,\mathrm{e}^{\mathrm{i}(\omega t+\varphi)},\, 0). \tag{2.11}$$

Unfortunately, this solution does not satisfy the boundary condition (2.10) in $z=\pm h/2$. Thus, one must complete this particular solution with a solution of the homogeneous equation (without forcing), so that the boundary condition at the upper and lower walls is satisfied. Due to the time and azimuthal dependence of the forcing, the homogeneous solution is to be searched as a sum of Kelvin modes of azimuthal wavenumber $m=1$ and angular frequency ω (see Greenspan, 1968). Using (2.10) and (2.11) and such a form of the homogeneous solution, one finds

$$\mathbf{v} = \mathbf{v}_{\text{part.}} + Ro\,\zeta\sum_{i=1}^{\infty} a_i \mathbf{v}_i(r,\,z)\mathrm{e}^{\mathrm{i}(\omega t+\varphi)}, \tag{2.12}$$

where $\mathbf{v}_i(r,\,z)\mathrm{e}^{\mathrm{i}(\omega t+\varphi)}$ is a Kelvin mode of axial wavenumber k_i, azimuthal wavenumber $m=1$ and frequency ω

$$\mathbf{v}_i(r,\,z) = \begin{pmatrix} u_i(r)\,\sin(k_i z) \\ v_i(r)\,\sin(k_i z) \\ w_i(r)\,\cos(k_i z) \\ p_i(r)\,\sin(k_i z) \end{pmatrix} \quad \text{with} \quad \begin{cases} u_i(r) = \mathrm{i}\dfrac{\omega r\delta_i\, J_1'(\delta_i r) + 2J_1(\delta_i r)}{r(\omega^2-4)} \\ v_i(r) = \dfrac{2r\delta_i\, J_1'(\delta_i r) + \omega J_1(\delta_i r)}{r(4-\omega^2)} \\ w_i(r) = \dfrac{\mathrm{i}\,k_i}{\omega} J_1(\delta_i r) \\ p_i(r) = J_1(\delta_i r) \end{cases}, \tag{2.13}$$

with $J_\nu(x)$ the Bessel function of the first kind and $J'_\nu(x)$ its x-derivative. The amplitude a_i of each Kelvin mode is

$$a_i = \frac{2\,\omega^2}{(\omega-2)(k_i^2+1)\,k_i\,J_1(\delta_i)\cos(k_i\,h/2)}, \tag{2.14}$$

the axial wavenumber k_i is the positive root of the constitutive relation

$$\delta_i^2 = \frac{4-\omega^2}{\omega^2}k_i^2, \tag{2.15}$$

and the radial wavenumber δ_i is solution of Kelvin's dispersion relation

$$\omega\,\delta_i\,J_1'(\delta_i) + 2J_1(\delta_i) = 0. \tag{2.16}$$

As long as $-2 < \omega < 2$, the dispersion relation admits an infinite, countable number of roots δ_i which are numbered in ascending order. A Kelvin mode can be associated to each root δ_i. The radial velocity $u_i(r)$ of the first Kelvin mode (corresponding to δ_1) is formed of one lobe and has no zero for $0 < r < 1$, the second Kelvin mode contains two lobes and one zero, the third contains three lobes and two zeros, and so on. The velocity field of the first Kelvin mode is shown in Fig. 2.3(a) : it contains two counter-rotating vortices, due to the presence of a single lobe of radial velocity and an azimuthal wavenumber $m = 1$. In the general case, the i-th Kelvin mode contains $2i$ vortices, and these Kelvin modes form a complete set. Their dispersion relation (2.15-2.16) is plotted on Fig. 2.4. The precession excites only the Kelvin modes with a given frequency ω corresponding to increasing wavenumbers k_i (as shown on Fig. 2.4 for $\omega = \omega_{3,4}$). When the wavenumber k_i of a Kelvin mode is equal to π/h, $3\pi/h$, $5\pi/h$... the mode 'fits' inside the height of the cylinder and becomes resonant. When ω is increased, each branch of the dispersion relation leads to an infinite number of resonances, with the wavenumber k_i of the Kelvin mode being equal to $\pi(2n-1)/h$ (n being an integer). Strictly speaking, each resonance labeled with (i,n) corresponds to a different Kelvin mode. In the following, all modes corresponding to the same branch of the dispersion relation (same index i) will be gathered in a family of modes which will be called the i-th Kelvin mode (for the sake of simplicity).

Equation (2.14) gives the amplitudes of the Kelvin modes forced by the precession. This equation is valid as long as the cylinder aspect ratio is not resonant, i.e. $\cos(k_i h/2) \neq 0$. In other words, the present linear analysis predicts a divergent amplitude of the i-th Kelvin mode if the forcing frequency ω is equal to one of the natural frequencies $\omega_{i,n}$ of the cylinder. Here, $\omega_{i,n}$ refers to the frequency obtained through (2.15) and (2.16) by taking $k_i = \pi(2n-1)/h$, with n an integer. One can show (Kudlick, 1966) that the set of natural frequencies $\omega_{i,n}$ is dense in the interval $-2 < \omega < 2$. This means that there is always a Kelvin mode arbitrary close to a resonance for any chosen forcing frequency ω. This emphasises the need of a theoretical prediction of the Kelvin mode amplitude at the resonance as it will be done in §2.4.1.

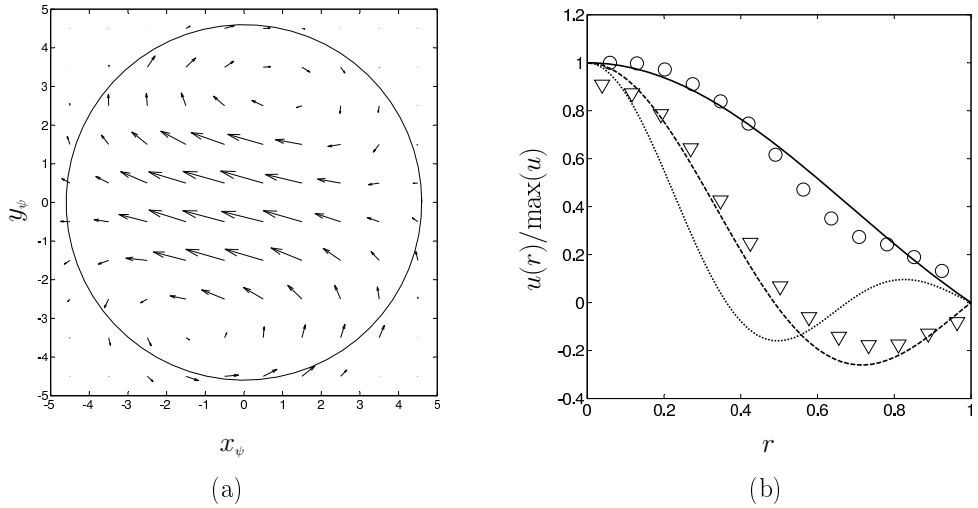

Figure 2.3: (a) Velocity field measured at $\omega = 0.9$, i.e. close to the first resonance $\omega_{1,1} = 0.996$ of mode $i = 1$ ($Re = 5500$, $h = 2$ and $Ro = 1.7 \times 10^{-3}$). (b) radial velocity along the x_ψ-axis. The circles $(\circ)$ correspond to the field displayed in (a). The triangles $(\triangledown)$ correspond to a velocity field at $\omega = 0.45$ with $Ro = 9.6 \times 10^{-3}$, i.e. close to $\omega_{1,2} = 0.51$. The related linear theoretical profiles are plotted in solid and dashed lines. The dotted line corresponds to the theoretical profile for the third Kelvin mode.

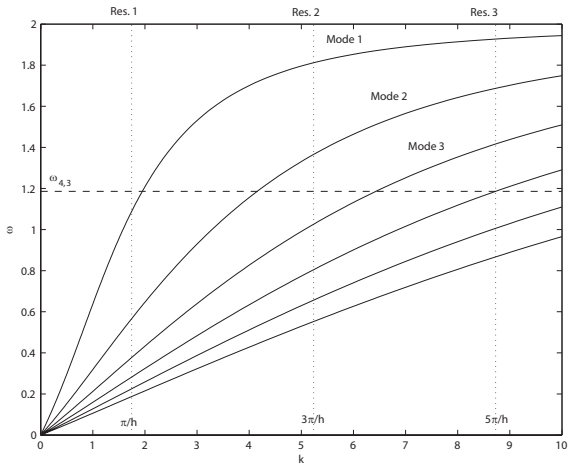

Figure 2.4: Dispersion relation of the Kelvin modes with an azimuthal wavenumber $m = 1$, given by (2.15) and (2.16). The dotted lines correspond to the resonances for an aspect ratio $h = 1.8$.

2.3.2 Kelvin modes : PIV measurements

We performed PIV measurements of the (u, v) transverse velocity field in the range $0.2 < \omega < 1.9$ and at Reynolds numbers between 2×10^3 and 2×10^5. The issue was, from the averaged velocity field in the permanent regime, to achieve the extraction of the linear amplitudes a_i of the main modes as defined by (2.14).

In figure 2.3(a) is shown the horizontal-velocity field at a frequency $\omega = 0.9$ close to the first resonance $\omega_{1,1} = 0.996$ of the mode $i = 1$, for $Re = 5500$ and $\theta = 1°$, the laser sheet being at an altitude $z = 0.29$. As previously mentionned, the flow in the reference frame of the cylinder mainly consists of two counter rotating vortices corresponding to the first Kelvin mode described by the above inviscid theory. However, it can be noted that the mode is not exactly aligned with the x_ψ-axis. This tilt angle is due to the viscous and nonlinear effects appearing at the resonance and will be analysed in detail in the next section. Figure 2.3(b) shows the radial velocity profile along the x_ψ-axis of this velocity field, as round symbols. The normalised value of the velocity decreases monotonically between $r = 0$ and $r = 1$, and is very close to the curve found theoretically (solid line) for the first Kelvin mode at this value of ω. Figure 2.3(b) also shows the radial velocity profile obtained for $\omega = 0.45$, i.e. close to the resonance of the second mode. It exhibits a positive lobe for $r < 0.5$, a negative lobe for $r > 0.5$ and a zero for $r \simeq 0.5$. This is characteristic of the second Kelvin mode, whose theoretical radial velocity is plotted as a dashed line. The third Kelvin mode (plotted as a dotted line) has three lobes of opposite radial velocity, but in this case the experimental data are very noisy and have not been plotted.

The presence of these Kelvin modes is better visualised by plotting the mean vorticity fields as done in Fig. 2.5, since the small scatter in the velocity field (such as a translation or a rotation) is hidden by the differentiation of $\mathbf{u}$ and the modification of the colorbar. The Kelvin modes are thus clearly distinguished by plotting the vorticity fields at various ω : even the fifth Kelvin mode is discernible at its first resonance $\omega_{5,1} = 0.2$. However, the spatial structure is arranged as a double spiral for the highest modes, whereas the theory predicts a series of lobes since the vorticity is expected to vanish for $\varphi = \pi/2 - \omega t$. In fact, such a spiral structure has already been observed theoretically for the Kelvin modes of a Gaussian vortex by Fabre *et al.* (2006). We thus think that this discrepancy might be due to a slight differential rotation in the geostrophic motion, coming from nonlinear and viscous effects.

For each experiment outside of the resonance, we have decomposed each velocity field into a sum of Kelvin modes. For this purpose, we use the fact that the Kelvin modes are orthogonal, such that the amplitude a_i of each Kelvin mode is simply given by the normalised scalar product $\langle \mathbf{u}_{\rm exp} | \mathbf{u}_i \rangle / \langle \mathbf{u}_i | \mathbf{u}_i \rangle$ (see appendix 2.6.2 for exact definition), where $\mathbf{u}_{\rm exp}$ (resp. $\mathbf{u}_i$) are the two transverse components of the measured (resp. theoretical) velocity field and the scalar product is defined as the average over the whole section. In fact, the method has to be slightly improved since this average can only be calculated for $r \leq 0.9$ instead of $r \leq 1$ (due to spurious vectors at the cylinder

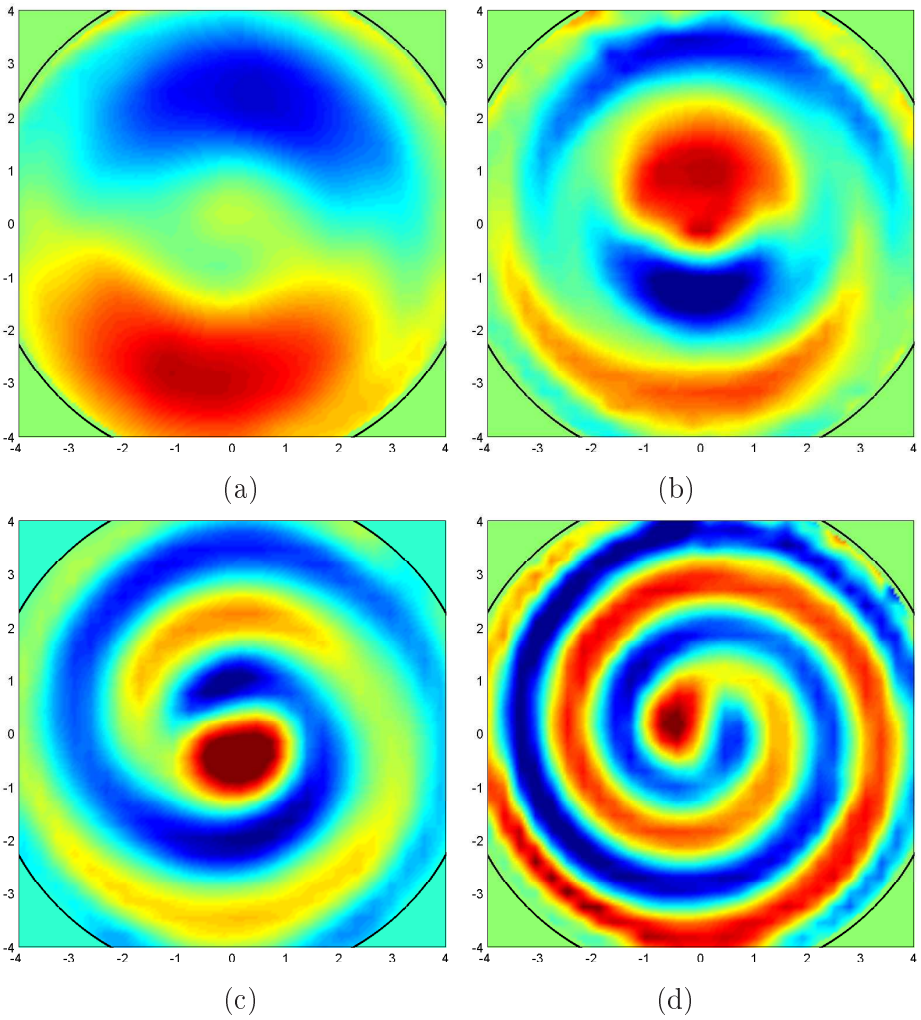

Figure 2.5: Vorticity fields of the first (a), second (b), third (c) and fifth (d) Kelvin mode, observed close to their first resonance (where k_i is close to π/h). Here, $h = 2$ and the flows are observed respectively for $\omega = 0.9, 0.45, 0.3, 0.2$. The Reynolds number is equal to 5500 (a), 11800 (b), 17700 (c) and 26600 (d) and the small parameter *Ro* is equal to 1.7×10^{-3} (a), 9.6×10^{-3} (b), 1.2×10^{-2} (c) and 1.4×10^{-2} (d).

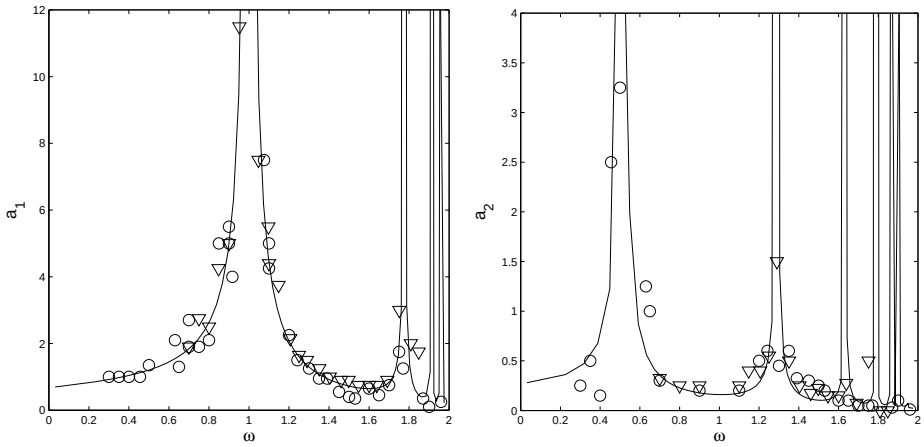

(a) (b)

Figure 2.6: Amplitude of the first mode $(i = 1)$ (a) and second mode $(i = 2)$ (b) for a cylinder of radius $R_c = 4.66$ cm and an aspect ratio $h = 2$. The angular velocity of the cylinder Ω_1 is equal to 2 rad s^{-1} ($\circ$) and 8 rad s^{-1} ($\triangledown$) so that the Reynolds number lies between 2×10^3 and 2×10^5. The solid line shows the prediction of the linear inviscid theory as done in §2.3.1.

wall) and because the mode can have a tilt angle α_i with respect to the x_ψ axis. This method, which is detailed in appendix 2.6.2, allows the precise determination of the amplitude and tilt angle of the first two Kelvin modes for each instantaneous velocity field.

In the permanent regime, the amplitude of the Kelvin modes is stationary and depends only on the frequency ω. It is plotted in Fig. 2.6 for the first two Kelvin modes and for two different Reynolds numbers. Despite a large scatter, experimental results are clearly independent of the Reynolds number outside of the resonances and very well predicted by the linear inviscid theory. As far as we know, this is the first exact measurement of the mode amplitudes forced by precession. The amplitudes measured at the resonances, for the first two modes are large and cannot be predicted by the linear inviscid theory. A nonlinear and viscous theory is necessary to predict the finite value of the amplitude in this case ; this is the scope of §2.4.

2.3.3 Transient stage

The experimental results can also give indications on the transient stage, since the amplitude a_i of each mode can be extracted for each instantaneous velocity field. Fig. 2.7(a) shows the temporal evolution of the amplitude of the first Kelvin mode just after the onset of the precession forcing, far from its resonance. The amplitude oscillates very rapidly and converges toward its permanent value a_1^0 which is plotted in Fig. 2.6. This curve can be fitted by a decaying exponential $a_1(t) = a_1^0[1 - \cos(\omega_t t)\mathrm{e}^{-t/t_s}]$ where ω_t corresponds to the frequency of the oscillation and t_s is the settling time. Since ω_t corresponds to the frequency in the rotating table reference frame, we have to subtract the dimensionalised angular velocity of the cylinder ω to obtain the

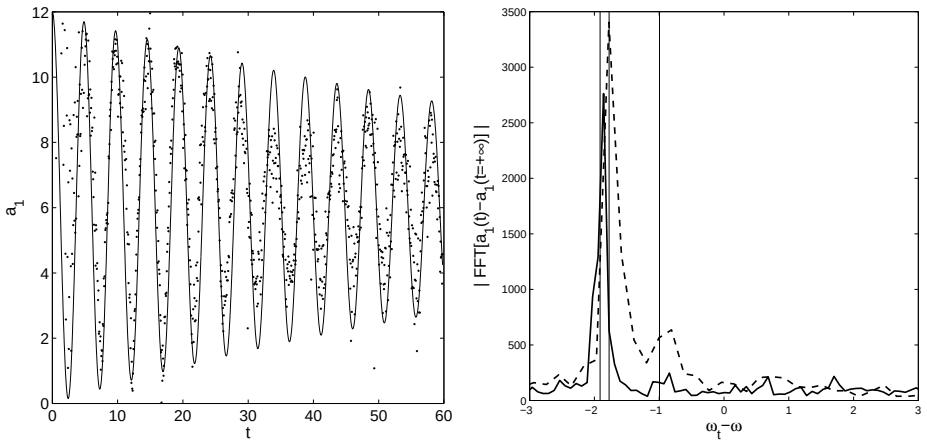

(a) (b)

Figure 2.7: (a) Transient dynamics of the first mode amplitude for a forcing frequency $\omega = 0.8$ and a Reynolds number $Re = 6640$. (b) Spectrum of the amplitude for $\omega = 0.8$ (solid line) and $\omega = 1.1$ (dashed line). The corresponding Reynolds numbers are $Re = 6640$ and $Re = 4830$ respectively. The Fourier transform of the temporal signals is plotted as a function of the transient dimensionless frequency $(\Omega_t - \Omega_1)/\Omega$ (given in the cylinder frame). The thin solid lines correspond to the first three resonances of the Kelvin mode $i = 1 : \omega_{1,1} = 0.996$, $\omega_{1,2} = 1.774$, $\omega_{1,3} = 1.912$. Here, $Ro = 3.5 \times 10^{-3}$ and $h = 2$.

frequency of the oscillation in the cylinder reference frame. By doing this, we find a non-dimensional frequency $\omega_t - \omega$ close to -1.8, and this was observed for any ω outside of a resonance. This value is close to the frequency of the second resonance of the first Kelvin mode $\omega_{1,2} = 1.774$. This can be understood by the fact that at $t = 0^+$, the velocity field which is equal to 0 in the bulk of the cylinder is the sum of the permanent solution (given by the inviscid theory) and a sum of free and decaying Kelvin modes with frequencies $-2 < \omega_{i,n} < 2$, n varying from 1 to infinity. Another methof to evaluate experimentally the initial amplitude of each free Kelvin mode is to plot the Fourier transform of the amplitude as a function of the dimensionalised frequency $\omega_t - \omega$, as shown on Fig. 2.7(b). A small peak is discernible around -1 (for both values of ω), which corresponds to the free Kelvin mode $\omega_{1,1} = 0.996$ and which is indicated by a thin solid line on the figure. A large peak is located near -1.8, which is close to all the other free Kelvin modes (with $i = 1$), whose frequencies $(\omega_{1,n})_{n\geq 2}$ lie between 1.774 and 2. It is thus not clear whether this large peak is due to a large amplitude of the second free Kelvin mode $\omega_{1,2}$ or to the constructive interference of all these modes $(\omega_{1,n})_{n\geq 2}$.

2.4 Flow inside a resonant cylinder

2.4.1 Nonlinear and viscous theory

As seen in §2.3.1, when the forcing frequency ω is equal to a natural frequency of the cylinder $\omega_{i,n}$, the linear inviscid theory predicts a divergent

amplitude of the i-th Kelvin mode. To predict correctly the mode amplitude in this case, one has to take into account the viscous effects or the nonlinear effects or both. As shown by Gans (1970*b*), if A_i is the mode amplitude, the secondary flow in the core of the cylinder due to the viscous boundary layers is $O(A_i Re^{-1/2})$. If the nonlinear effects are negligible, the correct scaling is obtained when this secondary flow is of the order of the forcing amplitude Ro. This gives a mode amplitude $A_i = O(RoRe^{1/2})$ which is $Re^{1/2}$ larger than the flow in the non-resonant case. On the other hand, if the viscous effects are negligible, the secondary flow is due to the nonlinear interaction of the Kelvin mode with itself. In this case, the secondary flow of same Fourier components is obtained at third order and is $O(|A_i|^2 A_i)$. This gives a mode amplitude $A_i = O(Ro^{1/3})$.

The distinguished scaling is obtained when the viscous and nonlinear effects are of same order, that is $Ro^{2/3} = O(Re^{-1/2})$. This leads to the definition of a viscous parameter η of order 1 and a slow time scale τ as follows

$$\eta = Re^{-1/2} Ro^{-2/3}, \quad \tau = Ro^{2/3}\, t. \tag{2.17a,b}$$

We now assume that the forcing frequency ω is close to a resonant frequency $\omega_{i,n}$ for the i-th Kelvin mode. The four-component velocity-pressure field corresponding to this Kelvin mode is expanded in powers of $Ro^{1/3}$ as follows

$$\mathbf{V}_i = Ro^{1/3}\,\mathbf{V}_1 + Ro^{2/3}\,\mathbf{V}_2 + Ro\,\mathbf{V}_3 + Ro^{4/3}\,\mathbf{V}_4 + \cdots . \tag{2.18}$$

The real velocity field is obtained by adding the complex conjugate in the above equation (the same is implicitly assumed in all the following equations). The nonlinear and viscous amplitude equations are obtained by injecting the above expansion (2.18) into the Navier–Stokes equation (2.8) and examining its different orders. The procedure is similar to the one used by Gans (1970*b*) except that here the nonlinear effects are included and the forcing frequency ω is arbitrary, whereas Gans (1970*b*) considered only the special case $\omega = 1$ which corresponds to a nutation angle $\theta = \pi/2$. The present analysis bears strong similarities with the weakly nonlinear analysis of parametric instabilities in rotating flows such as the elliptic instability (Waleffe, 1989; Sipp, 2000; Eloy *et al.*, 2003) or the instability of a rotating gas periodically compressed (Racz & Scott, 2007). Because this calculation is quite lengthy, most of its technical details have been postponed in appendices 2.6.3, 2.6.4 and 2.6.5.

Order $Ro^{1/3}$

At order $Ro^{1/3}$, the resonant flow satisfying the linear homogeneous equation

$$\left(\frac{\partial}{\partial t}\mathcal{I} + \mathcal{M}\right)\mathbf{V}_1 = \mathbf{0}, \tag{2.19}$$

is

$$\mathbf{V}_1 = A(\tau)\,\mathbf{v}_i\,\mathrm{e}^{\mathrm{i}(\omega t+\varphi)}, \tag{2.20}$$

where $\mathbf{v}_i$ is the i-th Kelvin mode given by (2.13), as it has been shown in §2.3.1. The amplitude A of the Kelvin mode $\mathbf{v}_i$ is assumed to vary on the

slow time scale τ and the other Kelvin modes (with $j \neq i$) are assumed to be non resonant so their amplitudes are given by (2.14).

The Kelvin mode $\mathbf{v}_i$ satisfies an inviscid boundary conditions. In a viscous boundary layer of thickness $O(Re^{-1/2})$, the complete flow is obtained by adding the viscous flow $\widetilde{\mathbf{V}}_1$ such that $\mathbf{V}_1 + \widetilde{\mathbf{V}}_1$ satisfies the viscous boundary condition (2.7). This viscous flow takes the form

$$\widetilde{\mathbf{V}}_1 = A\,\widetilde{\mathbf{v}}_i\,\mathrm{e}^{\mathrm{i}(\omega t+\varphi)}, \tag{2.21}$$

where $\widetilde{\mathbf{v}}_i$ is the viscous counterpart of the Kelvin mode $\mathbf{v}_i$ located in a viscous boundary layer of thickness $O(Re^{-1/2})$ near the walls (its complete expression is given in appendix 2.6.4). At this order the viscous flow $\widetilde{\mathbf{v}}_i$ is parallel to the walls (it has to compensate $\mathbf{V}_1$ which is also parallel to the wall because of the inviscid boundary condition). However, this viscous flow gives rise to an Ekman pumping at order Ro with a component perpendicular to the walls $\widetilde{\mathbf{V}}_3^{\perp} = O(\eta\widetilde{\mathbf{V}}_1)$. This gives a boundary condition for the inviscid flow at order Ro :

$$\mathbf{V}_3 \cdot \mathbf{n} = -\widetilde{\mathbf{V}}_3^{\perp} = -\eta A\,\widetilde{\mathbf{v}}_3 \cdot \mathbf{n}\,\mathrm{e}^{\mathrm{i}(\omega t+\varphi)} \quad \text{on the walls,} \tag{2.22}$$

where $\mathbf{n}$ is the unitary vector normal to the wall and $\widetilde{\mathbf{v}}_3 \cdot \mathbf{n}$ is a function of order 1 given in appendix 2.6.4.

Order $Ro^{2/3}$

As shown by Greenspan (1969), the nonlinear interaction of a Kelvin mode with itself gives rise to two velocity components. For a Kelvin mode of wavenumbers-frequency (k, m, ω) (where m is the azimuthal wavenumber, in our case $m = 1$), these two components are of the form $(2k, 0, 0)$ and $(0, 2m, 2\omega)$. In other words, the geostrophic mode $(0, 0, 0)$ and the mode $(2k, 2m, 2\omega)$ are not forced by nonlinear interactions.

At order $Ro^{2/3}$ the Navier–Stokes equation (2.8) becomes

$$\left(\frac{\partial}{\partial t}\mathcal{I} + \mathcal{M}\right)\mathbf{V}_2 + \text{c.c.} = \mathbf{N}(\mathbf{V}_1, \mathbf{V}_1) + \text{c.c.} \tag{2.23}$$

The solution of this equation is

$$\mathbf{V}_2 = |A|^2\,\mathbf{v}_{2k} + A^2\,\mathbf{v}_{2\omega}\mathrm{e}^{\mathrm{i}(2\omega t+2\varphi)} + \sum_{j=1}^{\infty} A_0^j(\tau)\mathbf{v}_0^j + \text{o.t.}, \tag{2.24}$$

where o.t. stands for 'other terms' of different Fourier components. The first two terms of (2.24) correspond to the particular solution of (2.23) (see Waleffe, 1989). In agreement with Greenspan (1969), they are of the form $(2k, 0, 0)$ and $(0, 2, 2\omega)$ (these velocity fields are given explicitly in appendix 2.6.3).

The third term of (2.24) is the solution of (2.23) without forcing, where we have only retained the axisymmetric geostrophic modes of Fourier components $(k, m, \omega) = (0, 0, 0)$. It is easy to show that this flow is a stationary azimuthal velocity field whose components can be written as $\mathbf{v}_0^j =$

$(0, v_0^j(r), 0, p_0^j(r))$ in cylindrical coordinates. At this point, the geostrophic flow is arbitrary and we choose to decompose it on the basis of the Bessel functions of the first kind such that its real field is

$$v_0^j(r) = -J_1(d_j r) \quad \text{with} \quad J_1(d_j) = 0, \tag{2.25}$$

with the roots d_j sorted in ascending order such that $d_j = j\pi + O(1)$. We chose to put a minus sign in the above expression such that a positive amplitude A_0^j corresponds to a slow down of the basic solid body rotation. As we will see below, this geostrophic flow is forced at order $Ro^{4/3}$ by the nonlinear interactions in the end wall boundary layers. Its saturation is due to viscous effects in the boundary layers and this geostrophic mode therefore appears at order $A_0 = O(Ro^{4/3}Re^{1/2}) = O(Ro^{2/3})$.

The velocity field $\mathbf{V}_2$ satisfies inviscid boundary conditions. As we did at order $Ro^{1/3}$, one has to add a viscous velocity field $\widetilde{\mathbf{V}}_2$ in a boundary layer of thickness $O(Re^{-1/2})$ in order to satisfy the viscous boundary condition at the walls. This viscous flow is decomposed into several components. First, the velocity fields $\mathbf{v}_{2k}$ and $\mathbf{v}_{2\omega}$ contribute to this viscous velocity field. Then the geostrophic flow corresponds to viscous corrections $\widetilde{\mathbf{v}}_0^j$ in the end wall boundary layers. And finally, the nonlinear interactions of $\mathbf{V}$ with $\widetilde{\mathbf{V}}$ and $\widetilde{\mathbf{V}}$ with itself act as a source term at order $Ro^{2/3}$ and give rise to a nonlinear part of the viscous flow $\widetilde{\mathbf{V}}_2^{\mathrm{NL}}$. If we are only interested in the axisymmetric and stationnary part of this viscous flow, it can be written as

$$\widetilde{\mathbf{V}}_2 = |A|^2\,\widetilde{\mathbf{v}}_{2k} + |A|^2\widetilde{\mathbf{v}}_2^{\mathrm{NL}} + \sum_{j=1}^{\infty} A_0^j(\tau)\widetilde{\mathbf{v}}_0^j + \text{o.t.}, \tag{2.26}$$

where the details of these velocity fields are given in appendices 2.6.4 and 2.6.5. This viscous flow $\widetilde{\mathbf{V}}_2$ is parallel to the walls at this order but it gives rise to an Ekman pumping at the end walls at the order $Ro^{4/3}$ of the form $\widetilde{\mathbf{V}}_4^{\perp} = O(\eta\widetilde{\mathbf{V}}_2)$. This pumping gives a boundary condition for the inviscid flow of the form

$$\mathbf{V}_4 \cdot \mathbf{n} = -\widetilde{\mathbf{V}}_4^{\perp} = -\eta|A|^2\widetilde{\mathbf{v}}_4^{\mathrm{NL}} \cdot \mathbf{n} - \eta\sum_{j=1}^{\infty} A_0^j(\tau)\widetilde{\mathbf{v}}_4^j \cdot \mathbf{n} + \text{o.t.}, \quad \text{on the walls,} \tag{2.27}$$

where the details of these fields are given in appendices 2.6.4 and 2.6.5 and where we have omitted the term due to $\widetilde{\mathbf{v}}_{2k}$ because it does not contribute to the forcing of the geostrophic mode at order $Ro^{4/3}$ as it will be shown below.

Order *Ro*

At order Ro, the Navier–Stokes equation becomes

$$\mathcal{I}\frac{\partial \mathbf{V}_1}{\partial \tau} + \left(\frac{\partial}{\partial t}\mathcal{I} + \mathcal{M}\right)\mathbf{V}_3 + \text{c.c.} = \zeta\,\mathbf{F}_0 e^{\mathrm{i}(\omega t+\varphi)} + \mathbf{N}(\mathbf{V}_1, \mathbf{V}_2) + \mathbf{N}(\mathbf{V}_2, \mathbf{V}_1) + \frac{\eta\mathcal{L}\,\mathbf{V}_1}{Re^{1/2}} + \text{c.c.} \tag{2.28}$$

The last term of this equation should not appear at this order but at order $Ro^{5/3}$. However, we have decided to take it into account in the analysis because its importance in evaluating the viscous decay has been shown in several papers (Kerswell & Barenghi, 1995; Eloy *et al.*, 2003; Racz & Scott, 2007). The integration of equation (2.28) is not needed. We introduce the scalar product

$$\mathbf{X} \odot \mathbf{Y} = \int_V (\overline{X}_r Y_r + \overline{X}_\varphi Y_\varphi + \overline{X}_z Y_z + \overline{X}_p Y_p) \mathrm{d}^3 V, \tag{2.29}$$

where the overbar stands for complex conjugation and V is the volume of the cylinder. A solvability condition for $\mathbf{V}_3$ is obtained by forming the scalar product of $\mathbf{v}_i \, \mathrm{e}^{\mathrm{i}(\omega t+\varphi)}$ with the equation (2.28) and dividing by $\mathbf{v}_i \odot \mathcal{I}\, \mathbf{v}_i$. It yields the following amplitude equation for A

$$\frac{\partial A}{\partial \tau} = \mathrm{i} f - \eta \left(\mu + \frac{\nu}{Re^{1/2}} \right) A + \mathrm{i} \left(\sigma |A|^2 - \sum_{j=1}^{\infty} \xi_j A_0^j \right) A, \tag{2.30}$$

where the calculation of the different coefficients is detailed in appendices 2.6.4 and 2.6.3. Some useful numerical values are given in Tables 2.1–2.3. In the above equation the term f comes from the forcing $\mathbf{F}_0$, the term ν is linked to the volume viscous damping. The term σ originates from the nonlinear interaction of $\mathbf{V}_1$ with $\mathbf{v}_{2k}$ and $\mathbf{v}_{2\omega}$. The terms ξ_j come from the nonlinear interaction of $\mathbf{V}_1$ with the geostrophic modes $\mathbf{v}_0^j$. The surface viscous damping term μ comes from the following relation

$$\mathbf{v}_i \, \mathrm{e}^{\mathrm{i}(\omega t+\varphi)} \odot \left(\frac{\partial}{\partial t} \mathcal{I} + \mathcal{M} \right) \mathbf{V}_3 = \int_S \overline{p_i} \, \mathrm{e}^{-\mathrm{i}(\omega t+\varphi)} \mathbf{V}_3 \cdot \mathbf{n} \, \mathrm{d}^2 S = \eta \mu A \left(\mathbf{v}_i \odot \mathcal{I}\, \mathbf{v}_i \right), \tag{2.31}$$

where S is the surface of the cylinder. This relation is obtained by integrating by parts the scalar product and using the fact that $\mathbf{v}_i \, \mathrm{e}^{\mathrm{i}(\omega t+\varphi)}$ is in the kernel of the operator $(\partial \mathcal{I}/\partial t + \mathcal{M})$ by construction. Since $\mathbf{V}_3 \cdot \mathbf{n}$ is known from the relation (2.22) and is proportional to ηA, the above relation leads to the evaluation of μ in (2.30). This term is a complex number whereas all the other coefficients of (2.30) are real. This means that the viscous boundary layers have two effects : the damping of the flow (the real part of μ is positive) and a detuning of the resonance (due to the non-zero imaginary part of μ).

Order $Ro^{4/3}$

At order $Ro^{4/3}$, if we retain only the geostrophic terms, the Navier–Sokes equation becomes

$$\sum_{j=1}^{\infty} \frac{\partial A_0^j}{\partial \tau} \mathcal{I}\, \mathbf{v}_0^j + \mathcal{M} \mathbf{V}_4 = \sum_{j=1}^{\infty} \frac{\eta \, A_0^j}{Re^{1/2}} \mathcal{L}\, \mathbf{v}_0^j + \text{o.t.}, \tag{2.32}$$

where the volume viscous term on the right hand side has been included for the same reason as in (2.28). The terms $\mathbf{N}(\mathbf{V}_2, \mathbf{V}_2)$ and $\mathbf{N}(\mathbf{V}_1, \mathbf{V}_3)$ do not appear in the above equation because they do not lead to geostrophic forcing.

i,n	$\omega_{i,n}$	δ_i	f	μ	σ	ξ	ν
1,1	1.088	2.691	-0.467	$1.799-0.268\mathrm{i}$	-0.1009	1.524	10.3
1,2	1.812	2.447	0.0328	$0.822-0.456\mathrm{i}$	6.157	170.2	33.4
1,3	1.927	2.420	-0.00522	$0.486-0.342\mathrm{i}$	39.10	1897	82.0
2,1	0.566	5.912	-0.0771	$1.707+0.041\mathrm{i}$	-8.058	2.736	38.0
2,2	1.366	5.602	-0.0187	$1.434-0.382\mathrm{i}$	10.06	75.51	58.8

Table 2.1: Values of the nonlinear and viscous parameters for an aspect ratio $h = 1.8$.

i,n	$\omega_{i,n}$	δ_i	f	μ	σ	ξ	ν
1,1	0.996	2.737	0.469	$1.728-0.128\mathrm{i}$	-0.2295	0.910	9.96
1,2	1.774	2.456	0.0418	$0.841-0.404\mathrm{i}$	4.289	94.28	28.2
1,3	1.911	2.424	-0.00696	$0.497-0.322\mathrm{i}$	26.50	1032	67.6
2,1	0.510	5.960	-0.0737	$1.579+0.112\mathrm{i}$	-9.582	1.921	38.0
2,2	1.285	5.618	-0.0209	$1.398-0.261\mathrm{i}$	6.695	45.70	53.8

Table 2.2: Values of the nonlinear and viscous parameters for an aspect ratio $h = 2$.

The amplitude equation for the geostrophic mode can be found by forming the scalar product [as defined by (2.29)] of $\mathbf{v}_0^j$ with (2.32) and dividing by $\mathbf{v}_0^j \odot \mathcal{I}\,\mathbf{v}_0^j$. It yields the amplitude equations for the geostrophic modes

$$\frac{\partial A_0^j}{\partial \tau} = \eta \chi_j |A|^2 - \eta \left(\frac{2}{h} + \frac{d_j^2}{Re^{1/2}} \right) A_0^j. \tag{2.33}$$

The last term comes from volume viscous effects by using the following equality

$$\mathbf{v}_0^j \odot \mathcal{L}\,\mathbf{v}_0^j = -d_j^2\, \mathbf{v}_0^j \odot \mathcal{I}\,\mathbf{v}_0^j. \tag{2.34}$$

The forcing term χ_j and the surface viscous damping $2/h$ originate from the relation

$$\mathbf{v}_0^j \odot \mathcal{M}\mathbf{V}_4 = \int_S p_0^j\, \mathbf{V}_4 \cdot \mathbf{n}\, \mathrm{d}^2 S = \eta \left(-\chi_j |A|^2 + \frac{2}{h} A_0^j \right) \left(\mathbf{v}_0^j \odot \mathcal{I}\,\mathbf{v}_0^j \right), \tag{2.35}$$

where we have integrated by parts the scalar product and used the fact that $\mathbf{v}_0^j$ is in the kernel of $\mathcal{M}$. The outward velocity $\mathbf{V}_4 \cdot \mathbf{n}$ is known from the relation (2.27); it allows to calculate the coefficients χ_j and $2/h$ as it is detailed in appendices 2.6.4 and 2.6.5. Here, the term due to $\widetilde{\mathbf{v}}_{2k}$ in $\mathbf{V}_4 \cdot \mathbf{n}$ has no influence since we only retained the geostrophic part of the flow (independent of z) in (2.32). Physically, the forcing of the geostrophic mode appears through the coefficient χ_j and is due to the nonlinear interaction of the flow with itself in the end wall boundary layers. Therefore, to have a geostrophic flow, both nonlinear and viscous effects are needed near the end walls.

i,n	h	ξ_1	ξ_2	ξ_3	ξ_4	ξ_5
1,1	1.8	0.277	0.144	-0.052	0.031	-0.021
1,2	1.8	0.701	0.062	-0.017	0.009	-0.006
1,3	1.8	0.767	0.049	-0.011	0.005	-0.003
2,1	2	-0.516	-0.132	0.316	0.127	-0.044

i,n	h	χ_1	χ_2	χ_3	χ_4	χ_5
1,1	1.8	4.743	1.308	-0.314	0.139	-0.077
1,2	1.8	240.2	27.56	-7.231	3.253	-1.811
1,3	1.8	2458	244.3	-64.13	28.82	-16.03
2,1	2	2.331	-1.044	7.969	3.388	-0.907

Table 2.3: Values of the first parameters ξ_i and χ_i for different resonances i,n and different aspect ratios h.

2.4.2 Discussion

In this section, we will discuss the results of the nonlinear viscous theory presented in §2.4.1 and compare it with experimental measurements.

Amplitude equations

The amplitude equations (2.30) and (2.33) give the time dependence of the Kelvin mode amplitude A and the amplitudes A_0^j of the geostrophic modes. A further simplification can be obtained by assuming that the Reynolds number is large when the nonlinear effects come into play. In this case, the volume viscous term $d_j^2 Re^{-1/2}$ can be neglected in front of the surface viscous term $2/h$ for the geostrophic modes. With this assumption, all geostrophic modes have the same natural decay time and one can define a single geostrophic amplitude $A_0 = A_0^j/\chi_j$ such that all amplitude equations for the geostrophic modes become identical. By defining a global parameter $\xi = \sum_{j=1}^{\infty} \chi_j \xi_j$, the final system can be reduced to two amplitude equations :

$$\frac{\partial A}{\partial \tau} = \mathrm{i}f\left(1 - \frac{A}{\zeta Ro^{2/3} a_i}\right) - \eta\left(\mu + \frac{\nu}{Re^{1/2}}\right) A + \mathrm{i}\left(\sigma|A|^2 - \xi A_0\right) A, \tag{2.36a}$$

$$\frac{\partial A_0}{\partial \tau} = \eta\left(|A|^2 - \frac{2}{h} A_0\right). \tag{2.36b}$$

In these equations, we have assumed that the frequency ω is not exactly equal to the resonant frequency $\omega_{i,n}$, which introduces an additional axial velocity in the solvability condition at order Ro, leading to the extra term $\mathrm{i}fA/(\zeta Ro^{2/3} a_i)$, where a_i is the amplitude of the Kelvin mode given by (2.14). This term vanishes at the resonance since a_i diverges in this case. On the other hand, if the forcing frequency is far enough, the resonant frequency

such that $a_i \ll Ro^{2/3}$, we recover the inviscid solution $A = \zeta Ro^{2/3} a_i$ of § 2.3.1.

The linear forcing parameter f and the nonlinear parameter σ (corresponding to the interaction of the Kelvin mode with itself) are given analytically in Appendix 2.6.3. The surface and volume viscous parameters μ and ν are given in Appendix 2.6.4. The term ξ is due to the nonlinear interaction of the Kelvin mode with the geostrophic modes and cannot be given analytically in a simple form. We thus show the variation of this parameter as a function of the aspect ratio h in Fig. 2.8 for five different resonances. It drastically decreases of ten decades when h increases from 0.1 to 10. This is due to the fact that the nonlinear forcing of the geostrophic mode is generated in the top and bottom boundary layers only, and is thus more efficient for small aspect ratios h.

The amplitude equations (2.36 *a, b*) describe the transient stage and the saturation of the mode amplitude A. They have been obtained for the distinguished scaling $Ro^{2/3} = O(Re^{-1/2})$ which corresponds to $\eta = O(1)$. However, one can easily obtain simplified equations when viscous effects are dominant by taking the limit $\eta \gg 1$. In this case, the amplitude equation for the geostrophic mode (2.36 *b*) is not needed anymore and the amplitude equation (2.36 *a*) simplifies into a linear equation for A with a forcing term. Its solution is an exponential convergence toward a fixed point with a characteristic time scale which is the natural viscous decay time of the Kelvin mode. The fixed point corresponds to $A = O(\eta^{-1})$ which gives $\mathbf{V}_i = O(Ro\,Re^{1/2})$ in agreement with the results of Gans (1970*b*). In this case, it is easy to show that the mode amplitude is maximum when the detuning of the forcing frequency compensates exactly the viscous detuning, i.e. $f/(\zeta Ro^{2/3} a_i) = -\eta \mathrm{Im}(\mu)$. When this is true, A is a pure imaginary number, which means that the mode is oriented with an angle of $\pi/2$ compared to the non-resonant case of §2.3.1.

When nonlinear effects are not negligible, the dynamics of the mode amplitude given by (2.36 *a, b*) becomes more complex. Some typical trajectories of A in the complex plane are shown in Fig. 2.9 for different values of the parameter η. If nonlinear effects are small which correspond to η large (or Re small compared to $Ro^{-4/3}$), the amplitudes of the Kelvin mode A and geostrophic mode A_0 converge toward a fixed point. This fixed point is easily obtained by equating the time-derivative in (2.36 *a, b*) to zero. It is worth pointing out that the first effect of nonlinearities is to detune the Kelvin mode. Indeed the terms originating from the nonlinear interaction of the mode with itself and with the geostrophic mode are both expressed as a real number multiplying iA. This form is identical to that of the detuning term i$Af/(\zeta Ro^{2/3} a_i)$ and the viscous detuning term $-\eta \mathrm{Im}(\mu)\mathrm{i}A$.

For larger values of the Reynolds number (or smaller values of η), the fixed point may become unstable. In this case, the trajectory of A in the complex plane converges toward a limit cycle as shown on Fig. 2.9. However, this cycle could not be observed experimentally because it corresponds to experimental parameters leading to instability as shown in the next section.

As noted by Gans (1970*b*) in the viscous regime, the resonances are important when the amplitude at the resonance (of the order of $Ro\sqrt{Re}f/\mu$

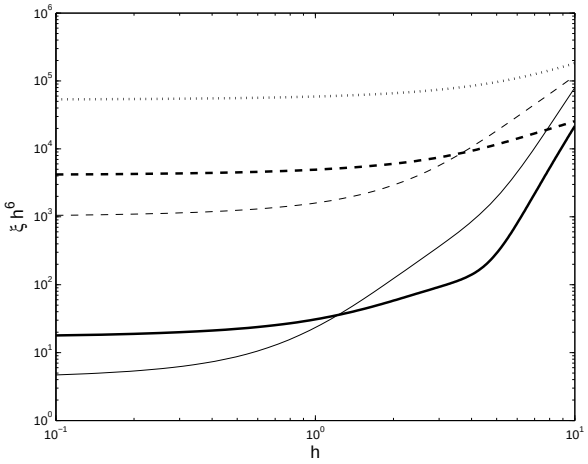

Figure 2.8: Numerical value of the nonlinear parameter ξ multiplied by h^6 quantifying the interaction of the resonant Kelvin mode with the geostrophic mode. The curves correspond to the first (thick lines) and second (thin lines) Kelvin modes at their first (solid line), second (dashed line) and third (dotted line) resonance.

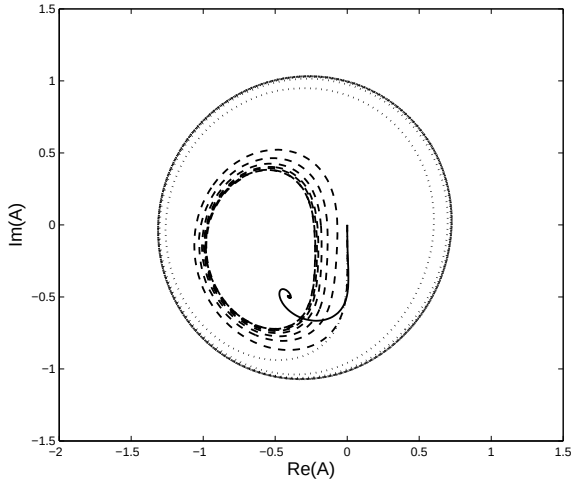

Figure 2.9: Phase portrait of the complex amplitude of the first Kelvin mode at its first resonance, obtained by integrating equations (2.36a,b). The Reynolds number is equal to 2.5×10^4 (solid line), 2.2×10^5 (dashed line) and 2.5×10^6 (dotted line) for a small parameter $Ro = 0.003$ as in the experiments. This corresponds to η equals 0.31, 0.10 and 0.03 respectively.

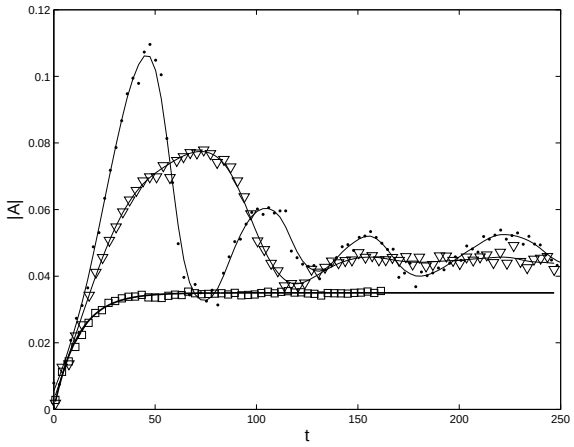

Figure 2.10: Time evolution of the amplitude of the first mode at the second resonance ($\omega = 1.812$ and $h = 1.8$) for $Re = 720$ (□), $Re = 2200$ (△) and $Re = 7400$ (•). The thick line corresponds to an exponential fit for $Re = 720$. The forcing amplitude is $Ro = 2.8 \times 10^{-3}$.

in the viscous regime) is much larger than the linear amplitude (of the order of Ro) outside of the resonance. Since the term f/μ decreases with the radial wavenumber δ as $\delta^{-7/2}$, we recover that the resonances are visible if $\delta < Re^{1/7}$ in the viscous regime. Doing the same analysis in the non linear regime, the resonance is visible only if the amplitude at the resonance, which scales as $(Rof/\sigma)^{1/3}$ is larger than the linear amplitude Ro outside of the resonance. Since f/σ scales as $\delta^{-11/2}$, we find that the resonance is important when $\delta < Ro^{-4/11}$. In the general case, the resonances are thus visible if the radial wavenumber δ is smaller than these two bounds scaling as $Re^{1/7}$ and $Ro^{-4/11}$ respectively.

Experimental amplitude at the resonance

Figure 2.10 shows the experimental measurement of the amplitude of the first Kelvin mode at its second resonance for three different Reynolds numbers. For small Reynolds numbers, the temporal evolution of the amplitude is exponential $A_f(1 - e^{-t/t_s})$, with a final amplitude A_f and a settling time t_s which can be easily obtained by a least-square fit. However, for higher Reynolds numbers, the amplitude strongly oscillates before reaching a quasi-stationary final amplitude. This may be due to the nonlinear effects (which create a decaying oscillation of the amplitude), but in fact it mostly comes from the onset of a three-dimensional instability which is slowly growing during the transient stage. This oscillation prevents the correct determination of the final amplitude and introduces a large error, which is taken as the difference between the maximum and the local minimum of the amplitude. This error is shown in the next figures as error bars on the amplitude.

To clearly demonstrate that the flow has become three-dimensionally unstable at high Reynolds numbers, we have plotted in Fig. 2.11(a) the instantaneous vorticity field found in the cylinder for the second resonance

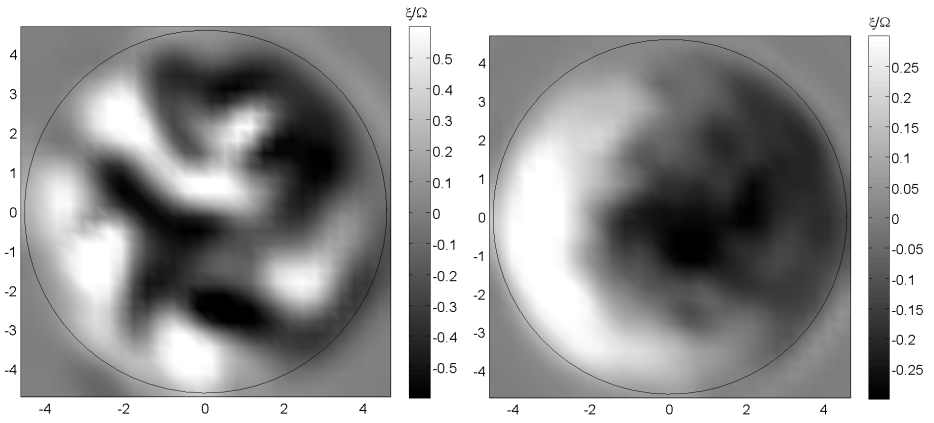

Figure 2.11: Instantaneous (a) and mean (b) vorticity field of the second resonance of the first Kelvin mode ($\omega = 1.812$ and $h = 1.8$) after destabilisation of the flow ($Re = 7400$ and $Ro = 2.8 \times 10^{-3}$).

of the first Kelvin mode. The vorticity is made of several small vortices, which completely hide the organised structure of the initial Kelvin mode. However, this Kelvin mode is recovered (at a smaller amplitude) when plotting the mean vorticity field calculated on 100 fields (i.e. during 50 rotation periods), as in Fig. 2.11(b). It is striking to see that although the flow seems completely turbulent, the resonant Kelvin mode is still present with an amplitude only slightly oscillating in time. In this case, the current nonlinear theory cannot apply anymore because other Kelvin modes have appeared because of an instability.

By plotting the transient regimes for each frequency ω, we were able to measure the final amplitude A decomposed on its norm $|A|$ and argument α such that $A = |A|e^{i\alpha}$. They are plotted in Fig. 2.12 as a function of the dimensionless frequency ω around the second resonance of the first Kelvin mode and for $\eta = 0.22$. This solution is compared to the theoretical viscous solutions (linear and nonlinear). What is intended here by viscous linear (respectively nonlinear) theory is the set of equations (2.36 *a, b*) in the limit $\eta \gg 1$ [respectively for $\eta = O(1)$]. Despite the large error bars, the comparison between experiment and theory clearly shows that both nonlinear and viscous effects are needed to predict the correct amplitude of the mode. The viscous effects saturate the amplitude of the mode at a finite value, and the nonlinear effects shift the maximum of the peak toward smaller frequencies ω. The overall agreement is excellent for the amplitude. However, the experimental determination of the orientation of the mode α is closer to the linear theory than to the nonlinear theory. This discrepancy may come from transient effects : the measurements can only be done during a small duration, due to the presence of an instability. When looking at the solid line of Fig. 2.9, we can understand that the amplitude might be correctly predicted although the argument is not at its final value.

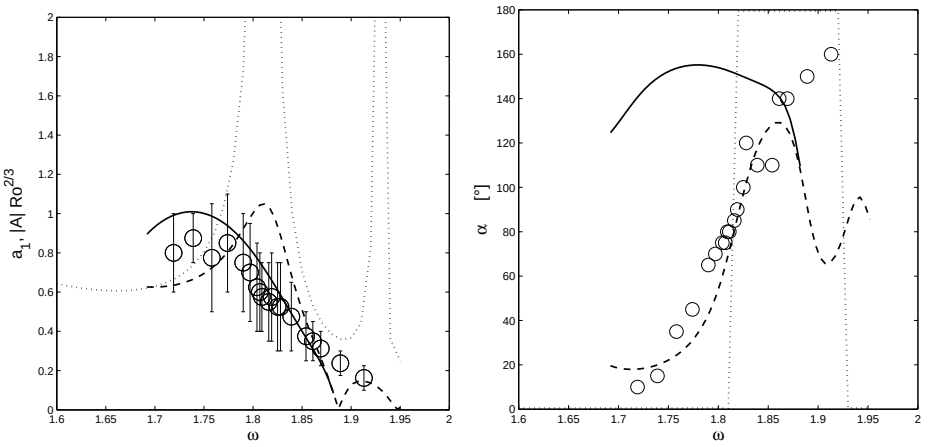

Figure 2.12: Amplitude (a) and orientation (b) of the first Kelvin mode around its second resonance. Experimental results (○) are obtained for an aspect ratio $h = 1.8$, Reynolds number $Re = 2500$ and Ro varying between 2.3×10^{-2} and 3.3×10^{-2} . The solid line corresponds to the non linear viscous theory at the second resonance of the first mode, the dashed line to the linear viscous theory and the dotted line to the linear inviscid theory.

Scaling at the resonance

Five series of experiments were conducted to study the dependence of the amplitude with the Reynolds number when the frequency ω is exactly equal to the resonant frequency $\omega_{i,n}$. For this purpose, Ω_1 and Ω_2 were varied in each experiment, by keeping a fixed dimensionless frequency ω. It has been done for the first three resonances of the first Kelvin mode and for the first two resonances of the second Kelvin mode. Figure 2.13 shows the final amplitude of the mode after the transient stage. The results are in excellent agreement with the present theoretical predictions, knowing that there are no fitting parameters. They clearly show that the amplitude scales with $Re^{1/2}$ at low Reynolds numbers and saturates due to nonlinear effects at large Reynolds numbers. This saturation value decreases rapidly with the number of the resonance n. There is a large uncertainty in the nonlinear regime because of the onset of the three-dimensional instability as discussed above, which makes the validation of the nonlinear saturation more difficult. However, there is an agreement up to 50%. It can be noted that the exact theory given by (2.30) and (2.33) and plotted as thin lines is very close to the approximate theory given by (2.36a,b) plotted as thick lines : this means that it is justified to neglect the volume viscous damping of the geostrophic modes in the regime we have studied.

The dimensionless settling time t_s measured during the transient response is also plotted for these resonances in Fig. 2.14 as a function of the Reynolds number. It is compared to the viscous time $Re/(Re^{1/2}\mu+\nu)$. Although there is a large scatter, the agreement seems to be good. The settling time is only measured in the viscous regime since it is impossible to determine the settling

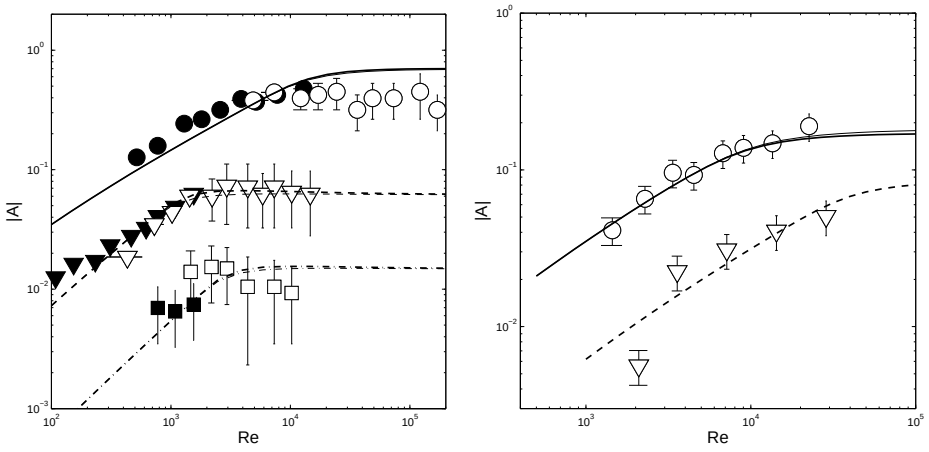

Figure 2.13: Amplitude of the first (a) and second (b) Kelvin modes as a function of the Reynolds number for the first (○, solid line), second (▽, dashed line), and third (□, dash-dotted line) resonances. Closed symbols correspond to a small cylinder $R_c = 1.5$ cm and open symbols to a large cylinder $R_c = 4.6$ cm. The thick lines correspond to the approximate theory (2.36) and the thin lines to the exact theory (2.30) and (2.33). For the first mode, $h = 1.8$; $Ro = 3.1 \times 10^{-3}$, 2.8×10^{-3} and 3.2×10^{-2} for the first, second and third resonance respectively. For the second mode $h = 2$; $Ro = 8.6 \times 10^{-3}$ and $Ro = 5 \times 10^{-3}$ for the first and second resonance respectively.

time in the nonlinear regime when the transient response is not exponential anymore (as shown in Fig. 2.10).

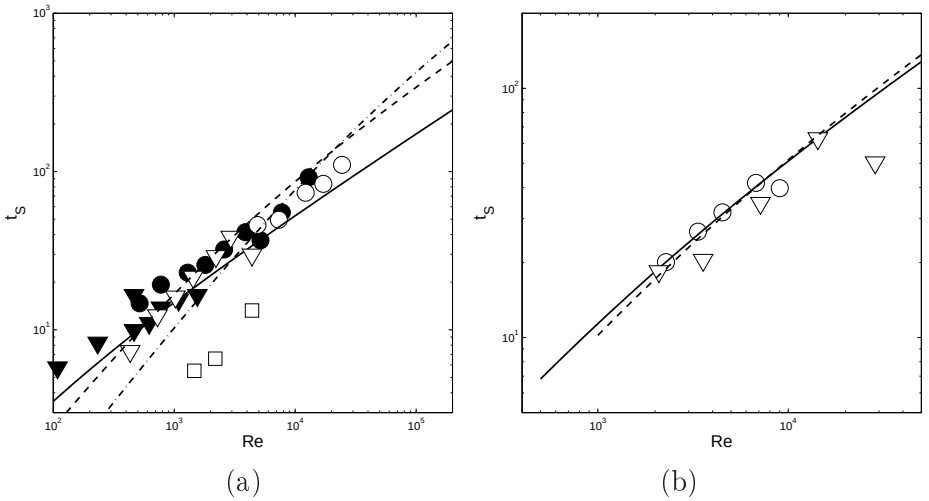

Figure 2.14: Settling time of the first (a) and second (b) modes as a function of the Reynolds number, obtained at the first (○, solid line), second (▽, dashed line) and third (□, dash-dotted line) resonances. Closed symbols correspond to a small cylinder and open symbols to a large cylinder. Same experimental parameters as in Fig. 2.13.

Figure 2.15 shows the argument α of the complex amplitude as a function of the Reynolds number for the same five resonances. At low Reynolds numbers, the angles are determined by the viscous theory and are equal to $\pm 90°$ (if viscous detuning are neglected). It means that, at the resonance, the mode is perpendicular to its direction in the linear inviscid theory (or far from the resonances). However, when the nonlinear effects become large, the phase shift occurs at a frequency different from $\omega_{i,n}$, and the angle is thus equal to $0°$ or $180°$ at $\omega = \omega_{i,n}$. The agreement with the experimental results is correct for the first resonance of the first mode. However, there is a large scatter for the other resonances, and it is hard to ensure the validity of the theoretical predictions.

Finally, we have measured the dependence of the amplitude A with the small parameter Ro by varying the precession angle from 0.5 to 10°. The measured amplitudes are plotted in Fig. 2.16 and compared to the theoretical predictions. We recover that the amplitude scales as $Ro^{2/3}$ in the viscous regime and then saturates at a fixed value for large precession angles. The agreement is again excellent in the viscous regime and fairly good in the nonlinear regime although the theory slightly overestimates the amplitude. This might be due once again to the appearance of a three-dimensional instability before the final amplitude has been reached. This relative discrepancy could be also due to the fact that the theoretical derivation assumes that $Ro^{1/3}$ is asymptotically small whereas it goes up to 0.5 when the precession angle is large.

Geostrophic modes

As was previously stated in §2.4.2, the nonlinear and viscous effects leed to the generation of a geostrophic mode. This mode is mainly responsible

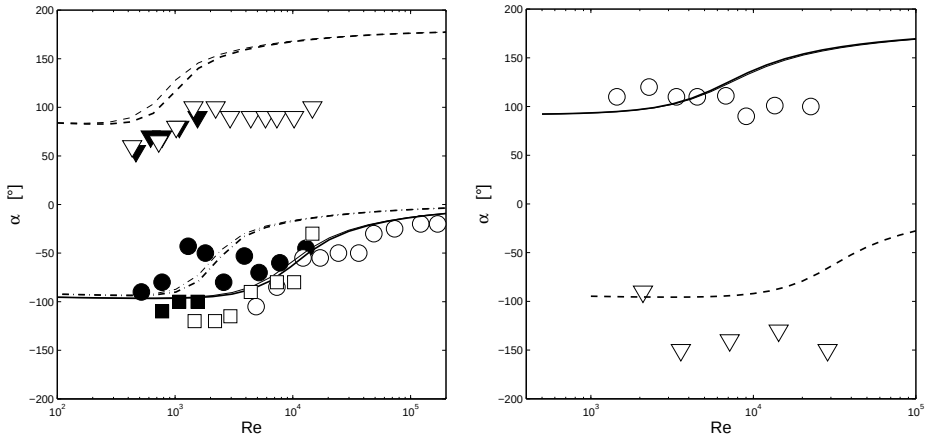

Figure 2.15: Orientation of the first (a) and second (b) modes as function of the Reynolds number, obtained at the first (○, solid line), second (▽, dashed line) and third (□, dash-dotted line) resonances. Closed symbols correspond to a small cylinder and open symbols to a large cylinder. The thick lines corresponds to the approximate theory (2.36) and the thin lines to the exact theory (2.30) and (2.33). Same experimental parameters as in Fig. 2.13.

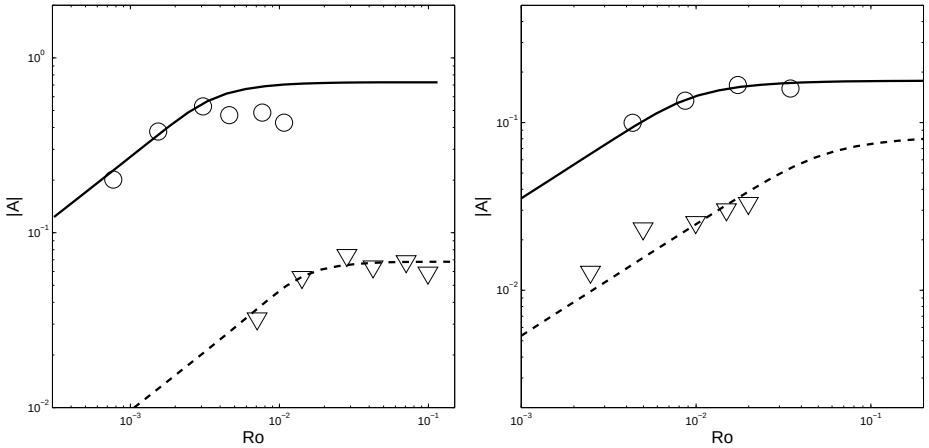

Figure 2.16: Amplitudes of the first (a) and second (b) modes as a function of the parameter *Ro* (proportional to the precessing angle θ), obtained at the first (○, solid line) and second (▽, dashed line) resonances. For the first mode, $h = 1.8$ and $Re = 11900$ (resp. 2150) for the first (resp. second) resonance. For the second mode, $h = 2$ and $Re = 9000$ (resp. 3600) for the first (resp. second) resonance.

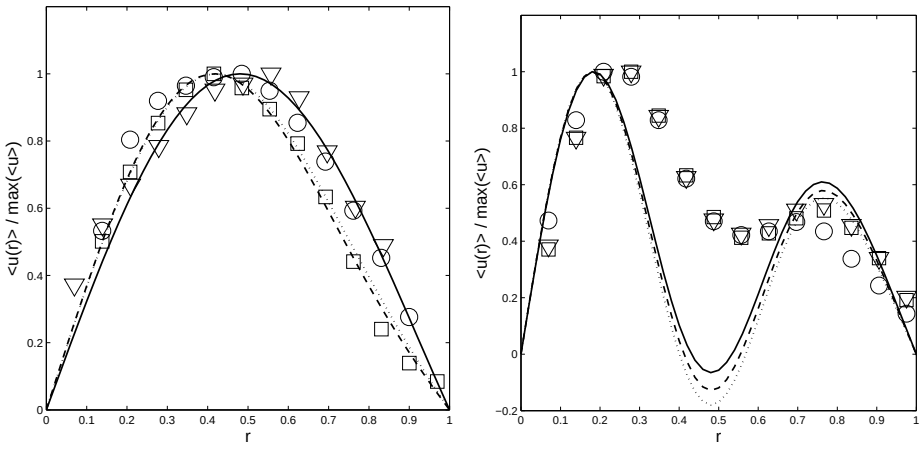

Figure 2.17: Velocity profile of the geostrophic mode ($m = 0$) for the first resonance of (a) the first ($\omega = 1.088,\ h = 1.8,\ Ro = 3.1\times10^{-3}$) and (b) the second ($\omega = 0.51,\ h = 2,\ Ro = 8.6\times10^{-3}$) Kelvin mode. (a) $Re = 1300$ ($\circ$, solid line), $Re = 4900$ ($\triangledown$, dashed line) and $Re = 12200$, ($\square$, dotted line); (b) $Re = 3900$ ($\circ$, solid line), $Re = 7800$ ($\triangledown$, dashed line) and $Re = 16000$ ($\square$, dotted line).

for the saturation of the mode amplitude since the parameter ξ is generally larger than the parameter σ in (2.36 a) as it appears in tables 2.1 and 2.2. It is thus essential to check if the theory predicts an accurate amplitude of the geostrophic mode. Figure 2.17 shows the velocity profile of the geostrophic mode for the first and second modes. It has been obtained by taking an azimuthal average of the azimuthal velocity (this way, the velocity of the Kelvin modes are conveniently removed). For the first mode, the measured profile is bell-shaped and depends very weakly on the Reynolds number. This is in excellent agreement with the nonlinear theory. For the second Kelvin mode, the geostrophic profile is more complex. It exhibits two velocity maxima, but still vanishes for $r = 1$. This is due to the simultaneous presence of several components $J_1(d_j r)$ in the geostrophic mode. It is again in fairly good agreement with the nonlinear theory, although the minimum is less pronounced in the experiments.

It is possible to decompose these profiles on the Bessel functions $J_1(d_j r)$ (d_j being the roots of the bessel function) in order to get the amplitudes A_0^j of the geostrophic mode as defined in (2.24) and (2.25). For the first Kelvin mode, the amplitude A_0^1 is much larger than the others since the geostrophic mode is mostly bell-shaped. We have thus plotted this amplitude A_0^1 as a function of the Reynolds number and the parameter Ro. In the viscous regime, the amplitude A_0^1 roughly scales as the Reynolds number and as $Ro^{4/3}$, since it scales as the square of the amplitude A. This means that the total geostrophic motion $A_0 Ro^{2/3} v_0$ scales as the square of the forcing parameter Ro. It can be noted that there are some small variations of the scaling ex-

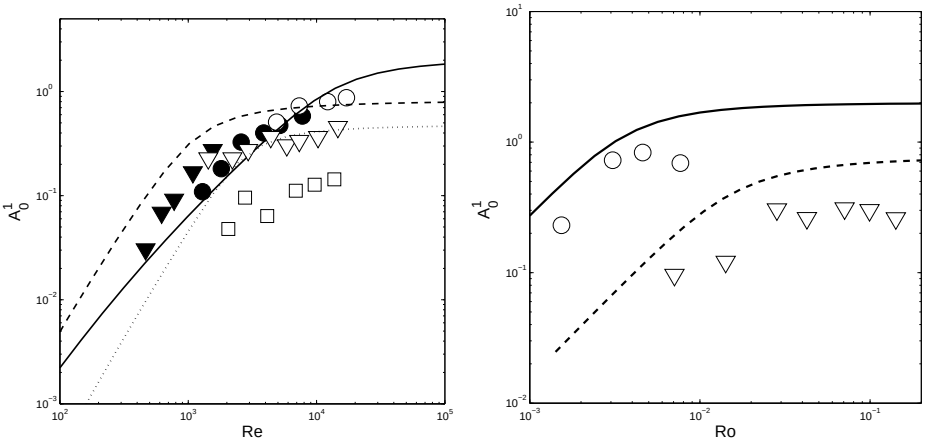

Figure 2.18: Amplitude of the geostrophic mode as a function of the Reynolds number (a) and the precession angle (b). The results are obtained with an aspect ratio $h = 1.8$ for the first mode at its first resonance ($\circ$, solid line, $\omega = 1.088$), its second resonance ($\triangledown$, dashed line, $\omega = 1.812$) and its third resonance ($\square$, dotted line, $\omega = 1.927$). Closed symbols correspond to a small cylinder and open symbols to a large cylinder. (a) $Ro = 3.1 \times 10^{-3}$, 2.8×10^{-3} and 3.2×10^{-2} for the first, second and third resonance respectively. ; (b) $Re = 12200$ for the first resonance and $Re = 2200$ for the second resonance.

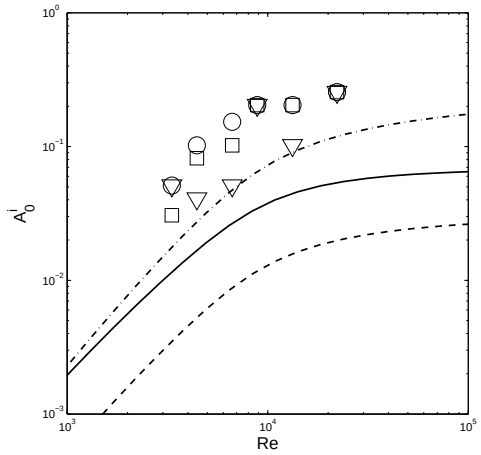

Figure 2.19: Amplitude of the geostrophic mode as a function of the Reynolds number, for the first resonance of the second mode. The different curves correspond to the first component A_0^1 (solid line, $\circ$), the second component A_0^2 (dashed line, $\triangledown$) and the third component A_0^3 (dash-dotted line, $\square$). The dimensionless parameters are $h = 2$, $Ro = 8.6 \times 10^{-3}$.

ponent among the resonances, which are due to the volumic diffusion terms $d_j^2 Re^{-1/2}$. In the nonlinear regime, the geostrophic amplitude A_0^1 saturates because the amplitude A also saturates. This means that the geostrophic motion scales as $Ro^{2/3}$ in this regime. The agreement between the experiment and the theory is good for the first two resonances : the scaling exponents and the multiplication factors are correct, although the theory slightly overestimates the amplitude of the first mode in the nonlinear regime. For the third resonance, the amplitude is much smaller in the experiments than in the theory, but the velocity of the geostrophic mode is very small in this case and the uncertainty is thus very high.

For the second Kelvin mode, the geostrophic profile contains more than one component and we thus need to plot the amplitudes A_0^j, j varying from 1 to 3. They are plotted in Fig. 2.19 and compared to the theory. It is surprising to see that here, the theory underestimates the amplitudes by a factor 10. Again this discrepancy could be due to the fact that $Ro^{1/3}$ is not very small and thus the asymptotic decomposition may not be valid anymore in this case.

2.5 Conclusion

In this paper we addressed both experimentally and theoretically the flow inside a rotating cylinder subject to a weak precession. We have shown that this flow can be expressed as a sum of Kelvin modes which have been measured for the first time using Particle Image Velocimetry. We have distinguished two cases depending on the precession frequency. When this forcing frequency is not equal to a natural frequency of a Kelvin mode, the flow is

said to be non-resonant and a linear inviscid theory can predict accurately the amplitude of the forced Kelvin modes in the limit of small precession amplitude and large Reynolds number. However, if the forcing frequency is resonant, this linear inviscid theory is unable to give the mode amplitude since it diverges. In this case, a viscous and nonlinear theory has been introduced to predict the finite value of the mode amplitude.

In the resonant case, there are two different regimes depending on the value of the Reynolds number. For small enough Reynolds numbers, nonlinear effects are negligible and taking into account the effects of both the viscous boundary layers and the volume viscous damping is enough to predict the dynamics of the resonant Kelvin mode as it has already been shown by Gans (1970*b*) in the particular case of a precession angle of 90°. It yields a saturation of the mode amplitude which scales as $Re^{1/2}$ in excellent agreement with the experimental results.

For larger Reynolds numbers, weakly nonlinear effects have to be taken into account together with viscous effects. It leads to the saturation of the mode amplitude at a value which scales as $\theta^{1/3}$, where θ is the precession angle supposedly small. It is thus independent of the Reynolds number. This scaling is correctly recovered experimentally. An interesting point is that experiments show the presence of a geostrophic motion, whose amplitude always scales as the square of the Kelvin mode amplitude, as can be predicted by the nonlinear and viscous theory. This small geostrophic motion has been observed and measured in the experiments and its amplitude has been shown to be correctly predicted by the theory for the first Kelvin mode.

In the present paper, we have characterised the stable flow inside a precessing cylinder in all regimes. In the future, these results can serve as a basis for a stability study of this flow. Indeed, it is known from McEwan (1970) and Manasseh (1992) that Kelvin modes can become unstable and even turbulent for large Reynolds numbers. Such a breakdown of the flow has been observed in our experiments, and always appeared at the transition between the viscous and the nonlinear regime, i.e. when the nonlinear effects cease to be negligible. The instability of the Kelvin modes is probably due to a triadic resonance similarly to the elliptic instability (Kerswell, 2002; Eloy *et al.*, 2003). A theoretical and experimental study is currently carried out to understand this instability better.

Finally, it would be interesting to know if the present theoretical framework can hold when the flow becomes unstable and eventually turbulent. Indeed, the Kelvin modes are still excited in this case, although they are hidden by the presence of a very disordered flow (which can still be expressed as a sum of Kelvin modes). This would have great consequences for industrial and geophysical applications for which the Reynolds numbers are usually a few decades higher than in the laboratory experiments.

Acknowledgments

We would like to thank Laurie Devesvre for preliminary results during the set-up of the laboratory experiment. This study has been carried out under the contract CEA-CNRS N° 004746.

2.6 Appendix

2.6.1 Four-component formulation

The operators appearing in equation (2.8) are defined by

$$\mathcal{I} = \begin{pmatrix} 1 & 0 & 0 & 0 \\ 0 & 1 & 0 & 0 \\ 0 & 0 & 1 & 0 \\ 0 & 0 & 0 & 0 \end{pmatrix}, \tag{2.37}$$

$$\mathcal{D} = \begin{pmatrix} 0 & 0 & -\mathrm{i} & 0 \\ 0 & 0 & 1 & 0 \\ \mathrm{i} & -1 & 0 & 0 \\ 0 & 0 & 0 & 0 \end{pmatrix}, \tag{2.38}$$

$$\mathcal{L} = \begin{pmatrix} \Delta - \dfrac{1}{r^2} & -\dfrac{2}{r^2}\dfrac{\partial}{\partial\varphi} & 0 & 0 \\ \dfrac{2}{r^2}\dfrac{\partial}{\partial\varphi} & \Delta - \dfrac{1}{r^2} & 0 & 0 \\ 0 & 0 & \Delta & 0 \\ 0 & 0 & 0 & 0 \end{pmatrix}, \tag{2.39}$$

where

$$\Delta = \frac{1}{r}\frac{\partial}{\partial r} + \frac{\partial^2}{\partial r^2}\frac{1}{r^2}\frac{\partial^2}{\partial\varphi^2} + \frac{\partial}{\partial z^2} \tag{2.40}$$

and

$$\mathcal{M} = \begin{pmatrix} 0 & -2 & 0 & \dfrac{\partial}{\partial r} \\ 2 & 0 & 0 & \dfrac{1}{r}\dfrac{\partial}{\partial\varphi} \\ 0 & 0 & 0 & \dfrac{\partial}{\partial z} \\ \dfrac{\partial}{\partial r} + \dfrac{1}{r} & \dfrac{1}{r}\dfrac{\partial}{\partial\varphi} & \dfrac{\partial}{\partial z} & 0 \end{pmatrix}. \tag{2.41}$$

The vectors $\mathbf{F}_0$ and $\mathbf{N}(\mathbf{v}_1, \mathbf{v}_2)$ are defined by

$$\mathbf{F}_0 = \begin{pmatrix} 0 \\ 0 \\ -r\omega \\ 0 \end{pmatrix}, \tag{2.42}$$

and

$$\mathbf{N}(\mathbf{v}_1, \mathbf{v}_2) = \begin{pmatrix} \mathbf{u}_1 \times (\boldsymbol{\nabla} \times \mathbf{u}_2) + \overline{\mathbf{u}}_1 \times (\boldsymbol{\nabla} \times \mathbf{u}_2) \\ 0 \end{pmatrix}. \tag{2.43}$$

2.6.2 Extraction of the mode amplitude a_i

The PIV measurements give the two components $\mathbf{u}_{\rm exp} = (u_{\rm exp}, v_{\rm exp})$ of the (real) transverse velocity field at a specific height z. We want to obtain the amplitudes a_i and the tilt angles α_i of the first 5 Kelvin modes whose transverse components are given in the reference frame of the rotating platform by $\mathbf{u}_i(r,\varphi,z) = \mathrm{e}^{\mathrm{i}\varphi}(u_i, v_i)\sin(k_i z)$, ($u_i$ and v_i being given in Eq. (2.13). We thus suppose that the experimental velocity field is given by

$$\mathbf{u}_{\rm exp}(r,\varphi,z) = \sum_i a_i \begin{pmatrix} -\mathrm{i}\sin(\varphi+\alpha_i)u_i(r) \\ \cos(\varphi+\alpha_i)v_i(r) \end{pmatrix}. \tag{2.44}$$

It can be noted that $\mathbf{u}_{\rm exp}$ is real since u_i is purely imaginary and v_i is purely real.

We introduce the scalar product $\langle \mathbf{X}|\mathbf{Y}\rangle = \int_0^{2\pi}\int_0^{0.9}(\overline{X}_r Y_r + \overline{X}_\varphi Y_\varphi)\, r\,\mathrm{d}r\,\mathrm{d}\varphi$ for which the Kelvin modes are almost orthogonal : they would be orthogonal if the integration was achieved over the whole section $0 < r < 1$. If we define the complex experimental velocity (which can be easily derived numerically)

$$\mathbf{u}^c_{\rm exp}(r,\varphi,z) = \mathbf{u}_{\rm exp}(r,\varphi,z) - \mathrm{i}\,\mathbf{u}_{\rm exp}(r,\varphi+\pi/2,z), \tag{2.45}$$

we find that the scalar product $\langle \mathbf{u}_i|\mathbf{u}^c_{\rm exp}\rangle$ is equal to :

$$\langle \mathbf{u}_i|\mathbf{u}^c_{\rm exp}\rangle = \sum_j M_{ij} a_j \mathrm{e}^{\mathrm{i}\alpha_j}\sin(k_j z), \tag{2.46}$$

where $M_{ij} = 2\pi\int_0^{0.9}(\overline{u_i}u_j + \overline{v_i}v_j) r\,dr$. If we consider only the five first Kelvin modes, we can invert numerically the 5×5 matrix M to get :

$$\left(a_i \mathrm{e}^{\mathrm{i}\alpha_i}\sin(k_i z)\right)_{i=1,5} = M^{-1}\left(\langle \mathbf{u}_i|\mathbf{u}^c_{\rm exp}\rangle\right)_{i=1,5}. \tag{2.47}$$

The tilt angles α_i of the Kelvin modes are thus equal to the argument of this expression and the amplitudes a_i to the modulus of this expression divided by $(\sin(k_i z))_{i=1,5}$.

2.6.3 Calculation of the nonlinear coefficients

The aim of this Appendix is to calculate the coefficients f, σ and ξ_j appearing in the nonlinear amplitude equation (2.30).

Order $Ro^{2/3}$

At order $Ro^{2/3}$, the particular solution of (2.23) is given by (2.24) where

$$\mathbf{v}_{2k} = \begin{pmatrix} 0 \\ a_{2k}\cos(2k_i z) \\ 0 \\ p_{2k}\cos(2k_i z) \end{pmatrix}, \quad \mathbf{v}_{2\omega} = \begin{pmatrix} \dfrac{\mathrm{i}}{r}a_{2\omega} \\ -\dfrac{1}{2}\dfrac{\mathrm{d}a_{2\omega}}{\mathrm{d}r} \\ 0 \\ p_{2\omega} \end{pmatrix}, \tag{2.48a,b}$$

with

$$a_{2k} = \frac{\mathrm{i}k_i}{\omega}\left(v_i w_i - \frac{1}{2k_i}\frac{\partial(u_i v_i)}{\partial r}\right), \qquad (2.49\,a,b)$$

$$a_{2\omega} = \frac{\delta_i^2}{(\omega^2-4)^2}\left[J_1^2(\delta_i r) - J_1^2(\delta_i)\, r^2\right]. \qquad (2.49\,a,b)$$

Order *Ro*

We first need to calculate the scalar product N, which is the norm of the velocity field

$$N = \mathbf{v}_i \odot \mathcal{I}\,\mathbf{v}_i = 2\pi h \frac{\omega^2\left(\omega + 2\delta_i^2 - 2\right) - 4\omega + 8}{\omega^2\left(4-\omega^2\right)^2} J_1^2(\delta_i) + \frac{\pi}{k_i}\sin(k_i h)\frac{\omega^2\left(\omega - \delta_i^2\omega - 2\right) - 4\omega + 8}{\omega^2\left(4-\omega^2\right)^2} J_1^2(\delta_i). \qquad (2.50)$$

It can be noted that the last term vanishes at the resonance. The term of forcing comes from

$$F = \mathbf{v}_i\,\mathrm{e}^{\mathrm{i}(\omega t+\varphi)} \odot \zeta\,\mathbf{F}_0 \mathrm{e}^{\mathrm{i}(\omega t+\varphi)} = 2\pi\zeta\frac{2\mathrm{i}}{\delta_i^2}\frac{\omega+2}{\omega}\sin\left(\frac{k_i h}{2}\right) J_1(\delta_i), \qquad (2.51)$$

which is a pure imaginary number. The coefficient of forcing f appearing in the amplitude equation (2.30) is simply

$$f = \frac{F}{\mathrm{i}N}, \qquad (2.52)$$

where N and F are given by (2.50) and (2.51).

The coefficient σ in (2.30) is separated in two parts. The first one comes from the nonlinear interaction of $\mathbf{V}_1$ with $\mathbf{v}_{2k}$

$$\sigma_{2k} = \mathbf{v}_i\,\mathrm{e}^{\mathrm{i}(\omega t+\varphi)} \odot \left[\mathbf{N}\left(\mathbf{v}_{2k}, \mathbf{v}_i\,\mathrm{e}^{\mathrm{i}(\omega t+\varphi)}\right) + \mathbf{N}\left(\mathbf{v}_i\,\mathrm{e}^{\mathrm{i}(\omega t+\varphi)}, \mathbf{v}_{2k} + \mathrm{c.c.}\right)\right], \qquad (2.53\mathrm{a})$$

$$= 2\pi h \int_0^1 \left(2k_i\, a_{2k}\, v_i w_i - a_{2k}\frac{\partial(u_i v_i)}{\partial r}\right) r\mathrm{d}r, \qquad (2.53\mathrm{b})$$

with a_{2k} given by (2.49 a). The other term comes from the interaction of $\mathbf{V}_1$ with $\mathbf{v}_{2\omega}$

$$\sigma_{2\omega} = \mathbf{v}_i\,\mathrm{e}^{\mathrm{i}(\omega t+\varphi)} \odot \mathbf{N}\left(\mathbf{v}_{2\omega}\mathrm{e}^{2\mathrm{i}(\omega t+\varphi)}, \overline{\mathbf{v}_i}\,\mathrm{e}^{-\mathrm{i}(\omega t+\varphi)}\right), \qquad (2.54\mathrm{a})$$

$$= 2\pi h\frac{\mathrm{i}k_i}{\omega}\int_0^1 \left(\frac{\mathrm{d}a_{2\omega}}{\mathrm{d}r}u_i w_i - \frac{2\mathrm{i}a_{2\omega}}{r}v_i w_i\right) r\mathrm{d}r, \qquad (2.54\mathrm{b})$$

where the term associated with $\mathbf{N}(\mathbf{v}_i, \mathbf{v}_{2\omega})$ has been omitted because its scalar product with $\mathbf{v}_i\,\mathrm{e}^{\mathrm{i}(\omega t+\varphi)}$ is zero. The final coefficient σ used in the amplitude equation (2.30) is

$$\sigma = \frac{\sigma_{2k} + \sigma_{2\omega}}{\mathrm{i}N}, \qquad (2.55)$$

where N, σ_{2k} and $\sigma_{2\omega}$ are given by (2.50), (2.53b) and (2.54b). The integrals appearing in the coefficients σ_{2k} and $\sigma_{2\omega}$ can be evaluated numerically. It is easy to see that σ_{2k} and $\sigma_{2\omega}$ are pure imaginary and therefore σ is real.

Finally the coefficients ξ_j describe the nonlinear interaction of the Kelvin mode with the j-th geostrophic mode

$$X_j = \mathbf{v}_i\,\mathrm{e}^{\mathrm{i}(\omega t+\varphi)} \odot \left[\mathbf{N}\left(\frac{1}{2}\mathbf{v}_0^j, \mathbf{v}_i\,\mathrm{e}^{\mathrm{i}(\omega t+\varphi)}\right) + \mathbf{N}\left(\mathbf{v}_i\,\mathrm{e}^{\mathrm{i}(\omega t+\varphi)}, \mathbf{v}_0^j\right)\right], \tag{2.56a}$$

$$= -2\pi h \int_0^1 \left(\frac{2\mathrm{i}k_i}{\omega} v_0^j u_i w_i + \frac{1}{r}\frac{\mathrm{d}(r v_0^j)}{\mathrm{d}r} u_i v_i\right) r\mathrm{d}r, \tag{2.56b}$$

where v_0^j is given by (2.25). The coefficient ξ_j of (2.30) is

$$\xi_j = -\frac{X_j}{\mathrm{i}N}, \tag{2.57}$$

where N and X_j are given by (2.50) and (2.56b). Again, the integral in (2.56b) is calculated numerically.

Some numerical values of the coefficients f, σ and ξ_j whose analytical expressions are given by (2.52), (2.55) and (2.57) are found in tables 2.1, 2.2 and 2.3.

2.6.4 Linear viscous boundary layers (Ekman pumping)

In this appendix we derive the viscous correction to the main flow $\mathbf{V}$ in the boundary layers. This correction can be written as

$$\widetilde{\mathbf{V}} = Ro^{1/3} A \left(\widetilde{\mathbf{v}}_i + Re^{-1/2}\,\widetilde{\mathbf{v}}_3\right) \mathrm{e}^{\mathrm{i}(\omega t+\varphi)} + \text{o.t.}, \tag{2.58}$$

with the boundary conditions $\mathbf{V} + \widetilde{\mathbf{V}} = 0$ on the walls and $\widetilde{\mathbf{V}}$ tends to zero far from the walls. In the previous expression, $\widetilde{\mathbf{v}}_i = (\widetilde{u}_i,\, \widetilde{v}_i,\, \widetilde{w}_i,\, \widetilde{p}_i)$ and $\widetilde{\mathbf{v}}_3 = (\widetilde{u}_3,\, \widetilde{v}_3,\, \widetilde{w}_3,\, \widetilde{p}_3)$ are of order 1. The added corrective flow (Ekman pumping) is denoted $\widetilde{\mathbf{v}}_3$ because, as we shall see below, this flow constitutes the normal boundary condition for the bulk flow $\mathbf{V}_3$ at order Ro. This calculation is classical and can be found in several sources (e.g. Greenspan, 1968; Gans, 1970b).

Lateral wall

At first, let us focus on the lateral wall $r = 1$. By taking into account the viscous effects in (2.8) and considering the rescaled coordinate

$$\widetilde{r} = Re^{-1/2}\,(1 - r), \tag{2.59}$$

one can write the linear Navier-Stokes equation valid close to the lateral wall

$$\left(\mathrm{i}\omega\mathcal{I} - Re^{1/2}\,\frac{\partial}{\partial\widetilde{r}}\mathcal{R}_l + \mathcal{M}_l - \frac{\partial^2}{\partial\widetilde{r}^2}\mathcal{I}\right)\widetilde{\mathbf{V}} = O\left(Re^{-1}\widetilde{\mathbf{V}}\right), \tag{2.60}$$

where the tensors $\mathcal{R}_l$ et $\mathcal{M}_l$ are defined as follow

$$\mathcal{R}_l = \begin{pmatrix} 0 & 0 & 0 & 1 \\ 0 & 0 & 0 & 0 \\ 0 & 0 & 0 & 0 \\ 1 & 0 & 0 & 0 \end{pmatrix} \quad \text{and} \quad \mathcal{M}_l = \begin{pmatrix} 0 & -2 & 0 & 0 \\ 2 & 0 & 0 & \mathrm{i} \\ 0 & 0 & 0 & \dfrac{\partial}{\partial z} \\ 1 & \mathrm{i} & \dfrac{\partial}{\partial z} & 0 \end{pmatrix}. \tag{2.61}$$

At order $Re^{1/2}$, one gets

$$\frac{\partial}{\partial \widetilde{r}}(\mathcal{R}_l\, \widetilde{\mathbf{v}}_i) = \mathbf{0}, \tag{2.62}$$

which leads to $\widetilde{u}_i = \widetilde{p}_i = 0$.

At order 1, (2.60) gives

$$\frac{\partial}{\partial \widetilde{r}}(\mathcal{R}_l\, \widetilde{\mathbf{v}}_3) = \left(\mathrm{i}\omega\mathcal{I} + \mathcal{M}_l - \frac{\partial^2}{\partial \widetilde{r}^2}\mathcal{I}\right) \widetilde{\mathbf{v}}_i. \tag{2.63}$$

The solution of this linear system with the boundary conditions $\mathbf{v}_i + \widetilde{\mathbf{v}}_i = 0$ in $\widetilde{r} = 0$ and $\widetilde{\mathbf{v}}_i$ vanishes to zero for $\widetilde{r} \gg 1$ is

$$\widetilde{v}_i(\widetilde{r},\, z) = -v_i(1)\, \sin(k_i z)\, \mathrm{e}^{-\kappa\widetilde{r}} \quad \text{and} \quad \widetilde{w}_i(\widetilde{r},\, z) = -w_i(1)\, \cos(k_i z)\, \mathrm{e}^{-\kappa\widetilde{r}} \tag{2.64}$$

where κ is given by

$$\kappa = \frac{1+\mathrm{i}}{\sqrt{2}}\sqrt{\omega}. \tag{2.65}$$

and

$$\widetilde{u}_3 = \widetilde{\mathbf{v}}_3 \cdot \mathbf{n} = -\alpha_i\, J_1(\delta_i)\, \sin k_i z, \quad \text{in } r = 1, \tag{2.66}$$

where

$$\alpha_i = \frac{1+\mathrm{i}}{\sqrt{2}} \frac{(\delta_i^2 - 1)\,\omega^2 + 4}{(4-\omega^2)\,\omega^{3/2}}. \tag{2.67}$$

End walls

An equivalent derivation can be done for the upper wall (the flow in the lower wall boundary layer is formally identical). Using the local rescaled coordinate

$$\widetilde{z} = Re^{1/2}\left(\frac{h}{2} - z\right), \tag{2.68}$$

one can rewrite the Navier-Stokes equation valid close to the upper wall

$$\left(\mathrm{i}\omega\mathcal{I} - Re^{1/2}\,\frac{\partial}{\partial \widetilde{z}}\mathcal{R}_u + \mathcal{M}_u - \frac{\partial^2}{\partial \widetilde{z}^2}\mathcal{I}\right) \widetilde{\mathbf{V}} = O\left(Re^{-1}\widetilde{\mathbf{V}}\right), \tag{2.69}$$

where the tensors $\mathcal{R}_u$ et $\mathcal{M}_u$ are defined as follow

$$\mathcal{R}_u = \begin{pmatrix} 0 & 0 & 0 & 0 \\ 0 & 0 & 0 & 0 \\ 0 & 0 & 0 & 1 \\ 0 & 0 & 1 & 0 \end{pmatrix} \quad \text{and} \quad \mathcal{M}_u = \begin{pmatrix} 0 & -2 & 0 & \dfrac{\partial}{\partial r} \\ 2 & 0 & 0 & \dfrac{\mathrm{i}}{r} \\ 0 & 0 & 0 & 0 \\ \dfrac{1}{r} + \dfrac{\partial}{\partial r} & \dfrac{\mathrm{i}}{r} & 0 & 0 \end{pmatrix}. \tag{2.70}$$

At order $Re^{1/2}$, one finds $\widetilde{w}_i = \widetilde{p}_i = 0$. At order 1, the projection of (2.69) onto the radial, azimuthal and pressure directions with the proper boundary conditions gives

$$\widetilde{u}_i(r,\widetilde{z}) = \mathrm{i}\,S(r)\,\mathrm{e}^{-\kappa_s\widetilde{z}} - \mathrm{i}\,D(r)\,\mathrm{e}^{-\kappa_d\widetilde{z}}, \tag{2.71a}$$

$$\widetilde{v}_i(r,\widetilde{z}) = S(r)\,\mathrm{e}^{-\kappa_s\widetilde{z}} + D(r)\,\mathrm{e}^{-\kappa_d\widetilde{z}}, \tag{2.71b}$$

where κ_s and κ_d are given by

$$\kappa_s = \frac{1+\mathrm{i}}{\sqrt{2}}\sqrt{\omega+2}, \quad \text{and} \quad \kappa_d = \frac{1-\mathrm{i}}{\sqrt{2}}\sqrt{2-\omega}, \tag{2.72}$$

and where S and D are given by

$$S(r) = \frac{\mathrm{i}\,u_i - v_i}{2}\sin(k_i h/2), \quad \text{and} \quad D(r) = \frac{-\mathrm{i}\,u_i - v_i}{2}\sin(k_i h/2). \tag{2.73}$$

The projection of (2.69) on the vertical direction gives

$$\widetilde{w}_3 = \left(\frac{2\mathrm{i}S}{r} + \mathrm{i}\frac{\mathrm{d}S}{\mathrm{d}r}\right)\frac{\mathrm{e}^{-\kappa_s\widetilde{z}}}{\kappa_s} - \mathrm{i}\frac{\mathrm{d}D}{\mathrm{d}r}\frac{\mathrm{e}^{-\kappa_d\widetilde{z}}}{\kappa_d}, \tag{2.74}$$

such that

$$\widetilde{w}_3 = \widetilde{\mathbf{v}}_3\cdot\mathbf{n} = -\beta_i\,\sin(k_i h/2)\,J_1(\delta_i r)\,, \quad \text{in } \widetilde{z}=0 \quad \text{i.e.} \quad z = h/2, \tag{2.75}$$

where

$$\beta_i = \frac{1-\mathrm{i}}{2\sqrt{2}}\delta_i^2\left[\frac{1}{(2-\omega)^{3/2}} + \frac{\mathrm{i}}{(2+\omega)^{3/2}}\right]. \tag{2.76}$$

Geostrophic flow

For the geostrophic flow, the viscous flow in the end wall boundary layers can be calculated with a similar method as for the Kelvin mode in 2.6.4. This viscous flow is of the form

$$\widetilde{\mathbf{V}} = Ro^{2/3}\sum_{j=1}^{\infty} A_0^j(\tau)\left(\widetilde{\mathbf{v}}_0^j + Re^{-1/2}\widetilde{\mathbf{v}}_4^j\right) + \text{o.t.}, \tag{2.77}$$

where $\widetilde{\mathbf{v}}_0^j = (\widetilde{u}_0^j, \widetilde{v}_0^j, \widetilde{w}_0^j, \widetilde{p}_0^j)$. One finds $\widetilde{w}_0^j = \widetilde{p}_0^j = 0$ and

$$\widetilde{u}_0^j = \frac{\mathrm{i}}{2}v_0^j\left(-\mathrm{e}^{-\kappa_1\widetilde{z}} + \mathrm{e}^{-\kappa_2\widetilde{z}}\right), \quad \text{and} \quad \widetilde{v}_0^j = -\frac{1}{2}v_0^j\left(\mathrm{e}^{-\kappa_1\widetilde{z}} + \mathrm{e}^{-\kappa_2\widetilde{z}}\right), \tag{2.78}$$

where $\kappa_1 = 1+\mathrm{i}$ and $\kappa_2 = 1-\mathrm{i}$. This leads to

$$\widetilde{w}_4^j = \widetilde{\mathbf{v}}_4^j\cdot\mathbf{n} = \widetilde{w}_4^j = \frac{1}{2}\left(\frac{\mathrm{d}v_0^j}{\mathrm{d}r} + \frac{v_0^j}{r}\right), \quad \text{in } z = h/2. \tag{2.79}$$

Viscous coefficients

The surface viscous coefficients appearing in (2.30) and (2.33) can now be calculated. If the surface of the cylinder is separated into two parts $S = S_l + S_e$, where S_l is the lateral wall and S_e the end walls, we have

$$\mu_l = \int_{S_l} p_i \sin(k_i z)\, \widetilde{\mathbf{v}}_3 \cdot \mathbf{n}\, \mathrm{d}^2 S = -\pi \left[h - \sin(k_i h)/k_i\right] \alpha_i J_1^2(\delta_i), \tag{2.80a}$$

$$\mu_e = \int_{S_e} p_i \sin(k_i z)\, \widetilde{\mathbf{v}}_3 \cdot \mathbf{n}\, \mathrm{d}^2 S, = -2\pi\beta_i \frac{(\delta_i^2-1)\omega^2+4}{\delta_i^2\omega^2} J_1^2(\delta_i) \sin^2\left(\frac{k_i h}{2}\right), \tag{2.80b}$$

where we have used the formulation of $\widetilde{\mathbf{v}}_3 \cdot \mathbf{n}$ found in (2.66) and (2.75). Now using the relation (2.31) the viscous coefficient μ used in (2.30) is simply

$$\mu = -\frac{\mu_l + \mu_e}{N}, \tag{2.81}$$

where N is given by (2.50).

For the geostrophic flow, we obtain by integrating by parts

$$\mu_0 = \int_{S_e} p_0^j\, \widetilde{\mathbf{v}}_4^j \cdot \mathbf{n}\, \mathrm{d}^2 S = -4\pi \int_0^1 {v_0^j}^2 r \mathrm{d}r, \tag{2.82}$$

where we have used $\widetilde{\mathbf{v}}_4^j \cdot \mathbf{n}$ as given by (2.79) and

$$N_0 = \mathbf{v}_0^j \odot \mathcal{I}\, \mathbf{v}_0^j = 2\pi h \int_0^1 {v_0^j}^2 r \mathrm{d}r, \tag{2.83}$$

which leads to a surface viscous coefficient $\mu_0/N_0 = -2/h$ as it appears in the amplitude equation (2.33).

The volume viscous coefficient ν is simply

$$\nu = \frac{-\mathbf{v}_i \odot \mathcal{L}\, \mathbf{v}_i}{\mathbf{v}_i \odot \mathcal{I}\, \mathbf{v}_i} = (k_i^2 + \delta_i^2). \tag{2.84}$$

Some useful numerical values of the viscous coefficients μ and ν obtained through (2.81) and (2.84) are given in tables 2.1 and 2.2.

2.6.5 Nonlinear viscous boundary layers

To calculate the forcing of the geostrophic flow by the Kelvin mode, we need to perform a weakly nonlinear analysis in the end wall boundary layer. We choose to focus on the upper wall boundary layer $z = h/2$ (the calculation is symmetric for the bottom wall) using the rescaled vertical coordinate $\widetilde{z}$ as defined by (2.68). Taking into account the nonlinear effects and considering only the forcing of geostrophic modes of angular frequency $\omega = 0$, the Navier-Stokes equation reads

$$\left(-Re^{1/2}\frac{\partial}{\partial \widetilde{z}}\mathcal{R}_u + \mathcal{M}_u - \frac{\partial^2}{\partial \widetilde{z}^2}\mathcal{I}\right)\widetilde{\mathbf{V}} = \mathbf{N}_u(\widetilde{\mathbf{V}},\widetilde{\mathbf{V}}) + \mathbf{N}_u(\mathbf{V},\widetilde{\mathbf{V}}) + \mathbf{N}_u(\widetilde{\mathbf{V}},\mathbf{V}) + \text{o.t.}, \tag{2.85}$$

where the operators $\mathcal{R}_u$ and $\mathcal{M}_u$ are defined in (2.70) and $\mathbf{N}_u$ is similar to the bilinear function $\mathbf{N}$ defined in (2.50) but adapted to the rescaled variable $\widetilde{z}$.

We now need to evaluate the right hand side of the above equation at order $Ro^{2/3}$ focusing on the geostrophic component (independent of t and ϕ). It leads to

$$\mathbf{N}_u(\widetilde{\mathbf{V}},\widetilde{\mathbf{V}}) = Ro^{2/3}|A|^2 \begin{pmatrix} \gamma_1(r,\widetilde{z}) \\ \kappa_1(r,\widetilde{z}) \\ 0 \\ 0 \end{pmatrix} + \text{o.t.} + O(Ro), \tag{2.86}$$

where

$$\gamma_1 = \overline{\widetilde{v}}_i \left(\frac{\widetilde{v}_i}{r} - \frac{\mathrm{i}}{r}\widetilde{u}_i\right) - \overline{\widetilde{u}}_i \frac{\partial \widetilde{u}_i}{\partial r} - \overline{\widetilde{w}}_3 \frac{\partial \widetilde{u}_i}{\partial \widetilde{z}}, \tag{2.87a}$$

$$\kappa_1 = \overline{\widetilde{u}}_i \left(\frac{\widetilde{v}_i}{r} - \frac{\partial \widetilde{v}_i}{\partial r}\right) - \overline{\widetilde{v}}_i \frac{\mathrm{i}\widetilde{v}_i}{r} - \overline{\widetilde{w}}_3 \frac{\partial \widetilde{v}_i}{\partial \widetilde{z}}, \tag{2.87b}$$

where $\widetilde{u}_i$ and $\widetilde{v}_i$ are given by (2.71 *a,b*) and $\widetilde{w}_3$ is given by (2.74). The other two terms are

$$\mathbf{N}_u(\mathbf{V},\widetilde{\mathbf{V}}) = Ro^{2/3}|A|^2 \begin{pmatrix} \gamma_2(r,\widetilde{z}) \\ \kappa_2(r,\widetilde{z}) \\ 0 \\ 0 \end{pmatrix} + \text{o.t.} + O(Ro), \tag{2.88a}$$

$$\mathbf{N}_u(\widetilde{\mathbf{V}},\mathbf{V}) = Ro^{2/3}|A|^2 \begin{pmatrix} \gamma_3(r,\widetilde{z}) \\ \kappa_3(r,\widetilde{z}) \\ 0 \\ 0 \end{pmatrix} + \text{o.t.} + O(Ro), \tag{2.88b}$$

where

$$\gamma_2 = \sin\frac{k_i h}{2}\left[v_i\left(-\frac{\mathrm{i}}{r}\widetilde{u}_i + \frac{\widetilde{v}_i}{r}\right) + u_i\frac{\partial \widetilde{u}_i}{\partial r} - \overline{w}_3\frac{\partial \widetilde{u}_i}{\partial \widetilde{z}} - k_i\widetilde{z}\,\overline{w}_i\frac{\partial \widetilde{u}_i}{\partial \widetilde{z}}\right], \tag{2.89a}$$

$$\kappa_2 = \sin\frac{k_i h}{2}\left[u_i\left(\frac{\widetilde{v}_i}{r} + \frac{\partial \widetilde{v}_i}{\partial r}\right) - \frac{\mathrm{i}}{r}v_i\widetilde{v}_i - \overline{w}_3\frac{\partial \widetilde{v}_i}{\partial \widetilde{z}} - k_i\widetilde{z}\,\overline{w}_i\frac{\partial \widetilde{v}_i}{\partial \widetilde{z}}\right], \tag{2.89b}$$

$$\gamma_3 = \sin\frac{k_i h}{2}\left[\widetilde{v}_i\left(-\frac{\mathrm{i}}{r}u_i + \frac{v_i}{r}\right) + \widetilde{u}_i\frac{\partial u_i}{\partial r}\right], \tag{2.89c}$$

$$\kappa_3 = \sin\frac{k_i h}{2}\left[-\widetilde{u}_i\left(\frac{v_i}{r} + \frac{\partial v_i}{\partial r}\right) + \frac{\mathrm{i}}{r}v_i\widetilde{v}_i\right], \tag{2.89d}$$

where $w_3 = -\widetilde{w}_3(\widetilde{z}=0)$.

The solution of (2.85) forced by the right hand side is sought at order $Ro^{2/3}$ of the form

$$\widetilde{\mathbf{V}} = Ro^{2/3}|A|^2\left(\widetilde{\mathbf{v}}_2^{\mathrm{NL}} + Re^{-1/2}\,\widetilde{\mathbf{v}}_4^{\mathrm{NL}}\right). \tag{2.90}$$

Examining (2.85) at order $Ro^{2/3}Re^{1/2}$ leads to $\widetilde{w}_2^{\mathrm{NL}} = \widetilde{p}_2^{\mathrm{NL}} = 0$. At order $Ro^{2/3}$, it leads to

$$\left(\frac{\partial^4}{\partial\widetilde{z}^4} + 4\right)\widetilde{u}_2^{\mathrm{NL}} = 2\left(\kappa_1 + \kappa_2 + \kappa_3\right) - \frac{\partial^2}{\partial\widetilde{z}^2}\left(\gamma_1 + \gamma_2 + \gamma_3\right), \quad (2.91\mathrm{a})$$

$$\widetilde{v}_2^{\mathrm{NL}} = -\frac{1}{2}\left(\gamma_1 + \gamma_2 + \gamma_3 + \frac{\partial^2\widetilde{u}_2^{\mathrm{NL}}}{\partial\widetilde{z}^2}\right). \quad (2.91\mathrm{b})$$

The solution of the above system is a sum of the particular solution of (2.91 *a*) and the solution of the homogeneous system of the form $\widetilde{u}_2^{\mathrm{NL}} = a_1\exp(-1+\mathrm{i})\widetilde{z} + a_2\exp(-1-\mathrm{i})\widetilde{z}$. The particular solution is found with a symbolic calculation software where the coefficients a_1 and a_2 are adjusted to satisfy the boundary conditions $\widetilde{u}_2^{\mathrm{NL}} = \widetilde{v}_2^{\mathrm{NL}} = 0$ in $\widetilde{z} = 0$ (the boundary condition of vanishing $\widetilde{\mathbf{v}}_2^{\mathrm{NL}}$ for $\widetilde{z} \gg 1$ is ensured by the selection of the vanishing exponential in the particular solution).

Taking (2.85) at order $Ro^{2/3}$ also gives the form of the flow orthogonal to the wall at order $Ro^{2/3}Re^{-1/2}$ which satisfies

$$\frac{\partial}{\partial\widetilde{z}}\widetilde{w}_4^{\mathrm{NL}} = -\left(\frac{1}{r} + \frac{\partial}{\partial r}\right)\widetilde{u}_2^{\mathrm{NL}}. \quad (2.92)$$

Once this is integrated, the normal flow is $\widetilde{\mathbf{v}}_4^{\mathrm{NL}}\cdot\mathbf{n} = \widetilde{w}_4^{\mathrm{NL}}(\widetilde{z}=0)$. The coefficients χ_j needed for the amplitude equation (2.33) can now be obtained

$$\chi_j = \frac{4\pi}{N_0}\int_0^1 p_0^j\left(\widetilde{\mathbf{v}}_4^{\mathrm{NL}}\cdot\mathbf{n} - \widetilde{w}_4^{\mathrm{SB}}\right) r\mathrm{d}r + \mathrm{c.c.}, \quad (2.93)$$

where N_0 is given by (2.83) and

$$\widetilde{w}_4^{\mathrm{SB}} = \int_0^1 \widetilde{\mathbf{v}}_4^{\mathrm{NL}}\cdot\mathbf{n}\, r\mathrm{d}r + \mathrm{c.c.}, \quad (2.94)$$

corresponds to the flow associated with a modification of the solid body rotation frequency.

3. ÉTUDE EXPÉRIMENTALE DE L'INSTABILITÉ DE PRÉCESSION

Dans le chapitre 2 nous avons étudié d'un point de vue théorique et expérimental l'écoulement d'un fluide dans un cylindre en précession en l'absence d'instabilité. Nous avons montré que cet écoulement primaire, aussi appelé écoulement de base est une superposition de modes de Kelvin. Dans ce chapitre nous menons une étude expérimentale sur la stabilité d'un écoulement résonant. Nous montrons qu'un mode de Kelvin résonnant peut induire une instabilité par résonance triadique avec deux modes de Kelvin libres. Ce chapitre reprend une publication parue dans la revue *Physics of Fluids* sous le titre "Instability of a fluid inside a precessing cylinder". Dans cet article l'angle de précession est noté α, ici nous le noterons θ afin d'unifier les notations de ce manuscrit de thèse. La coordonnée cylindrique notée θ dans l'article sera notée φ dans cette étude.

Abstract

In this paper, we report experimental results on the stability of a fluid inside a precessing and resonant cylinder. Above a critical Reynolds number, the Kelvin mode forced by precession triggers an instability which saturates at intermediate Re and which leads to a turbulent flow at high Reynolds numbers. Particle Image Velocimetry measurements in two different sections of the cylinder have revealed the 3D structure of this instability. It is composed of two free Kelvin modes whose wavenumbers and frequencies respect the conditions for a triadic resonance with the forced Kelvin mode, as is obtained for the elliptical instability. Moreover, an experimental diagram of stability has been established by varying both the precessing angle and the Reynolds number. It shows a good agreement with a scaling analysis based on a triadic resonance mechanism.

3.1 Introduction

The knowledge of the flow forced by a precessional motion is of critical importance in several domains. In aeronautics, the liquid propellant contained in a flying object can be forced by precession. The resulting flow can create a destabilizing torque on the object and thus modify its trajectory dangerously. In geophysics the Earth's precession modifies the flow of its liquid core and is therefore of signicative importance in understanding the geodynamo (among other effects such as convection, boundary layers, elliptic or tidal instability (see Malkus, 1989)). The flow inside a cylinder subjected to precession can be decomposed as a sum of a shear along the cylinder axis and a superposition of Kelvin modes which become resonant for particular precession frequencies. McEwan (1970) first observed that this flow can become unstable and even turbulent for large Reynolds numbers. This behavior has also been reported by Manasseh (1992, 1994, 1996), and Kobine (1995). Several scenarios have been proposed to explain this instability. Studying the case of an infinite cylinder, Mahalov (1993) proposed a mechanism of triadic resonance between the flow shear and two Kelvin modes. Kerswell (1999) suggested that a given Kelvin mode can trigger a triadic resonance with two other Kelvin modes leading to an instability. Another scenario, suggested by Kobine (1995, 1996) is that the main flow could be modified by a geostrophic mode (due to nonlinear effects) eventually leading to a centrifugal instability.

3.2 Presentation of the problem

An experimental set-up has been built to study the precession of a cylinder of height H along its axis $\hat{\mathbf{z}}$ and radius R, full of water of kinematic viscosity ν. More details about the set-up can be found in Meunier *et al.* (2008). The cylinder rotates at the angular frequency Ω_1 (measured with an accuracy of 0.1%) around its axis. It is mounted on a platform which rotates at the angular frequency Ω_2 (measured with an accuracy of 0.2%). Once the spin-up stage is completed, the cylinder is tilted with an angle θ (determi-

ned with an absolute accuracy of $\pm 0.1°$) with respect to the rotation axis of the platform. Particle Image Velocimetry (PIV) measurements in transverse sections of the cylinder are made. To perform the acquisition of a PIV field, we use small markers illuminated with a thin light sheet created by a Yag pulsed laser. The particle images are recorded by a camera mounted on the rotating platform. The horizontal velocity and the axial vorticity fields in the cylinder frame of reference are thus measured. More details about PIV treatment can be found in Meunier & Leweke (2003).

In the following, variables are made dimensionless by using R and $\Omega = \Omega_1 + \Omega_2 \cos\theta$ as characteristic length and characteristic frequency. The dynamics of this precessing system depends on four dimensionless numbers : the aspect ratio $h = H/R$, the frequency ratio $\omega = \Omega_1/\Omega$, the Rossby number $Ro = \Omega_2 \sin\theta/\Omega$ and the Reynolds number $Re = \Omega R^2/\nu$. The cylindrical coordinates are used in the reference frame of the cylinder and noted (r, φ, z), where $z = 0$ corresponds to the mid-height section of the cylinder.

3.3 Structure of the instability

Figure 3.1 shows the axial and instantaneous flow vorticity for a small precessing angle ($\theta = 1°$) and different Reynolds numbers. The laser sheet is at an altitude $z \simeq h/4$. For $Re = 3500$ (Fig. 3.1(a)), the flow mainly consists of two stationary counter rotating vortices. A classical linear and inviscid theory is sufficient to explain this observation. By assuming a small Rossby number (weak precession, negligible nonlinear effects) and a large Reynolds number (negligible viscous effects), the linearized Euler equation at order $O(Ro)$ is

$$\frac{\partial \mathbf{v}}{\partial t} + 2\hat{\mathbf{z}} \times \mathbf{v} + \nabla p = -2Ro\, \omega\, r\, \cos(\omega t + \varphi)\, \hat{\mathbf{z}}, \tag{3.1}$$

where $2\hat{\mathbf{z}} \times \mathbf{v}$ is the dimensionless Coriolis force and p the dimensionless pressure including all potential terms.
The right-hand side of Eq. (3.1) is the precession forcing which forces a particular solution of Eq. (3.1) : $\mathbf{v}_{\text{part}} = -2Ro\, r\, \sin(\omega t + \varphi)\, \hat{\mathbf{z}}$. This solution does not satisfy the boundary conditions of no outward flow at $z = \pm h/2$. Thus, we must complete this solution with a solution of the homogeneous equation (Eq. (3.1) without forcing), so that the boundary condition at the upper and lower walls is satisfied. Due to time and azimuthal dependance of the forcing, the homogeneous solution is a sum of Kelvin modes of azimuthal wavenumber $m = 1$ and angular frequency ω. Finally the solution of Eq. (3.1) is

$$\mathbf{v} = \mathbf{v}_{\text{part}} + \sum_{i=1}^{\infty} a_i \mathbf{v}_i\,(m = 1, \omega, k_i)\,, \tag{3.2}$$

where $\mathbf{v}_i\,(m, \omega, k_i)$ is a Kelvin mode of amplitude a_i and whose axial wavenumber k_i depends on ω by the dispersion relation

$$\begin{aligned} \omega k_i \sqrt{4/\omega^2 - 1} \quad & J_m'\left(k_i \sqrt{4/\omega^2 - 1}\right) \\ & + 2 J_m\left(k_i \sqrt{4/\omega^2 - 1}\right) = 0, \end{aligned} \tag{3.3}$$

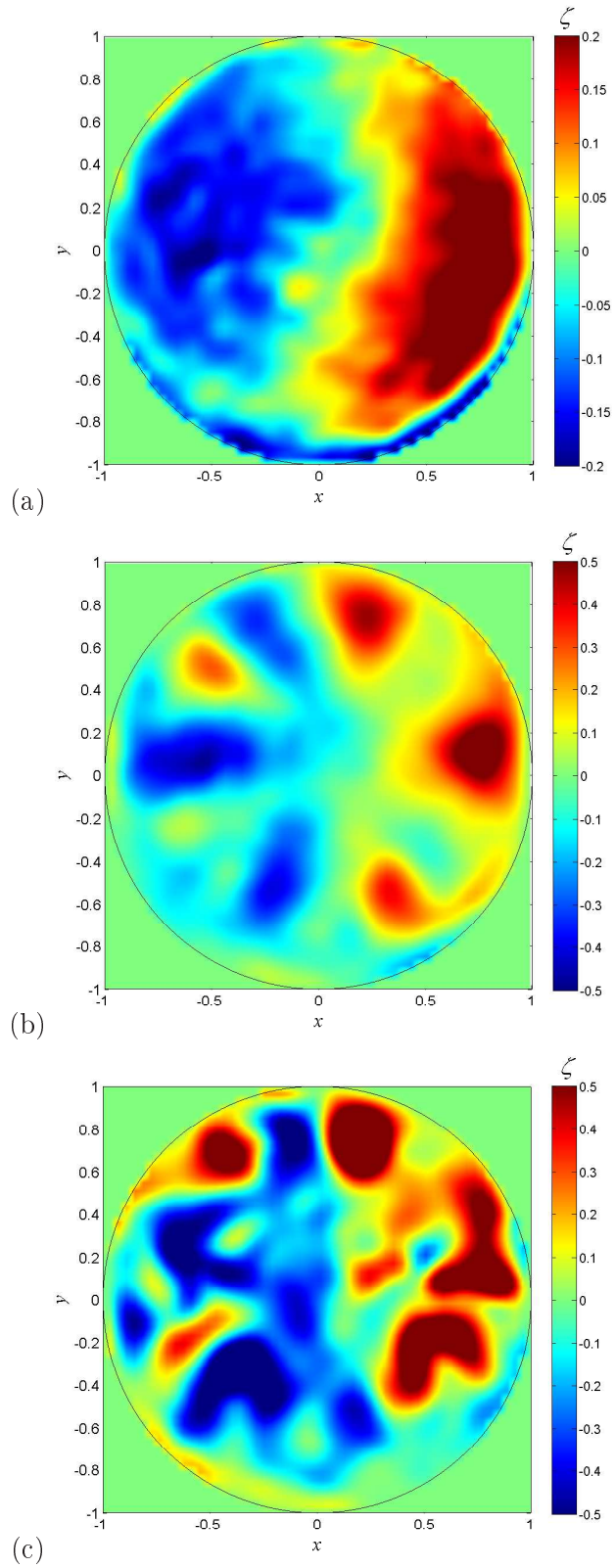

Figure 3.1: Axial vorticity ζ of the flow for different Reynolds numbers at $z = h/4$. (a) For $Re = 3500$ the stable flow exhibits the forced Kelvin mode. (b) For $Re = 6000$ the flow is unstable and exhibits a free Kelvin mode with $m_1 = 5$ superimposed to the forced Kelvin mode. (c) For $Re = 24400$ the flow is turbulent. For these three cases $h = 1.62$, $\omega = 1.18$, $|Ro| = 0.0031$.

where J_m is the Bessel function of the first kind, J'_m its derivative. The axial vorticity ζ_i of the i-th Kelvin mode is

$$\zeta_i = J_m\left(k_i\sqrt{4/\omega^2 - 1}r\right)\sin\left(k_i z\right)\cos\left(\omega t + m\varphi\right). \tag{3.4}$$

When k_i is equal to $(2n+1)\pi/h$, with n an integer number, the i-th Kelvin mode 'fits' inside the height of the cylinder and becomes resonant. In our experiments (i.e for $h = 1.62$ and $\omega = 1.18$) the first Kelvin mode (which is theoretically characterized by two lobes of vorticity) is resonant (its axial wavenumber, noted k, is equal to π/h). Because the amplitude a_1 is predicted to diverge by a linear analysis it is necessary to include viscous (see Gans, 1970*b*) and nonlinear effects. We have shown in Meunier *et al.* (2008) that a_1 scales as $RoRe^{1/2}$ for low Reynolds numbers (viscous regime, $Re^{1/2}|Ro|^{2/3} \ll 1$) and as $Ro^{1/3}$ for large Reynolds numbers (nonlinear regime, $Re^{1/2}|Ro|^{2/3} \gg 1$). Since the non-resonant mode amplitudes scale as Ro, the resonant mode is always predominant.

Figure 3.1(b) is a PIV measurement of the axial and instantaneous vorticity field for $Re = 6500$. For such a value of Re the flow seen in Fig. 3.1(a) is unstable and the unstable mode exhibits a ring with 10 lobes of vorticity with alternate sign. It corresponds to a free Kelvin mode (i.e a solution of Eq. (3.1) without forcing) whose azimuthal wavenumber, noted m_1 equals 5. This mode $m_1 = 5$ is superimposed to the forced Kelvin mode $m = 1$ shown in Fig. 3.1(a). (As seen on Fig. 3.1(b) the average vorticity is negative for $x < 0$ and positive for $x > 0$). Such a flow, which is three-dimensional and non-stationary, corresponds to the instability discovered by McEwan (1970) and studied by Manasseh (1992) using visualizations, which was called "resonant collapse" since it decreases the amplitude of the forced Kelvin mode. Indeed, the same structure has been observed for other aspect ratios ($h = 1.8$ and $h = 2$) and it also leads to the decrease of the forced Kelvin mode's amplitude. The visualization of a sequence of instantaneous PIV fields shows that the free Kelvin mode rotates as a function of time at a dimensionless frequency $\omega_1 = -0.34 \pm 11\%$ in the cylinder frame of reference. For this Reynolds number, the unstable mode beats probably due to a nonlinear coupling with the geostrophic mode. However, the amplitude of this unstable mode is stationary close to the threshold (i.e. $Re \simeq 4600$).

Figure 3.1(c) represents the axial and instantaneous vorticity field for even larger Reynolds numbers ($Re = 24400$). For such a value of Re the flow is disordered and seems to be turbulent. As suggested by Kerswell (1999), this disordered flow could be the result of successive instabilities : a cascade of bifurcations could lead to a turbulent state. It can be noted that the Kelvin mode $m = 1$ forced by precession is still present since the average vorticity is still negative for $x < 0$ and positive for $x > 0$.

Figure 3.2 is a PIV measurement of the axial and instantaneous vorticity field measured in a section of the cylinder lower than in Fig. 3.1. The laser sheet is at mid-height of the cylinder ($z = 0$). According to Eq. (3.4) the vorticity of the forced Kelvin mode $m = 1$ and of the free Kelvin mode $m_1 = 5$ is equal to 0. At this altitude a structure with 12 lobes of alternate vorticity is clearly observed. It corresponds to a free Kelvin mode whose azimuthal

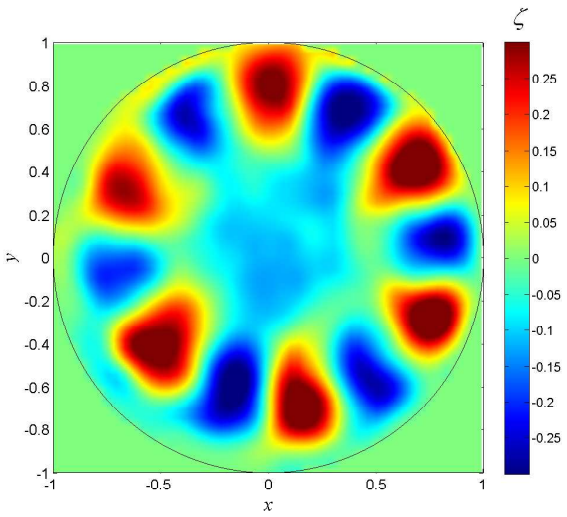

Figure 3.2: Vorticity field of the unstable flow at mid-height of the cylinder for the same parameters as in figure 1(*b*) ($h = 1.62$, $\omega = 1.18$, $|Ro| = 0.0031$, $Re = 6500$).

wavenumber, noted m_2, is equal to 6. Because it does not vanish at $z = 0$ its axial vorticity is given by Eq. (3.4) where $\sin(k_2 z)$ has been changed in $\cos(k_2 z)$. This free Kelvin mode rotates at a dimensionless angular frequency $\omega_2 = 0.79 \pm 2.5\%$ in the cylinder frame of reference.

The axial velocity (which is in quadrature with respect to the axial vorticity given by Eq. (3.4)) of the free Kelvin mode $m_1 = 5$ (resp. $m_2 = 6$) is a cosine (resp. sine) function of z. Boundary conditions of no outward flow at $z = \pm h/2$ imply that the axial wavenumber of the free Kelvin mode $m_1 = 5$ (resp. $m_2 = 6$) is discretized as follows : $k_1 = (2n_1 + 1)\pi/h$ (resp. $k_2 = 2n_2\pi/h$), n_1 (resp. n_2) being an integer.

Furthermore, figure 3.1(b) and figure 3.2 show that the unstable Kelvin modes correspond to the first branch of the dispersion relation since there is only one ring of vortices. We can thus infer that $k_1 = \pi/h$ (resp. $k_2 = 2\pi/h$) since the point $(k_1 = \pi/h, \omega_1 \approx -0.34)$ (resp. $(k_2 = 2\pi/h, \omega_1 \approx 0.79)$) then falls very close to the first branch of the dispersion relation (3.3) for $m_1 = 5$ (resp. $m_2 = 6$) (Fig. 3.3).

3.4 Discussion

These experiments have allowed to determine the structure of the instability of a fluid inside a precessing and resonant cylinder. We have found that the unstable flow is the sum of three Kelvin modes : the forced one, and two free modes. The azimuthal wavenumber and the angular frequency of these free modes have been measured and satisfy the conditions for a triadic resonance with the forced Kelvin mode

$$m_2 - m_1 = 1, \ \omega_2 - \omega_1 \approx \omega, \ k_2 - k_1 = k, \tag{3.5}$$

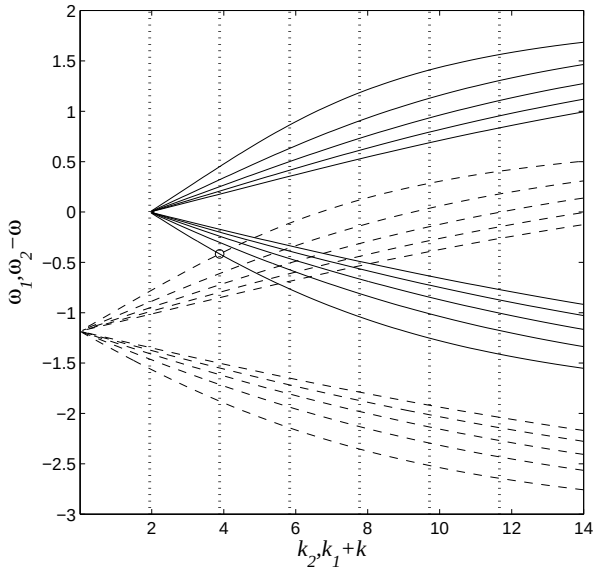

Figure 3.3: Dispersion relations of the Kelvin modes. The solid lines (resp. dashed lines) correspond to the first five branches of the Kelvin modes with azimuthal wavenumber $m_1 = 5$ (resp. $m_2 = 6$). Solid lines have been translated by $k = \pi/h$ and dashed lines have been translated by $\omega = 1.18$. Vertical dotted lines correspond $k = n\pi/h$, with n an integer, ($h = 1.62$, $\omega = 1.18$).

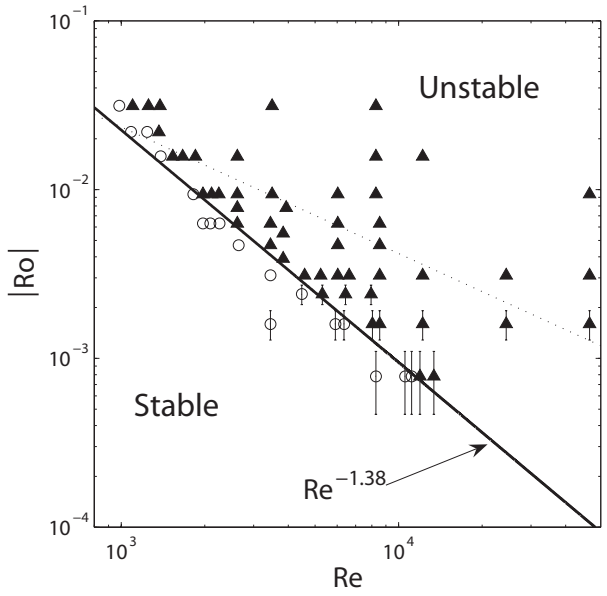

Figure 3.4: Stability diagram of the flow inside a precessing cylinder for ($h = 1.62$, $\omega = 1.18$). Circles represent stable experiments. Blacks triangles represent unstable experiments. The solid line is an experimental 'fit' of the threshold. The dashed line separates the viscous and the nonlinear domains of the base flow.

where $k = \pi/h$ is the axial wavenumber of the forced Kelvin mode. This suggests that the nonlinear coupling of the three Kelvin modes can trigger an instability, in a similar way as for the elliptical instability (see Eloy *et al.*, 2003; Kerswell, 2002).

The resonant condition given in Eq. (3.5) corresponds to the crossing points of the dashed and solid lines in Fig. 3.3, where the two dispersion relations are plotted in the same plane ; the dispersion relation with $m_1 = 5$ (resp. $m_2 = 6$) being horizontally (resp. vertically) translated of k (resp. translated of $-\omega$). It can be noted that there is an infinite and denumerable number of possible resonances. However, the free Kelvin modes observed experimentally correspond to the crossing point surrounded by a circle on Fig. 3.3. These modes satisfy exactly the boundary conditions at $z = \pm h/2$ (i.e. the crossing point lies on a vertical dotted line in Fig. 3.3). This exact resonance is only valid for $h = 1.62$. For $h \approx 1.62$ 'detuning' effects shall come into play and thus decrease the instability growth rate.

For $h \simeq 1.62$ two free Kelvin modes involving different branches of the dispersion relations or different azimuthal wavenumbers m_1 and m_2 can exactly resonate with the forced Kelvin mode. Nevertheless, it can be shown that there can not be exact resonances for $m_1 \leq 4$ for the first branches of the dispersion relations. Thus, the aspect ratio $h = 1.62$ corresponds to the exact resonance of the Kelvin modes with the smallest wavenumbers. Since volume viscous effects increase with the wavenumbers of the free Kelvin modes, $h = 1.62$ is expected to be the aspect ratio for which the flow is the most unstable. However, the previous observations are very general and do not depend on the fact that the triadic resonance is exact or not. Indeed, experiments with an arbitrary aspect ratio ($h = 1.8$) have shown exactly the same instability.

Finally we have plotted in Fig. 3.4 the stability diagram of this instability in the Re-$|Ro|$ plane. The majority of the experiments close to threshold are in the viscous domain for the base flow. This means that the amplitude of the forced mode scales as $a_1 \sim RoRe^{1/2}$ (see Meunier *et al.*, 2008). Based on similarities with the elliptic instability, the inviscid growth rate σ of the present triadic instability is expected to scale as the amplitude of the forced Kelvin mode : $\sigma \sim a_1$. The natural decay rate of Kelvin modes is due both to the boundary viscous layers and volume viscous effects. The surface (resp. volume) decay rate σ_{surf} (resp. σ_{vol}) scales as $\sigma_{\text{surf}} \sim -Re^{-1/2}$ (resp. $\sigma_{\text{vol}} \simeq -[m_1 + k_1^2(4/\omega^2 - 1)]Re^{-1}$). In our experiments, $\sigma_{\text{surf}} \simeq \sigma_{\text{vol}}$ for $Re \simeq 3000$. When the instability is saturated by volume (i.e. $Re < 3000$), (resp. boundary, i.e. $Re > 3000$) viscous effects, the amplitude of the forced Kelvin at which the flow becomes unstable satisfies $a_{1c} \sim Re^{-1}$ (resp. $a_{1c} \sim Re^{-1/2}$). Thus the Rossby number at which the flow becomes unstable scales as $Ro_{\text{crit}} \sim Re^{-3/2}$ (resp. $Ro_{\text{crit}} \sim Re^{-1}$). A 'fit' of the experimental threshold gives $Ro_{\text{crit}} \sim Re^{-1.38}$ (solid line), which is coherent with the theoretical scalings.

3.5 Conclusion

In this paper we studied experimentally the flow inside a precessing and resonant cylinder. At a given Rossby number the flow is stable for small enough Reynolds numbers and exhibits a Kelvin mode forced by the precessional motion. Increasing the Reynolds number above a critical value the flow becomes unstable (and even turbulent for high Re). Measurements in two different cylinder sections have revealed the presence of two Kelvin modes with high azimuthal wavenumbers. Their frequencies and their wavenumbers satisfy the conditions for a triadic resonance with the forced Kelvin mode. Thus, this paper has confirmed the scenario suggested by Kerswell (1999) that a Kelvin mode can be destabilized by a triadic resonance mechanism. So, the precessional instability is very general since it appears as soon as a Kelvin wave has been excited (through precession, compression, in the nonlinear stages of the elliptical instability or in the turbulent flow of a rotating cylinder). A stability diagram has also been established and showed that the scaling of the critical Ro as a function of Re is coherent with standard scaling laws in triadic resonances.

A linear stability analysis based on a mechanism of triadic resonance between Kelvin modes is currently under progress and will be the subject of a foregoing paper.

This study has been carried out under the contract CEA-CNRS N°012171.

4. ANALYSE LINÉAIRE DE STABILITÉ ET DYNAMIQUE FAIBLEMENT NON-LINÉAIRE

Dans le chapitre 3 nous avons étudié l'instabilité d'un fluide dans un cylindre en précession. Nous avons montré expérimentalement que cette instabilité est due à un mécanisme de résonance triadique entre le mode résonnant forcé par la précession et deux modes de Kelvin libres. Dans ce chapitre nous menons une analyse linéaire de stabilité afin de prédire les caractéristiques de l'instabilité. Nous développons également une analyse faiblement non-linéaire afin de prédire la dynamique de l'écoulement instable. Les résultats théoriques de ce chapitre sont comparés aux résultats expérimentaux. Le contenu de ce chapitre va être prochainement soumis à la revue *Journal of Fluid Mechanics*, sous le titre "Precessional instability of a fluid cylinder".

Abstract

In this paper, the instability of a fluid inside a precessing cylinder is addressed theoretically and experimentally. The precessional motion forces Kelvin modes in the cylinder which can become resonant for given precessional frequencies and cylinder aspect ratios. When the Reynolds number is large enough, these forced resonant Kelvin modes eventually become unstable. A linear stability analysis based on a triadic resonance between a forced Kelvin mode and two additional free Kelvin modes is carried out. This analysis allows to predict the spatial structure of the instability and its threshold. These predictions are compared to the vorticity field measured by Particle Image Velocimetry with an excellent agreement. When the Reynolds number is further increased, nonlinear effects appear. A weakly nonlinear theory is developed semi-empirically by introducing a geostrophic mode which is triggered by the nonlinear interaction of a free Kelvin mode with itself in the presence of viscosity. Amplitude equations are obtained coupling the forced Kelvin mode, the two free Kelvin modes and the geostrophic mode. They show that the instability saturates to a fixed point just above threshold. Increasing the Reynolds number leads to a transition from a steady saturated regime to an intermittent flow in good agreement with experiments. Surprisingly, this weakly nonlinear model still gives a correct estimate of the mean flow inside the cylinder even far from the threshold when the flow is turbulent.

4.1 Introduction

The goal of this paper is to explain the onset of turbulence observed in a precessing cylinder completely filled by a fluid.

The motion of precession is obtained when an object is in rotation around an axis which is itself rotating around a second axis. The knowledge of the flow forced by a precessional motion is of critical importance in several domains. In aeronautics (see Stewartson, 1958; Gans, 1984; Garg *et al.*, 1986; Agrawal, 1993; Bao & Pascal, 1997; Lambelin *et al.*, 2009), the presence of a fluid (such as a propellant liquid) inside a flying object (spacecraft, rocket, satellite...) can have dangerous consequences on the stability of this object. Indeed the presence of a weak precessing angle, due to a non-axisymmetry of the object, can lead to a large amplitude of the contained flow when it is resonant. This flow can in turn create a torque on the flying object which destabilizes the precessing angle and thus lead to the deviation of its trajectory. A good understanding of the behavior of such a fluid–structure coupled system requires a precise knowledge of the hydrodynamics of the contained fluid.

In external geophysics, atmospheric vortices such as hurricanes or tornadoes are also subject to precessional forcing. Indeed, their axes rotate with the earth rotation around the polar axis. The fluid is thus in precession with an angle α equal to the co-latitude. This is exactly the kind of flow which is studied in this paper. Usually, the precession of atmospheric vortices is neglected and only Coriolis effects are taken into account. However, the

question remains whether precession has a significative effect on the cyclone dynamics and notably on its stability.

This problem is also relevant to internal geophysics. Indeed, the Earth precession induces a forcing on its liquid core and thus generates a strong turbulent flow. Because the Earth core is made of a conductive fluid (melt iron) such a flow could be responsible for the geodynamo effect which generates the Earth magnetic field, as proposed by Malkus (1968) and Kerswell (1996). However, other effects such as convection, boundary layers, elliptic or tidal instability have also been proposed to explain the source of energy for the geodynamo.

The dynamics of a fluid inside a precessing spheroidal cavity was first studied by Poincaré (1910). He showed that the flow is a solid body rotation around an axis of rotation which is undetermined in the absence of viscosity. By introducing the viscosity in a thin boundary layer (Ekman layer), Busse (1968) determined this axis of rotation and the amplitude of the rotation. He also determined the critical latitudes where occurs a breakdown of the Ekman layer. This breakdown gives rise to strong shear zones in the bulk of the flow. These shear zones can be axisymmetric and are thus very well visualized in experiments (see Malkus, 1968; Vanyo *et al.*, 1995; Noir, 2000). Noir *et al.* (2003) numerically showed that they are due to nonlinear interactions in the Ekman layer. This breakdown of the flow also excites inertial waves which propagate along characteristic surfaces at a specific angle. They were predicted numerically by Kerswell (1995); Tilgner (1999*b*,*c*); Noir *et al.* (2001*b*) and observed experimentally by Noir *et al.* (2001*a*). Finally, when the precession rate is sufficiently large, Malkus (1968) and Vanyo *et al.* (1995) observed that the flow is unstable and rapidly degenerates into a turbulent state. However, it is still unclear whether this turbulent flow is due to a local instability in the Ekman layer or in the shear zones or if it results from a global instability such as a triadic resonance (Lorenzani & Tilgner, 2001; Kerswell, 1993).

The presence of inertial waves in a precessing spheroid is simply due to the presence of the Coriolis force linked to the global rotation of the fluid. In a cylindrical geometry, inertial waves are also present and interfere in order to construct global modes of the fluid flow, known as Kelvin modes (Kelvin, 1880). These modes are neutral in the absence of viscosity, with a frequency smaller than twice the angular velocity of the fluid (Saffman, 1992). By taking into account viscous boundary layers on the walls of the cylinder Kudlick (1966) and Greenspan (1968) have extended the invscid theory to predict the viscous decay rates of a Kelvin mode. McEwan (1970), Kobine (1995) and Kerswell & Barenghi (1995) experimentally confirmed these predictions.

The precession can excite the Kelvin modes if they have the same frequency as the precession. This was first shown experimentally by McEwan (1970) who used a tilted top end rotating at a different angular velocity than the cylinder, in order to model the forcing by precession. He observed through Kalliroscope visualisations that the flow becomes resonant at the frequencies of the Kelvin modes with the correct wavelength. This was further confirmed experimentally by Manasseh (1992) and Kobine (1995) for a real precessing cylinder. The amplitude of these modes can be predicted theoretically out-

side of their resonances by a simple linear and inviscid theory. However, at the resonance, viscous effects have to be added in order to predict the amplitude saturation. Gans (1970*b*) showed that this amplitude scales as the square root of the Reynolds number when viscous effects are taken into account because of Ekman pumping inside the boundary layers. Meunier *et al.* (2008) have extended this result by adding the effect of nonlinear interactions of the Kelvin modes, which leads to the appearance of a geostrophic motion inside the cylinder.

McEwan (1970) and later Manasseh (1992) also showed that the flow is highly unstable in the vicinity of a resonant frequency. Indeed, after persisting in an apparently laminar form, they observed that the flow becomes unstable and degenerates abruptly into a fine-scale disordered state. They called this transition to turbulence the phenomenon of "resonant collapse" because it was associated with an amplitude decrease of the resonant Kelvin mode. This breakdown behavior was also observed by Thompson (1970) who studied the case of a partly filled and tilted cylinder. By performing experiments in a precessing cylinder, Manasseh (1992) catalogued different breakdown regimes by a letter scheme (A–G), where Type A breakdown results in the generation of turbulence with the smallest scales. McEwan (1970), Thompson (1970) and Manasseh (1992) also observed that for a precise range of parameters the unstable flow can relaminarize after breakdown leading to a cycle of breakdowns and relaminarizations. Because their experiments did not give any informations on global fluid velocities, the physical mechanism leading to breakdown was unclear. Mahalov (1993) showed theoretically that the precessing flow inside an infinite cylinder is unstable and that the instability mechanism is triggered by a triadic resonance between the vertical shear created by the precession force and two free Kelvin modes. However, this mechanism does not explain why the flow is more unstable at the resonance of a forced Kelvin mode. Recently, Lagrange *et al.* (2008) showed that the unstable flow indeed exhibits two free Kelvin modes which satisfy the conditions for a triadic resonance with the resonant forced Kelvin mode and not with the vertical shear. This mechanism will be used in this paper to carry out a linear stability analysis.

The mechanism of triadic resonance has been extensively studied to explain the elliptical instability (Moore & Saffman, 1975; Tsai & Widnall, 1976) as an interaction between the ellipticity of the vortex and two free Kelvin modes. The growth rate of this instability was later calculated analytically using local theories by Bayly (1986) and Waleffe (1990). Theoretical predictions have been widely validated numerically (Mason & Kerswell, 1999) and experimentally (Eloy *et al.*, 2000, 2003). Such a triadic resonance occurs when the difference in the wavenumbers and frequencies between the two free Kelvin modes is equal to the wavenumber and frequency of the elliptical forcing (see the review by Kerswell, 2002). Such a mechanism can be generalized to the destabilization of a Kelvin mode by the interaction of three Kelvin modes, as proposed by Mason & Kerswell (1999) and Kerswell (1999) to explain the secondary instability of the elliptic instability. In this paper, we will use exactly the same procedure, except that the Kelvin mode is now forced by precession instead of being forced by an elliptic instability.

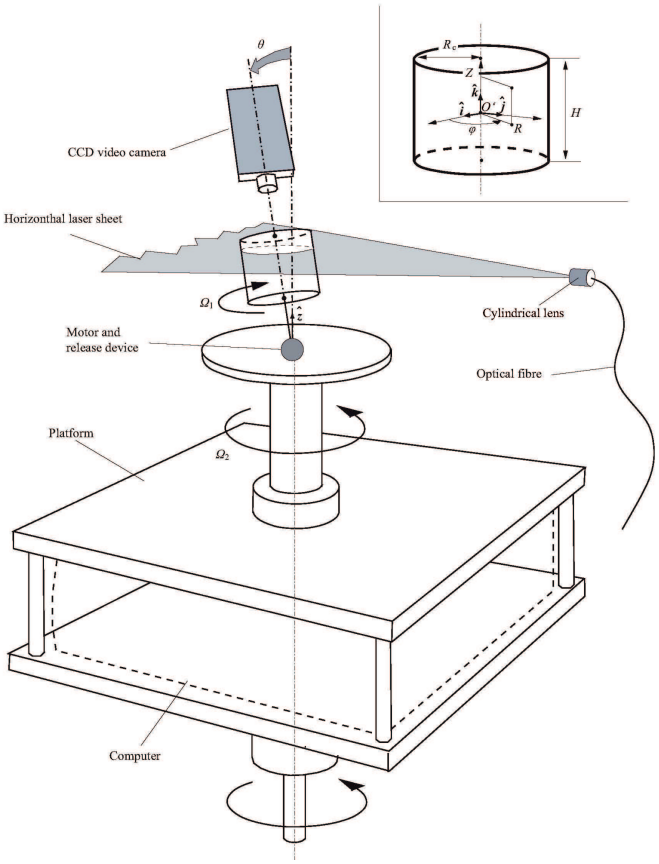

Figure 4.1: Sketch of the experimental setup. A cylinder of radius R_c and height H rotates around its axis at the angular velocity Ω_1. It is mounted on a platform which rotates at the angular velocity Ω_2. The angle between the two axes of rotation is the precessing angle θ. A camera fixed above the cylinder in the platform frame is used to perform PIV measurements in the luminous plane of a horizontal laser sheet. Polar coordinates (R, φ, Z) are defined in the cylinder rotating frame.

The paper is organized as follows. Section 4.2 presents the problem of a precessing cylinder and the experimental setup. Section 4.3 is dedicated to the base flow. The governing equations are derived and the classical linear and inviscid theory is recalled. Viscous effects are also added in order to calculate the base flow inside a resonant cylinder. A linear stability analysis based upon a mechanism of triadic resonance between Kelvin modes is developed in § 4.4. The results (growth rate,stability diagram...) are discussed and compared with experiments in § 4.5. Section 4.6 is dedicated to a weakly nonlinear theory taking into account the influence of a geostrophic mode. This theory is also compared to experimental results. Conclusions and discussion in the more general context of rotating flows are finally given in § 4.7.

4.2 Presentation of the problem and experimental setup

An experimental setup has been built to study the flow inside a precessing cylinder. This experimental setup is sketched in figure 4.1 and described briefly in the following. Readers should refer to Meunier *et al.* (2008) for an extensive description.

A right cylinder of height H and radius R_c filled with water rotates at the angular velocity Ω_1 around its axis and is mounted on a platform which rotates at the angular velocity Ω_2. Each axis having its own driving motor, these angular velocities can be varied independently. The angular velocity Ω_1 can be increased up to 60 rad s^{-1} and is measured with an accuracy of 0.1%. The angular velocity of the platform Ω_2 can only be varied from 0.1 to 6 rad s^{-1} and is measured with an accuracy of 0.2% when the precession frequency is larger than 0.2 rad s^{-1}. Two different cylinders with the same aspect ratio $h = H/R_c = 1.62 \pm 0.3\%$ but different dimensions ($H = 2.72$ cm and $H = 7.50$ cm) are used. Because the Reynolds number depends on R_c, these two cylinders allow to vary the Reynolds number over a large range [1000, 50000].

The cylinder axis is tilted relative to the axis of the platform with an angle θ, which can be increased up to 15° and which is determined with an absolute accuracy of $\pm 0.1°$. A release device mounted on the platform and controlled externally allows to tilt the cylinder during the motion of the platform. The release device is composed of an electromagnet designed to keep the cylinder in a vertical position during the spin–up phase. Once the electromagnet is turned off, a drawback spring pulls the cylinder into its tilted position.

PIV measurements have been performed by seeding the flow with small markers illuminated with a thin light sheet created by a yttrium aluminum garner (YAG) pulsed laser. An external cylindrical lens is used to provide this laser sheet which is fixed relative to the laboratory frame. However, because the precessing angle θ is small, the laser sheet can be considered normal to the cylinder axis at first order. The height z of the laser sheet can be varied along the height of the cylinder. In our experiments we have chosen $z = 0$ (midheight of the cylinder) and $z = h/4$. These two positions allow to measure a maximum transverse velocity for the Kelvin modes observed in our experiments. A video camera mounted on the rotating platform and aligned with the axis of the cylinder is used to record the PIV images. To obtain the velocity field in the cylinder reference frame the two successive images are rotated around the centre of the cylinder and then treated by a cross–correlation algorithm detailed in Meunier & Leweke (2003) leading to the transverse velocity field and the axial vorticity. The power is brought up to the platform by a rotating collector through the vertical axis to supply the camera, the cylinder motor, the electro-magnet and the acquisition computer.

For the acquisition of a PIV field we proceed as follows. The cylinder is first kept vertical and rotates at Ω_1. The platform rotates at Ω_2. Once the spin–up stage is completed (i.e the flow is in solid body rotation), the cylinder is tilted in precession and a first acquisition of 85 PIV fields is

launched. This first acquisition allows to study the transient stage of the instability, i.e. the growth of the Kelvin modes. A second PIV acquisition is started when the transient stage is completed ; usually 10 minutes later. This second acquisition allows to study the permanent stage.

Some visualizations were also performed by using Kalliroscope particles which are known to reveal the structure of the flow in a rotating fluid (see McEwan, 1970; Manasseh, 1992). The tank is illuminated from the side with a vertical luminous sheet created by a 5 Watts Argon laser going through a cylindrical lens. A very slight shearing motion in any section of the cylinder is sufficient to align the Kalliroscope particles, thus changing the light intensity seen by an observer. This provides an extremely sensitive indicator of relative fluid motion. This method does not give any quantitative results but is a quick and efficient way to determine the wavelength of the base flow or to see if the flow is stable or unstable.

4.3 Base flow

In this section we give the governing equations for a precessing flow and we derive the classical solution which is valid before the appearance of the instability. This solution is linear and inviscid when the flow is non-resonant, but viscous effects have to be taken into account when one Kelvin mode is resonant. This solution will be used as a base flow for the linear stability analysis carried out in § 4.4.

4.3.1 Formulation

A cylinder with radius R_c and height H is completely filled of a fluid with density ρ and kinematic viscosity ν. As shown in figure 4.1, the cylinder rotates around its own axis $(O', \hat{\mathbf{k}})$ at the constant angular frequency Ω_1. The cylinder is mounted on a platform rotating at the constant angular frequency Ω_2 around an axis $\hat{\mathbf{z}}$. There is an angle θ between the two axes of rotation creating a precessing motion of the cylinder. The rotation vector of the cylinder in the laboratory reference frame is given by $\boldsymbol{\Omega} = \Omega_1 \hat{\mathbf{k}} + \Omega_2 \hat{\mathbf{z}}$ and is time-dependent because $\hat{\mathbf{k}}$ rotates around $\hat{\mathbf{z}}$.

To have simple boundary conditions, it is easier to solve the problem in the cylinder frame of reference $(O', \hat{\mathbf{i}}, \hat{\mathbf{j}}, \hat{\mathbf{k}})$, ($O'$ being the center of mass of the cylinder) in which the radius vector $\mathbf{R}$ is defined by its cylindrical coordinates (R, φ, Z) (see Fig. 4.1). In this reference frame, the Navier–Stokes equations satisfied by the velocity field $\mathbf{U}$ and the pressure field P for an incompressible fluid are

$$\frac{\partial \mathbf{U}}{\partial T} + (\mathbf{U}\cdot\boldsymbol{\nabla})\,\mathbf{U} + 2\,\boldsymbol{\Omega}\times\mathbf{U} + \boldsymbol{\Omega}\times(\boldsymbol{\Omega}\times\mathbf{R}) + \frac{\mathrm{d}\,\boldsymbol{\Omega}}{\mathrm{d}\,T}\times\mathbf{R} + \boldsymbol{\Gamma}_{O'} = -\frac{1}{\rho}\boldsymbol{\nabla}P + \nu\Delta\mathbf{U}, \tag{4.1a}$$

$$\boldsymbol{\nabla}\cdot\mathbf{U} = 0, \tag{4.1b}$$

with the viscous boundary condition $\mathbf{U} = \mathbf{0}$ on the cylinder walls.

In equation (4.1a), the first two terms are the usual inertial terms, the third and fourth term are the Coriolis and centrifugal accelerations, and the

fifth term is the acceleration of the rotation vector. The last left-hand side term is potential and refers to the acceleration of the centroid O' of the cylinder. The two right-hand side terms of (4.1a) are the usual pressure and viscous terms.

By using R_c and $\Omega^{-1} = (\Omega_1 + \Omega_2 \cos\theta)^{-1}$ as characteristic length and time, the Navier–Stokes equations for the dimensionless velocity field $\mathbf{u}(\mathbf{r}, t)$ become

$$\begin{aligned} \frac{\partial \mathbf{u}}{\partial t} + 2\hat{\mathbf{k}} \times \mathbf{u} + \boldsymbol{\nabla} p &= -2Ro\,\omega r\,\cos(\omega t + \varphi)\,\hat{\mathbf{k}} \\ &+ \mathbf{u} \times (\boldsymbol{\nabla} \times \mathbf{u}) - 2Ro\,\boldsymbol{\delta} \times \mathbf{u} + \frac{\Delta \mathbf{u}}{Re}, \qquad (4.2a) \\ \boldsymbol{\nabla} \cdot \mathbf{u} &= 0, \qquad (4.2b) \end{aligned}$$

with

$$\omega = \frac{\Omega_1}{\Omega},\ Ro = \frac{\Omega_2 \sin\theta}{\Omega},\ Re = \frac{\Omega R_c^2}{\nu},\ \boldsymbol{\delta} = \cos(\omega t)\,\hat{\mathbf{i}} - \sin(\omega t)\,\hat{\mathbf{j}}. \quad (4.3\,a\text{–}d)$$

In this dimensionless form, $h = H/R_c$ is the aspect ratio of the cylinder. The dimensionless pressure field $p(\mathbf{r}, t)$ includes all the potential terms (see Meunier *et al.*, 2008, for the detail of p). The boundary condition of the velocity field is

$$\mathbf{u} = \mathbf{0} \quad \text{at the walls } (r = 1 \text{ or } z = \pm h/2). \qquad (4.4)$$

The Navier–Stokes equations (4.2 *a, b*) with the boundary condition (4.4) govern the flow inside a precessing cylinder. This set of equations has been obtained without any approximation and is thus valid for any value of the experimental parameters. As it appears from these equations, the problem is entirely governed by four dimensionless parameters. The amplitude of the forcing term is called a Rossby number Ro because it represents the ratio between the vorticity of the flow and the solid body rotation Ω. The dimensionless frequency ω of the forcing term fixes the frequency of the Kelvin modes which are excited. The cylinder aspect ratio h selects the structure of the Kelvin modes, and the Reynolds number Re quantifies the viscous damping. In the following we will limit ourselves to the case of asymptotically small Rossby number Ro and large Reynolds number Re. This assumption is coherent with atmospherical and geophysical observations. It is also the relevant limit for a stable flow or at the onset of instability.

In the following the four-component and complex vector associated to the velocity-pressure field $(\mathbf{u}, p)$ will be noted $\mathbf{v}$, such that $(\mathbf{u}, p) = \mathbf{v} + \bar{\mathbf{v}}$ with $\bar{\mathbf{v}}$ the complex conjugate of $\mathbf{v}$. Using this formulation the Navier–Stokes equations (4.2 *a, b*) rewrite

$$\begin{aligned} \left(\frac{\partial}{\partial t}\mathcal{I} + \mathcal{M}\right)\mathbf{v} + \text{c.c.} = Ro\,\mathbf{F}_0 \mathrm{e}^{\mathrm{i}(\omega t + \varphi)} + \mathbf{N}(\mathbf{v}, \mathbf{v}) &+ Ro\,(\mathcal{D}\,\mathrm{e}^{\mathrm{i}(\omega t + \varphi)} + \text{c.c.})\mathbf{v} \\ &+ \frac{\mathcal{L}\,\mathbf{v}}{Re} + \text{c.c.}, \qquad (4.5) \end{aligned}$$

where the operators $\mathcal{D}$, $\mathcal{I}$, $\mathcal{L}$, $\mathcal{M}$, the forcing vector $\mathbf{F}_0$ and the bilinear function $\mathbf{N}$ are defined in Appendix 4.8.1. The symbol c.c. stands for the complex conjugate.

4.3.2 Non-resonant cylinder

In order to solve (4.5), an asymptotically small Rossby number Ro and a large Reynolds number Re are assumed. In this limit $\mathbf{v}$ is $O(Ro)$ and the Navier–Stokes equation (4.5) at order $O(Ro)$ becomes

$$\left(\frac{\partial}{\partial t}\mathcal{I}+\mathcal{M}\right)\mathbf{v}=Ro\,\mathbf{F}_0\mathrm{e}^{\mathrm{i}(\omega t+\varphi)}. \tag{4.6}$$

The no-slip boundary condition (4.4) becomes at this order a condition of no outward flow

$$\mathbf{u}\cdot\mathbf{n}=0 \quad \text{at the walls } (r=1 \text{ or } z=\pm h/2), \tag{4.7}$$

where $\mathbf{n}$ is an unitary vector normal to the wall.

The set of equations (4.6) and (4.7) is a linear system whose second term represents the forcing due to precession. This system admits a particular solution $\mathbf{v}_{\text{part.}}=\left(0,\,0,\,Ro\,\mathrm{i}\,r\,\mathrm{e}^{\mathrm{i}(\omega t+\varphi)},\,0\right)$ which is a shear along the cylinder axis. Because it does not satisfy the boundary condition (4.7) at $z=\pm h/2$, it must be completed with a solution of the homogeneous equation (i.e. equation (4.6) without forcing term). Due to time and azimuthal dependence of the forcing and particular solution, the homogeneous solution can be written a sum of Kelvin modes of azimuthal wavenumber $m=1$ and angular frequency ω (see Greenspan, 1968). Gathering the particular solution and the Kelvin modes yields the solution of (4.6) and (4.7)

$$\mathbf{v}=\mathbf{v}_{\text{part.}}+\sum_{i=1}^{\infty}\varepsilon_i\mathbf{v}_{1,\omega,k_i}, \tag{4.8}$$

where $\mathbf{v}_{1,\omega,k_i}$ is a Kelvin mode of azimuthal wavenumber $m=1$, frequency ω and axial wavenumber k_i. Its structure is composed of two travelling waves of opposite wavenumber $\pm k_i$ in order to form a stationnary wave and match the parity of the forcing

$$\mathbf{v}_{1,\omega,k_i}=\mathbf{u}_{1,\omega,k_i}(r)\,\mathrm{e}^{\mathrm{i}(\omega t+\varphi+k_i z)}-\mathbf{u}_{1,\omega,-k_i}(r)\,\mathrm{e}^{\mathrm{i}(\omega t+\varphi-k_i z)}. \tag{4.9}$$

The vector $\mathbf{u}_{m,\omega,k_i}$ is found by solving the homogeneous equation and is given in Appendix 4.8.1. The boundary condition in $r=1$ imposes that the axial wavenumber k_i is the positive root of the constitutive relation

$$\delta_i^2=\frac{4-\omega_i^2}{\omega_i^2}k_i^2, \tag{4.10}$$

where the radial wavenumber δ_i is solution of Kelvin's dispersion relation $D(1,\omega,\delta_i)=0$ with

$$D(m,\omega,\delta)=\omega\delta J_m'(\delta r)+2mJ_m(\delta r). \tag{4.11}$$

This condition ensures that $\mathbf{v}$ vanishes at $r=1$. In equation (4.11) $J_m(x)$ is the Bessel function of the first kind and $J_m'(x)$ its x–derivative. For a given azimuthal wavenumber and for a given frequency ω such that $-2<\omega<2$,

the dispersion relation (4.11) admits an infinite and countable number of real roots δ_i numbered in ascending order. The i-th roots corresponds to the i-th Kelvin mode.

A PIV measurement of the first Kelvin mode ($i = 1$) is shown in figure 4.2(a). It represents the axial and instantaneous vorticity field ζ. This mode is characterized by two counter rotating vortices which induce a velocity along the y-axis (tilted axis). In the general case, the i-th Kelvin mode contains $2i$ vortices.

The amplitude ε_i of each Kelvin mode is real and can be calculated by imposing a vanishing velocity at $z = \pm h/2$. For this purpose, the z-velocity of the particular solution $\mathbf{v}_{\text{part.}}$ is decomposed on the set of Bessel functions which characterize the z-component of the Kelvin modes. It leads to the inviscid and nonlinear amplitude $\varepsilon_i = Ro\, a_i$ of the Kelvin modes, where a_i is given in (4.49) of Appendix 4.8.1. The evolution of ε_i as a function of the forcing frequency ω is plotted in figure 4.2(b) for the first Kelvin mode. It shows a series of divergences corresponding to the natural frequencies $\omega_{i,n}$ of the cylinder (the notation $\omega_{i,n}$ stands for the n-th resonance of the i-th Kelvin mode). These resonances occur when the z-velocity of the Kelvin mode vanishes, i.e. when the wavenumber k_i of the Kelvin mode is equal to $(2n-1)\pi/h$ with n the number of the resonance.

It can be demonstrated (Kudlick, 1966) that there is always a Kelvin mode arbitrarily close to a resonance for any forcing frequency ω. It is thus necessary to add viscous effects in order to predict the saturation of the Kelvin mode amplitude ε_i at a resonance. These results are recalled in the next section.

4.3.3 Resonant cylinder

To predict the saturation of the amplitude at a resonant frequency it is necessary to include the viscous effects (Gans, 1970b) and/or the nonlinear effects (Meunier *et al.*, 2008). In the present paper, the amplitude is always saturated by viscous effects because $|Re^{1/2}Ro^{2/3}| \ll 1$. In other words, the instability appears before nonlinearities become significant in the base flow. Moreover, because volume viscous effects are $O((m^2+\delta_i^2)Re^{-1}) = O(Re^{-1})$ and surface viscous effects are $O(Re^{-1/2})$ volume viscous effects will be neglected for the saturation of the resonant Kelvin mode amplitude. As shown by Gans (1970b), the resonant Kelvin mode of amplitude ε_i generates a secondary flow at order $O(\varepsilon_i Re^{-1/2})$ in the core of the cylinder due to Ekman pumping in the viscous boundary layers. The correct scaling is obtained when this secondary flow is of the order of the forcing amplitude Ro. This gives a mode amplitude $\varepsilon_i = O(Ro\,Re^{1/2})$ which is $Re^{1/2}$ larger than the flow in the non-resonant case. Applying a solvability condition on the secondary flow allows to calculate analytically the amplitude of the resonant Kelvin mode close, and at the resonance (Meunier *et al.*, 2008) :

$$\varepsilon_i = \frac{\mathrm{i}fRo}{\frac{s}{Re^{1/2}} + \mathrm{i}\frac{f}{a_i}}, \tag{4.12}$$

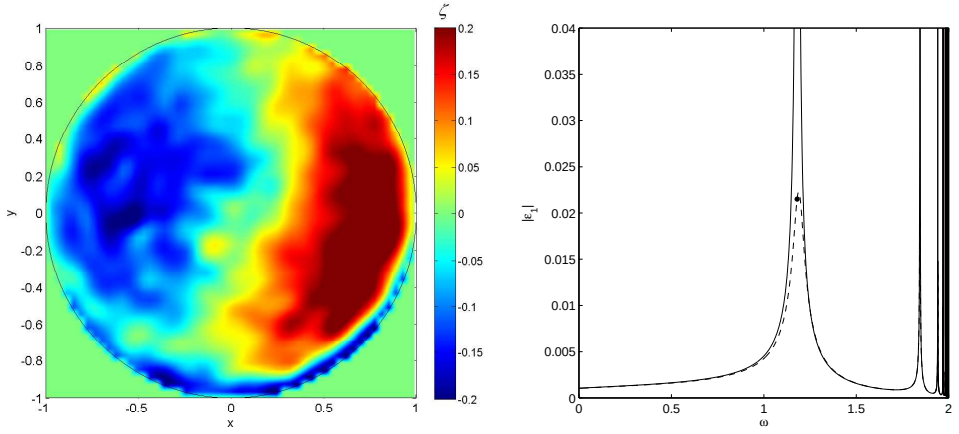

(a) (b)

Figure 4.2: (a) Axial vorticity field ζ of the first Kelvin mode measured by PIV at its first resonance ($\omega = 1.18$), in the absence of instability. (b) Amplitude of the first Kelvin mode as a function of ω. The solid line corresponds to the linear and inviscid theory given by equation (4.49) and the dashed line to the viscous theory given by equation (4.12). The point is the value of $|\varepsilon_1|$ for $\omega = 1.18$ at the exact resonance. $h = 1.62$, $Re \approx 3500$ and $Ro = -0.0031$.

where the linear forcing parameter f is real and given in Appendix 4.8.1. The surface viscous parameter s is a complex number with a positive real part and is given in Appendix 4.8.2. The term $1/a_i$ represents the detuning damping of the forced Kelvin mode if the frequency ratio ω is not exactly equal to a resonance frequency. This viscous amplitude is represented as a dashed line on figure 4.2(b) for $Re = 3500$. It is close to the inviscid amplitude $\varepsilon_i = Ro\, a_i$ (solid line) far from the resonance and saturates at the resonance (i.e. when $a_i = \infty$) at a finite value $\varepsilon_i = f Ro\, Re^{1/2}/s$ represented by a point. It can be noted that the mode amplitude is maximum when the detuning of the forcing frequency compensates exactly the viscous detuning, i.e. $f/a_i = -Re^{-1/2}\mathrm{Im}(s)$ and not at the exact resonance.

At resonance, the base flow is an order $Re^{1/2}$ larger than far from the resonance and may thus be subject to stronger instabilities. In the following, the forcing frequency ω will be assumed to be a natural frequency of the cylinder such that the base flow is composed of a predominant Kelvin mode $\mathbf{v}_{1,\omega,k_i}$ with an amplitude ε_i given by (4.12). For the sake of clarity the index i will be dropped such that the amplitude of the resonant Kelvin mode is noted ε instead of ε_i. Its axial wavenumber is simply noted k and its radial wavenumber δ. We also assume that $|RoRe^{1/2}| \ll 1$ such that ε is a small parameter. This assumption allows to carry out an asymptotic and linear stability analysis of the base flow described here.

4.4 Linear stability analysis

As described in the literature (see Manasseh, 1996; Kobine, 1996), when the Reynolds number or the Rossby number is increased above a certain

threshold (which depends on h and ω), the flow inside the cylinder becomes unstable. PIV measurements in two different sections of the cylinder have revealed the three-dimensional structure of this instability (see Lagrange *et al.*, 2008). It is composed of two free Kelvin modes whose wavenumbers and frequencies respect the conditions for a triadic resonance with the forced Kelvin mode, in a similar manner as for the elliptical instability (see Malkus, 1989; Eloy *et al.*, 2000; Kerswell, 2002). In this paper, a linear stability analysis based on such a mechanism is presented. It allows to predict the structure of the instability, its growth rate, and the stability threshold.

4.4.1 Governing equations for the perturbation

To perform a stability analysis, a perturbation defined by its four component and complex velocity-pressure field $\widetilde{\mathbf{v}}$ is added to the base flow. The total flow $\mathbf{v}$ in the precessing cylinder is thus the sum of the resonant base flow $\mathbf{v}_{1,\omega,k}$ (given by (4.9)), whose amplitude ε is given by (4.12), the perturbation $\widetilde{\mathbf{v}}$ and some lower order terms : the particular solution $\mathbf{v}_{\text{part.}}$ and the non-resonant Kelvin modes $\mathbf{v}_{1,\omega,k_i}$

$$\mathbf{v} = \varepsilon \mathbf{v}_{1,\omega,k} + \widetilde{\mathbf{v}} + \mathbf{v}_{\text{part.}} + \sum_i \varepsilon_i \mathbf{v}_{1,\omega,k_i}. \tag{4.13}$$

We recall that the dominant term $\varepsilon \mathbf{v}_{1,\omega,k}$ is of order $RoRe^{1/2}$. The other terms of the base flow ($\mathbf{v}_{\text{part.}}$ and $\sum \varepsilon_i \mathbf{v}_{1,\omega,k_i}$) are of order Ro.

Substituting this decomposition (4.13) into (4.5) yields the equation satisfied by the perturbation $\widetilde{\mathbf{v}}$:

$$\left(\frac{\partial}{\partial t}\mathcal{I} + \mathcal{M}\right)\widetilde{\mathbf{v}} + \text{c.c.} = \mathbf{N}\left(\widetilde{\mathbf{v}}, \varepsilon \mathbf{v}_{1,\omega,k}\right) + \mathbf{N}\left(\varepsilon \mathbf{v}_{1,\omega,k}, \widetilde{\mathbf{v}}\right) + \frac{1}{Re}\mathcal{L}\widetilde{\mathbf{v}} + \text{o.t.} + \text{c.c.} \tag{4.14}$$

We recall that $\mathcal{I}$, $\mathcal{M}$, $\mathbf{N}$ and $\mathcal{L}$ are operators given in Appendix 4.8.1. The left-hand side term of equation (4.14) is the linear unsteady term of the homogeneous equation. The first and second right-hand side terms represent the nonlinear interaction between the resonant Kelvin mode and the perturbation. They are of order $O(RoRe^{1/2}\,\widetilde{\mathbf{v}})$. The third term is the classical viscous term for the perturbation. It is of order $O(Re^{-1}\,\widetilde{\mathbf{v}})$. The notation o.t. stands for 'other terms' and includes the nonlinear interaction of the four-component vector $\mathbf{v}_{\text{part.}} + \sum \varepsilon_i \mathbf{v}_{1,\omega,k_i} + \widetilde{\mathbf{v}}$ with itself and the term $Ro\,(\mathcal{D}\,\mathrm{e}^{\mathrm{i}(\omega t+\varphi)} + \text{c.c.})\mathbf{v}$. In these terms, the leading order is $O(Ro\,\widetilde{\mathbf{v}})$, which is negligible compared to the nonlinear terms of order $O(RoRe^{1/2}\,\widetilde{\mathbf{v}})$ explicited in (4.14). Terms of order $O(ReRo^2)$ and $O(\widetilde{\mathbf{v}}^2)$ are also neglected in this linear analysis. Note that the forcing term $Ro\,\mathbf{F}_0\mathrm{e}^{\mathrm{i}(\omega t+\varphi)}$ from (4.5) does not appear in equation (4.14) because it has been cancelled out by the unsteady term of the particular solution.

The flow is assumed to satisfy a no-slip boundary condition

$$\widetilde{\mathbf{v}} = \mathbf{0} \quad \text{at the walls } (r = 1 \text{ or } z = \pm h/2). \tag{4.15}$$

The equation (4.14) and the boundary condition (4.15) describe the evolution of the linear perturbation $\widetilde{\mathbf{v}}$ in the limit of small amplitudes ε.

In order to solve the system of equations (4.14-4.15) the four-component velocity-pressure field $\widetilde{\mathbf{v}}$ is expanded in powers of ε as follows

$$\widetilde{\mathbf{v}} = \mathbf{v}^{(0)} + \varepsilon \mathbf{v}^{(1)} + O\left(\varepsilon^2\right). \tag{4.16}$$

The equation for the growth rate of the instability is obtained by substituting the above expansion (4.16) into the Navier–Stokes equation (4.14) and examining its two first orders. Note that in this study we will consider the critical scaling $Re^{-1/2} = O(\varepsilon)$ such that boundary viscous effects are of the same order as $\mathbf{N}\left(\widetilde{\mathbf{v}}, \varepsilon \mathbf{v}_{1,\omega,k}\right)$ and $\mathbf{N}\left(\varepsilon \mathbf{v}_{1,\omega,k}, \widetilde{\mathbf{v}}\right)$.

4.4.2 Description of the free Kelvin modes

At order 0, equation (4.14) is the homogeneous equation

$$\left(\frac{\partial}{\partial t}\mathcal{I} + \mathcal{M}\right)\mathbf{v}^{(0)} = 0. \tag{4.17}$$

Because viscous effects are of order $Re^{-1/2}$ (boundary viscous effects) or Re^{-1} (volume viscous effects), an inviscid boundary condition is assumed at this order

$$\mathbf{v}^{(0)} \cdot \mathbf{n} = 0 \quad \text{at the walls } (r = 1 \text{ or } z = \pm h/2). \tag{4.18}$$

The resolution of the set of equations (4.17-4.18) is classical and its solution is a linear combination of free Kelvin modes. Each free Kelvin mode $\mathbf{v}_j$ is composed of two travelling waves of opposite wavenumber k_j in order to satisfy the boundary condition (4.18) at the top and bottom of the cylinder

$$\mathbf{v}_j = \mathbf{u}_{m_j,\omega_j,k_j}(r)\, \mathrm{e}^{\mathrm{i}(\omega_j t + m_j \varphi + k_j z)} \pm \mathbf{u}_{m_j,\omega_j,-k_j}(r)\, \mathrm{e}^{\mathrm{i}(\omega_j t + m_j \varphi - k_j z)}. \tag{4.19}$$

We recall that the expression of the four-component vector $\mathbf{u}_{m_j,\omega_j,k_j}$ is given in Appendix 4.8.1. At this order the amplitude A_j of a free Kelvin mode is undefined but its azimuthal wavenumber m_j, its frequency ω_j and its axial wavenumber k_j are connected through the dispersion relation $D(m_j, \omega_j, \delta_j) = 0$ given by equation (4.11) such that the radial velocity vanishes at $r = 1$. In figure 4.3 the first branches of the dispersion relation are plotted for $m_j = 6$ (solid line).

The condition of no normal flow at the top and the bottom discretizes the vertical wavenumber k_j as a multiple of π/h. It also separates the free Kelvin modes into two categories with different parity, depending on the choice of sign between the two waves of opposite wavenumber k_j in (4.19). The plus sign allows to consider free Kelvin modes whose axial velocity (resp. vorticity) is a sine (resp. cosine) function of z and the axial wavenumber satisfies $k_j = (2n-1)\pi/h$ with n an integer. The minus sign allows to consider free Kelvin modes whose axial velocity (resp. vorticity) is a cosine (resp. sine) function of z, with $k_j = 2n\pi/h$.

To examine the mechanism of triadic resonance, the perturbation $\mathbf{v}^{(0)}$ will be assumed to be, at leading order, a combination of two free Kelvin modes $\mathbf{v}_1$ and $\mathbf{v}_2$ with unknown amplitudes A_1 and A_2

$$\mathbf{v}^{(0)} = A_1 \mathbf{v}_1 + A_2 \mathbf{v}_2, \tag{4.20}$$

where the amplitudes are varying slowly with time such that time derivatives will appear at next order.

4.4.3 Influence of the Ekman layers

It can be noted that the dispersion relation and the determination of the structure of the free Kelvin modes are obtained with an inviscid boundary condition on the cylinder walls (equation (4.18)). This condition does not match the viscous boundary condition given by equation (4.15). There will thus remain a wall parallel flow at the leading order for the free Kelvin modes. This problem can be solved by adding a viscous flow, in a viscous boundary layer of thickness $O(Re^{-1/2})$ near the walls. However this resulting viscous flow has a component perpendicular to the walls, of order $O(Re^{-1/2})$ called Ekman pumping. This pumping is an exponential decreasing function inside the Ekman layers. Note that in our problem we have an Ekman pumping due to the lateral wall and the top and bottom walls of the cylinder. The calculous of Ekman layers is classical. An exhaustive description is given in Greenspan (1968). For the particular case of Kelvin modes, the reader could refer to Kudlick (1966).

4.4.4 Triadic resonance

Experiments have demonstrated (see Lagrange *et al.*, 2008) that the instability of a fluid inside a precessing cylinder is due to a triadic resonance between the resonant Kelvin mode $\varepsilon\mathbf{v}_{1,\omega,k}$ and two free Kelvin modes $\mathbf{v}_1$ and $\mathbf{v}_2$. These three modes can be coupled by the nonlinear terms $\mathbf{N}\left(\widetilde{\mathbf{v}}, \varepsilon\mathbf{v}_{1,\omega,k}\right)$ and $\mathbf{N}\left(\varepsilon\mathbf{v}_{1,\omega,k}, \widetilde{\mathbf{v}}\right)$ in equation (4.14) when their Fourier components are chosen appropriately. The nonlinear interaction between the first mode $\mathbf{v}_1$ and the forced mode $\mathbf{v}_{1,\omega,k}$ has a Fourier component $\mathrm{e}^{\mathrm{i}(\omega_1 t + m_1\varphi \pm k_1 z)}\mathrm{e}^{\mathrm{i}(\omega t + \varphi \pm kz)}$. This term has a Fourier component $\mathrm{e}^{\mathrm{i}(\omega_2 t + m_2\varphi \pm k_2 z)}$ identical to that of the second mode $\mathbf{v}_2$ only when the frequencies and wavenumbers satisfy the resonance condition

$$m_2 - m_1 = 1, \tag{4.21a}$$

$$\omega_2 - \omega_1 = \omega, \tag{4.21b}$$

$$|k_2 - k_1| = k. \tag{4.21c}$$

If these conditions are satisfied, the nonlinear interaction between $\mathbf{v}_2$ and the forced mode $\mathbf{v}_{1,\omega,k}$ has also the same Fourier component as $\mathbf{v}_1$. It can be noted that the last equation of this system offers two possibilities which are $k_2 - k_1 = k$ and $k_1 - k_2 = k$. However, in all our calculations the first case has always been the most unstable one.

The first condition imposes that the two free Kelvin modes have azimuthal wavenumbers separated by one. This is different from the elliptic instability where they should be separated by 2 (Kerswell, 2002). This comes from the fact that, here, the forcing term has an azimuthal wavenumber $m = 1$, unlike the ellipticity which has an azimuthal wavenumber $m = 2$.

To find Kelvin modes satisfying the resonance condition, we plot on the same graph the dispersion relation of the second mode $\mathbf{v}_2$ and the dispersion relation of the first mode $\mathbf{v}_1$ translated by k along the abscissae and by ω along the ordinate. An example is shown in Fig. 4.3 for $m_2 = 6$ and $m_1 = 5$. At each crossing point between the dispersion relation of mode 1 (dashed lines) and mode 2 (solid line) the conditions of resonance are fulfilled. Since there is an infinite number of branches for each mode and an infinity of possible azimuthal wavenumber m_2, there is a triple-infinite number of resonances. We will label these resonant combinations (m_2, l_1, l_2), where l_1 (resp. l_2) is the branch number of the dispersion relation for the first mode (resp. second mode). As an example, the lowest order resonant combination $(m_2 = 6, l_1 = 1, l_2 = 1)$ is marked by a circle on Fig. 4.3. This combination will be found to be the most unstable and it will be extensively studied and compared to the experiments. It can be noted that the study can be restricted to free Kelvin modes with $m_j \geq 0$ because the dispersion relation (4.11) satisfies the following symmetry $D(m_j, \omega_j, \delta_j) = -D(-m_j, -\omega_j, \delta_j)$.

An additional condition arises because the free Kelvin modes must have a zero normal velocity at the top and the bottom, which quantifies the wavenumbers k_j as multiples of π/h. It is the case in Fig. 4.3 where the resonant combination $(6, 1, 1)$ is located on a dash-dotted line ($k_2 = 2\pi/h$). This case of exact resonance only appears for specific aspect ratios (here $h = 1.62$) which allow to have an intersection between the three lines. The principal aspect ratios h allowing exact resonances are listed in Table 4.1 (resp. Table 4.2) for the combinations $(m_2, 1, 1)$ (resp. $(m_2, 2, 2)$) when the first Kelvin mode is excited at its first resonance and where $k_1 = \pi/h$. Most of the resonances are obtained for small aspect ratios (for which the resonance frequency is large) and large azimuthal wavenumbers. Note that there does not exist any exactly resonant combinations $(m_2, 1, 1)$ (resp. $(m_2, 2, 2)$) with $m_2 \leq 5$ (resp. $m_2 \leq 3$). This is why the instabilities observed in the experiments usually have high azimuthal wavenumbers. Finally, it can be noted that since the forced Kelvin mode is resonant, its axial wavenumber k is an *odd* multiple of π/h. Thus equation (4.21c) implies that the two free Kelvin modes have different parities with respect to z (i.e. free Kelvin modes with a different sign in equation (4.19)). By contrast, at the anti-resonance of the forced Kelvin mode, the axial wavenumber k is an *even* multiple of π/h. Thus the two free Kelvin modes have the same parities with respect to z. In this condition it can be shown that a mechanism of triadic resonance between Kelvin modes can't lead to the instability.

Most of the time, a combination (m_2, l_1, l_2) is not exactly resonant because the crossing point is not on a dash-dotted line (i.e. $k_j \neq n\pi/h$, with n an integer). The free Kelvin modes thus do not satisfy the boundary condition (4.18) at the top and bottom of the cylinder and should not be considered. However, the problem can still be solved by introducing small detuning parameters Δk_1 and Δk_2which measure the distance between the wavenumber k_1 (or k_2) and the closest $n\pi/h$:

$$\Delta k_j = \min_{n \in \mathbb{N}^*} \left(\left| n\frac{\pi}{h} - k_j \right| \right) \operatorname{sgn}\left(n\frac{\pi}{h} - k_j \right). \tag{4.22}$$

In figure 4.3 these detunings correspond to the relative distance between

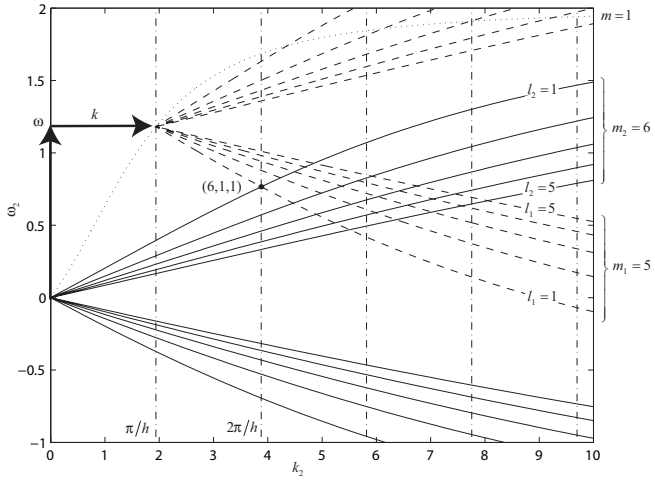

Figure 4.3: Dispersion relations of the free Kelvin modes ($h = 1.62$, $\omega = 1.18$). Solid lines (resp. dashed lines) correspond to the first five branches of the dispersion relation of the free Kelvin modes with an azimuthal wavenumber $m_2 = 6$ (resp. $m_1 = 5$). The dotted line represents the dispersion relation of the forced Kelvin mode ($m = 1$), which is used to translate the dispersion relations of the first mode horizontally by $k = \pi/h$ and vertically by $\omega = 1.18$. Resonant free Kelvin modes correspond to a crossing point for the case $k_2 - k_1 = k$. Vertical dash-dotted lines indicate the discretisation of the axial wavenumber $k_2 = n\pi/h$ for which the free Kelvin mode 'fits' inside the cylinder.

a crossing point and the closer vertical dash-dotted line. These detunings will only modify the problem at order ε if they are of order $O(\varepsilon)$. Note that, as long as ω is a resonant frequency, the detuning parameters satisfy $\Delta k_1 = \Delta k_2$.

4.4.5 Amplitude Equations

As mentioned previously, at leading order the perturbation $\widetilde{\mathbf{v}}$ is a combination of two free Kelvin modes with unknown amplitudes. We now assume that A_1 and A_2 vary slowly with time such that $\partial A_j/\partial t$ is of order ε. We will consider that this combination is not exactly resonant and that detuning effects Δk_j are also of order ε.

At order ε equation (4.14) becomes

$$\begin{aligned}\varepsilon\left(\frac{\partial}{\partial t}\mathcal{I}+\mathcal{M}\right)\mathbf{v}^{(1)}+\text{c.c.} &= \left(-\frac{\partial}{\partial t}\mathcal{I}+\mathrm{i}\Delta k_j\mathcal{M}_\Delta\right)\mathbf{v}^{(0)}+\mathbf{N}\left(\mathbf{v}^{(0)},\varepsilon\mathbf{v}_{1,\omega,k}\right)\\ &+ \mathbf{N}\left(\varepsilon\mathbf{v}_{1,\omega,k},\mathbf{v}^{(0)}\right)+\frac{\mathcal{L}\mathbf{v}^{(0)}}{Re}+\text{c.c.} \qquad (4.23)\end{aligned}$$

In equation (4.23) the left-hand side term is the linear operator applied to the solution at order ε. The first right-hand side term is composed by the slow unsteady part of the perturbation of order 0 and by its detuning term. The operator $\mathcal{M}_\Delta$ is defined in Appendix 4.8.2 and is obtained via a Taylor expansion of the Fourier component $\mathrm{e}^{\mathrm{i}\Delta k_j z}$ of the free Kelvin modes. The second and third right hand side term represent the nonlinear interaction

h	10.8	3.60	1.62	1.09	0.886	0.758
$\omega_{1,1}$	0.1639	0.5501	1.181	1.503	1.636	1.718
m_2	7	6	6	7	8	9
$n_1 n_2$	1.16	1.07	4.11	15.4	34.4	64.5
$\lvert RoRe\rvert_{\text{crit}}$	5.41	7.14	7.11	8.60	10.4	12.4

h	0.669	0.601	0.547	0.504	0.467	0.436
$\omega_{1,1}$	1.772	1.811	1.841	1.863	1.881	1.895
m_2	10	11	12	13	14	15
$n_1 n_2$	108	170	253	358	496	666
$\lvert RoRe\rvert_{\text{crit}}$	14.5	16.8	19.2	21.7	24.3	27.1

Table 4.1: Theoretical results considering the $(m_2, 1, 1)$ combinations with $k_2 = 2\pi/h$ and $k_1 = k = \pi/h$. The combination is exactly resonant only for a specific aspect ratio h (given in the first row) at its associated frequency $\omega_{1,1}$ (given in the second row) and for an azimuthal wavenumber of the second mode m_2 (given in the third row). The fourth row gives the value of $n_1 n_2$ which is the square of the inviscid growth rate. The last row gives the stability threshold without volume viscous effects and is calculated with equation (4.33).

h	9.57		1.13	0.880	0.744	0.651	0.581
$\omega_{1,1}$	0.1867		1.477	1.640	1.727	1.783	1.822
m_2	4		4	5	6	7	8
$n_1 n_2$	3.15×10^{-3}		8.42	30.4	71.0	138	242
$\lvert RoRe\rvert_{\text{crit}}$	106		10.5	11.2	12.5	14.0	15.8

h	0.527	0.484	0.448	0.417	0.391	0.368	0.348
$\omega_{1,1}$	1.851	1.873	1.890	1.904	1.915	1.924	1.932
m_2	9	10	11	12	13	14	15
$n_1 n_2$	24.3	36.6	52.9	74.4	101	134	174
$\lvert RoRe\rvert_{\text{crit}}$	17.6	19.6	21.7	23.9	26.2	28.6	31.0

Table 4.2: Theoretical results considering the $(m_2, 2, 2)$ combinations with $k_2 = 2\pi/h$ and $k_1 = k = \pi/h$.

between the resonant Kelvin mode and the two free Kelvin modes. These terms represent the mechanism of triadic resonance. The last term of this equation is the volume viscous term. It should not appear at this order but at order ε^2 since $\varepsilon = O\left(Re^{-1/2}\right)$. However we have decided to take it into account in the analysis because its importance in saturating the growth rate of the instability has been shown in several papers (Kerswell & Barenghi, 1995; Eloy *et al.*, 2003; Racz & Scott, 2007).

The perturbation $\mathbf{v}^{(1)}$ can be decomposed as

$$\mathbf{v}^{(1)} = \sum_{j=1}^{2} \mathbf{v}_j^{(1)} = \sum_{j=1}^{2} \left(\mathbf{u}_j^{+} \mathrm{e}^{\mathrm{i}(\omega_j t + m_j \varphi + k_j z)} \pm \mathbf{u}_j^{-} \mathrm{e}^{\mathrm{i}(\omega_j t + m_j \varphi - k_j z)} \right). \tag{4.24}$$

where the sign is chosen such that each component j has the same parity as the corresponding free Kelvin mode (a plus sign if there is a plus in (4.19)). In this case the left-hand side term in equation (4.23) has the same parity than the right-hand side terms.

Inserting the expression (4.24) for $\mathbf{v^{(1)}}$ and the expression (4.20) for $\mathbf{v^{(0)}}$ in (4.23) gives an equation for $\mathbf{v_j}$. A solvability condition is then obtained by forming the scalar product defined by (4.51) of $\mathbf{v}_1$ (resp. $\mathbf{v}_2$) with this equation. It yields two coupled amplitude equations for A_1 and A_2

$$\frac{\partial A_1}{\partial t} = \bar{\varepsilon} n_1 A_2 - \frac{1}{Re^{1/2}} s_1 A_1 - \frac{1}{Re} v_1 A_1 - \mathrm{i} q_1 \Delta k_1 A_1, \tag{4.25a}$$

$$\frac{\partial A_2}{\partial t} = \varepsilon n_2 A_1 - \frac{1}{Re^{1/2}} s_2 A_2 - \frac{1}{Re} v_2 A_2 - \mathrm{i} q_2 \Delta k_2 A_2. \tag{4.25b}$$

The terms $\partial A_j / \partial t$ come from the scalar product $\mathbf{v}_j \odot \frac{\partial}{\partial t} \mathcal{I} \mathbf{v}_j$.

The terms n_1 and n_2 are real and represent the interaction, through the nonlinear term of the Navier–Stokes equation, of a free Kelvin mode with the forced mode. These terms come from the scalar product $\mathbf{v}_j \odot \left[\mathbf{N}\left(\mathbf{v}^{(0)}, \varepsilon \mathbf{v}_{1,\omega,k}\right) + \mathbf{N}\left(\varepsilon \mathbf{v}_{1,\omega,k}, \mathbf{v}^{(0)}\right) \right] + \text{c.c.}$ They are given in Appendix 4.8.2.

The coefficients s_1 and s_2 represent the surface viscous damping of the two free Kelvin modes due to Ekman boundary layers. They come from the rest of the scalar product $\mathbf{v}_j \odot \left(\frac{\partial}{\partial t} \mathcal{I} + \mathcal{M} \right) \mathbf{v}^{(1)}$ which almost vanishes because $\mathbf{v}_j$ is in the kernel of the operator $\frac{\partial}{\partial t} \mathcal{I} + \mathcal{M}$. This rest corresponds to the pressure of the free Kelvin mode p_j times the normal velocity of $\mathbf{v}_j^{(1)}$ integrated over the cylinder walls. This normal velocity is given by the boundary condition (4.15) at order ε and is thus the opposite of the Ekman pumping associated with the free Kelvin modes, as explained in section 4.4.3. This is why these terms are proportional to $Re^{-1/2}$. The coefficients s_j are complex numbers with a positive real part and can be analytically calculated (see Appendix 4.8.2 and Kudlick, 1966).

The coefficients v_1 and v_2 are real and represent the volume viscous damping of the two free Kelvin modes. They originate from the scalar product $\mathbf{v}_j \odot \mathcal{L} \mathbf{v}_j$ and can be decomposed into two parts : one proportional to k_j^2, another proportional to m_j^2 as shown in Appendix 4.8.2. The free Kelvin modes with a high azimuthal wavenumber are thus strongly damped by volume viscous effects. Although these terms should appear at higher order in

the asymptotic expansion, they have be taken account here to allow for the selection of modes with the largest wavelengths.

The real coefficients q_1 and q_2 represent the damping of the two free Kelvin modes by detuning effects. These terms originate from the scalar product $\mathbf{v}_j \odot \mathcal{M}_\Delta \mathbf{v}_j$. They can be analytically calculated and are given in Appendix 4.8.2. These terms vanish when the two free Kelvin modes are exactly resonant.

In the following, viscous and detuning effects are gathered in a single coefficient

$$\alpha_j = \frac{1}{Re^{1/2}} s_j + \frac{1}{Re} v_j + \mathrm{i} q_j \Delta k_j, \tag{4.26}$$

corresponding to the linear decay term.

4.4.6 Growth rate of the instability

Assuming that the amplitudes A_1 and A_2 are growing exponentially ($A_j \sim \mathrm{e}^{\sigma t}$), the equation for the complex growth rate σ is obtained by canceling the determinant of the linear system (4.25)

$$(\sigma + \alpha_1)(\sigma + \alpha_2) = |\varepsilon|^2 n_1 n_2. \tag{4.27}$$

This relation leads to an analytical expression for the complex growth rate. The temporal growth rate σ^{r} of the instability is simply the real part of σ. The flow is thus unstable when σ^{r} is positive for a given resonant Kelvin mode combination. The growth rate is a function of ε and Re only, or alternatively a function of Ro and Re.

For an exactly resonant combination (no detuning effect) and at infinite Reynolds number, the linear saturation terms α_j vanish such that the growth rate is simply given by $\sigma^{\mathrm{r}} = |\varepsilon| (n_1 n_2)^{1/2}$. As expected (based on similarities with the elliptic instability) it is proportional to the amplitude $|\varepsilon|$ of the forced Kelvin mode. The flow is unstable if the coefficient $n_1 n_2$ is positive, which is always true for Kelvin modes with dispersion relations of opposite slopes. This can be shown by looking at the signs of n_1 and n_2 (see Appendix 4.8.2) and confirms the result by Fukumoto (2003) proved with energetic methods. These coeficients are given in Tables 4.1 and 4.2 for the principal exact resonances. They increase drastically when the aspect ratio decreases. This comes from the fact that the velocity of the base flow increases and it does not mean that the precessing cylinder is more unstable as it will be seen later.

When linear saturation terms are introduced ($\alpha_j \neq 0$), the growth rate of the instability decreases. At infinite Reynolds numbers only detuning effects play a role and the growth rate thus takes the simple form

$$\sigma^{\mathrm{r}} = \left[|\varepsilon|^2 n_1 n_2 - \frac{1}{4} (q_1 \Delta k_1 - q_2 \Delta k_2)^2 \right]^{1/2}. \tag{4.28}$$

Detuning effects stabilize the flow and their influence can be studied by varying the aspect ratio. Such a variation allows to observe several combinations (m_2, l_1, l_2) which become exactly resonant (i.e. $\Delta k_j = 0$) for particular values of h, listed in Table 4.1 and 4.2.

For an exact resonance, detuning effects vanish and the instability is damped by viscous effects only. An asymptotic expression can be obtained for large Reynolds numbers (when $\mathrm{Im}(\alpha_j) \ll \varepsilon(n_1 n_2)^{1/2}$)

$$\sigma^{\mathrm{r}} = |\varepsilon| \, (n_1 n_2)^{1/2} - \frac{\mathrm{Re}\{\mathrm{s}_1 + \mathrm{s}_2\}}{2Re^{1/2}} - \frac{v_1 + v_2}{2Re}, \tag{4.29}$$

where the two damping terms are due to surface and volume viscous damping. These viscous effects stabilize the flow at low amplitude ε and thus allow to calculate the threshold of the instability.

4.4.7 Instability threshold

Assuming that the real part of σ vanishes in (4.27) leads after some calculation to an expression for the amplitude $\varepsilon_{\mathrm{crit}}$ at which the instability appears. Since this amplitude of the forced Kelvin mode is given by Eq. (4.12), we can thus determine the critical Rossby number at which the instability appears

$$|Ro_{\mathrm{crit}}| = \frac{1}{|f|} \left\{ \frac{\alpha_1^{\mathrm{r}} \alpha_2^{\mathrm{r}}}{n_1 n_2} \left[1 + \left(\frac{\alpha_1^{\mathrm{i}} - \alpha_2^{\mathrm{i}}}{\alpha_1^{\mathrm{r}} + \alpha_2^{\mathrm{r}}} \right)^2 \right] \right\}^{1/2} \left| \frac{s}{Re^{1/2}} + \frac{\mathrm{i}f}{a_i} \right|, \tag{4.30}$$

where α_j^{r} and α_j^{i} are respectively the real and imaginary parts of α_j defined in (4.26). We recall that f is the linear forcing parameter and s the surface viscous parameter of the forced Kelvin mode, given in Appendix 4.8.1 and 4.8.2. The coefficient a_i corresponds to the inviscid amplitude of the forced Kelvin mode and is given in Appendix 4.8.1. Note that equation (4.30) is not valid if $\alpha_1^{\mathrm{r}} + \alpha_2^{\mathrm{r}} = 0$, which means that the inviscid threshold is not the limit of the viscous threshold for large Re number. Different scalings for the critical Rossby number are obtained depending on the predominant damping effect in α_j.

In the experiments, free Kelvin modes with fairly large azimuthal wavenumbers have been observed. In this case, the volume viscous damping of order $(m_j^2 + \delta_j^2)Re^{-1}$ can be larger than surface viscous damping or order $Re^{-1/2}$ if the Reynolds number is below a critical value defined by

$$Re_1 = \frac{v_1^{\mathrm{r}} v_2^{\mathrm{r}}}{s_1^{\mathrm{r}} s_2^{\mathrm{r}}} \left(1 + \frac{\left(s_1^{\mathrm{i}} - s_2^{\mathrm{i}}\right)^2}{\left(s_1^{\mathrm{r}} + s_2^{\mathrm{r}}\right)^2} \right)^{-1}. \tag{4.31}$$

For Reynolds numbers between 1 and Re_1, the critical Rossby number scales as $Re^{-3/2}$, as shown schematically in Fig. 4.4. A simple expression can be found in this regime

$$\left| RoRe^{3/2} \right|_{\mathrm{crit}} = \left| \frac{s}{f} \right| \left(\frac{v_1 v_2}{n_1 n_2} \right)^{1/2}. \tag{4.32}$$

At intermediate Reynolds numbers ($Re \gg Re_1$), surface viscous effects become dominant. The critical Rossby number then scales as Re^{-1} (see Fig. 4.4) and leads to an expression

$$|RoRe|_{\mathrm{crit}} = \left| \frac{s}{f} \right| \left\{ \frac{s_1^{\mathrm{r}} s_2^{\mathrm{r}}}{n_1 n_2} \left[1 + \left(\frac{s_1^{\mathrm{i}} - s_2^{\mathrm{i}}}{s_1^{\mathrm{r}} + s_2^{\mathrm{r}}} \right)^2 \right] \right\}^{1/2}. \tag{4.33}$$

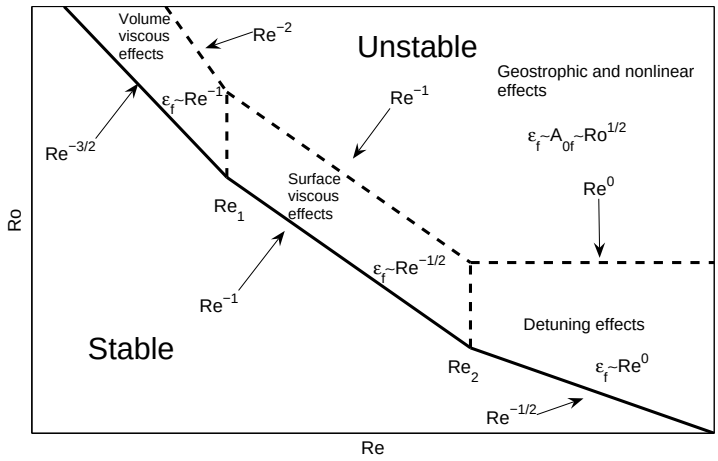

Figure 4.4: Schematic of the scaling of the critical Rossby number at which the instability appears as a function of the Reynolds number. The scalings for the fixed point determined by the non-linear equations are also shown. The expressions of the transition Reynolds numbers Re_1 and Re_2 are given in (4.31) and (4.34).

This regime is the most frequent in experiments and we thus give the values of the critical $|RoRe|$ for the principal resonances in Tables 4.1 and 4.2. The most unstable resonances (given by the smallest Rossby numbers) are found for the large aspect ratios h, although the inviscid growth rates $(n_1 n_2)^{1/2}$ are larger at small h. This is due to the strong increase of ε with h.

When the combination is not exactly resonant, detuning effects can also damp the instability. They appear at high Reynolds numbers, when surface viscous terms become smaller than detuning terms, i.e. for $Re \ll Re_2$ defined by

$$Re_2 = \frac{\left(s_1^{\mathrm{r}} + s_2^{\mathrm{r}}\right)^2 + \left(s_1^{\mathrm{i}} - s_2^{\mathrm{i}}\right)^2}{\left(q_1 \Delta k_1 - q_2 \Delta k_2\right)^2}. \tag{4.34}$$

In this regime, the critical Rossby number still depends on the Reynolds number since the forced Kelvin mode scales as $Re^{1/2}$. The critical Rossby number thus scales as Re^{-1} and leads to a simple expression

$$\left|Ro\,Re^{1/2}\right|_{\mathrm{crit}} = \left|\frac{s}{f}\right| \frac{\left(s_1^{\mathrm{r}} s_2^{\mathrm{r}}\right)^{1/2}}{s_1^{\mathrm{r}} + s_2^{\mathrm{r}}} \frac{\left|q_1 \Delta k_1 - q_2 \Delta k_2\right|}{\left(n_1 n_2\right)^{1/2}}. \tag{4.35}$$

It can be noted that this expression is valid for Re asymptoting to infinity and takes into account the values of the viscous coefficients s_j. It is different from thevalue that would be obtained at infinite Reynolds number by assuming $\sigma^{\mathrm{r}} = 0$ in (4.28), but the two theories give identical threshold when $s_1 = s_2$.

4.5 Discussion

In this section we discuss the general properties of the precessional instability as a function of the dimensionless parameters Re, h and ω and we

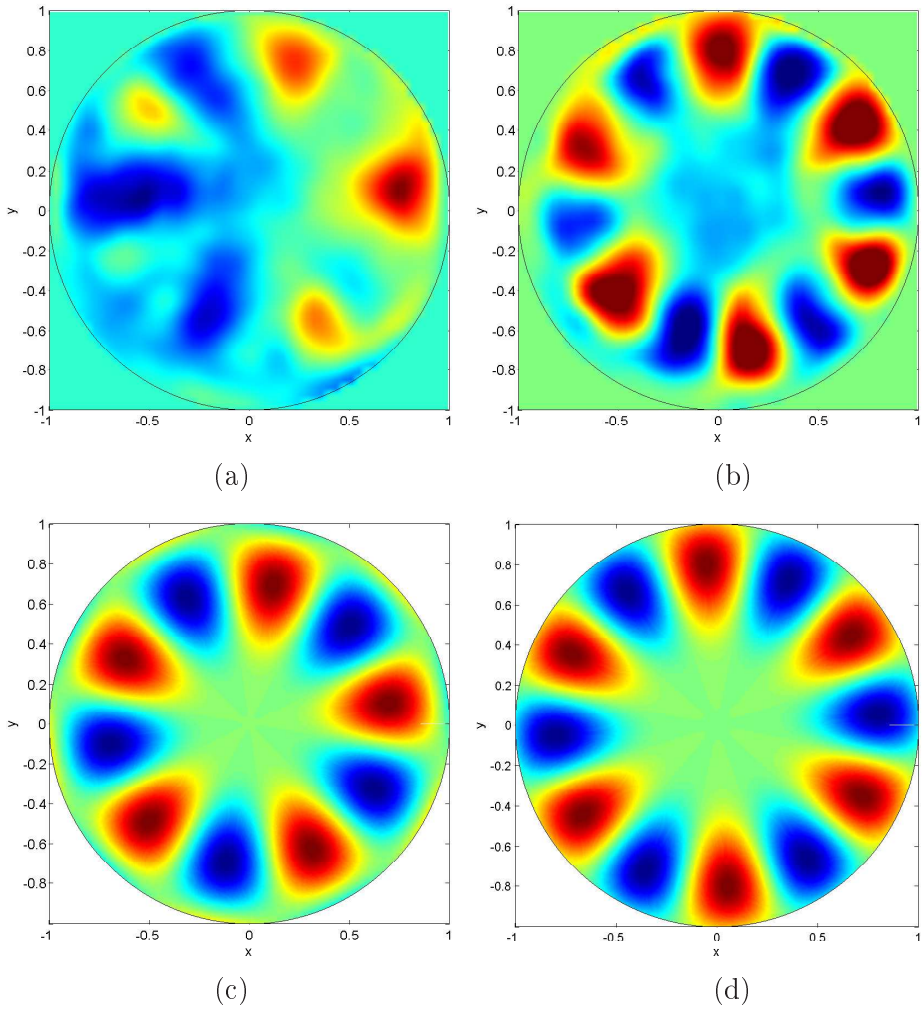

Figure 4.5: Experimental (a, b) and theoretical (c, d) axial and instantaneous vorticity fields of the free Kelvin modes $m_1 = 5$ and $m_2 = 6$. $h = 1.62$, $\omega = 1.18$ and $Ro = -0.0031$. (a) $Re = 6000$. (b) $Re = 6500$.

compare these predictions to experimental results for a particular aspect ratio. We limit our study to the instabilities driven by the first forced Kelvin mode.

4.5.1 Prediction of the unstable modes

In our previous paper (Lagrange *et al.*, 2008), we have observed experimentally that the unstable flow exhibits two free Kelvin modes with azimuthal wavenumbers 5 and 6 at the first resonance of the first Kelvin mode ($h = 1.62$ and $\omega = 1.18$). Their experimental axial and instantaneous vorticity fields are plotted in figures $4.5(a)$ and $4.5(b)$. They correspond exactly to the free Kelvin modes predicted theoretically for this aspect ratio. Indeed, the resonant combination (6, 1, 1) is more unstable than any other combinations (with different azimuthal wavenumbers m_j and branch numbers l_j).

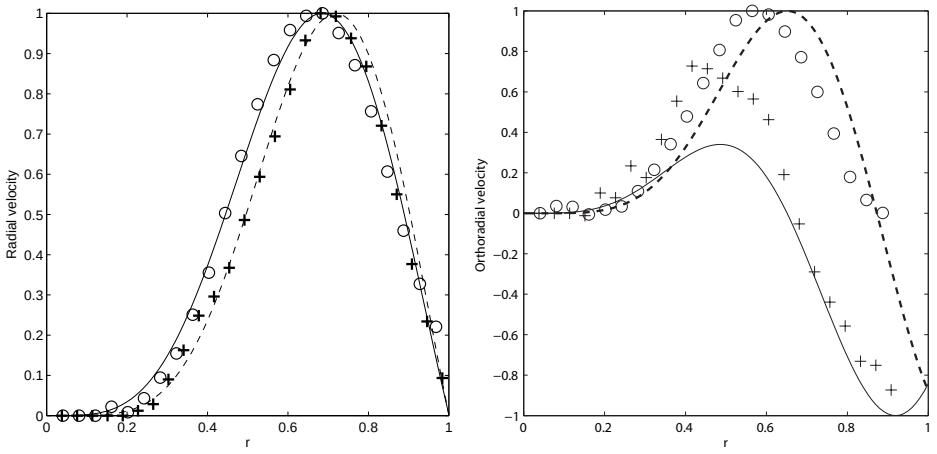

Figure 4.6: Radial (a) and orthoradial (b) velocity profiles of the free Kelvin modes $m_1 = 5$ (+, solid line), and $m_2 = 6$ (∘, dashed line), in arbitrary units. $h = 1.62$, $\omega = 1.18$, $Re = 6000$ for $m_1 = 5$; $Re = 6500$ for $m_2 = 6$.

The theoretical axial vorticity fields of the free Kelvin modes are shown in figures 4.5(c) and 4.5(d) and look very similar to the experimental fields. They both have one ring of 10 (or 12) alternate vortices meaning that they correspond to the first branch of the dispersion relations ($l_1 = l_2 = 1$) for $m_1 = 5$ and $m_2 = 6$. Furthermore, the radial position of these vortices seems to be well predicted : the maximum of the azimuthal average vorticity is located theoretically at $r = 0.80$ and experimentally at $r \approx 0.83$ for the second mode with $m_2 = 6$. The agreement is not as good for the first mode with $m_1 = 5$ ($r = 0.70$ theoretically compared to $r \approx 0.57$ experimentally) because of the presence of the forced Kelvin mode ($m = 1$).

To better compare the structure of the unstable modes we have plotted in figure 4.6 the theoretical and the experimental radial and orthoradial velocities of the free Kelvin modes as a function of r. They have been obtained by taking the azimuthal and the temporal average of the velocity fields and they are given in arbitrary units. The radial velocity profiles of the free Kelvin modes are very similar and look like bell-shaped profiles. Because the two free Kelvin modes satisfy a condition of no outward flow at $r = 1$, their radial velocities vanishes at $r = 1$. The orthoradial velocity profiles are more complicated. The orthoradial velocity profile of the free Kelvin mode $m_1 = 5$ shows two extrema while for the mode $m_2 = 6$, it shows one extremum. Experiments roughly confirm these two different orthoradial velocity profiles.

Finally, theory also predicts that the free Kelvin mode $m_1 = 5$ (resp. $m_2 = 6$) has an axial vorticity which is a sine (resp. cosine) function of the altitude z. This parity is confirmed by experiments since the free Kelvin mode $m_1 = 5$ (resp. $m_2 = 6$) has been observed at $z = 0$ (resp. $z = h/4$).

These experimental observations confirm the mode predicted by the linear stability analysis and therefore validate the mechanism of triadic reso-

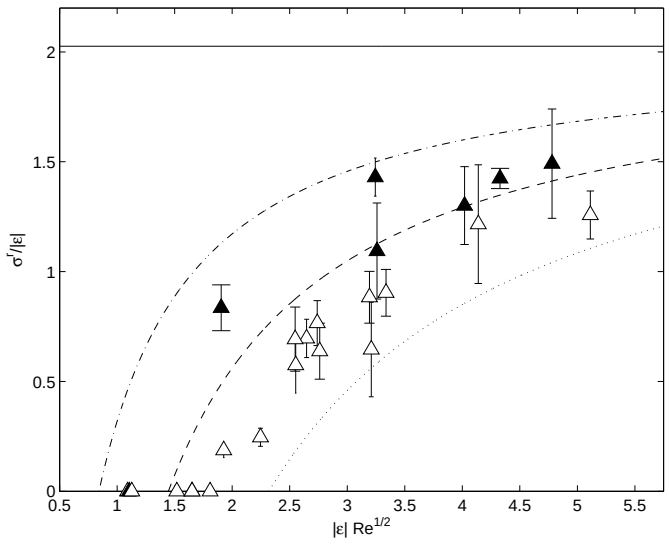

Figure 4.7: Growth rate $\sigma^{\mathrm{r}}/|\varepsilon|$ of the precessional instability for $h = 1.62$ and $\omega = 1.18$. The inviscid prediction is represented by the horizontal solid line. The dash–dotted line is the viscous prediction without volume viscous effects. The dashed line is the full viscous prediction for $Re = 6000$. The dotted line is the viscous prediction for $Re = 1000$. Filled symbols (▲) correspond to experiments with $6000 < Re < 24400$. Open symbols (△) correspond to experiments with $1000 < Re < 6000$.

nance proposed in this paper.

4.5.2 Prediction of the growth rate

In this section, we compare the theoretical growth rate σ^{r}, with the experimental results. We restrict our analysis to the first resonance of the first Kelvin mode for $h = 1.62$, such that there is no detuning effects.

Figure 4.7 represents the evolution of the growth rate as a function of the forcing. In the inviscid case, the theory gives a constant value $\sigma^{\mathrm{r}}/|\varepsilon| = (n_1 n_2)^{1/2}$ represented by a solid line. When surface viscous effects are added, it can be easily shown (dividing (4.27) by $|\varepsilon|^2$) that the rescaled growth rate $\sigma^{\mathrm{r}}/|\varepsilon|$ is a function of $|\varepsilon| Re^{1/2}$ only. This is why we have plotted the growth rate in these coordinates. This viscous prediction is plotted as a dash-dotted line in Fig. 4.7. The growth rate increases with the forcing and tends toward the inviscid growth rate at infinite Reynolds number. It vanishes at a specific value of $|\varepsilon| Re^{1/2} = 0.843$ corresponding to the critical Rossby number (given in Table 4.1). This prediction is only valid for Reynolds numbers large compared to Re_1. Below this Reynolds number, volume viscous effects must be taken into account. The theoretical prediction with all viscous terms is plotted as a dashed line for $Re = 6000$ and as a dotted line for $Re = 1000$. They show the same trend but remain weaker.

Experimental measurements of the growth rate are also plotted as symbols on the same graph. As expected, experimental measurements are below the growth rate with surface viscous terms only. They are represented as filled (resp. open) symbols when their Reynolds number is larger (resp. smaller)

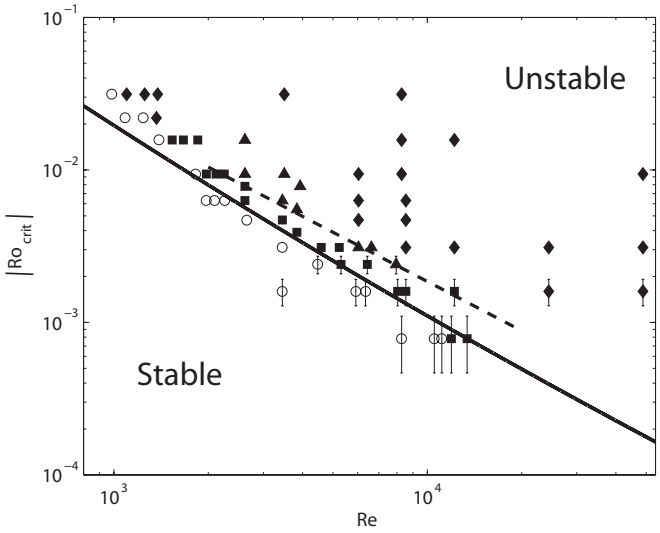

Figure 4.8: Stability diagram of the flow inside a precessing cylinder for $h = 1.62$ and $\omega = 1.18$. The stable and unstable domain are separated by the solid line which corresponds to the prediction (4.30). Open symbols (○) represent stable experiments and filled symbols represent unstable experiments. Unstable experiments can be either stationary (■), intermittent (▲) or turbulent (♦). The dashed line corresponds to the transition from a stationary to an intermittent flow in the weakly non-linear model.

than the Reynolds number of the dashed line ($Re = 6000$). The symbols always fall within the correct band of growth rate, which is an excellent confirmation of the theoretical calculation.

Experimentally, the growth rate was measured by an exponential fit of the amplitude of the free Kelvin mode $m_1 = 5$ at the onset of the instability. Note that the instability can appear before the amplitude $|\varepsilon|$ of the forced Kelvin mode has reached its stationary value given by equation (4.12). So here $|\varepsilon|$ corresponds to the measured amplitude of the first Kelvin mode at the onset of instability and not the value given by (4.12).

4.5.3 Critical Rossby number as a function of *Re*

Figure 4.8 represents the critical Rossby number Ro_{crit} as a function of Re when the first Kelvin mode is forced at its first resonance. The prediction is issued from equation (4.30) and is represented by a solid line which divides the (Re, Ro)-plane into a stable domain and an unstable domain. Stable experiments are represented by circles and unstable experiments are represented by black symbols. These experiments were done on a very large range of precessing angle (0.25° to 10°) and Reynolds number (10^3 to 5×10^4). It is striking to see such an agreement between experiments and theory with no fitting parameter in the theory. However, there are some slight discrepancies at high Rossby numbers. They may come from non-linear effects in the base flow which arise because the amplitude of the forced Kelvin mode $\varepsilon \sim Ro\,Re^{1/2}$ is no longer a small parameter. Note also that the uncertainty is larger at small Rossby number because the precessing angle (equal to 0.25°)

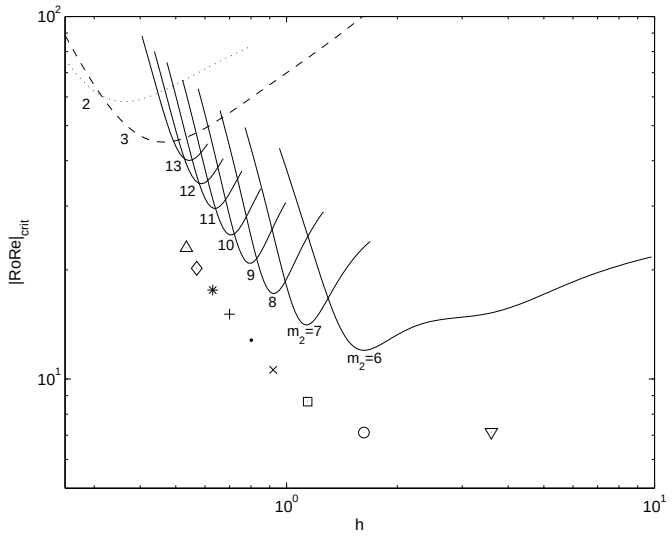

Figure 4.9: Critical $|RoRe|$ number of the most unstable modes as a function of h for the first resonance of the first Kevlin mode ($\omega = \omega_{1,1}$). Each solid line corresponds to the full theory at $Re = 6500$ for a resonant combination $(m_2, 1, 1)$. Symbols correspond to the predictions without detuning and without volume viscous effects (thus valid at any Reynolds number, see Table 4.1) for the same combinations with $m_2 = 6$ ($\circ, \triangledown$), $m_2 = 7$ ($\square$), $m_2 = 8$ ($\times$), $m_2 = 9$ ($\bullet$), $m_2 = 10$ ($+$), $m_2 = 11$ ($*$), $m_2 = 12$ ($\diamond$), $m_2 = 13$ ($\triangle$). The dashed line (resp. dotted line) corresponds to a combination $(3, 1, 1)$ (resp. $(2, 1, 1)$) which can not be exactly resonant.

becomes comparable to the uncertainty of $\pm 0.1°$.

Because the Reynolds number is varied over a large range (one decade), the experiments allow to confirm the scalings for the critical Rossby number. As was shown earlier, at moderate Reynolds number, ($Re \ll Re_1 = 3000$) the Rossby number scales as $Re^{-3/2}$. At large Reynolds numbers ($Re \gg Re_1 = 3000$, the Rossby number scales as Re^{-1}.

4.5.4 Critical *RoRe* number as a function of h

Now that the theory has been validated experimentally by the two previous sections, we use these predictions to study the general properties of the precessional instability as the parameters h and/or ω are varied. In this section, the aspect ratio is varied over a large range, from 0.2 to 10. However, the frequency ω always corresponds to the first resonance of the first Kelvin mode $\omega_{1,1}$.

Figure 4.9 shows the evolution of the threshold as a function of h. Several bands of instability corresponding to different resonant Kelvin mode combinations $(m_2, 1, 1)$ are observed. Each band reaches a minimum when the combination is exactly resonant, i.e. when detuning effects vanish. The most unstable combination (i.e. minimum threshold) is the $(6, 1, 1)$ resonant combination for $h = 1.62$, studied experimentally in this paper.

We have seen in section 4.4.7 that, when volume viscous effects are neglected, the stability threshold only depends on the product $RoRe$. This is

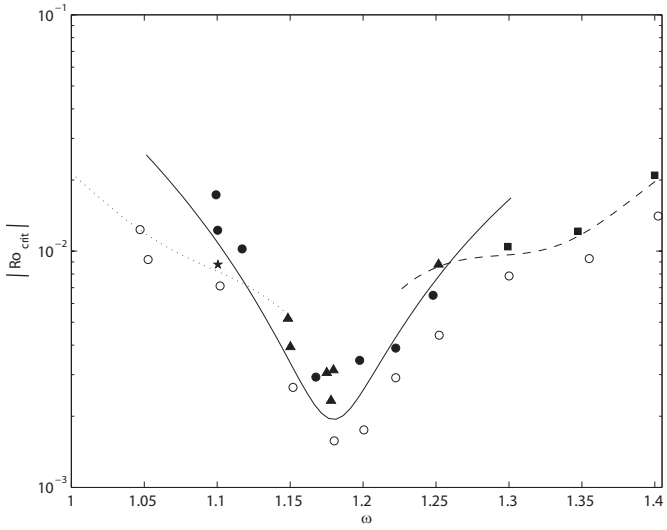

Figure 4.10: Critical Rossby number as a function of ω. Resonant Kelvin mode combinations $(7,1,1)$ (dotted line), $(6,1,1)$ (solid line) and $(5,1,1)$ (dashed line) are observed. Stable experiments are represented by circles ($\circ$) and unstable experiments by black symbols. PIV experiments are represented by a black star ($\star$) for the $(7,1,1)$ combination, black triangles ($\blacktriangle$) for the $(6,1,1)$ combination and black squares ($\blacksquare$) for the $(5,1,1)$ combination. Black circles ($\bullet$) correspond to unstable experiments visualized by using Kalliroscope particles. $h = 1.62$, $Re = 6500$.

why we have plotted the threshold as $|RoRe|$ in figure 4.9, such that the prediction without volume viscous effects is independent of the Reynolds number and plotted as a symbol for each exactly resonant combination. The gap between the symbol the corresponding solid line indicate the influence of the volume viscous effects at $Re = 6500$.

The combinations $(2,1,1)$ and $(3,1,1)$ are special because they are not close to an exact resonance (which ensures a small detuning) although they are the most unstable for small aspect ratios.

Finally note that some resonant Kelvin mode combinations $(m_2,2,2)$ (not represented in figure 4.9) can be more unstable than the combinations $(m_1,1,1)$ represented in very small intervals of aspect ratios when $h < 1$.

4.5.5 Critical Rossby number as a function of ω

In this section the aspect ratio and the Reynolds number are fixed and the frequency ω is varied around the first resonance of the first Kelvin mode. Figure 4.10 represents the critical Rossby number as a function of ω, for $h = 1.62$ and $Re = 6500$. Several bands of instability corresponding to different azimuthal wavenumbers $m_2 = 7$ (dotted line), $m_2 = 6$ (solid line) and $m_2 = 5$ (dashed line) are predicted. This is due to the change of ω which allow to couple different Kelvin modes (since $\omega_2 - \omega_1 = \omega$). These predictions are well confirmed by PIV measurements which reveal the correct azimuthal wavenumber. Moreover, the theoretical threshold is in very good agreement with experiments.

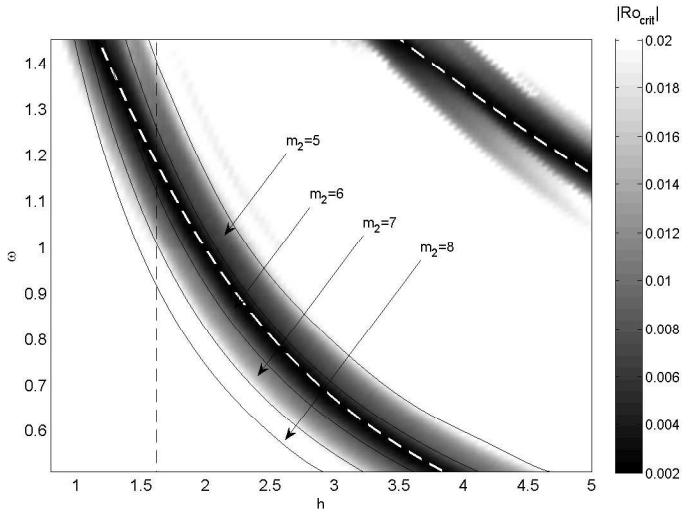

Figure 4.11: Critical Rossby number as a function of h and ω, by considering that the first Kelvin mode is forced by precession. The resonant Kelvin mode combinations $(5,1,1)$, $(6,1,1)$, $(7,1,1)$, $(8,1,1)$ are observed. The white dashed lines correspond to the first (lower left) and second (upper right) resonance of the first Kelvin mode. Fig. 4.10 corresponds to the vertical dashed line at $h = 1.62$. $Re = 6500$.

The most unstable combination is the $(6,1,1)$ mode and is obtained close to $\omega = 1.18$. This can be easily understood because this is where the amplitude ε of the forced Kelvin mode is maximum (at its resonance). Around the resonance, the amplitude of the forced Kelvin mode decreases as $1/(\omega - \omega_{1,1})$, which lead to weaker instabilities for the combinations $(5,1,1)$ and $(7,1,1)$.

This proves that the easiest way to trigger an instability is to force the base flow at a resonance frequency. For example, here, a precessing angle of $\theta \approx 0.5°$ is sufficient to observe the $(6,1,1)$ resonant Kelvin mode combination. Outside of the resonant frequency it is necessary to have a minimum precessing angle of $\theta \approx 7°$ (resp. $\theta \approx 2°$) to observe the $(7,1,1)$ (resp. $(5,1,1)$) resonant Kelvin mode combination at the same Reynolds number.

4.5.6 Critical Rossby number as a function of h and ω

In this section we study the general problem of the precessional instability at a given Reynolds number when both the aspect ratio and the frequency are varied. We consider only instabilities triggered by the first forced Kelvin mode. The critical Rossby number in the plane (h, ω) is represented in figure 4.11. It was obtained numerically by calculating the analytical coefficients of the amplitude equations (4.25) for various azimuthal wavenumbers ($m_2 = 1$ to 15) and for various branches ($l_j = 1$ to 5) on a very fine mesh of the plane (h, ω). This calculation took about a month on a standard computer.

On this figure, the most unstable regions correspond to the dark areas, i.e. where the critical Rossby number is small. There are two unstable regions, which are located around the resonances of the first Kelvin mode, represented

by white dashed lines. As explained in the previous section, this can be easily understood because the amplitude of the forced Kelvin mode ε is maximum there.

The black thin lines separate different resonant Kelvin mode combinations with azimuthal wavenumbers $m_2 = 5$ to 8. It is surprising to see that each combination creates a band which is almost parallel to the resonance curve. This explains why there are only a few combinations which are resonant (here only 4 combinations) when varying the aspect ratio. The combination $(6, 1, 1)$ is the most unstable one because it is centered on the resonance curve almost over the whole range of aspect ratios considered here. It is curious to see that it is exactly resonant twice (for $h = 1.62$ and $h = 3.6$).

At higher Reynolds numbers, other combinations might become more unstable and thus create other bands of instabilities in between these combinations. However, one can have a rough idea of the stability diagram at any Reynolds number by simply assuming that the critical Rossby number is inversely proportional to the Reynolds number (as it is the case when surface viscous terms are considered).

Note that the previous figures correspond to the critical Rossby number along the white dashed line (for Fig. 4.9) and along the black dashed line (for Fig. 4.10). Note also that the combinations represented in figure 4.11 always satisfy $k_2 - k_1 = k$ (combinations satisfying $k_1 - k_2 = k$ are always more stable).

4.6 Weakly nonlinear theory

This section is devoted to the prediction of the instability saturation by nonlinear effects. The analysis will be restricted to the most unstable case, i.e. the exact resonance of the first Kelvin mode ($h = 1.62$, $\omega = 1.18$).

4.6.1 Geostrophic flow

Experiments have shown that the unstable Kelvin modes $m_1 = 5$ and $m_2 = 6$ mentioned previously give rise to a mode with a cylindrical symmetry which corresponds to a stationary azimuthal velocity field. This geostrophic Kelvin mode appears at order $O\left({A_j}^2 Re^{-1/2}\right)$. It is due to the nonlinear interaction in the Ekman layers of the unstable Kelvin modes with their respective viscous flows (see Meunier *et al.*, 2008). The role of the geostrophic mode is essential in the weakly nonlinear analysis because it saturates the amplitude of the resonant and the unstable Kelvin modes. Note that the nonlinear interaction of a Kelvin modes with itself has also a saturating effect. However, in our experiments, this saturating effect is less significative than the saturation due to the geostrophic mode.

Finding an analytical expression of the geostrophic flow is a very complex problem. To avoid this difficulty and to keep in the analysis the fewest number of mode possible, an empirical formulation has been used for the geostrophic mode based on experimental measurements. For $h = 1.62$ and $\omega = 1.18$ (i.e. first resonance of the first Kelvin mode) experiments have shown that the free Kelvin modes $m_1 = 5$ and $m_2 = 6$ lead to a geostrophic

Kelvin mode whose profile is close to the profile of the free Kelvin mode

$$\mathbf{v}_0 = -J_5\left(d_2 r\right)\mathbf{u}_\varphi, \tag{4.36}$$

where $\mathbf{u}_\varphi$ is the orthoradial unit vector and J_5 is the Bessel function of the first kind. The parameter d_2 is the second root of J_5 (i.e. $d_2 = 12.339$). We will assume that this geostrophic mode is added to the perturbation with an amplitude A_0.

4.6.2 Weakly nonlinear amplitude equations

Adding this geostrophic mode leads to a total flow

$$\mathbf{v} = \varepsilon\mathbf{v}_{1,\omega,k} + A_1\mathbf{v}_1 + A_2\mathbf{v}_2 + A_0\mathbf{v}_0 + \text{o.t.} \tag{4.37}$$

We recall that ε is the amplitude of the forced Kelvin mode $\mathbf{v}_{1,\omega,k}$ given by (4.9). Vectors $\mathbf{v}_1$ and $\mathbf{v}_2$ are the two free Kelvin modes of the triadic resonance, whose amplitudes are A_1 and A_2. These vectors are given by equation (4.19). The notation o.t. stands for 'other terms' and includes the Ekman layer pumping flows and the non-resonant Kelvin modes.

Inserting (4.37) into the Navier–Stokes equation (4.5) and forming the scalar product of this equation with $\mathbf{v}_{1,\omega,k}$, $\mathbf{v}_1$, $\mathbf{v}_2$ and $\mathbf{v}_0$, leads to the following weakly nonlinear amplitude equations

$$\frac{\partial\varepsilon}{\partial t} = \mathrm{i}fRo \;-\; \alpha\varepsilon \;-\; \mathrm{i}\xi A_0\varepsilon + \lambda\overline{A_1}A_2, \tag{4.38a}$$

$$\frac{\partial A_1}{\partial t} = \bar{\varepsilon}n_1 A_2 - \alpha_1 A_1 - \mathrm{i}\xi_1 A_0 A_1 - \mathrm{i}\sigma_1\left|A_1\right|^2 A_1, \tag{4.38b}$$

$$\frac{\partial A_2}{\partial t} = \varepsilon n_2 A_1 - \alpha_2 A_2 - \mathrm{i}\xi_2 A_0 A_2 - \mathrm{i}\sigma_2\left|A_2\right|^2 A_2, \tag{4.38c}$$

$$\frac{\partial A_0}{\partial t} = \frac{1}{Re^{1/2}}\left(-\frac{2}{h}A_0 + \chi_1\left|A_1\right|^2 + \chi_2\left|A_2\right|^2\right). \tag{4.38d}$$

The first equation (4.38a) governs the temporal evolution of the forced Kelvin mode amplitude ε. All the coefficients of this equation can be calculated analytically. The first right hand-side term is the forcing due to the precessional motion, with a linear forcing parameter f given in Appendix 4.8.1. The second term is due to the surface viscous damping of the amplitude of the forced Kelvin mode and is thus proportional to $\alpha = s/Re^{1/2}$ (s being given in Appendix 4.8.2). The third term comes from the nonlinear interaction of the forced Kelvin mode with the geostrophic mode. The parameter ξ can be calculated knowing the radial profile of the geostrophic mode given by (4.36) (see Appendix 4.8.3). The last term is the saturating term due to the nonlinear interaction between the two free Kelvin modes with a parameter λ given in Appendix 4.8.3. In the absence of instability, the amplitude ε grows and saturates due to viscous damping at a value $\mathrm{i}fRo/\alpha$.

Equations (4.38b) and (4.38c) represent the temporal evolutions of the free Kelvin mode amplitudes A_1 and A_2. All the parameters of these equations can also be calculated analytically. These equations are similar to the linear amplitude equations (4.25a) and (4.25b) with nonlinear effects added.

f	s	ξ	λ		
0.226	$1.86 - 0.42\mathrm{i}$	0.165	6.503		
n_1	s_1	v_1	ξ_1	σ_1	χ_1
-1.672	$1.61 - 0.06\mathrm{i}$	87.16	-0.066	-83.784	10000
n_2	s_2	v_2	ξ_2	σ_2	χ_2
-2.456	$1.81 - 0.13\mathrm{i}$	102.68	-0.365	48.987	10000

Table 4.3: Numerical values for the parameters appearing in the nonlinear amplitude equations (4.38). For these values, $h = 1.62$ and $\omega = 1.18$ (first resonance of the first Kelvin mode). They correspond to the $(6, 1, 1)$ resonant combination for the case $k_2 - k_1 = k$.

The first right hand-side term of these equations represents the nonlinear interaction of the forced Kelvin mode with a free Kelvin mode (n_1 and n_2 are given in Appendix 4.8.2). The surface, volume viscous and detuning parameters are included in α_1 and α_2 given by equation (4.26). The third term of these equations was not considered before and comes from the nonlinear interactions of the free Kelvin modes with the geostrophic mode (parameters ξ_j are given in Appendix 4.8.3). The last term of equations (4.38b) and (4.38c) correspond to the interactions of a free Kevin mode with itself (parameters σ_j are given in Appendix 4.8.3).

Equation (4.38d) describes the evolution of the geostrophic Kelvin mode amplitude A_0. The first right hand-side term represents the surface viscous damping of the geostrophic Kelvin mode. Note that for this mode volume viscous effects have been neglected relative to surface viscous effects. The second and the third terms of this equation represent the nonlinear interaction of each free Kelvin mode with its Ekman pumping flow. The parameters χ_1 and χ_2 are difficult to calculate analytically. Because modes $m_1 = 5$ and $m_2 = 6$ are similar we shall assume that χ_1 and χ_2 are equal. Their value will be adjusted to fit the experimental data.

We thus have a system of four nonlinear amplitude equations with only one fitting parameter $\chi_1 = \chi_2$. The numerical values of the parameters are given in Table 4.3. We will analyse in the following the properties of this dynamical system and compare them to experimental results.

4.6.3 Nonlinear evolution of the amplitudes

A numerical solution of the system (4.38) is shown in figure 4.12(a). This figure represents the temporal evolution of the amplitude of the free Kelvin mode $m_1 = 5$ for three Reynolds numbers. This corresponds to the most unstable case of the first resonance of the first Kelvin mode ($h = 1.62$, $\omega = 1.18$), for which the numerical values of the parameters are given in Table 4.3.

In the stable regime ($Re = 3500$, $\circ$), the amplitude of the first Kelvin mode A_1 remains equal to 0. The amplitudes of the second Kelvin mode A_2 and the geostrophic mode A_0 are equally null. However, the amplitude ε of

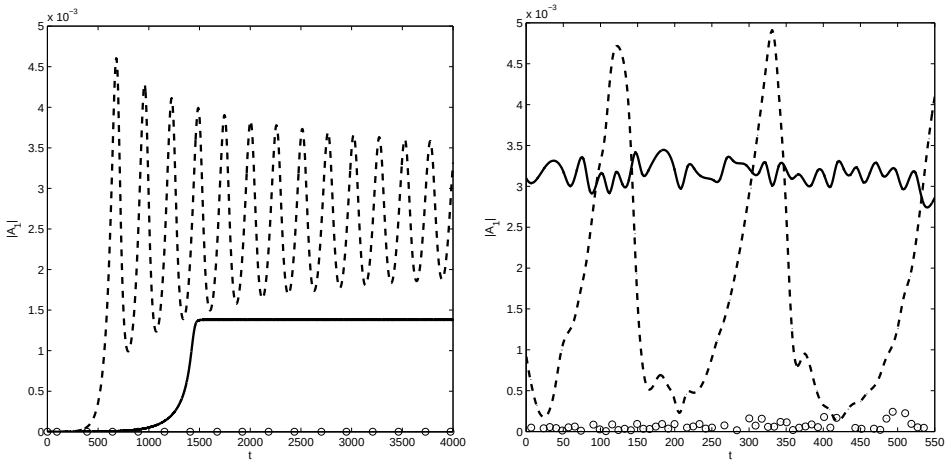

Figure 4.12: Amplitude of the free Kelvin mode $m_1 = 5$ as a function of the dimensionless time t showing the three different regimes of the nonlinear evolution of the instability. (a) Numerical simulation. (b) Experimental results. It is obtained at $Re = 3500$ (○), $Re = 4500$ (solid line) and $Re = 6000$ (dashed line). $h = 1.62$, $\omega = 1.18$, $Ro = -0.0031$.

the forced Kelvin mode grows and saturates at the viscous value given by equation (4.12) with $a_i = \infty$.

Just above the instability threshold ($Re = 4500$, solid line) the amplitude A_1 grows and then saturates at a given value. This unstable and stationary flow thus exhibits a fixed point that will be noted $(\varepsilon_f, A_{1f}, A_{2f}, A_{0f})$. Numerically, the instability saturation is found to be caused mainly by the nonlinear the term $i\xi A_0 \varepsilon$. In other words, the geostrophic mode is responsible of the saturation because it reduces the amplitude of the forced Kelvin mode.

At higher Reynolds number ($Re = 6000$, dashed line), the flow is still unstable but we also observe that the amplitudes are now oscillating, even in the permanent regime. This means that the fixed point $(\varepsilon_f, A_{1f}, A_{2f}, A_{0f})$ has become unstable and the flow is said to be unstable and intermittent. Such a flow can be understood with the following reasoning. First, the amplitudes A_1 and A_2 grow exponentially due to the terms $\bar{\varepsilon} n_1 A_2$ and $\varepsilon n_2 A_1$ in equations (4.38b) and (4.38c). Then, the geostrophic mode is forced through the coefficients χ_1 and χ_2 appearing in equation (4.38d). This geostrophic mode grows slowly in time (since its characteristic time is of the order of $hRe^{1/2}$), which creates a delay to the saturation of the instability. This saturation is achieved by a decrease of ε through the coefficient ξ in equation (4.38a). As soon as the amplitude ε gets smaller than the critical value for the onset of instability, the amplitudes of the free Kelvin modes vanish quickly. It leads to a slow decrease of A_0 and consequently to an increase of ε. Then the instability can grow up again. This phenomenon being repetitive, amplitude oscillations are observed in time. Our experiments have clearly shown that the amplitude oscillations are due to the geostrophic term in equation (4.38a), which is delayed compared to the amplitudes of the free

Kelvin modes.

Figure 4.12(b) shows three experimental measurements of $|A_1|$ at the same Reynolds numbers as in figure 4.12(a). We find again the three different regimes depending on the Reynolds number : stable, unstable and stationary, unstable and intermittent. The transition from stable to unstable flow is very well predicted theoretically, since it corresponds to the linear threshold of the instability : it was plotted on the stability diagram of Fig. 4.8 in the last section. The transition from an unstable stationary flow to an unstable intermittent flow is also in excellent agreement with the predictions. Indeed, this transition has been plotted in Fig. 4.8 as a dashed line. It clearly separates the stationary experiments (□) from the intermittent experiments (▲). This agreement validates the nonlinear system (4.38).

However, the theory does not predict very well the quantitative value of the fixed point A_{1f} in the stationary case : the experimental value is twice larger than the theoretical one. In a similar way, in the intermittent case, the amplitude of the oscillations are not very well predicted by the theory. Nevertheless, the theoretical period of these oscillations $t_{\text{th}} = 250$ matches well the experimental one $t_{\text{exp}} = 290$.

4.6.4 Fixed point

The system (4.38) admits two fixed points. The first one is trivial and corresponds to $A_{1f} = A_{2f} = A_{0f} = 0$ and ε_f given by equation (4.12) with $a_i = \infty$. The second one is obtained by looking for a solution of the system (4.38) which satisfies $\partial\,\varepsilon/\partial\,t = \partial\,|A_j|\,/\partial\,t = \partial\,A_0/\partial\,t = 0$. This solution can be obtained analytically and its complete calculation is reported in Appendix 4.8.3. In this section we only give asymptotical results by considering that viscous and detuning effects or geostrophic and nonlinear effects are dominant for the saturation of the instability.

Just above the threshold, the viscous and the detuning effects are stronger than geostrophic and nonlinear effects for the damping of the instability. Under this assumption, the terms ξ_j and σ_j can be neglected in equations (4.38b) and (4.38c). However, the amplitude of the forced Kelvin mode ε is still affected by the geostrophic and nonlinear term $\xi\varepsilon A_0$. Then, a simple expression for the fixed point ε_f can be obtained

$$\varepsilon_f = \left[\frac{\alpha_1^{\text{r}}\alpha_2^{\text{r}}}{n_1 n_2}\left(1 + \frac{\left(\alpha_1^{\text{i}} - \alpha_2^{\text{i}}\right)^2}{\left(\alpha_1^{\text{r}} + \alpha_2^{\text{r}}\right)^2}\right)\right]^{1/2}. \tag{4.39}$$

We recall that α_j^{r} and α_j^{i} are respectively the real and imaginary parts of the linear saturating term α_j given in equation (4.26).

As for the instability threshold, the linear saturation term can be either volume viscous effects ($Re \ll Re_1$), surface viscous effects ($Re_1 \ll Re \ll Re_2$) or detuning effects ($Re \gg Re_2$). This leads to various scalings for the amplitude of the forced Kelvin mode ε_{f} at the fixed point. These scalings are indicated on Fig. 4.4.

Far from the threshold, the geostrophic and the nonlinear effects are stronger than the viscous and the detuning effects. Under this assumption,

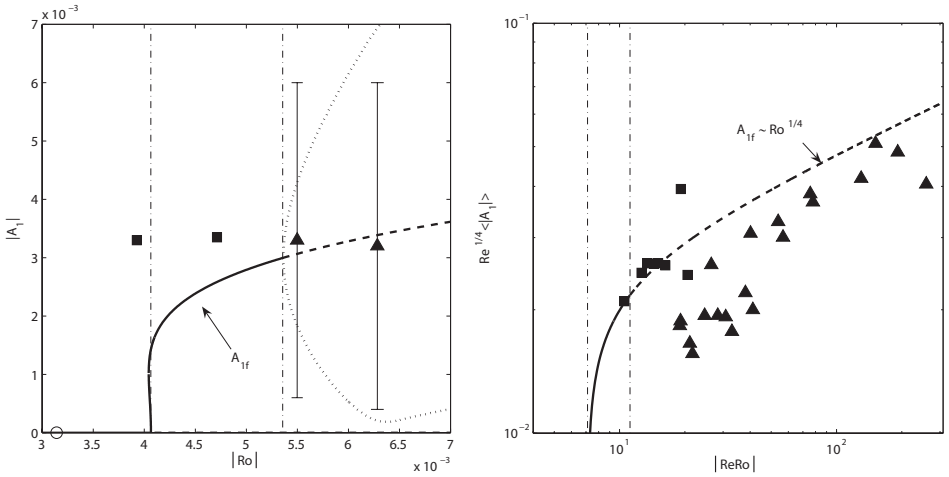

Figure 4.13: Amplitude of the free Kelvin mode $m_1 = 5$ as a function of *Ro* for $Re = 3664$ (a) and as a function of *RoRe* without volume viscous effects (b). The fixed point calculated from the weakly nonlinear theory is represented by a solid line in the unstable and stationnary regime and by a dashed line in the unstable and intermittent regime. Dotted lines represent the maximum and the minimum of oscillations of A_1. Dash–dotted lines represent the two thresholds. Squares (■) represent unstable and stationary experiments. Triangles (▲) represent the mean value of $|A_1|$ in the unstable and intermittent regime. Errorbars indicate the maximum and minimum value A_1. $h = 1.62$, $\omega = 1.18$.

the terms α_j can be neglected in equations (4.38b) and (4.38c), which leads to a simple expression for the fixed point

$$\varepsilon_f = \left[\frac{(\alpha_1^{\mathrm{r}}\alpha_2^{\mathrm{r}})^{1/2}}{|\alpha_1^{\mathrm{r}} + \alpha_2^{\mathrm{r}}|} \left| \frac{Rof}{(n_1 n_2)^{1/2}} \right| \left| \frac{\widetilde{\xi}_1 - \widetilde{\xi}_2}{\xi} \right| \right]^{1/2}. \tag{4.40}$$

The definition of the parameters $\widetilde{\xi}_j$ is given in Appendix 4.8.3.

A simple expression for the fixed point A_{0f} can also be obtained

$$A_{0f} = \left[\frac{|(\alpha_1^{\mathrm{r}} + \alpha_2^{\mathrm{r}})|}{(\alpha_1^{\mathrm{r}}\alpha_2^{\mathrm{r}})^{1/2}} \left| \frac{Rof\,(n_1 n_2)^{1/2}}{\xi\left(\widetilde{\xi}_1 - \widetilde{\xi}_2\right)} \right| \right]^{1/2}. \tag{4.41}$$

This fixed point do not depend on the Reynolds number : it is completely determined by the nonlinear terms. From equations (4.40) and (4.41) we observe that ε_f and A_{0f} scale as $\sim Ro^{1/2}$. The transition between the two regimes is shown schematically in figure 4.4 as a dashed line. It is simply found by equating (4.40) and (4.39) and leads again to three different scalings depending on the Reynolds number (see Fig. 4.4).

4.6.5 Fixed point and mean flow

In this section we compare the theoretical fixed point with the experimental results. The exact value of the fixed point $A_{1,\mathrm{f}}$ can be calculated by solving

numerically the polynomial equation (4.90). It is plotted in Fig. 4.13(a) as a function of Ro for $Re = 3664$ (thick line). We observe that the instability is weakly subcritical because the fixed point can exist for Rossby numbers slightly smaller than the linear threshold represented by the first vertical dash-dotted line. However, we were not able to assess the nature of the bifurcation experimentally because it would require to vary the precessing angle with an accuracy of 0.01°.

The second vertical dash-dotted line represents the transition from stationary to intermittent flow, i.e. the destabilization of the fixed point. The dashed line is the value of the unstable fixed point $A_{1,\mathrm{f}}$ and the two dotted branches represent the maximum and minimum values of $|A_1|$ obtained numerically, by integrating the nonlinear system. They show that the bifurcation is supercritical.

Experimental time-averaged values of $|A_1|$ are also shown on this graph as symbols. They are in rough agreement with the value of the fixed point. In the intermittent regime, the error bars indicate the maximum and minimum of the oscillations of $|A_1|$, which are of the same order of the theoretical predictions.

For high Reynolds numbers (i.e. $Re \gg Re_1$) volume viscous effects can be neglected compared to surface viscous effects. Under this assumption (and in the absence of detuning effects), it can be shown that $Re^{1/4}A_{1f}$ only depends on $ReRo$ by rescaling the nonlinear equations. This is why we have plotted this quantity in Fig. 4.13(b) in order to collapse all the experimental results on a single curve. The theoretical value of the fixed point (shown as a line) increases and scales as $Ro^{1/4}$ far from the threshold.

The mean amplitude $< |A_1| >$ found experimentally is also plotted on the same graph and we observe that this mean amplitude is slightly overestimated by the fixed point A_{1f}, especially at low $ReRo$. This may come from the effect of volume viscous terms which are neglected in this theory. However, the scaling for the mean flow is well predicted for high $ReRo$ numbers. This means that the mean flow inside a precessing cylinder can be fairly well predicted even for very high Reynolds number (up to $Re \simeq 40,000$). It is surprising to see that this weakly nonlinear model is still efficient one decade above the threshold of the instability, in a regime where the flow is turbulent.

Figure 4.14(a) compares the fixed point ε_f with the experimental mean amplitude $\langle|\varepsilon|\rangle$ of the forced Kelvin mode. As above, neglecting the volume viscous terms implies that $Re^{1/2}\varepsilon_f$ only depends on $ReRo$, which allow to collapse all the experimental results on a single curve. Below the threshold (first dash–dotted line, $|ReRo| < 7.11$) the flow is stable such that ε_f is equal to the viscously saturated amplitude (4.12), which is plotted as a thick dash–dotted line (extended by a dotted line above the threshold). Above the threshold the flow is unstable such that ε tends to the fixed point ε_f represented by a solid line. This fixed point becomes unstable above the second dash–dotted line ($|ReRo| = 11.2$), meaning that the flow becomes intermittent. The fixed point is then plotted as a dashed line and scales as $\varepsilon_f \sim Ro^{1/2}$ (independently of the Reynolds number).

By comparing the fixed point and the experiments one can observe that even if the experimental values are underestimated at low $ReRo$, the discre-

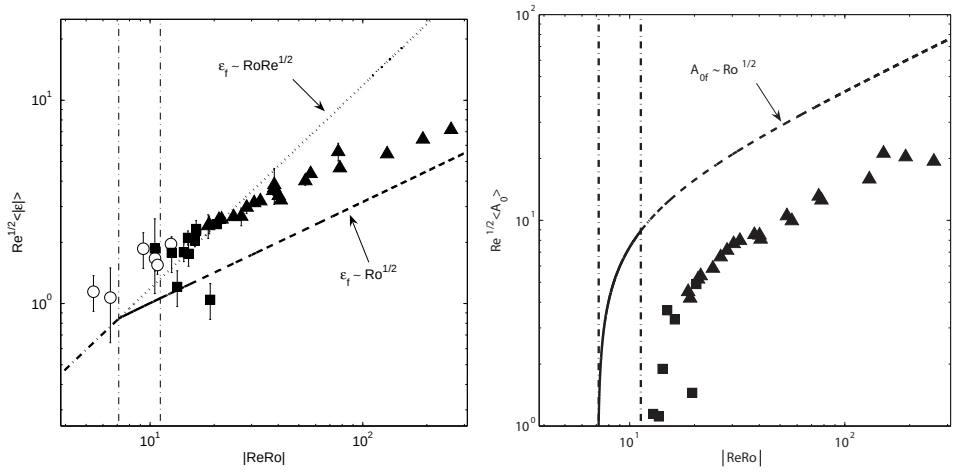

(a) (b)

Figure 4.14: Amplitude of the forced Kelvin mode (a) and the geostrophic Kelvin mode (b) as a function of *RoRe* (volume viscous effects were neglected). The viscous saturating amplitude from equation (4.12) is represented by a dash–dotted line below the threshold (first vertical dash–dotted line) and a dotted line above the threshold. The fixed point (solid or dashed line) is compared to the experimental time averaged values $\langle|\varepsilon|\rangle$ (a) and $\langle A_0\rangle$ (b). These values are represented by circles (○) (stable flow), squares (■) (unstable and stationary flow) or triangles (▲) (unstable and intermittent flow). $h = 1.62$, $\omega = 1.18$.

pancy decreases at high $ReRo$. Moreover, the scaling for the mean flow is fairly well predicted. As explained previously this good agreement is surprising because the flow is turbulent at these high Reynolds numbers.

Finally, Fig. 4.14(b) compares the fixed point A_{0f} with the experimental mean amplitude $\langle A_0\rangle$ of the geostrophic Kelvin mode. Once again, neglecting the volume viscous terms allow to collapse all the results on a single curve $Re^{1/2}A_0$ as a function of $ReRo$. Below the threshold (first dash–dotted line, $|ReRo| < 7.11$) the flow is stable such that $A_{0f} = 0$. Above the threshold the fixed point (solid line) increases and becomes unstable above the second dash–dotted line (dashed line). The fixed point scales as $A_{0f} \sim Ro^{1/2}$ at high Reynolds numbers. Even if the experimental values are strongly overestimated, the scaling for the mean flow is correctly predicted at high $ReRo$.

We have shown in this section that a weakly nonlinear model is able to predict the properties of the instability at the threshold but also the characteristics of the flow at high Reynolds number in a very turbulent regime.

4.7 Conclusion

In this paper the instability of a fluid inside a precessing cylinder has been theoretically studied and compared with experiments.

Precession forces a Kelvin mode which is resonant for particular frequencies and thus is dominant compared to the rest of the flow. A linear stability analysis based on a mechanism of triadic resonance between Kelvin modes

has been carried out and allows to obtain an analytical expression for the instability growth rate and threshold. We have shown that it is damped by volume viscous effects at low Reynolds numbers and by surface viscous effects due to Ekman layers at high Reynolds numbers. We have also shown that when a Kelvin mode combination is not exactly resonant the growth rate of the instability is also damped by detuning effects.

The structure of the unstable Kelvin modes, the growth rate of the instability and the stability diagram are in excellent agreement with experimental results. We deduce from this theory the general properties of the precessing instability for any aspect ratio and precession frequency. Several bands of instabilities with different azimuthal wavenumbers are predicted, which are confirmed experimentally. The instability always occur close to a resonance of a forced Kelvin mode since the amplitude of the base flow is larger than far from a resonance.

A weakly nonlinear analysis has also been carried out by taking into account the interactions between the two free Kelvin modes. The instability is saturated by the presence of a geostrophic mode which lowers the amplitude of the forced Kelvin mode. This weakly nonlinear model allows to predict the nature of the bifurcation and the properties of the unstable saturated flow just above the threshold. This model also predicts correctly the presence of an intermittent flow at higher Reynolds number. Finally, it is surprising to see that this low order model gives correct estimates for the mean velocity inside the cylinder at very high Reynolds numbers even when the flow is turbulent.

The nonlinear model is essentially based on the fact that the nonlinear interaction of a Kelvin mode with itself in the Ekman layers leads to the presence of a geostrophic mode. However, this interaction vanishes in the inviscid case and viscous effects are needed in order to predict the generation of the geostrophic mode. In this paper, this term was adjusted to the experiments by a fitting parameter. A correct analysis of nonlinear and viscous interaction of Kelvin modes would thus be highly useful in order to get analytical expressions for the generation of geostrophic motion.

In the future, it would be interesting to see if this instability mechanism can be observed in an ellipsoid, as predicted theoretically by Kerswell (1993). This could highly improve the comprehension of the flow inside the outer core of the earth and thus shed light on the geodynamo that takes place there.

It would also be interesting to see how these Kelvin modes interact with a magnetic field if the liquid is conductor. Since the structure of the unstable flow is here predicted for any Reynolds number, a theoretical study of the growth of the magnetic field in such a flow is now possible. This could explain the results by Gans (1970*a*) who observed an unstable magnetic field in a precessing cylinder full of liquid sodium.

Finally, the destabilization of a fluid-filled gyroscope by precession has been extensively studied under the assumption that the flow inside the gyroscope is stable and laminar. These results can now be extended to the case of an unstable fluid cylinder owing to the model presented in this paper.

Acknowledgments

We would like to thank Wietze Herreman for very fruitful discussions, especially concerning the weakly nonlinear theory. This study was carried out under CEA-CNRS contract No. 012171.

4.8 Appendix

4.8.1 Base flow calculation

The operators appearing in the complex Navier–Stokes equation (4.5) are defined by

$$\mathcal{I} = \begin{pmatrix} 1 & 0 & 0 & 0 \\ 0 & 1 & 0 & 0 \\ 0 & 0 & 1 & 0 \\ 0 & 0 & 0 & 0 \end{pmatrix}, \tag{4.42}$$

$$\mathcal{D} = \begin{pmatrix} 0 & 0 & -\mathrm{i} & 0 \\ 0 & 0 & 1 & 0 \\ \mathrm{i} & -1 & 0 & 0 \\ 0 & 0 & 0 & 0 \end{pmatrix}, \tag{4.43}$$

$$\mathcal{L} = \begin{pmatrix} \Delta - \frac{1}{r^2} & -\frac{2}{r^2}\frac{\partial}{\partial\varphi} & 0 & 0 \\ \frac{2}{r^2}\frac{\partial}{\partial\varphi} & \Delta - \frac{1}{r^2} & 0 & 0 \\ 0 & 0 & \Delta & 0 \\ 0 & 0 & 0 & 0 \end{pmatrix}, \tag{4.44}$$

where

$$\Delta = \frac{1}{r}\frac{\partial}{\partial r} + \frac{\partial^2}{\partial r^2} + \frac{1}{r^2}\frac{\partial^2}{\partial\varphi^2} + \frac{\partial^2}{\partial z^2}, \tag{4.45}$$

and

$$\mathcal{M} = \begin{pmatrix} 0 & -2 & 0 & \frac{\partial}{\partial r} \\ 2 & 0 & 0 & \frac{1}{r}\frac{\partial}{\partial\varphi} \\ 0 & 0 & 0 & \frac{\partial}{\partial z} \\ \frac{\partial}{\partial r} + \frac{1}{r} & \frac{1}{r}\frac{\partial}{\partial\varphi} & \frac{\partial}{\partial z} & 0 \end{pmatrix}. \tag{4.46}$$

The vectors $\mathbf{F}_0$ and $\mathbf{N}(\mathbf{v}_1, \mathbf{v}_2)$ are defined by

$$\mathbf{F}_0 = \begin{pmatrix} 0 \\ 0 \\ -r\omega \\ 0 \end{pmatrix}, \tag{4.47}$$

and

$$\mathbf{N}(\mathbf{v}_1, \mathbf{v}_2) = \begin{pmatrix} (\mathbf{v}_1 + \overline{\mathbf{v}_1}) \times (\nabla \times \mathbf{v}_2) \\ 0 \end{pmatrix}. \tag{4.48}$$

The linear and inviscid amplitude a_i of the Kelvin modes $\mathbf{v}_{1,\omega_i,k_i}(r)$ inside a precessing cylinder in the non–resonant case is

$$a_i = \frac{\omega^2}{(\omega - 2)\left(k_i^2 + 1\right) k_i J_1(\delta_i) \cos(k_i h/2)}. \tag{4.49}$$

The vector $\mathbf{u}_{m_i,\omega_i,k_i}(r)$ of a Kelvin mode appearing in equation (4.9) is defined by

$$\begin{aligned}\mathbf{u}_{m_i,\omega_i,k_i}(r) &= \begin{pmatrix} U_{m_i,\omega_i,k_i}(r) \\ V_{m_i,\omega_i,k_i}(r) \\ W_{m_i,\omega_i,k_i}(r) \\ P_{m_i,\omega_i,k_i}(r) \end{pmatrix} \\ &= \begin{pmatrix} \frac{-1}{4-\omega_i^2}\left(\omega_i\delta_i J'_{m_i}(\delta_i r) + 2\frac{m_i}{r}J_{m_i}(\delta_i r)\right) \\ \frac{-\mathrm{i}}{4-\omega_i^2}\left(2\delta_i J'_{m_i}(\delta_i r) + \frac{\omega_i m_i}{r}J_{m_i}(\delta_i r)\right) \\ \mathrm{i}\frac{k_i}{\omega_i}J_{m_i}(\delta_i r) \\ -\mathrm{i}J_{m_i}(\delta_i r) \end{pmatrix}. \end{aligned} \tag{4.50}$$

We introduce the scalar product

$$\mathbf{X}\odot\mathbf{Y} = \int_V \left(\overline{X_r}Y_r + \overline{X_\varphi}Y_\varphi + \overline{X_z}Y_z + \overline{X_p}Y_p\right) d^3V, \tag{4.51}$$

The forcing term f appearing in equation (4.12) is defined by

$$f = \frac{1}{\mathrm{i}}\frac{\mathbf{v}_{1,\omega,k}\odot\mathbf{F}_0 e^{\mathrm{i}(\omega t+\varphi)}}{\mathbf{v}_{1,\omega,k}\odot\mathcal{I}\mathbf{v}_{1,\omega,k}}. \tag{4.52}$$

For a resonant Kelvin mode, a simple expression of f is

$$f = \frac{(\omega+2)\,\omega\left(4-\omega^2\right)^2}{\delta^2 h J_1(\delta)\left[\omega^2(\omega+2\delta^2-2)-4\omega+8\right]}. \tag{4.53}$$

4.8.2 Linear stability analysis coefficients

Nonlinear coefficients

The nonlinear coefficients n_1 and n_2 appearing in equation (4.25) are defined by

$$n_1 = \frac{\mathbf{v}_1\odot\left[\mathbf{N}(\mathbf{v}_{1,\omega,k},\mathbf{v}_2)+\mathbf{N}(\mathbf{v}_2,\overline{\mathbf{v}}_{1,\omega,k})\right]}{\mathbf{v}_1\odot\mathcal{I}\mathbf{v}_1}, \tag{4.54a}$$

$$n_2 = \frac{\mathbf{v}_2\odot\left[\mathbf{N}(\mathbf{v}_{1,\omega,k},\mathbf{v}_1)+\mathbf{N}(\mathbf{v}_1,\mathbf{v}_{1,\omega,k})\right]}{\mathbf{v}_2\odot\mathcal{I}\mathbf{v}_2}, \tag{4.54b}$$

where the vectors $\mathbf{v}_{1,\omega,k}$ and $\mathbf{v}_j$ are respectively given by equations (4.9) and (4.19). Note that the definition of n_j does not depend on the choice of the sign plus or minus in equation (4.19).

By using the formula $\nabla\times\mathbf{v}_K = \frac{2}{\mathrm{i}\omega}\frac{\partial}{\partial z}\mathbf{v}_K$ for a Kelvin mode $\mathbf{v}_K$, a development of (4.54a) and (4.54b) can be given as

$$n_1 = -8\pi h\frac{\pm\frac{k_2}{\omega_2}-\frac{k}{\omega}}{\mathbf{v}_1\odot\mathcal{I}\mathbf{v}_1}\int_0^1 \begin{vmatrix} U_{m,\omega,\pm k} & U_{m_1,\omega_1,k_1} & \overline{U}_{m_2,\omega_2,k_2} \\ V_{m,\omega,\pm k} & V_{m_1,\omega_1,k_1} & \overline{V}_{m_2,\omega_2,k_2} \\ W_{m,\omega,\pm k} & W_{m_1,\omega_1,k_1} & \overline{W}_{m_2,\omega_2,k_2} \end{vmatrix} r\,dr, \tag{4.55}$$

and

$$n_2 = 8\pi h \frac{\pm\frac{k_1}{\omega_1} - \frac{k}{\omega}}{\mathbf{v}_2 \odot \mathcal{I}\mathbf{v}_2} \int_0^1 \begin{vmatrix} U_{m,\omega,\pm k} & U_{m_1,\omega_1,k_1} & \overline{U}_{m_2,\omega_2,k_2} \\ V_{m,\omega,\pm k} & V_{m_1,\omega_1,k_1} & \overline{V}_{m_2,\omega_2,k_2} \\ W_{m,\omega,\pm k} & W_{m_1,\omega_1,k_1} & \overline{W}_{m_2,\omega_2,k_2} \end{vmatrix} rdr, \qquad (4.56)$$

where the operator $|.|$ is the determinant.
The plus sign corresponds to the case $k_2 - k_1 = k$.
The minus sign corresponds to the case $k_1 - k_2 = k$.
We recall that equations (4.55) and (4.56) are only valid for free Kelvin modes with different parities with respect to z, i.e. at (or close to) a resonance of the forced Kelvin mode.

Viscous coefficients

The boundary viscous coefficient s_j appearing in equation (4.25) is defined by

$$\frac{s_j}{Re^{1/2}} = \frac{\mathbf{v}_j \odot \left(\frac{\partial}{\partial t}\mathcal{I} + \mathcal{M}\right)\mathbf{v}_j^{(1)}}{\mathbf{v}_j \odot \mathcal{I}\mathbf{v}_j}, \qquad (4.57)$$

where $\mathbf{v}_j^{(1)}$ is the vector appearing in equation (4.24). Integrating by part, we can show that

$$\begin{aligned} \mathbf{v}_j \odot \left(\frac{\partial}{\partial t}\mathcal{I} + \mathcal{M}\right)\mathbf{v}_j^{(1)} &= -\overline{\mathbf{v}_j^{(1)} \odot \left(\frac{\partial}{\partial t}\mathcal{I} + \mathcal{M}\right)\mathbf{v}_j} \\ &+ \int_{\text{surface}} \left(\overline{\mathbf{v}}_j^{\perp} \cdot \mathbf{v}_j^{(1)p} + \overline{\mathbf{v}}_j^{p} \cdot \mathbf{v}_j^{(1)\perp}\right) dS, \qquad (4.58) \end{aligned}$$

where $\perp$ stands for the perpendicular component to the wall and the subscript p stands for the pressure component. The first right-hand side term of this last equation equals 0 because $\mathbf{v}_j$ is in the kernel of the operator $\left(\frac{\partial}{\partial t}\mathcal{I} + \mathcal{M}\right)$. The first term in the surface integral is also equal to 0 because $\mathbf{v}_j^{\perp}$ vanishes at the walls since it is a free Kelvin mode. The second term inside the integral can be calculated because $\mathbf{v}_j^{(1)\perp}$ is given by the no-slip boundary condition at order ε, which means that it is the opposite of the Ekman pumping (of order $Re^{-1/2} \sim \varepsilon$) created by the Kelvin modes $\mathbf{v}_j$ of order one. The determination of the velocity in the boundary layer is classical. The reader could refer to Greenspan (1968) or for the peculiar case of Kelvin modes to Kudlick (1966). The viscous coefficients can thus be calculated as

$$s_j = 2\frac{I_j'^r + I_j'^z}{\mathbf{v}_j \odot \mathcal{I}\mathbf{v}_j}, \qquad (4.59)$$

where

$$I_j'^r = 2\pi h \overline{P}_{m_j,\omega_j,k_j}(1)\left[\frac{-\mathrm{i}}{K_j}\left(m_j V_{m_j,\omega_j,k_j}(1) + k_j W_{m_j,\omega_j,k_j}(1)\right)\right], \qquad (4.60)$$

and

$$I_j'^z = \frac{\sqrt{2}\pi\,(1-\mathrm{i})}{\omega_j^2}\left(\frac{J_{m_j}^2(\delta_j)}{(2-\omega_j)^{3/2}}+\frac{\mathrm{i}J_{m_j}^2(\delta_j)}{(2+\omega_j)^{3/2}}\right)\left[\left(\delta_j^2-m_j^2\right)\omega_j^2+4m_j^2\right], \tag{4.61}$$

with

$$K_j = \left(\frac{|\omega_j|}{2}\right)^{1/2}(1+\mathrm{i}\,\mathrm{sgn}(\omega_j))\,. \tag{4.62}$$

The same boundary viscous effects appear on the forced Kelvin mode $\mathbf{v_{1,\omega,k}}$ and can be calculated in the same manner. If we note $\widetilde{\mathbf{v}}_{1,\omega,k}$ the Ekman pumping created by the Kelvin mode $\mathbf{v}_{1,\omega,k}$, the boundary viscous coefficient s appearing in equation (4.12) is given by

$$\frac{s}{Re^{1/2}} = \frac{\mathbf{v}_{1,\omega,k}\odot\left(\frac{\partial}{\partial t}\mathcal{I}+\mathcal{M}\right)\widetilde{\mathbf{v}}_{1,\omega,k}}{\mathbf{v}_{1,\omega,k}\odot\mathcal{I}\mathbf{v}_{1,\omega,k}} = \frac{2}{Re^{1/2}}\frac{I'^r+I'^z}{\mathbf{v}_{1,\omega,k}\odot\mathcal{I}\mathbf{v}_{1,\omega,k}}, \tag{4.63}$$

where I'^r and I'^z are respectively given by $I_j'^r$ and $I_j'^z$ with $m_j=1$, $\omega_j=\omega$ and $k_j=k$.

The volume viscous coefficient v_j appearing in equation (4.25) is defined by

$$v_j = -\frac{\mathbf{v}_j\odot\mathcal{L}\mathbf{v}_j}{\mathbf{v}_j\odot\mathcal{I}\mathbf{v}_j} = k_j^2+\delta_j^2. \tag{4.64}$$

Detuning coefficients

The detuning coefficient q_j appearing in equation (4.25) is defined by

$$q_j = \frac{\mathbf{v}_j\odot\mathcal{M}_\Delta\mathbf{v}_j}{\mathbf{v}_j\odot\mathcal{I}\mathbf{v}_j}, \tag{4.65}$$

with

$$\mathcal{M}_\Delta = \frac{1}{\mathrm{i}k_j}\begin{pmatrix}0&0&0&0\\0&0&0&0\\0&0&0&\frac{\partial}{\partial z}\\0&0&\frac{\partial}{\partial z}&0\end{pmatrix}. \tag{4.66}$$

The calculation gives

$$q_j = -8\pi h\frac{k_j}{\omega_j}\int_0^1 J_{m_j}^2(\delta_j r)\,r\,dr\Big/\mathbf{v}_j\odot\mathcal{I}\mathbf{v}_j. \tag{4.67}$$

4.8.3 Nonlinear calculation

The aim of this Appendix is to calculate the coefficients σ_j, ξ_j and λ appearing in the weakly nonlinear amplitude equations (4.38).

Coefficients σ_j

The nonlinear interaction of a Kelvin mode $\mathbf{v}_j$ with itself gives rise to a flow $\mathbf{v}_{2_j}$ such that

$$\left(\frac{\partial}{\partial t}\mathcal{I}+\mathcal{M}\right)\mathbf{v}_{2_j}+\text{c.c.}=\mathbf{N}\left(\mathbf{v}_j,\mathbf{v}_j\right)+\text{c.c.} \tag{4.68}$$

As shown by Waleffe (1989), $\mathbf{v}_{2_j}$ has two velocity components because $\mathbf{v}_j$ is the sum of two waves with opposite axial wavenumbers $+k_j$ and $-k_j$. For a Kelvin mode (m_j, ω_j, k_j) these two components are of the form ($2m_j$, $2k_j$, 0) and (0, 0, $2k_j$) and correspond to the two vectors

$$\mathbf{v}_{2k_j}=\pm\begin{pmatrix}0\\ a_{2k_j}\cos\left(2k_jz\right)\\ 0\\ p_{2k_j}\cos\left(2k_jz\right)\end{pmatrix},\mathbf{v}_{2\omega_j}=\pm\begin{pmatrix}\frac{\mathrm{i}m_j}{r}a_{2\omega_j}\\ -\frac{1}{2}\frac{da_{2\omega_j}}{dr}\\ 0\\ p_{2\omega_j}\end{pmatrix}, \tag{4.69}$$

with

$$a_{2k_j}=4\frac{\mathrm{i}k_j}{\omega_j}\left(\mathrm{i}V_{m_j,\omega_j,k_j}W_{m_j,\omega_j,k_j}+\frac{1}{2k_j}\frac{d}{dr}\left(U_{m_j,\omega_j,k_j}V_{m_j,\omega_j,k_j}\right)\right), \tag{4.70}$$

and

$$a_{2\omega_j}=4\frac{\delta_j^2}{\left(\omega_j^2-4\right)^2}\left[J_{m_j}^2\left(\delta_jr\right)-J_{m_j}^2\left(\delta_j\right)r^{2m_j}\right]. \tag{4.71}$$

For a free Kelvin mode with a minus (resp. plus) sign in its definition (4.19) the plus (resp. minus) sign must be chosen in equation (4.69). The coefficient σ_j in (4.38) is separated into two parts. The first one comes from the nonlinear interaction of $\mathbf{v}_j$ and $\mathbf{v}_{2k_j}$

$$\sigma_{2k_j}=\mathbf{v}_j\odot\left[\mathbf{N}\left(\mathbf{v}_{2k_j},\mathbf{v}_j\right)+\mathbf{N}\left(\mathbf{v}_j,\mathbf{v}_{2k_j}+\text{c.c.}\right)\right]. \tag{4.72}$$

The calculation gives

$$\sigma_{2k_j}=8\pi h\int_0^1\left(2\mathrm{i}k_j\,a_{2k_j}V_{m_j,\omega_j,k_j}W_{m_j,\omega_j,k_j}+a_{2k_j}\frac{d\left(U_{m_j,\omega_j,k_j}V_{m_j,\omega_j,k_j}\right)}{dr}\right)rdr, \tag{4.73}$$

with a_{2k_j} given by equation (4.70).

The other term comes from the interaction of $\mathbf{v}_j$ with $\mathbf{v}_{2\omega_j}$

$$\sigma_{2\omega_j}=\mathbf{v}_j\odot\mathbf{N}\left(\mathbf{v}_{2\omega_j}\mathrm{e}^{2\mathrm{i}(\omega_jt+m_j\varphi)},\overline{\mathbf{v}_j}\right). \tag{4.74}$$

The calculation gives

$$\sigma_{2\omega_j}=8\pi h\frac{\mathrm{i}k_j}{\omega_j}\int_0^1\left(\frac{da_{2\omega_j}}{dr}\mathrm{i}U_{m_j,\omega_j,k_j}W_{m_j,\omega_j,k_j}+\frac{2m_j\,a_{2\omega_j}}{r}V_{m_j,\omega_j,k_j}W_{m_j,\omega_j,k_j}\right)rdr. \tag{4.75}$$

The final coefficient σ_j used in the weakly nonlinear amplitude equations (4.38) is

$$\sigma_j = -\frac{\sigma_{2k_j} + \sigma_{2\omega_j}}{\mathrm{i}\,\mathbf{v}_j \odot \mathcal{I}\mathbf{v}_j}. \tag{4.76}$$

Coefficients ξ_j

The coefficients ξ_j of (4.38) describe the nonlinear interaction of the j-th free Kelvin mode with the geostrophic mode

$$\xi_j = \mathrm{i}\mathbf{v}_j \odot \left[\mathbf{N}\left(\frac{1}{2}\mathbf{v}_0, \mathbf{v}_j\right) + \mathbf{N}\left(\mathbf{v}_j, \mathbf{v}_0\right)\right] / \mathbf{v_j} \odot \mathcal{I}\mathbf{v_j}. \tag{4.77}$$

We then obtain

$$\xi_j = 8\mathrm{i}\pi h \frac{\int_0^1 \left(\frac{2k_j}{\omega_j} v_0 U_{m_j,\omega_j,k_j} W_{m_j,\omega_j,k_j} + \frac{1}{r}\frac{d}{dr}\left(r v_0\right) U_{m_j,\omega_j,k_j} V_{m_j,\omega_j,k_j}\right) r dr}{\mathbf{v}_j \odot \mathcal{I}\mathbf{v}_j}, \tag{4.78}$$

where v_0 is the orthoradial component of the geostrophic flow given by (4.36). For the forced Kelvin mode, $\mathbf{v}_j \odot \mathcal{I}\mathbf{v}_j$ is replaced by $\mathbf{v}_{1,\omega,k} \odot \mathcal{I}\mathbf{v}_{1,\omega,k}$ in (4.78) in order to obtain the coefficient ξ.

Coefficient λ

The parameter λ describes the nonlinear interaction between the first and the second free Kelvin mode. This parameter appears in equation (4.38a) and is given by

$$\lambda = \frac{\mathbf{v}_{1,\omega,k} \odot \left[\mathbf{N}\left(\mathbf{v}_1, \mathbf{v}_2\right) + \mathbf{N}\left(\mathbf{v}_2, \overline{\mathbf{v}}_1\right)\right]}{\mathbf{v}_{1,\omega,k} \odot \mathcal{I}\mathbf{v}_{1,\omega,k}}. \tag{4.79}$$

We obtain

$$\lambda = \pm 8\pi h \frac{\frac{k_2}{\omega_2} - \frac{k_1}{\omega_1}}{\mathbf{v}_{1,\omega,k} \odot \mathcal{I}\mathbf{v}_{1,\omega,k}} \int_0^1 \begin{vmatrix} U_{m,\omega,\pm k} & U_{m_1,\omega_1,k_1} & \overline{U}_{m_2,\omega_2,k_2} \\ V_{m,\omega,\pm k} & V_{m_1,\omega_1,k_1} & \overline{V}_{m_2,\omega_2,k_2} \\ W_{m,\omega,\pm k} & W_{m_1,\omega_1,k_1} & \overline{W}_{m_2,\omega_2,k_2} \end{vmatrix} r dr. \tag{4.80}$$

The plus sign corresponds to the case $k_2 - k_1 = k$.
The minus sign corresponds to the case $k_1 - k_2 = k$.

4.8.4 Fixed point

To obtain a fixed point $(\varepsilon_f, A_{1f}, A_{2f}, A_{0f})$ of the nonlinear amplitude equations (4.38), we search a solution $(\varepsilon, A_1, A_2, A_0)$ such that $\frac{\partial \varepsilon}{\partial t} = \frac{\partial A_0}{\partial t} = 0$ and $A_j = A_j^0 \mathrm{e}^{\mathrm{i}\tilde{\omega}t}$ with $\frac{\partial A_j^0}{\partial t} = 0$ and $\tilde{\omega}$ real. Then, the fixed point satisfies the following system

$$\varepsilon\left(\alpha+\mathrm{i}\xi A_0\right)=\mathrm{i}fRo, \tag{4.81a}$$

$$\alpha_1+\mathrm{i}\left(\widetilde{\omega}+\xi_1 A_0+\sigma_1\left|A_1^0\right|^2\right)=\overline{\varepsilon}n_1\frac{A_2^0}{A_1^0}, \tag{4.81b}$$

$$\alpha_2+\mathrm{i}\left(\widetilde{\omega}+\xi_2 A_0+\sigma_2\left|A_2^0\right|^2\right)=\varepsilon n_2\frac{A_1^0}{A_2^0}, \tag{4.81c}$$

$$\frac{h}{2}\left(\chi_1\left|A_1^0\right|^2+\chi_2\left|A_2^0\right|^2\right)=A_0. \tag{4.81d}$$

Here, we have neglected the term $\lambda\overline{A_1}A_2$ because it was very small in our case, but it can be easily added and the system can be solved in the same manner. The product of (4.81b) by (4.81c) is real such that the modulus of (4.81b) over (4.81c) equals the modulus of the real part of (4.81b) over the real part of (4.81c). Thus it comes

$$\left|\frac{A_1^0}{A_2^0}\right|=\left|\frac{n_2\alpha_1^{\mathrm{r}}}{n_1\alpha_2^{\mathrm{r}}}\right|^{1/2}. \tag{4.82}$$

Equation (4.81d) allows to obtain $|A_1^0|$ and $|A_{2f}^0|$ as functions of A_0

$$\left|A_1^0\right|=A_{1f}=\left[\frac{2\left|n_1\alpha_2^{\mathrm{r}}\right|}{h\left(\chi_1\left|n_1\alpha_2^{\mathrm{r}}\right|+\chi_2\left|n_2\alpha_1^{\mathrm{r}}\right|\right)}A_0\right]^{1/2}, \tag{4.83}$$

$$\left|A_2^0\right|=A_{2f}=\left[\frac{2\left|n_2\alpha_1^{\mathrm{r}}\right|}{h\left(\chi_1\left|n_1\alpha_2^{\mathrm{r}}\right|+\chi_2\left|n_2\alpha_1^{\mathrm{r}}\right|\right)}A_0\right]^{1/2}. \tag{4.84}$$

These two equations allow to replace $\sigma_1\left|A_1^0\right|^2$ and $\sigma_2\left|A_2^0\right|^2$ in equations (4.81b) and (4.81c) as a function of A_0. Thus (4.81) rewrites

$$\varepsilon\left(\alpha+\mathrm{i}\xi A_0\right)=\mathrm{i}fRo, \tag{4.85a}$$

$$\alpha_1+\mathrm{i}\left(\widetilde{\omega}+\widetilde{\xi}_1 A_0\right)=\overline{\varepsilon}n_1\frac{A_2^0}{A_1^0}, \tag{4.85b}$$

$$\alpha_2+\mathrm{i}\left(\widetilde{\omega}+\widetilde{\xi}_2 A_0\right)=\varepsilon n_2\frac{A_1^0}{A_2^0}, \tag{4.85c}$$

$$\frac{h}{2}\left(\chi_1\left|A_1^0\right|^2+\chi_2\left|A_2^0\right|^2\right)=A_0, \tag{4.85d}$$

with

$$\widetilde{\xi}_1=\xi_1+\frac{2\sigma_1\left|n_1\alpha_2^{\mathrm{r}}\right|}{h\left(\chi_1\left|n_1\alpha_2^{\mathrm{r}}\right|+\chi_2\left|n_2\alpha_1^{\mathrm{r}}\right|\right)}, \tag{4.86}$$

and

$$\widetilde{\xi}_2=\xi_2+\frac{2\sigma_2\left|n_2\alpha_1^{\mathrm{r}}\right|}{h\left(\chi_1\left|n_1\alpha_2^{\mathrm{r}}\right|+\chi_2\left|n_2\alpha_1^{\mathrm{r}}\right|\right)}. \tag{4.87}$$

The product of equations (4.85b) and (4.85c) gives a complex equation, whose imaginary part gives the nonlinear frequency of the free Kelvin modes

$$\widetilde{\omega}=-\frac{\mathrm{Im}\left\{\left(\alpha_1+\mathrm{i}\widetilde{\xi}_1 A_0\right)\left(\alpha_2+\mathrm{i}\widetilde{\xi}_2 A_0\right)\right\}}{\alpha_1^{\mathrm{r}}+\alpha_2^{\mathrm{r}}}, \tag{4.88}$$

and whose real part thus leads to

$$\begin{aligned} |\varepsilon| &= \varepsilon_f \\ &= \left\{ \frac{\alpha_1^{\mathrm{r}} \alpha_2^{\mathrm{r}}}{n_1 n_2 \left(\alpha_1^{\mathrm{r}} + \alpha_2^{\mathrm{r}}\right)^2} \left\{ \left(\alpha_1^{\mathrm{r}} + \alpha_2^{\mathrm{r}}\right)^2 + \left[\left(\alpha_1^{\mathrm{i}} - \alpha_2^{\mathrm{i}}\right) + \left(\widetilde{\xi_1} - \widetilde{\xi_2}\right) A_0 \right]^2 \right\} \right\}^{1/2}. \end{aligned} \tag{4.89}$$

By equating (4.89) and the modulus of (4.85a) divided by $(\alpha + \mathrm{i}\xi A_0)$ we obtain an equation of order 4 for A_0

$$\begin{aligned} \frac{\alpha_1^{\mathrm{r}} \alpha_2^{\mathrm{r}} \left[\alpha^{\mathrm{r}2} + \left(\xi A_0 + \alpha^{\mathrm{i}}\right)^2 \right]}{\left(\alpha_1^{\mathrm{r}} + \alpha_2^{\mathrm{r}}\right)^2} \left\{ \left(\alpha_1^{\mathrm{r}} + \alpha_2^{\mathrm{r}}\right)^2 + \left[\left(\alpha_1^{\mathrm{i}} - \alpha_2^{\mathrm{i}}\right) + \left(\widetilde{\xi_1} - \widetilde{\xi_2}\right) A_0 \right]^2 \right\} \\ - Ro^2 f^2 n_1 n_2 = 0. \end{aligned} \tag{4.90}$$

This equation has a unique real and positive solution which is A_{0f}, except in the subcritical regime, where it can have two positive roots. Note that if we take into account the term λ in equation (4.38a), the equation for A_0 becomes an equation of order 6 instead of 4. Once A_{0f} is known, ε_f can be determined via equation (4.89) and A_{1f} and A_{2f} by equations (4.83) and (4.84).

5. INSTABILITÉ DU DEUXIÈME MODE DE KELVIN

Dans le chapitre 4 nous avons étudié la stabilité de l'écoulement de base lorsque celui-ci correspond au premier mode de Kelvin excité à une fréquence proche de sa première résonance. Dans ce chapitre nous considérons cette fois-ci que l'écoulement de base est le deuxième mode de Kelvin, excité à sa première résonance. Les prédictions de l'analyse linéaire de stabilité du chapitre 4 pour le deuxième mode de Kelvin sont comparées avec les résultats expérimentaux.

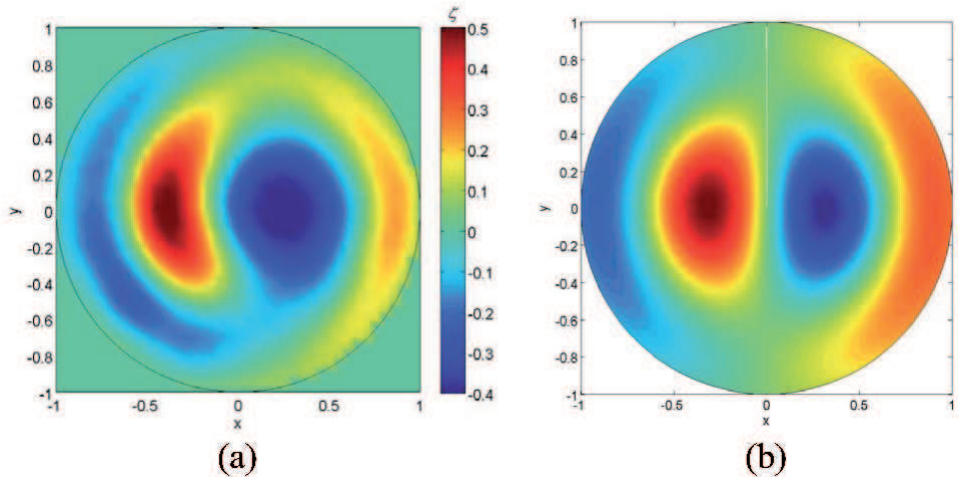

Figure 5.1: Champ de vorticité adimensionnée ζ du deuxième mode de Kelvin excité à sa première résonance avant l'apparition de l'instabilité ; (a) expérience, (b) théorie. Pour (a) la nappe laser est positionnée à une altitude $z = h/4$. $h = 1.62$, $\omega = 0.628$, $Re \approx 4500$, $Ro \approx 0.019$.

h	$\omega_{2,1}$	f	s
1.62	0.628	-0.040	$1.842 - 0.047\mathrm{i}$

Table 5.1: Valeurs numériques des coefficients apparaissant dans l'équation (4.12) permettant de calculer la saturation en amplitude du deuxième mode de Kelvin forcé à sa première résonance. $h = 1.62$, $\omega = 0.628$.

5.1 Écoulement de base

Pour $h = 1.62$ la première résonance du deuxième mode de Kelvin est obtenue pour $\omega = 0.628$. Des mesures PIV avec une nappe laser placée au trois quart de la hauteur du cylindre ont révélé la structure du deuxième mode de Kelvin puisque ce mode a une vorticité (resp. vitesse) axiale qui varie comme le sinus (resp. cosinus) de l'altitude z. La figure 5.1(a) montre que ce mode est caractérisé par quatre tourbillons deux à deux contra-rotatifs, comme nous l'avons déjà vu dans le chapitre 2. La structure de ce mode est bien prédite par la théorie linéaire (section 2.3.1) comme nous pouvons le voir en comparant les figures 5.1(a) et 5.1(b). La légère dissymétrie observée sur le champ expérimental est liée à la présence du mode géostrophique créé par le couplage non-linéaire dans les couches limites du deuxième mode de Kelvin avec lui même.

L'amplitude du deuxième mode de Kelvin forcé à sa première résonance est prédite par la théorie visqueuse présentée dans la section 2.4 (équation (4.12)). Les valeurs numériques des paramètres f et s représentant respectivement le forçage par précession (expression analytique donnée par (4.53)) et les effets visqueux de surface (expression donnée par (4.63)) saturant l'amplitude du deuxième mode de Kelvin sont donnés dans la Table 5.1.

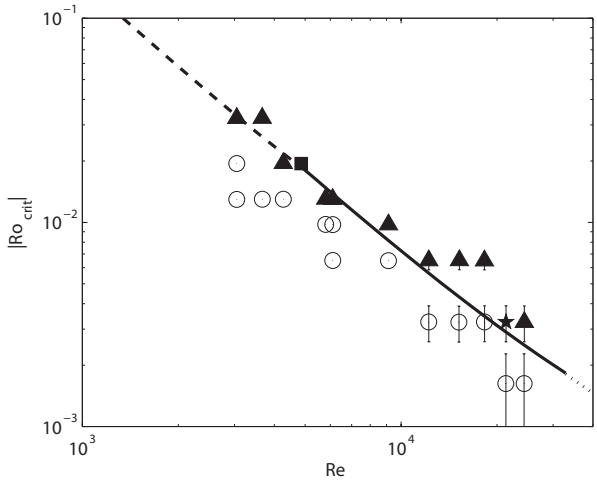

Figure 5.2: Diagramme de stabilité du deuxième mode de Kelvin excité à sa première résonance. Expériences stables (○). Expériences instables (▲). Expérience instable avec visualisation d'un mode ayant un nombre d'onde azimutal $m = 2$ (■), $m = 7$ (⋆). La courbe représente la théorie issue de l'analyse linéaire de stabilité présentée au chapitre 4. Les combinaisons de modes de Kelvin $(7, 2, 3)$ (trait discontinu), $(8, 2, 3)$ (trait continu) et $(9, 2, 3)$ (trait en pointillés) sont prédites comme étant les plus instables. $h = 1.62$, $\omega = 0.628$.

5.2 Diagramme de stabilité

Afin d'établir facilement un diagramme de stabilité nous avons réalisé des expériences avec des particules de Kalliroscope éclairées par une source de lumière. En faisant varier le nombre de Reynolds (entre 3000 et 25000) et le nombre de Rossby (entre 0.0015 i.e. $\theta = 0.25^\circ$ et 0.03 i.e. $\theta = 5^\circ$) nous avons visualisé la dynamique de l'écoulement et déterminé le seuil d'instabilité. Le diagramme de stabilité pour le deuxième mode de Kelvin excité à sa première résonance est représenté sur la figure 5.2. Il fait apparaître une transition nette entre écoulement stable et écoulement instable.

Afin de prédire cette transition nous avons appliqué la théorie issue de l'analyse linéaire de stabilité que nous avons présenté au chapitre 4 en supposant cette fois-ci que le mode de base $\mathbf{v}_{1,\omega,k}$ est le deuxième mode de Kelvin. Nous rappelons que l'analyse linéaire de stabilité est basée sur un mécanisme de résonance triadique entre l'écoulement de base et deux modes de Kelvin libres. Ces modes de Kelvin libres sont caractérisés par leur nombre d'onde azimutal m_j, leur fréquence ω_j, leur nombre d'onde axial k_j et vérifient la relation de dispersion (4.11). Pour trouver les modes de Kelvin libres $\mathbf{v}_1$ et $\mathbf{v}_2$ vérifiant la condition de résonance $m_2 - m_1 = 1$, $\omega_2 - \omega_1 = \omega$ et $|k_2 - k_1| = k$ il suffit de tracer sur le même graphique la relation de dispersion du second mode $\mathbf{v}_2$ et la relation de dispersion du premier mode $\mathbf{v}_1$ translatée de k suivant l'axe des abscisses et translatée de ω suivant l'axe des ordonnées. La figure 5.3 représente les relations de dispersion des modes libres $m_1 = 7$ et $m_2 = 8$ dans le cas $k_2 - k_1 = k$. En ne considérant que les cinq premières branches de chaque relation de dispersion il existe alors

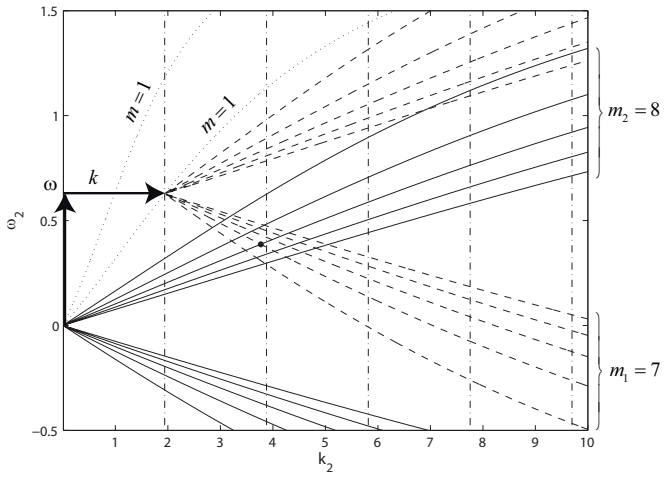

Figure 5.3: Relations de dispersion des modes de Kelvin $m_1 = 7$ (courbes en trait discontinu) et $m_2 = 8$ (courbes en trait continu). Les courbes en pointillés représentent les deux premières branches de la relation de dispersion $m = 1$. La relation de dispersion $m_1 = 7$ a été translatée horizontalement de $k = \pi/h$ et verticalement de $\omega = 0.628$. Les modes de Kelvin résonnants correspondent aux points d'intersection des relations de dispersion $m_1 = 7$ et $m_2 = 8$. La combinaison $(8, 2, 3)$ est représentée par un point. Les courbes verticales correspondent à $k_2 = n\pi/h$ avec n un entier non nul.

25 points d'intersection définissant une combinaison résonnante de modes de Kelvin libres. Nous rappelons qu'une combinaison est notée sous la forme d'un triplet (m_2, l_1, l_2) ; l_j étant le numéro de la branche de la relation de dispersion des modes m_j. En faisant varier m_2 de 1 à 15 et en considérant le cas $k_1 - k_2 = k$ le taux de croissance associé à 750 combinaisons résonnantes a été calculé en utilisant l'équation (4.27). Ce calcul assez couteux en temps (1 jour) prévoit alors que les combinaisons (7, 2, 3), (8, 2, 3) et (9, 2, 3) sont les plus instables lorsque le deuxième mode de Kelvin est forcé à sa première résonance. Ce résulat est surprenant puisque c'est la première fois que des combinaisons n'ayant pas les mêmes numéros de branches l_1 et l_2 sont prédites comme étant les plus instables. La combinaison (8, 2, 3) est représentée sur la figure 5.3. Elle correspond au point d'intersection entre la deuxième branche de la relation de dispersion $m_1 = 7$ et la troisième branche de la relation de dispersion $m_2 = 8$. Ce point d'intersection ne passant pas par une droite verticale sur la figure 5.3 la combinaison (8, 2, 3) n'est pas exactement résonnante (i.e. les modes de Kelvin libres ne vérifient pas les conditions limites en haut et en bas du cylindre) et l'instablité est saturée par des effets de detuning notés $q_j \Delta k_j$, q_j étant donné par la formule (4.65) et Δk_j représentant la distance entre le point d'intersection et la droite verticale la plus proche. De même, les combinaisons (7, 2, 3) et (8, 2, 3) ne sont pas exactement résonantes.

A partir de l'équation (4.30) donnant le nombre de Rossby critique en fonction du nombre de Reynolds pour les combinaisons (7, 2, 3), (8, 2, 3) et (9, 2, 3) nous avons tracé sur la figure 5.2 le seuil d'instabilité théorique. Comme nous pouvons le voir sur cette figure ce seuil d'instabilité est en très

(m_2, l_1, l_2)	$(7, 2, 3)$	$(8, 2, 3)$	$(9, 2, 3)$
$n_1 n_2$	8.90	9.12	9.09
s_1	$1.542 - 0.120\mathrm{i}$	$1.549 - 0.119\mathrm{i}$	$1.555 - 0.118\mathrm{i}$
s_2	$1.692 + 0.071\mathrm{i}$	$1.687 + 0.074\mathrm{i}$	$1.679 + 0.076\mathrm{i}$
v_1	194.6	230.6	269.2
v_2	330.1	379.5	431.5
$q_1 \Delta k_1$	0.042	0.014	-0.010
$q_2 \Delta k_2$	-0.033	-0.011	0.008

Table 5.2: Valeurs numériques des coefficients permettant de calculer le nombre de Rossby critique (via l'équation (4.30)) pour les combinaisons (7, 2, 3), (8, 2, 3) et (9, 2, 3) lorsque le deuxième mode de Kelvin est excité à sa première résonance. $h = 1.62$, $\omega = 0.628$.

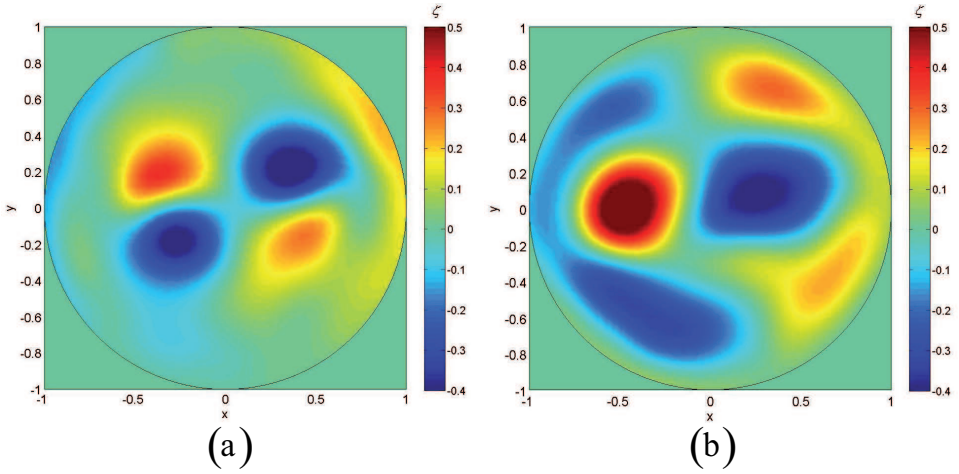

Figure 5.4: Champ de vorticité adimensionnée de l'écoulement instable, en $z = 0$ (a) et en $z = h/4$ (b). $h = 1.62$, $\omega = 0.628$, $Re \approx 4500$, $Ro \approx 0.019$.

bon accord avec les expériences. Les valeurs numériques des coefficients $n_1 n_2$ (coefficient représentant l'intéraction non-linéaire entre les modes de Kelvin), s_j (effets visqueux surfaciques), v_j (effets visqueux volumiques), $q_j \Delta k_j$ (effets de detuning) permettant de caluler le nombre de Rossby critique sont donnés dans la Table 5.2.

5.3 Structure des modes instables

Nous avons voulu vérifier la structure de l'instabilité en réalisant des mesures PIV. La figure 5.4(a) montre que pour $Re \approx 4500$ et $Ro \approx 0.019$ l'écoulement est instable et un mode de Kelvin avec un nombre d'onde azimutal $m_1 = 2$ est observé quand on place la nappe laser à mi-hauteur du cylindre. En déplaçant cette nappe au trois quart de la hauteur du cylindre un mode de Kelvin $m_2 = 3$ semble être observé (voir figure 5.4(b)). Nous

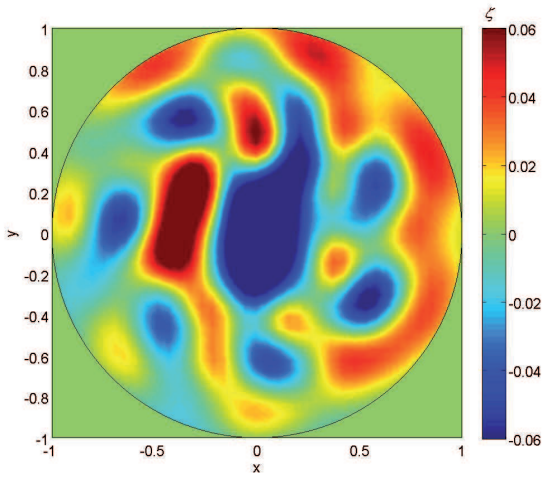

Figure 5.5: Champ de vorticité adimensionnée de l'écoulement instable, en $z = 0$. $h = 1.62$, $\omega = 0.628$, $Re \approx 22400$, $Ro \approx 0.0032$.

pensons que la position légèrement dissymétrique des lobes de vorticité de ce mode est due au fait que sur la figure 5.4(b) la vorticité du mode de base (figure 5.1) n'a pas été soustraite. Ces deux modes de Kelvin ne sont pas prédits par la théorie : on devrait voir des modes $m_1 = 7$ et $m_2 = 8$.

Une des hypothèses que nous avons avancé pour expliquer ce désaccord est que les modes $m_1 = 2$ et $m_2 = 3$ sont issus de la déstabilisation des modes libres de l'instabilité primaire ($m_1 = 7$ et $m_2 = 8$). Nous avons alors réalisé des expériences de PIV en régime transitoire afin de visualiser la première bifurcation vers l'instabilité. Les résultats de ces expériences n'ont pas validé notre hypothèse puisque les modes $m_1 = 2$ et $m_2 = 3$ sont apparus en premier dans le régime transitoire. L'explication de la présence de ces modes reste donc un problème ouvert.

En augmentant le nombre de Reynolds nous avons également observé un mode dont le nombre d'onde azimutal semble être $m = 7$. Ce mode est représenté sur la figure 5.5. Nous pensons que les deux vortex contra-rotatifs observés au centre du cylindre sont dûs à la présence de deux bulles dans le fluide au moment de l'expérience. Le mode $m = 7$ ayant été observé à mi-hauteur du cylindre sa vorticité axiale varie comme le cosinus de l'altitude z. La combinaison (8, 2, 3) prédite théoriquement comme étant la plus instable pour $Re \approx 22400$ est composée d'un mode de Kelvin $m_1 = 7$ dont la vorticité axiale varie comme le sinus de l'altitude. Pour expliquer ce désaccord nous avons pensé que le mode $m = 7$ était visualisé expérimentalement car la nappe laser n'était pas positionnée exactement à mi-hauteur du cylindre. Ceci aurait pû expliquer la faible échelle de grandeur de la vorticité du mode $m = 7$ montrée sur la figure 5.5. Néanmoins cette hypothèse semble peu problable puisque dans ces conditions le mode $m_2 = 8$ devrait également être visible sur la figure 5.5. Nous pensons toutefois qu'il serait nécessaire d'effectuer de nouvelles mesures en positionnant le plus précisément possible la nappe laser en $z = 0$. De même afin de savoir si nous avons affaire à une

combinaison composée de modes $m_1 = 6$ et $m_2 = 7$ ou $m_1 = 7$ et $m_2 = 8$ il serait nécessaire d'effectuer des mesures PIV avec une nappe laser positionnée au trois quart de la hauteur du cylindre.

Finalement l'étude de la stabilité du deuxième mode de Kelvin excité à sa première résonance a montré que le seuil d'instabilité est très bien prédit par la théorie. Néanmoins, les expériences que nous avons réalisé n'ont pas permis de valider la prédiction de la structure des modes instables. De nouvelles expériences devront être réalisées afin de confirmer nos premières observations.

6. ÉTUDE DE LA DÉSTABILISATION PAR LE CISAILLEMENT VERTICAL

Dans ce chapitre nous revenons sur l'étude menée par Mahalov (1993). Son analyse théorique a montré que le cisaillement suivant l'axe du cylindre, forcé par la précession, peut résonner avec deux modes de Kelvin libres (de nombres d'onde azimutaux $m_1 = 0$ et $m_2 = 1$) dans le cas hypothétique d'un cylindre infini. Dans ce chapitre nous allons regarder si un tel mécanisme de résonance triadique reste possible pour un cylindre de taille finie et nous comparerons les prédictions avec les résultats expérimentaux.

6.1 Étude théorique

Dans cette section nous effectuons une analyse linéaire de stabilité de l'écoulement de cisaillement, qui est d'ordre $O(Ro)$. Nous nous plaçons loin des résonances des modes de Kelvin, leur amplitude est donc du même ordre que l'écoulement de cisaillement et vaut $\varepsilon_i = Ro\, a_i$, avec a_i donné en Appendice 4.8.1. Le but est de regarder si un mécanisme de résonance triadique entre l'écoulement de cisaillement et deux modes de Kelvin libres peut conduire à une instabilité dans le cas d'un cylindre de taille finie. Cette analyse suit le même principe que celle que nous avons détaillée dans la section 4.4 pour l'étude de la stabilité d'un mode de Kelvin résonnant. Nous décrivons ici les grandes lignes de cette analyse.

Pour commencer nous rappelons que la solution particulière du système linéaire (2.9-2.10) est

$$\mathbf{v}_{\text{part.}} = \left(0,\, 0,\, Ro\,\mathrm{i}\,r\,\mathrm{e}^{\mathrm{i}(\omega t+\varphi)},\, 0\right). \tag{6.1}$$

Cette solution représente un cisaillement selon l'axe de révolution du cylindre. Nous pouvons la représenter comme une onde dont le nombre d'onde axial est $k_{\text{part.}} = 0$. Nous supposons que cette solution représente l'écoulement de base d'un fluide dans un cylindre en précession.

Nous considérons une perturbation linéaire $\widetilde{\mathbf{v}}$ de la solution de cisaillement. Dans ce cas l'écoulement total $\mathbf{v}$ à l'intérieur du cylindre est

$$\mathbf{v} = \mathbf{v}_{\text{part.}} + \widetilde{\mathbf{v}} + \text{a.t.}, \tag{6.2}$$

où a.t. signifie 'autres termes' et inclut les modes de Kelvin.

L'équation que sastifait $\widetilde{\mathbf{v}}$ est obtenue en injectant la décomposition (6.2) dans l'équation de Navier–Stokes (4.5). Nous obtenons

$$\begin{aligned}\left(\frac{\partial}{\partial t}\mathcal{I}+\mathcal{M}\right)\widetilde{\mathbf{v}}+\text{c.c.} \;&=\; \left(Ro\,\mathcal{D}\mathrm{e}^{\mathrm{i}(\omega t+\varphi)}+\text{c.c.}\right)\widetilde{\mathbf{v}}+\mathbf{N}\left(\widetilde{\mathbf{v}},\mathbf{v}_{\text{part.}}\right)\\ &+\; \mathbf{N}\left(\mathbf{v}_{\text{part.}},\widetilde{\mathbf{v}}\right)+\frac{\mathcal{L}\widetilde{\mathbf{v}}}{Re}+\text{a.t.}+\text{c.c.},\end{aligned} \tag{6.3}$$

avec $\mathcal{I}$, $\mathcal{M}$, $\mathcal{D}$ et $\mathbf{N}$ des opérateurs donnés en Appendice 4.8.1. Le terme de gauche de l'équation (6.3) est le terme d'instationnarité de l'équation de Navier–Stokes. Le premier terme de droite correspond au terme de Coriolis issu du produit vectoriel $2\delta \times \mathbf{v}$, δ est défini par l'équation (2.2.1) et représente la partie instationnaire du vecteur rotation $\mathbf{\Omega}$ du fluide. Ce terme est $O(Ro\widetilde{\mathbf{v}})$. Les deuxièmes et troisièmes termes de droite dans l'équation (6.3) représentent l'intéraction non-linéaire du cisaillement avec la perturbation. Ces termes sont $O(Ro\widetilde{\mathbf{v}})$. Le dernier terme est le terme visqueux de l'équation de Navier–Stokes et est d'ordre $O(Re^{-1}\widetilde{\mathbf{v}})$. Ici la notation a.t. inclut tous les termes d'ordre négligeable devant $O(Ro\widetilde{\mathbf{v}})$ ainsi que les termes d'ordre $O(Ro\widetilde{\mathbf{v}})$ faisant intervenir les modes de Kelvin.

Enfin nous supposons que l'écoulement satisfait une condition limite de type non visqueuse

$$\widetilde{\mathbf{v}} = \mathbf{0} \quad \text{sur les parois } (r = 1 \text{ et } z = \pm h/2). \tag{6.4}$$

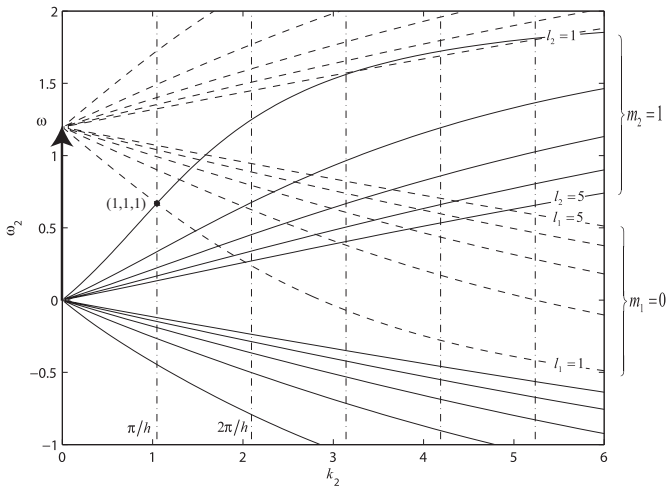

Figure 6.1: Relations de dispersion des modes de kelvin $m_1 = 0$ (branches en trait discontinu) et $m_2 = 1$ (branches en trait continu). La relation de dispersion $m_1 = 0$ a été translatée verticalement de $\omega = 1.20$. Les droites verticales en pointillés correspondent à $k_2 = n\pi/h$, avec n un entier non nul. La combinaison de modes de Kelvin $(1, 1, 1)$ est exactement résonnante pour $h = 3$.

L'équation (6.3) et la condition limite (6.4) décrivent l'évolution de la perturbation linéaire $\widetilde{\mathbf{v}}$.

Le petit paramètre de l'équation (6.3) est le nombre de Rossby ; nous décomposons donc $\widetilde{\mathbf{v}}$ en une série linéaire de puissances de Ro

$$\widetilde{\mathbf{v}} = \mathbf{v}^{(0)} + Ro\mathbf{v}^{(1)} + O\left(Ro^2\right). \tag{6.5}$$

En insérant cette décomposition dans l'équation (6.3) nous obtenons les problèmes d'ordre 0 et 1 en Ro. A l'ordre 0 nous retrouvons l'équation (4.17) qui définit les modes de Kelvin libres $\mathbf{v}_j$

$$\mathbf{v}_j = \mathbf{u}_{m_j,\omega_j,k_j}(r)\,\mathrm{e}^{\mathrm{i}(\omega_j t + m_j\varphi + k_j z)} \pm \mathbf{u}_{m_j,\omega_j,-k_j}(r)\,\mathrm{e}^{\mathrm{i}(\omega_j t + m_j\varphi - k_j z)}, \tag{6.6}$$

avec ω_j la fréquence, m_j le nombre d'onde azimutal et k_j le nombre d'onde axial du mode numéro j. Le vecteur $\mathbf{u}_{m_j,\omega_j,k_j}$ est donné en Appendice 4.8.1. Nous rappelons que le choix du signe $\pm$ dans l'équation (6.6) permet de fixer la parité du mode par rapport à z. Si le signe plus (resp. moins) est choisi la vorticité axiale du mode est alors un cosinus (resp. sinus) de l'altitude z.

En supposant que $\mathbf{v}^{(0)}$ est une combinaison linéaire de deux modes de Kelvin d'amplitudes A_1 et A_2

$$\mathbf{v}^{(0)} = A_1\mathbf{v}_1 + A_2\mathbf{v}_2, \tag{6.7}$$

la condition de résonance de ces modes avec l'écoulement de cisaillement s'écrit

$$m_2 - m_1 = 1, \tag{6.8a}$$
$$\omega_2 - \omega_1 = \omega, \tag{6.8b}$$
$$k_2 - k_1 = k_{\text{part.}} = 0. \tag{6.8c}$$

Cette condition est représentée sur la figure 6.1 pour des modes $m_1 = 0$ et $m_2 = 1$ et correspond aux points d'intersection des branches des relations de dispersion. Notez que par rapport aux chapitres 4 et 5 la relation de dispersion des modes $m_1 = 0$ n'est pas translatée horizontalement puisque l'écoulement de base (i.e. le cisaillement) a un nombre d'onde axial nul : $k_{\text{part.}} = 0$. Il en découle que $k_1 = k_2$; ce qui signifie que les deux modes de Kelvin libres doivent avoir le même nombre d'onde axial pour pouvoir résonner. La vitesse axiale des modes de Kelvin libres est une fonction cosinus ou sinus de l'altitude z et doit s'annuler en haut et en bas du cylindre afin de satisfaire la condition limite (6.4). Ainsi, des modes de Kelvin libres tels que $k_1 = k_2$ ont des vitesses de même parité par rapport à z. Les modes de Kelvin doivent donc être choisis avec le même signe dans leur définition (6.6). Dans la suite nous choisirons des modes de Kelvin libres résonnants definis avec un signe moins dans l'équation (6.6). Leur parité par rapport à z est alors

$$\mathbf{v}_j \sim \begin{pmatrix} \sin(k_1 z) \\ \sin(k_1 z) \\ \cos(k_1 z) \\ \sin(k_1 z) \end{pmatrix}. \tag{6.9}$$

Les produits scalaires de $\mathbf{v}_1$ et $\mathbf{v}_2$ avec le problème d'ordre 1 en Ro permettent d'obtenir les équations d'amplitude pour les modes de Kelvin libres

$$\frac{\partial A_1}{\partial t} = Ro\, n_{1\text{part.}} A_2 - \frac{1}{Re^{1/2}} s_1 A_1 - \frac{1}{Re} v_1 A_1 - \mathrm{i} q_1 \Delta k_1 A_1, \tag{6.10a}$$

$$\frac{\partial A_2}{\partial t} = Ro\, n_{2\text{part.}} A_1 - \frac{1}{Re^{1/2}} s_2 A_2 - \frac{1}{Re} v_2 A_2 - \mathrm{i} q_2 \Delta k_2 A_2. \tag{6.10b}$$

Les termes $\frac{\partial A_j}{\partial t}$ viennent du produit scalaire de $\mathbf{v}_j$ avec le terme instationnaire de l'équation d'ordre 1 en Ro.

Les coefficients $n_{1\text{part.}}$ et $n_{2\text{part.}}$ sont réels et représentent l'intéraction nonlinéaire entre le cisaillement et les modes de Kelvin libres résonnants. Ces coefficients sont analogues aux coefficients n_1 et n_2 du chapitre 4.

Les coefficients s_1 et s_2 représentent l'atténuation des deux modes de Kelvin libres par les effets visqueux de surface dûs aux couches d'Ekman. Ces coefficients sont des nombres complexes avec une partie réelle positive et sont calculés analytiquement (voir Appendice 4.8.2).

Les coefficients v_1 et v_2 sont réels et représentent l'atténuation des modes de Kelvin libres par effets visqueux de volume. Ils peuvent également être calculés analytiquement et sont donnés en Appendice 4.8.2.

Les coefficients q_1 et q_2 (calculés analytiquement dans l'Appendice 4.8.2) sont réels et représentent l'atténuation des modes de Kelvin par les effets de detuning. Nous rappelons que Δk_j représente la distance entre un point d'intersection et la droite verticale la plus proche sur la figure 6.1. Par exemple, pour le point $(m_2, l_1, l_2) = (1, 1, 1)$; l_j étant le numéro d'une branche de la relation de dispersion des modes m_j ; nous avons $\Delta k_j = 0$. On dit que la combinaison $(1, 1, 1)$ est excactement résonnante.

Les coefficients $n_{1\text{part.}}$ et $n_{2\text{part.}}$ sont définis par

$$n_{1\text{part.}} = \frac{\mathbf{v}_1 \odot \left[\overline{\mathcal{D}}\mathrm{e}^{-\mathrm{i}(\omega t+\varphi)}\mathbf{v}_2 + \mathbf{N}\left(\mathbf{v}_{\text{part.}}, \mathbf{v}_2\right) + \mathbf{N}\left(\mathbf{v}_2, \overline{\mathbf{v}}_{\text{part.}}\right)\right]}{\mathbf{v}_1 \odot \mathcal{I}\mathbf{v}_1}, \tag{6.11a}$$

$$n_{2\text{part.}} = \frac{\mathbf{v}_2 \odot \left[\mathcal{D}\mathrm{e}^{\mathrm{i}(\omega t+\varphi)}\mathbf{v}_1 + \mathbf{N}\left(\mathbf{v}_{\text{part.}}, \mathbf{v}_1\right) + \mathbf{N}\left(\mathbf{v}_1, \mathbf{v}_{\text{part.}}\right)\right]}{\mathbf{v}_2 \odot \mathcal{I}\mathbf{v}_2}. \tag{6.11b}$$

Nous pouvons vérifier que

$$\overline{\mathcal{D}}\mathrm{e}^{-\mathrm{i}(\omega t+\varphi)}\mathbf{v}_2 \sim \mathcal{D}\mathrm{e}^{\mathrm{i}(\omega t+\varphi)}\mathbf{v}_1 \sim \begin{pmatrix} \cos(k_1 z) \\ \cos(k_1 z) \\ \sin(k_1 z) \\ \cos(k_1 z) \end{pmatrix}. \tag{6.12}$$

De même en utilisant la relation $\nabla \times \mathbf{v}_j = \frac{2}{\mathrm{i}\omega_j}\frac{\partial}{\partial z}\mathbf{v}_j$ nous montrons que

$$\begin{aligned} \left[\mathbf{N}\left(\mathbf{v}_{\text{part.}}, \mathbf{v}_2\right) + \mathbf{N}\left(\mathbf{v}_2, \overline{\mathbf{v}}_{\text{part.}}\right)\right] &\sim \left[\mathbf{N}\left(\mathbf{v}_{\text{part.}}, \mathbf{v}_1\right) + \mathbf{N}\left(\mathbf{v}_1, \mathbf{v}_{\text{part.}}\right)\right] \\ &\sim \frac{\partial \mathbf{v}_j}{\partial z} \sim \begin{pmatrix} \cos(k_1 z) \\ \cos(k_1 z) \\ \sin(k_1 z) \\ \cos(k_1 z) \end{pmatrix}. \end{aligned} \tag{6.13}$$

Nous observons donc que les termes des équations (6.12) et (6.13) ont une parité différente de celle des modes de Kelvin $\mathbf{v}_j$. Les modes de Kelvin libres doivent vérifier des conditions limites en haut et en bas du cylindre, leur nombre d'onde axial k_1 est donc un multiple de π/h. Dans ce cas nous obtenons

$$n_{1\text{part.}} = n_{2\text{part.}} \sim \int_{-h/2}^{h/2} \sin(k_1 z)\cos(k_1 z)\, dz = 0. \tag{6.14}$$

Cela signifie qu'un mécanisme de résonance triadique entre le cisaillement vertical et deux modes de Kelvin libres ne peut pas conduire à une instabilité dans le cas d'un cylindre fini.

Dans le cas d'un cylindre infini la définition des modes de Kelvin diffère de l'équation (6.6) et devient

$$\mathbf{v}_j = \mathbf{u}_{m_j,\omega_j,k_j}(r)\,\mathrm{e}^{\mathrm{i}(\omega_j t + m_j\varphi \pm k_j z)}. \tag{6.15}$$

Un mode de Kelvin est alors une onde progressive et la question de la parité de cette onde vis-à-vis de z ne se pose plus puisque cette onde n'a pas à

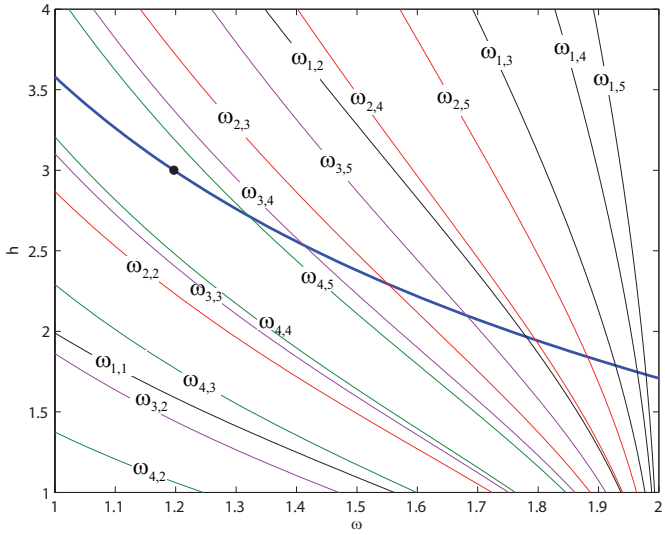

Figure 6.2: Détermination du rapport de fréquence et du rapport d'aspect permettants de se trouver loin des résonances du 1^{er} (courbes noires), 2^{e} (courbes rouges), 3^{e} (courbes violettes), 4^{e} (courbes vertes) modes de Kelvin et permettant d'avoir une résonance exacte entre l'écoulement de cisaillement et les modes de Kelvin libres $m_1 = 0$ et $m_2 = 1$ (courbe bleue). La notation $\omega_{i,n}$ signifie résonance numéro n du mode de Kelvin numéro i. Le point noir représente le choix de l'expérience : $\omega = 1.20$, $h = 3$.

vérifier des conditions limites en haut et en bas du cylindre. Il en découle alors que les coefficients $n_{1\text{part.}}$ et $n_{2\text{part.}}$ ne sont pas nuls et sont donnés par l'équation (6.11) avec $\mathbf{v}_j$ défini par (6.15). Une expression analytique du taux de croissance non visqueux $\sigma = (n_{1\text{part.}} n_{2\text{part.}})^{1/2}$ est donnée par Mahalov (1993). Ce dernier démontre alors que la combinaison (1, 1, 1) (représentée sur la figure 6.1) a le taux de croissance maximum et donc est la plus instable.

6.2 Étude expérimentale et discussion

Nous venons de prouver théoriquement qu'une instabilité par résonance triadique entre le cisaillement vertical et deux modes de Kelvin libres n'est pas possible dans un cylindre de taille finie. Afin d'observer la dynamique de l'écoulement de précession lorsque le cisaillement vertical est du même ordre que les modes de Kelvin, nous avons mené une campagne de mesures expérimentales. Nous avons choisi un rapport d'aspect h et un rapport de fréquence ω permettant de rester loin des résonances des modes de Kelvin et permettant que la combinaison (1, 1, 1) soit exactement résonnante. Ces deux conditions sont représentées sur la figure 6.2. Sur cette figure les cinq premières résonances des quatres premiers modes de Kelvin sont représentées et notées $\omega_{i,n}$ (résonance numéro n du mode numéro i). Ces courbes sont obtenues en cherchant les solutions de l'équation

$$D\left(m_i,\, \omega_{i,n},\, \frac{\left(4-{\omega_{i,n}}^2\right)^{1/2}}{|\omega_{i,n}|} k_n\right) = 0, \tag{6.16}$$

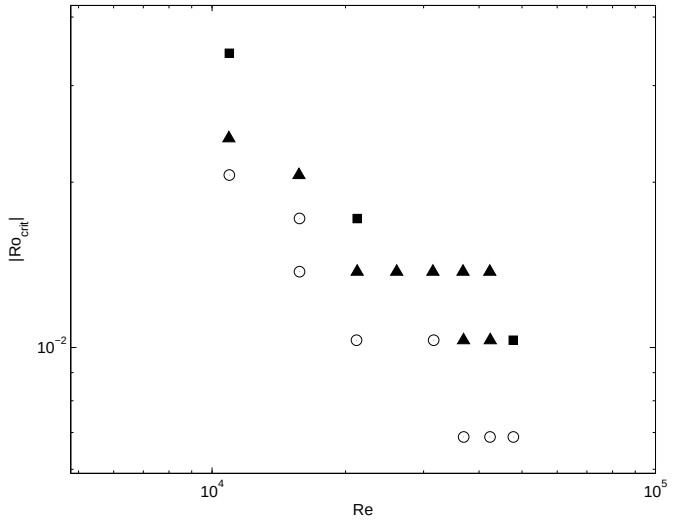

Figure 6.3: Diagramme de stabilité pour un écoulement de base de cisaillement. Expériences stables (○). Expériences instables (▲) visualisées avec des particules de Kalliroscope. Expériences instables (■) avec visualisation par PIV de modes libres ayant des nombres d'onde azimutaux $m_1 = 4$ et $m_2 = 5$. Le rapport de fréquence et le rapport d'aspect valent $\omega = 1.20$ et $h = 3$.

avec $k_n = (2n-1)\pi/h$ et D la relation de dispersion des modes de Kelvin, donnée par l'équation (4.11). La courbe bleue représentée sur la figure 6.2 donne le rapport d'aspect et la fréquence permettant d'avoir une résonance exacte pour la combinaison $(1,1,1)$. Cette courbe est obtenue en cherchant les solutions de l'équation

$$\omega_2(k_2 = \pi/h,\, l_2 = 1) = \omega_1(k_1 = \pi/h,\, l_1 = 1) + \omega_{i,n}(k = pi/h), \qquad (6.17)$$

où $\omega_j(k_j = \pi/h,\, l_j = 1)$ signifie : la valeur de ω_j pour $k_j = \pi/h$ et $l_j = 1$ (première branche des relations de dispersion). Nous avons retenu $h = 3$ et $\omega = 1.20$ et nous vérifions sur la figure 6.1 que la combinaison $(1,1,1)$ est effectivement exactement résonnante.

Des visualisations avec des particules de Kalliroscope ont permis d'établir un diagramme de stabilité de l'écoulement (voir figure 6.3). Des mesures PIV ont révélé la structure de l'instabilité pour une nappe laser placée à mi-hauteur puis au trois quart de la hauteur du cylindre. Cette structure est représentée sur la figure 6.4 et fait apparaître des modes de Kelvin libres avec des nombres d'onde azimutaux $m_1 = 4$ et $m_2 = 5$. Comme nous venons de le voir dans la section 6.1, l'apparition de cette instabilité ne peut pas être prédite par un mécanisme de résonance triadique entre le cisaillement vertical et deux modes de Kelvin libres.

Une hypothèse que nous avons émise pour expliquer l'apparition des modes $m_1 = 4$ et $m_2 = 5$ est que l'instabilité est dûe à un mécanisme de résonance triadique entre un mode de Kelvin forcé par la précession et deux modes de Kelvin libres. En considérant que le premier mode de Kelvin

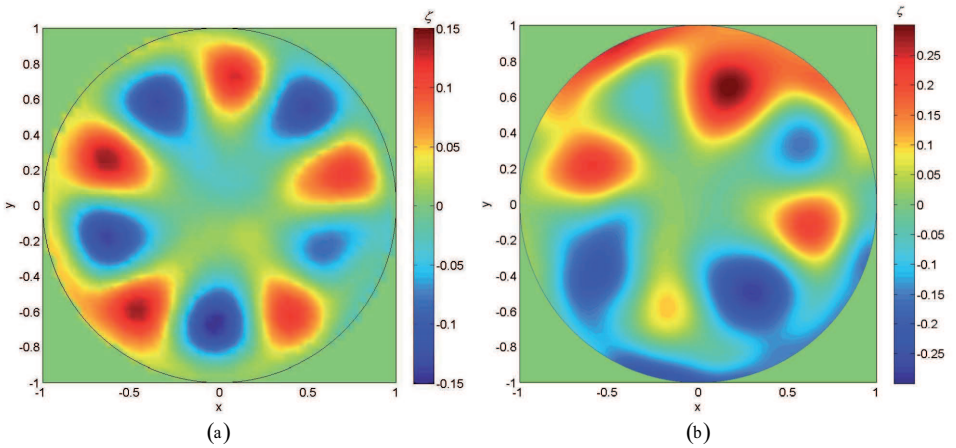

Figure 6.4: Structure de l'instabilité, en $z = 0$ (a), $Re \approx 47800$, $Ro \approx -0.0103$ et en $z = h/4$ (b), $Re \approx 21100$, $Ro \approx -0.0172$. Pour (a) et (b) $h = 3$ et $\omega = 1.20$.

($i = 1$) est forcé par la précession, nous avons montré que la combinaison résonnante $(5, 1, 1)$ ne peut pas conduire à une intabilité car les modes de Kelvin libres ont la même parité par rapport à z. La même conclusion reste valable lorsqu'on considère que le deuxième mode de Kelvin ($i = 2$) est forcé par la précession. Il se pourrait alors que l'instabilité observée fasse intervenir un mode de Kelvin forcé ayant un numéro i supérieur à 2. En effet, la figure 6.2 indique que pour $h = 3$ et $\omega = 1.20$ nous sommes proches de la cinquième résonance ($n = 5$) du quatrième mode ($i = 4$) et de la quatrième résonance ($n = 4$) du troisième mode (i=3). Ces modes étant prédominants, il sont alors de très bons candidats pour conduire à une instabilité via un mécanisme de résonance triadique avec deux modes de Kelvin libres. Il serait donc nécessaire d'appliquer l'analyse linéaire de stabilité du chapitre 4 pour ces modes de Kelvin forcés.

Il se pourrait également que l'écoulement instable fasse intervenir le cisaillement vertical via un mécanisme différent d'une résonance triadique. De nouvelles mesures expérimentales pourraient éventuellement permettre de proposer un mécanisme rendant compte de l'instabilité quand le cisaillement vertical est du même ordre que les modes de Kelvin.

7. CONCLUSION ET PERSPECTIVES

7.1 Conclusion

Dans cette étude nous nous sommes intéressés d'un point de vue expérimental et théorique à la dynamique d'un fluide dans un cylindre en précession. Nous avons montré dans le chapitre 2 que l'écoulement associé à cette dynamique est un cisaillement selon l'axe du cylindre auquel se superposent des modes de Kelvin. Pour la première fois les caractéristiques de ces modes ont été mesurées par PIV. Quand la fréquence de précession est différente d'une fréquence propre d'un mode de Kelvin l'écoulement est dit non-résonnant et une théorie valable à petit nombre de Rossby (i.e. théorie linéaire) et grand nombre de Reynolds (i.e. théorie non visqueuse) permet de prédire précisément l'amplitude des modes de Kelvin forcés par la précession. Lorsque la fréquence de forçage est résonnante cette théorie prédit alors une divergence en amplitude pour le mode de Kelvin forcé. Nous avons alors développé une théorie visqueuse et non-linéaire afin de prédire la saturation en amplitude du mode de Kelvin résonnant. Cette théorie montre qu'en fonction du nombre de Reynolds il existe deux régimes de saturation distincts. Pour des nombres de Reynolds suffisamment petits, les effets non-linéaires sont négligeables et la prise en compte des effets visqueux de volume et de couche limite est suffisante pour prédire la saturation en amplitude du mode de Kelvin résonnant ; comme l'avait démontré Gans (1970*b*) dans le cas particulier d'un angle de précession de 90°. Cela conduit à une saturation en amplitude qui varie comme en $Re^{1/2}$, ce qui est en excellent accord avec les expériences. Pour des nombres de Reynolds suffisamment grands, les effets faiblement non-linéaires doivent être pris en compte en plus des effets visqueux. Cela conduit à une saturation de l'amplitude qui varie comme $Ro^{1/3}$; Ro étant proportionnel à l'angle de précession. Cette saturation de l'amplitude est donc indépendante du nombre de Reynolds et le scaling non-linéaire est bien vérifié par les expériences. Ces expériences ont également montré la présence d'un mode géostrophique dont l'amplitude varie comme le carré de l'amplitude du mode de Kelvin résonnant, comme cela a été démontré par la théorie visqueuse et non-linéaire. L'amplitude de ce mode géostrophique a été mesurée et est correctement prédite par la théorie visqueuse non-linéaire lorsqu'on considère que le premier mode de Kelvin est excité par la précession.

Dans le chapitre 3 nous nous sommes intéressés à l'écoulement instable d'un fluide dans un cylindre en précession, instabilité observée auparavant par McEwan (1970), Manasseh (1992, 1994, 1996) et Kobine (1995, 1996). Dans le cas d'un écoulement résonnant, des mesures PIV dans deux sections différentes du cylindre ont révélé la présence de deux modes de Kelvin avec des grands nombres d'onde azimutaux au-delà du seuil d'instabilité. Nous avons montré que leurs fréquences et leurs nombres d'onde vérifient une condition de résonance triadique avec le mode forcé. Nous avons ainsi confirmé le mécanisme d'instabilité suggéré par Kerswell (1999) : un mode de Kelvin peut se coupler avec deux modes libres pour donner naissance à une instabilité par résonance triadique, comme cela est le cas pour l'instabilité elliptique (voir Kerswell, 2002).

Dans le chapitre 4 une analyse linéaire de stabilité basée sur un méca-

nisme de résonance triadique entre modes de Kelvin a été développée et a permis d'établir une expression analytique du taux de croissance. Cette analyse a montré que le taux de croissance varie comme l'amplitude du mode forcé et est saturé par des effets visqueux de volume (atténuation en Re^{-1}) pour les faibles nombres de Reynolds et par des effets visqueux de surface (atténuation en $Re^{-1/2}$) dus aux couches d'Ekman pour des grands nombres de Reynolds. Nous avons également montré que dans le cas d'une combinaison de modes de Kelvin ne vérifiant pas exactement les conditions limites en haut et en bas du cylindre, le taux de croissance est saturé par des effets de détuning. A partir de l'équation du taux de croissance, nous avons alors obtenu une expression analytique du seuil d'instabilité Ro_{crit} et montré que ce seuil varie comme $Re^{-3/2}$ pour les faibles nombres de Reynolds et comme Re^{-1} pour les grands nombres de Reynolds.

Dans le cas où le premier mode de Kelvin est forcé, la structure des modes instables et le taux de croissance de l'instabilité prédits sont en très bon accord avec les résultats expérimentaux. De plus, les expériences ont confirmé la prédiction du seuil d'instabilité. Nous avons également déduit les caractéristiques de l'instabilité de précession lorsque le rapport d'aspect et/ou le rapport de fréquence est varié. Plusieurs bandes d'instabilité avec des nombres d'onde azimutaux différents sont alors prédites et confirmées par les expériences. De plus, les modes $m_1 = 5$ et $m_2 = 6$ sont prédits comme étant toujours les plus instables pour $1.3 \leq h \leq 10$.

Enfin nous avons observé que plus la fréquence de précession est proche d'une résonance et plus le seuil d'instabilité est faible (i.e. plus le Ro_{crit} est petit). Cela est dû au fait qu'à une fréquence de résonance, l'amplitude du mode forcé (donc le taux de croissance) est maximale.

Des mesures expérimentales concernant la stabilité du deuxième mode de Kelvin forcé à sa première résonance ont également été menées et ont montré que le seuil d'instabilité est correctement prédit (voir chapitre 5). Par contre, la prédiction de la structure des modes instables n'a pu être validée par les expériences et de nouvelles mesures devraient être réalisées afin de comprendre ce désaccord.

Une analyse faiblement non-linéaire a également été développée en prenant en compte les interactions non-linéaires des modes de Kelvin libres avec eux-mêmes dans les couches limites (voir chapitre 4). On observe alors que l'instabilité est saturée par la présence d'un mode géostrophique qui a pour effet de diminuer l'amplitude du mode forcé. Cette théorie faiblement non-linéaire permet de prédire la nature de la bifurcation qui est de type sous-critique. Elle permet également de prédire, en très bon accord avec les expériences (pour le premier mode de Kelvin forcé à sa première résonance), le seuil de transition entre un écoulement instable saturé et un écoulement instable présentant une oscillation des amplitudes des modes de Kelvin. Enfin, et de façon surprenante, ce modèle théorique à faibles degrés de libertés permet d'estimer l'écoulement moyen à l'intérieur du cylindre pour des très grands nombres de Reynolds, même lorsque cet écoulement est turbulent.

Dans le chapitre 6 nous sommes revenus sur la théorie de Mahalov (1993) qui a démontré que l'écoulement d'un fluide dans un cylindre infini en précession était instable par un mécanisme de résonance triadique entre le cisaille-

ment vertical et deux modes de Kelvin libres de nombres d'onde azimutaux $m_1 = 0$ et $m_2 = 1$. Nous avons prouvé théoriquement qu'un tel mécanisme n'est plus possible dans le cas d'un cylindre fini. Des expériences ont été réalisées en choisissant un rapport d'aspect et un rapport de fréquence tels que le cisaillement vertical soit du même ordre que les modes de Kelvin excités par la précession. Nous avons observé que l'écoulement devient instable avec l'apparition de modes de Kelvin libres ayant des nombres d'onde azimutaux $m_1 = 4$ et $m_2 = 5$. Un mécanisme de résonance triadique entre le premier (puis le deuxième) mode de Kelvin et deux modes libres ne permet pas d'expliquer l'apparition de cette instabilité, son origine reste donc pour le moment inconnue.

7.2 Les perspectives

Outre la reprise d'une nouvelle campagne de mesures par PIV pour confirmer nos premières observations concernant la stabilité du deuxième mode de Kelvin et la stabilité du cisaillement, cette étude ouvre de nombreuses perspectives.

Une des premières perspectives que nous voudrions explorer est de savoir si le mécanisme de résonance triadique entre modes de Kelvin, responsable de l'instabilité d'un écoulement dans un cylindre en précession, peut expliquer l'instabilité d'un fluide dans un ellipsoïde en précession, comme cela a été prédit théoriquement par Kerswell (1993). Une telle étude permettrait d'améliorer notre compréhension de l'écoulement à l'intérieur du noyau liquide de la Terre et pourrait ouvrir de nouvelles perspectives pour expliquer la génération du champ magnétique terrestre.

Par ailleurs, il serait intéressant de savoir comment les modes de Kelvin réagissent en présence d'un champ magnétique. Pour étudier la stabilité de ce champ magnétique, une expérience de précession avec un fluide conducteur d'électricité (avec du Gallistan pour commencer) pourrait être réalisée. Ainsi l'étude expérimentale de Gans (1970*a*) pourrait être étendue, ce dernier ayant observé que le champ magnétique généré par du sodium liquide en précession devient instable.

Dans le domaine de l'aéronautique, notre analyse de la dynamique d'un fluide dans un cylindre en précession pourrait permettre de prédire les caractéristiques de vol de certains objets volants, par exemple quand l'écoulement du fluide carburant devient instable.

Enfin dans le contexte des phénomènes atmosphériques, une étude intéressante consisterait à réaliser des expériences avec un fluide de masse volumique constante, enfermé dans un cylindre ayant un faible rapport d'aspect et étant animé d'un mouvement de précession. Nous avons démontré dans le chapitre 4 que pour $h < 0.5$ des modes de Kelvin avec des faibles nombres d'onde azimutaux sont prédits comme étant les plus instables. La visualisation expérimentale de ces modes pourrait représenter la première étape d' un projet qui consisterait à déterminer l'influence de la rotation terrestre sur la dynamique des cyclones. Dans une seconde étape nous pourrions inclure une stratification axiale dans notre fluide et étudier la stabilité de son écoulement dans un cylindre en précession.

ANNEXE

A. DYNAMIQUE D'UN FLUIDE DANS UN CYLINDRE EN PRÉCESSION

Dans cette annexe, la publication parue dans *Mécanique & Industries*, Vol. 10 No. 3-4 (Mai-Août 2009), p. 187, sous le titre "Dynamics of a fluid inside a precessing cylinder" est reproduite.

Mécanique & Industries 10, 187–194 (2009)
© AFM, EDP Sciences 2009
DOI: 10.1051/meca/2009048

www.mecanique-industries.org

Mécanique & Industries

Dynamics of a fluid inside a precessing cylinder

Romain Lagrange[1,a], Patrice Meunier[1], Christophe Eloy[1] and François Nadal[2]

[1] Institut de Recherche sur les Phénomènes Hors Équilibre / Université de Provence, IRPHE – UMR 6594, Technopôle de Château-Gombert, 49, rue Joliot Curie, B.P. 146, 13384 Marseille Cedex 13, France
[2] Commissariat à l'Énergie Atomique (CEA/CESTA), France

Received 20 April 2009

Abstract – The instability of a fluid inside a precessing cylinder is studied theoretically and experimentally. This study is motivated by aeronautics and geophysics applications. Precessional motion forces hydrodynamics waves called Kelvin modes whose structure and amplitude are predicted by a linear inviscid theory. When a forced Kelvin mode is resonant, a viscous and weakly nonlinear theory has been developed to predict its saturated amplitude. We show that this amplitude scales as $Re^{1/2}$ for low Reynolds numbers and as $\theta^{1/3}$ (where θ is the precessing angle) for high Reynolds numbers. These scalings are confirmed by PIV measurements. For Reynolds numbers sufficiently large, this forced flow becomes unstable. A linear stability analysis based on a triadic resonance between a forced Kelvin mode and two free modes has been carried out. The precessing angle for which the flow becomes unstable is predicted and compared successfully to experimental measurements. A weakly nonlinear theory was developed and allowed to show that the bifurcation of the instability of precession is subcritical. It also showed that, depending on the Reynolds number, the unstable flow can be steady or intermittent. Finally, this weakly nonlinear theory allowed to predict, with a good agreement with experiments, the mean flow in the cylinder; even if it is turbulent.

Key words: Precession / Kelvin modes / instability / triadic resonance

Résumé – Dynamique d'un fluide dans un cylindre en précession. L'instabilité d'un fluide dans un cylindre en précession est étudiée théoriquement et expérimentalement. Les domaines d'application de cette étude se retrouvent en aéronautique et en géophysique. La précession force des ondes hydrodynamiques appelées modes de Kelvin, dont la structure et l'amplitude sont prédites par une théorie linéaire non visqueuse. Quand un mode de Kelvin forcé est résonnant, une théorie visqueuse et faiblement non linéaire a été développée pour prédire la saturation de son amplitude. Nous montrons que cette amplitude varie comme $Re^{1/2}$ pour des faibles nombres de Reynolds, et comme $\theta^{1/3}$ (θ étant l'angle de précession) pour les grands nombres de Reynolds. Ces scalings sont confirmés par des mesures PIV. Pour des nombres de Reynolds suffisamment grands l'écoulement forcé devient instable. Une analyse de stabilité linéaire basée sur un mécanisme de résonance triadique entre le mode de Kelvin forcé et deux modes de Kelvin libres a été développée. L'angle de précession pour lequel l'écoulement devient instable est prédit et confirmé par les expériences. Une théorie faiblement non linéaire a été développée et a permis de montrer que la bifurcation de l'instabilité est sous critique. Cette théorie a également montré qu'en fonction du nombre de Reynolds, l'écoulement instable peut être stationnaire ou intermittent. Finalement cette théorie faiblement non linéaire permet de prédire, en bon accord avec les expériences, l'écoulement moyen dans le cylindre, même lorsque cet écoulement est turbulent.

Mots clés : Précession / modes de Kelvin / instabilité / résonance triadique

[a] Corresponding author: lagrange@irphe.univ-mrs.fr

Article published by EDP Sciences

Nomenclature

A	Amplitude of the resonant base flow
A^*	Complex conjugate of A
A_0	Amplitude of the geostrophic mode
A_1	Amplitude of the first free Kelvin mode
A_2	Amplitude of the second free Kelvin mode
d_2	Second root of the Bessel function of the first kind and of order 5
f	Forcing parameter
H	Cylinder height
h	Aspect ratio of the cylinder
i	Complex number $\sqrt{-1}$
J_m	Bessel function of the first kind and of order m
$J_m^{'}$	Derivative of J_m
k	Axial wavenumber of the resonant base flow
k_1	Axial wavenumber of the first free Kelvin mode
k_2	Axial wavenumber of the second free Kelvin mode
m	Azimuthal wavenumber of the resonant base flow
m_1	Azimuthal wavenumber of the first free Kelvin mode
m_2	Azimuthal wavenumber of the second free Kelvin mode
N_1	Non-linear coupling term between the resonant base flow and the second free Kelvin mode
N_2	Non-linear coupling term between the resonant base flow and the first free Kelvin mode
R	Radius of the cylinder
r	Classical cylindrical coordinate
Re	Reynolds number
Ro	Rossby number
S_1	Boundary viscous effects for the first free Kelvin mode
S_2	Boundary viscous effects for the second free Kelvin mode
$\mathbf{u}_\varphi$	Classical unit vector of the cylindrical base
V_1	Volume viscous effects for the first free Kelvin mode
V_2	Volume viscous effects for the second free Kelvin mode
z	Cylindrical coordinate along the cylinder axis. $z = 0$ being the mid-height of the cylinder
δ	Parameter of the constitutive relation for the resonant base flow
δ_1	Parameter of the constitutive relation for the first free Kelvin mode
δ_2	Parameter of the constitutive relation for the second free Kelvin mode
σ	Growth rate of the instability
θ	Precessing angle
ν	Kinematic viscosity
ξ	Interaction coefficient between the geostrophic mode and the resonant base flow
ξ_1	Interaction coefficient between the geostrophic mode and the first free Kelvin mode
ξ_2	Interaction coefficient between the geostrophic mode and the second free Kelvin mode
φ	Classical cylindrical coordinate
χ_1	Non-linear coefficient for the first free Kelvin mode
χ_2	Non-linear coefficient for the second free Kelvin mode
Ω	Axial component of the fluid rotation vector
Ω_1	Angular frequency of the cylinder
ω_1	Dimensionless angular frequency of the first free Kelvin mode
Ω_2	Angular frequency of the platform, rad.s^{-1}
ω_2	Dimensionless angular frequency of the second free Kelvin mode
ω	Frequency ratio

1 Introduction

The knowledge of the flow forced by a precessional motion is of critical importance in several domains. In aeronautics, a flying object whose liquid propellant is forced by precession can have its trajectory dangerously modified. In geophysics the Earth precession modifies the flow of its liquid core and is therefore of significative importance in understanding the dynamo effect (among other effects such as convection, boundary layers, elliptic or tidal instability [1]).

Experiments such as the one carried out by McEwan [2] clearly show that the container precession forces a flow which can be decomposed as a sum of inertial waves (also called Kelvin modes). For low Reynolds numbers this flow is stable. For large Reynolds numbers it becomes unstable and can degenerate into a turbulent flow. This behavior was also reported by Manasseh [3–5], and Kobine [6]. Among several scenarios, Kerswell [7] suggested that a given Kelvin mode can trigger a triadic resonance with two other Kelvin modes leading to an instability. We have demonstrated that this mechanism of triadic resonance between Kelvin modes (which bears similarity with the elliptic instability [8,9]) is indeed responsible of the instability of precession.

The paper is organized as follows. Section 2 is dedicated to a presentation of the problem. Parameters and dimensionless numbers are introduced and a short presentation of the experimental set-up is described. In Section 3 the base flow, ie. the flow before the instability, is presented. Classical results concerning a non-resonant flow are recalled and extended in the case of a resonant flow. In Section 4 the instability is experimentally presented and a linear stability analysis is described. Finally, a weakly nonlinear theory is developed in Section 5 in order to explain the transition from an unstable and stationary flow to an unstable and intermittent flow.

2 Presentation of the problem

The flow inside a precessing cylinder of height H and radius R, full of fluid of kinematic viscosity ν is considered. This cylinder rotates at the angular frequency Ω_1 around its axis. It is mounted on a platform which rotates at the angular frequency Ω_2 as shown in Figure 1. The angle between the two axes of rotation is the precession angle θ. In the following, variables are made dimensionless by using R and $\Omega = \Omega_1 + \Omega_2 \cos\theta$ as characteristic length and frequency. The dynamics of this precessing system depends on four dimensionless numbers:

- the aspect ratio $h = H/R$;
- the frequency ratio $\omega = \Omega_1/\Omega$;
- the Rossby number $Ro = \Omega_2 \sin\theta/\Omega$;
- the Reynolds number $Re = \Omega R^2/\nu$.

An experimental set-up was built in the laboratory, allowing Particle Image Velocimetry (PIV) measurements of the velocity fields in a transverse section of the cylinder.

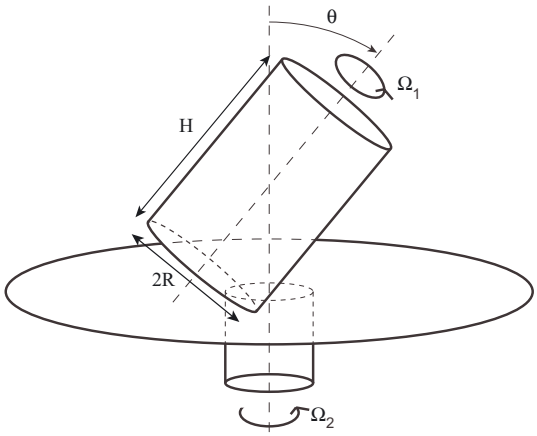

Fig. 1. Sketch of a precessing cylinder.

To perform the acquisition of a PIV field, small markers illuminated with a thin light sheet created by a Yag pulsed laser were used. Particle images were recorded by a camera mounted on the rotating platform. The horizontal velocity and the axial vorticity fields in the cylinder frame of reference were thus measured. More details about PIV treatment can be found in [10] and a precise description of the experimental set-up is given in [11].

3 Base flow

In Figure 2a the axial flow vorticity is showed in the cylinder reference frame for a small Rossby number: $Ro = 0.0031$, and a moderate Reynolds number: $Re = 3500$. Two counter rotating vortices are observed. It corresponds to a Kelvin mode which is forced by precession. Owing to the time and azimuthal dependence of the precession forcing, this Kelvin mode has an azimuthal wavenumber $m = 1$ and an angular frequency ω (see [12]). Its velocity field is

$$\mathbf{V_b} = A\mathbf{v_b}(r,z)\,\mathrm{e}^{\mathrm{i}(\omega t+\varphi)} + \text{c.c} \tag{1}$$

where A is the amplitude, c.c denotes the complex conjugate and

$$\mathbf{v_b}(r,z) = \begin{pmatrix} u_b(r)\sin(kz) \\ v_b(r)\sin(kz) \\ w_b(r)\cos(kz) \end{pmatrix}$$

$$\text{with} \begin{cases} u_b(r) = \mathrm{i}\dfrac{\omega r\delta J_1'(\delta r) + 2J_1(\delta r)}{2r(\omega^2-4)} \\ v_b(r) = \dfrac{2r\delta J_1'(\delta r) + \omega J_1(\delta r)}{2r(4-\omega^2)} \\ w_b(r) = \mathrm{i}\dfrac{k}{2\omega}J_1(\delta r) \end{cases} \tag{2}$$

In this expression $J_1(r)$ is the Bessel function of the first kind and $J_1'(r)$ its r-derivative.

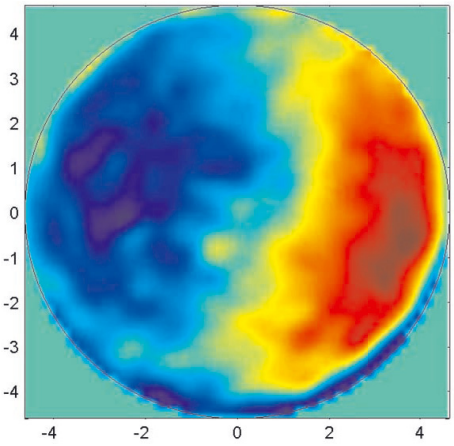

(a)

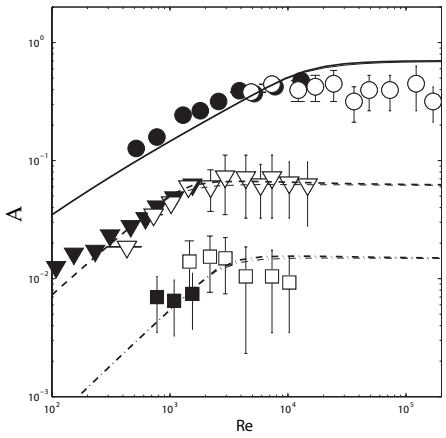

(b)

Fig. 2. (a) Vorticity field of the first Kelvin mode measured by PIV at its first resonance, in the absence of instability ($h = 1.62$, $\omega = 1.18$, $Re \approx 3500$, $Ro = 0.0031$). (b) Amplitude of the first Kelvin mode obtained at the first (solid line), second (dashed line) and third (dotted line) resonance. Symbols are experimental results ($h = 1.8$, $\theta = 2°$).

The parameter δ satisfies the constitutive relation

$$\delta^2 = \frac{4-\omega^2}{\omega^2}k^2 \tag{3}$$

where the axial wavenumber k depends on ω according to the following dispersion relation with $m = 1$

$$\omega\delta J_m^{'}(\delta) + 2mJ_m(\delta) = 0 \tag{4}$$

At a given ω this dispersion relation has an infinite number of solutions. Each solution corresponds to a Kelvin mode forced at the frequency ω. The Kelvin mode showed in Figure 2 is the first Kelvin mode. It corresponds to the mode with the smallest axial wavenumber k.

A classical linear and inviscid theory can predict the amplitude A of a forced Kelvin mode. This theory shows that $A \sim Ro$ and depends on ω. However, when the mode is resonant (i.e. $k = n\pi/h$, with n an odd number) its amplitude A diverges. A viscous [13] and weakly nonlinear [11] theory is then necessary to predict the amplitude saturation. Figure 2b represents the saturation of the first Kelvin mode as a function of Re for its first three resonances. We showed [11] that for small Reynolds numbers (viscous regime, $\mathrm{Re}^{1/2}\mathrm{Ro}^{2/3} \ll 1$), A scales as $Ro\sqrt{Re}$ due to viscous effects in the Ekman layers. For larger Reynolds numbers (nonlinear regime, $\mathrm{Re}^{1/2}\mathrm{Ro}^{2/3} \gg 1$)), A scales as $Ro^{1/3}$. Predictions of [11] are in good agreement with PIV measurements represented by symbols in Figure 2b.

4 Instability

As shown in the literature [5,6], the flow inside a precessing cylinder becomes unstable when the Reynolds or the Rossby number is increased. Figure 3 is a PIV measurement of the axial and instantaneous vorticity field for $\mathrm{Re} = 6500$ and $Ro = 0.0031$. For such a value of Re and Ro the flow depicted in Figure 2a is unstable and the unstable mode exhibits a ring with 10 lobes of vorticity with alternate signs. It corresponds to a free Kelvin mode with azimuthal wavenumber $m_1 = 5$. Its velocity field is

$$\mathbf{V_1} = A_1\mathbf{v_1}(r,z)\,\mathrm{e}^{\mathrm{i}(\omega_1 t + m_1\varphi)} + \mathrm{c.c} \tag{5}$$

where

$$\mathbf{v}_1(r,z) = \begin{pmatrix} u_1(r)\sin(k_1 z) \\ v_1(r)\sin(k_1 z) \\ w_1(r)\cos(k_1 z) \end{pmatrix}$$

$$\text{with} \begin{cases} u_1(r) = 2\mathrm{i}\dfrac{\omega_1 r\delta_1 J_{m_1}^{'}(\delta_1 r) + 2m_1 J_{m_1}(\delta_1 r)}{r(\omega_1^2 - 4)} \\ v_1(r) = 2\dfrac{2r\delta_1 J_{m_1}^{'}(\delta_1 r) + m_1\omega_1 J_{m_1}(\delta_1 r)}{r(4-\omega_1^2)} \\ w_1(r) = 2\mathrm{i}\dfrac{k_1}{\omega_1}J_{m_1}(\delta_1 r) \end{cases} \tag{6}$$

In (5) and (6), ω_1 is the dimensionless frequency of the mode $m_1 = 5$ and k_1 its axial wavenumber. The parameter δ_1 satisfies the constitutive relation (3) with ω_1 and k_1 instead of ω and k. Parameters ω_1 and δ_1 also satisfy the dispersion relation (4) with $m = 5$.

If the position of the PIV laser sheet is moved from $z = h/4$ to $z = 0$ (mid-height of the cylinder) a second free Kelvin mode is observed. It exhibits 12 lobes of vorticity with alternate signs and thus corresponds to a free Kelvin mode whose azimuthal wavenumber is $m_2 = 6$. Its velocity field is

$$\mathbf{V_2} = A_2\mathbf{v_2}(r,z)\,\mathrm{e}^{\mathrm{i}(\omega_2 t + m_2\varphi)} + \mathrm{c.c} \tag{7}$$

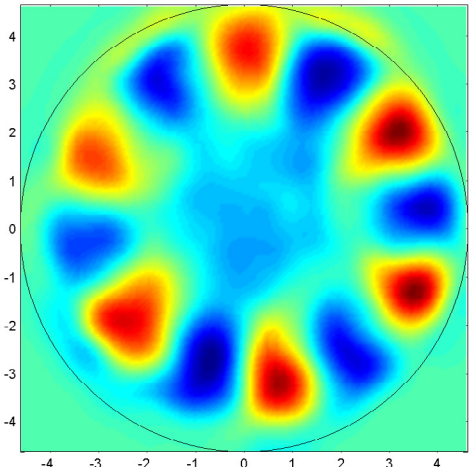

(a)

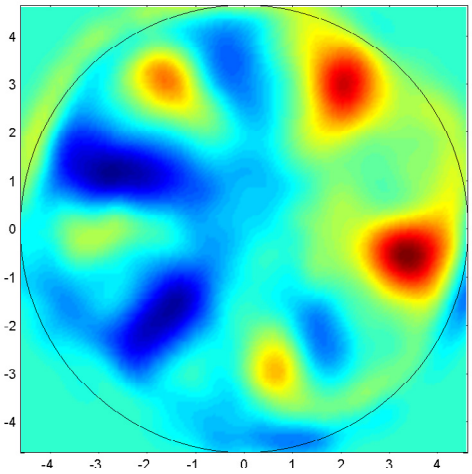

(b)

Fig. 3. Vorticity field of the free modes which constitute the instability of a precessing cylinder. (a) Vorticity field measured at mid-height of the cylinder. (b) Vorticity field measured at $z = h/4$ showing the mode $m = 5$ superimposed with the forced Kelvin mode of Figure 2a ($h = 1.62$, $\omega = 1.18$, $Re \approx 6000$, $Ro = 0.0031$).

where

$$\mathbf{v}_2(r,z) = \begin{pmatrix} u_2(r)\cos(k_2 z) \\ v_2(r)\cos(k_2 z) \\ w_2(r)\sin(k_2 z) \end{pmatrix}$$

$$\text{where} \begin{cases} u_2(r) = 2\dfrac{\omega_2 r\delta_2 J'_{m_2}(\delta_2 r) + 2m_2 J_{m_2}(\delta_2 r)}{r(\omega_2^2 - 4)} \\ v_2(r) = 2\mathrm{i}\dfrac{2r\delta_2 J'_{m_2}(\delta_2 r) + m_2\omega_2 J_{m_2}(\delta_2 r)}{r(\omega_2^2 - 4)} \\ w_2(r) = -2\dfrac{k_2}{\omega_2} J_{m_2}(\delta_2 r) \end{cases} \tag{8}$$

In (7) and (8), ω_2 is the dimensionless frequency of the mode $m_2 = 6$ and k_2 its axial wavenumber. The parameter δ_2 satisfies the constitutive relation (3) with ω_2 and k_2 instead of ω and k. Parameters ω_2 and δ_2 also satisfy the dispersion relation (4) with $m = 6$.

The frequencies of the two free Kevin modes shown in Figure 3 were experimentally measured and their axial wavenumbers were deduced. We have demonstrated that the resonant base flow and the free Kelvin modes satisfy the resonant condition $m_2 - m_1 = 1$, $\omega_2 - \omega_1 = \omega$ and $k_2 - k_1 = k$. This corresponds to a mechanism of triadic resonance between the three Kelvin modes.

More information about experimental results presented here can be found in [14].

To better confirm this mechanism of triadic resonance, a linear stability analysis has been developed. The first step is to find the free Kelvin modes satisfying the resonant condition. They correspond to the crossing points of the two dispersion relations shown in Figure 4a. When these points are determined, the structure of the associated free Kelvin modes is known. Then, because of a solvability condition, equations of evolution for the amplitudes A_1 and A_2 of the two free Kelvin modes can be obtained. If the base flow is a forced Kelvin mode of amplitude A, these equations are

$$\begin{cases} \partial_t A_1 = A^* N_1 A_2 - \frac{1}{\sqrt{Re}} S_1 A_1 - \frac{1}{Re} V_1 A_1 \\ \partial_t A_2 = A N_2 A_1 - \frac{1}{\sqrt{Re}} S_2 A_2 - \frac{1}{Re} V_2 A_2 \end{cases} \tag{9}$$

where

$$N_1 = \mathrm{i}\pi h\left(\frac{k}{\omega} - \frac{k_2}{\omega_2}\right)\int_0^1 \begin{vmatrix} u_2 & u_b^* & u_1^* \\ v_2 & v_b^* & v_1^* \\ w_2 & w_b^* & w_1^* \end{vmatrix} r\mathrm{d}r \Big/ \mathbf{v_1}\odot\mathbf{v_1} \tag{10}$$

$$N_2 = \mathrm{i}\pi h\left(\frac{k}{\omega} - \frac{k_1}{\omega_1}\right)\int_0^1 \begin{vmatrix} u_b & u_1 & u_2^* \\ v_b & v_1 & v_2^* \\ w_b & w_1 & w_2^* \end{vmatrix} r\mathrm{d}r \Big/ \mathbf{v_2}\odot\mathbf{v_2} \tag{11}$$

where $|.|$ is the determinant and the scalar product $\odot$ between two vectors $\mathbf{U_1} = (U_{1r}, U_{1\varphi}, U_{1z})$ and $\mathbf{U_2} = (U_{2r}, U_{2\varphi}, U_{2z})$ being defined as

$$\mathbf{U_1}\odot\mathbf{U_2} = \int_0^1\int_0^{2\pi}\int_{-h/2}^{h/2}\left(U_{1r}^* U_{2r} + U_{1\varphi}^* U_{2\varphi} + U_{1z}^* U_{2z}\right) \times r\,\mathrm{d}r\,\mathrm{d}\varphi\,\mathrm{d}z \tag{12}$$

The terms N_1 and N_2 represent the interaction, through the nonlinear term of the Navier Stokes equation, of a free Kelvin mode with the resonant base mode. The terms $1/Re$ represent the influence of volume viscous effects and terms $1/\sqrt{Re}$ the influence of boundary viscous effects through Ekman suction. Constants S_1, S_2, V_1, V_2 can be

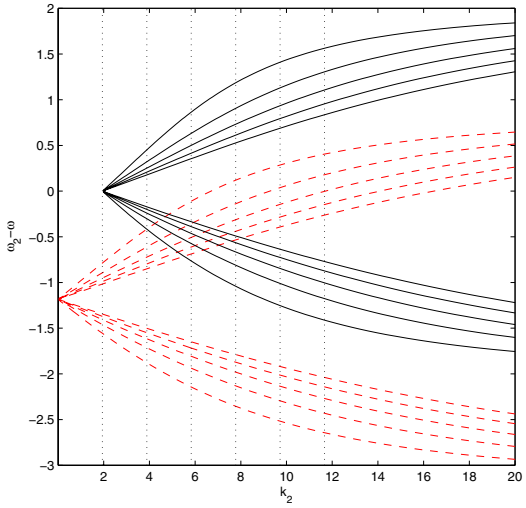

(a)

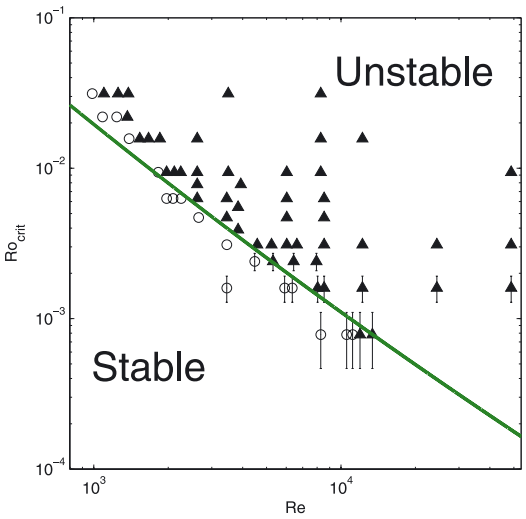

(b)

Fig. 4. (a) Dispersion relations of the Kelvin modes. The solid lines (resp. dashed lines) correspond to the first five branches of the Kelvin modes with azimuthal wavenumber $m_1 = 5$ (resp. $m_2 = 6$). Solid lines have been translated by $k = \pi/h$ and dashed lines have been translated by $\omega = 1.18$. Vertical dotted lines correspond $k = n\pi/h$, with n an integer. (b) Critical Rossby number as a function of the Reynolds number. Circles represent stable experiments and triangles unstable experiments. The theory is represented using a solid green curve. $h = 1.62$, $\omega = 1.18$.

analytically calculated (see Kudlick [15] for the peculiar case of a Kelvin mode with an azimuthal wavenumber $m = 1$ and with $\omega = 1$).

Looking for A_1 and A_2 with exponential time dependence $e^{\sigma t}$, the equation for the growth rate σ is the following

$$\left(\sigma + \frac{1}{\sqrt{Re}}S_1 + \frac{1}{Re}V_1\right)\left(\sigma + \frac{1}{\sqrt{Re}}S_2 + \frac{1}{Re}V_2\right) = |A|^2 N_1 N_2 \quad (13)$$

Table 1. Values of the parameters for the base flow (at the first resonance) and the two free Kelvin modes $m_1 = 5$ and $m_2 = 6$, $h = 1.62$.

ω	k	f	S	ξ	
1.18	1.939	− 0.452	1.86 − 0.42i	0.165	
ω_1	k_1	S_1	V_1	ξ_1	N_1
− 0.416	1.940	1.605 − 0.058i	87.159	−0.066	−0.418
ω_2	k_2	S_2	V_2	ξ_2	N_2
0.766	3.880	1.813 − 0.129i	102.676	−0.365	−0.614

The inviscid growth rate of the instability is then $\sigma = |A|\sqrt{N_1 N_2}$. The study of the signs of N_1 and N_2 (given by (10) and (11)) shows that the free Kelvin modes associated to a crossing point between branches of the dispersion relation with same monotony cannot lead to an instability. This fact was underlined using energetic methods by [16].

Including viscous effect in the calculus of σ we showed that for $h = 1.62$ and $\omega = 1.18$ (first resonance of the first Kelvin mode) the interaction between free Kelvin modes with azimuthal wavenumbers equals 5 and 6 are the most unstable, as observed in the experiments. We also plotted the stability diagram in the plane (Re,Ro) in Figure 4b. It shows (green solid curve) that the critical Rossby number scales as $Re^{-3/2}$ for $Re \ll 3000$ and as Re^{-1} for $Re \gg 3000$. These two scale factors were well confirmed by PIV measurements.

5 Weakly nonlinear theory

It is possible to add nonlinear interactions between the different modes. It results in a supplementary mode with a cylindrical symmetry and whose structure, determined experimentally, is

$$\mathbf{V_0} = A_0 J_5(d_2 r)\,\mathbf{u}_\varphi \quad (14)$$

In this expression A_0 is the amplitude of the geostrophic mode, d_2 is the second root of J_5 (i.e. $d_2 = 12.339$) and $\mathbf{u}_\varphi$ is the unit vector of the cylindrical base.

This mode is essential because it saturates the growth rate of the instability thanks to 'detuning' effects. The dynamics of the precessing flow is then entirely determined by the following amplitude equations

$$\begin{cases} \partial_t A = 2if\,Ro - \dfrac{1}{\sqrt{Re}}SA - i\xi A_0 A \\ \partial_t A_1 = A^* N_1 A_2 - \dfrac{1}{\sqrt{Re}}S_1 A_1 - i\xi_1 A_0 A_1 \\ \partial_t A_2 = A N_2 A_1 - \dfrac{1}{\sqrt{Re}}S_2 A_2 - i\xi_2 A_0 A_2 \\ \partial_t A_0 = \dfrac{1}{\sqrt{Re}}\left(\dfrac{-2}{h}A_0 + \chi_1 |A_1|^2 + \chi_2 |A_2|^2\right) \end{cases} \quad (15)$$

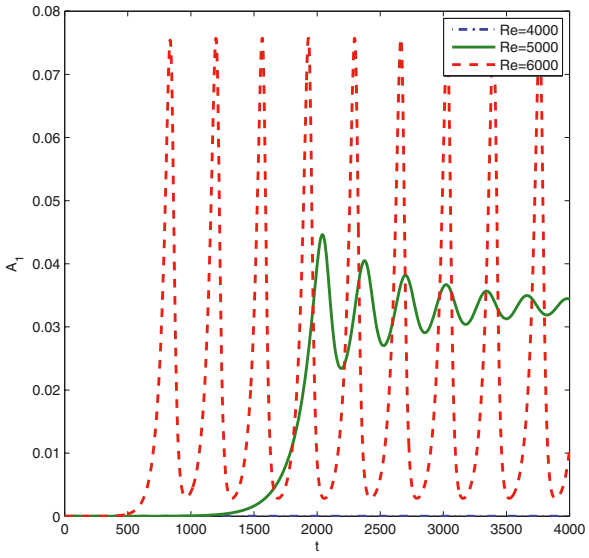

(a)

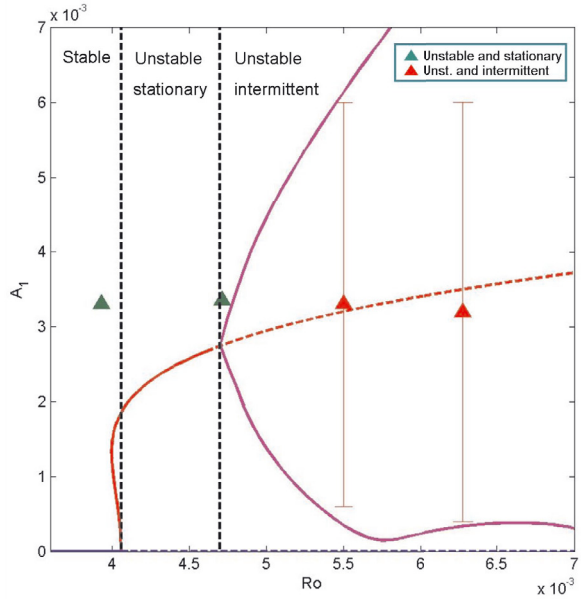

(b)

Fig. 5. (a) Amplitude of the free Kelvin mode $m_1 = 5$ as a function of the dimensionless time, for three different Reynolds numbers. For $Re = 4000$ (blue dotted line) the flow is stable. For $Re = 5000$ (green solid line) the flow is unstable and stationary. For $Re = 6000$ (red dashed line) the flow is unstable and intermittent: $h = 1.62$, $\omega = 1.18$, $Ro = 0.0031$. (b) Amplitude of the free Kelvin mode $m_1 = 5$ as a function of Ro. The bifurcation for the transition from a stable flow to an unstable flow is subcritical. The one which corresponds to the transition from an unstable and stationary flow to an unstable and intermittent flow is supercritical. The fixed point calculated from the weakly nonlinear theory is represented by the continuous red curve and is extended using a dashed line when the flow becomes unstable and intermittent. Continuous purple curves represent the maximum and the minimum of oscillations of A_1. Green triangles (resp. red) represent unstable and stationary experiments (resp. unstable and intermittent). Parameters are: $h = 1.62$, $\omega = 1.18$, $Re = 3664$.

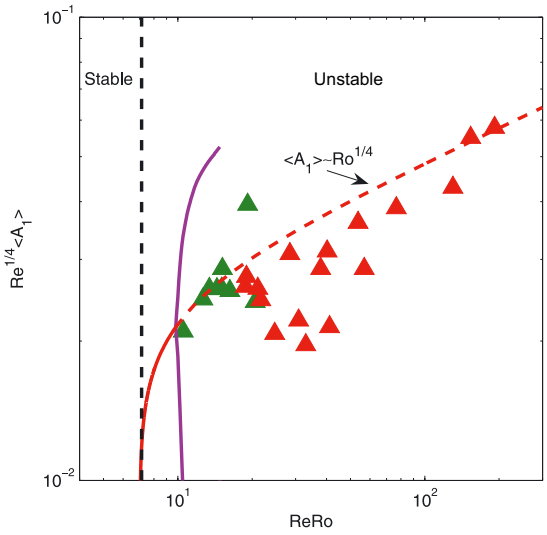

(a)

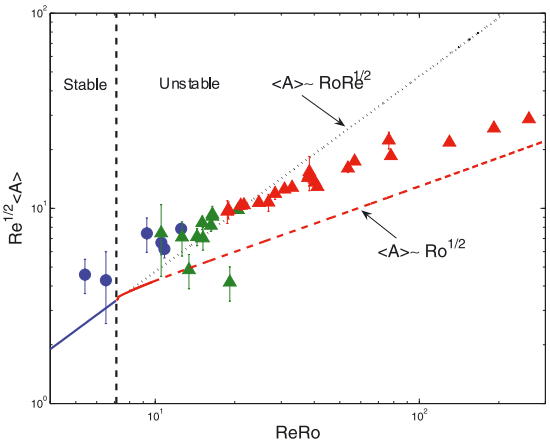

(b)

Fig. 6. Amplitude of the mode $m_1 = 5$ (a) and of the base mode (b) as a function of $RoRe$ (Volume viscous effects were neglected). The fixed point (red continuous curve and then discontinuous) is compared with the experimental mean values $\langle A_1 \rangle$ et $\langle A \rangle$. These values are represented by blue circles (stable flow), green triangles (unstable and stationary flow) or red triangles (unstable and intermittent flow). Parameters are: $h = 1.62$, $\omega = 1.18$.

Terms $\xi A_0 A$, $\xi_1 A_0 A_1$ and $\xi_2 A_0 A_2$ are the 'detuning' effects mentioned previously. They can be calculated analytically (see [11]). Terms $\chi_1 |A_1|^2$ and $\chi_2 |A_2|^2$ represent the nonlinear interactions of a free Kelvin mode with itself. They were assumed to be equal and they were fitted from experiments ($\chi_1 = \chi_2 = 10\,000$).

A numerical solution of (15) is shown in Figure 5a. Parameters are given in Table 1. Figure 5a represents the temporal evolution of A_1 as a function of the Reynolds number, for $h = 1.62$ and $\omega = 1.18$. For a Reynolds number slightly over the threshold, the instability saturates and the amplitudes (A_1 but also A, A_2 and A_0) are stationary. Amplitudes become intermittent when the

Reynolds number is increased, and the dynamics can even be chaotic for very high Reynolds numbers. This dynamics was confirmed by experiments (Fig. 5b). The resolution of (15) also showed that the instability is subcritical (Fig. 5b). Experimentally, we were not able to verify the nature of the bifurcation because it would require to vary the precessing angle with 1/100-degree increments.

For high Re, the theory showed that the fixed point of the amplitude equations only depends on $ReRo$ (Fig. 6). The amplitude A_1 (resp. A) scales as $Ro^{1/4}$ (resp. $Ro^{1/2}$) for high $ReRo$. By comparing this fixed point with the experimental mean value of the amplitudes ($\langle A\rangle$ et $\langle A_1\rangle$), we observed that the scalings are preserved and remain pertinent even if the flow becomes turbulent.

6 Conclusion

Particle Image Velocimetry measurements showed that the fluid dynamics inside a precessing cylinder consists in a stable flow for low Reynolds numbers and an unstable flow for larger Reynolds numbers. The stable flow can be predicted by a linear inviscid model and is shown to be a superposition of Kelvin modes. In the peculiar case of a resonant flow, a viscous and weakly nonlinear theory was developed to predict the amplitude saturation of the resonant Kelvin mode. This theory was confirmed by experimental results.

For larger Reynolds numbers, the structure of the unstable flow was measured using PIV. It was demonstrated that the mechanism of the precession instability is a triadic resonance between the forced base flow and two free Kelvin modes. A stability analysis based upon a this mechanism allowed to predict the most unstable free Kevin modes and to obtain an analytical expression for the growth rate. A stability diagram was also established in good agreement with experiments.

A weakly nonlinear analysis has also been carried out to take into account the interaction between the Kelvin modes. It showed that a geostrophic mode appears whose effect is to saturate the instability and that the bifurcation of the precession instability is subcritical. It also showed that, depending on the Reynolds number, the unstable flow can be steady or intermittent. Finally, the fixed point of the nonlinear amplitude equations allowed to predict correctly the scaling of the mean value mode amplitudes. Although this weakly nonlinear theory is based on a limited number of modes, it gives remarkable good results when compared to the experiments, even if the flow appears turbulent in this case.

Acknowledgements. This study was carried out under CEA-CNRS Contract No. 012171.

References

[1] W.V.R. Malkus, An experimental study of global instabilities due to tidal (elliptical) distortion of a rotating elastic cylinder, Geophys. Astrophys. Fluid Dynamics 48 (1989) 123–134
[2] A. McEwan, Inertial oscillations in a rotating fluid cylinder, J. Fluid Mech. 40 (1970) 603–640
[3] R. Manasseh, Breakdown regimes of inertia waves in a precessing cylinder, J. Fluid Mech. 243 (1992) 261–296
[4] R. Manasseh, Distortions of inertia waves in a rotating fluid cylinder forced near its fundamental mode resonance, J. Fluid Mech. 265 (1994) 345–370
[5] R. Manasseh, Nonlinear behaviour of contained inertia waves, J. Fluid Mech. 315 (1996) 151–173
[6] J. Kobine, Azimuthal flow assiociated with inertial wave resonance in a precessing cylinder, J. Fluid Mech. 319 (1996) 387–406
[7] R. Kerswell, Secondary instabilities in rapidly rotating fluids: inertial wave breakdown, J. Fluid Mech. 382 (1999) 283–306
[8] R. Kerswell, Elliptical instability, Ann. Rev. Fluid Mech. 34 (2002) 83–113
[9] C. Eloy, P. Le Gal, S. Le Dizès, Elliptic and triangular instabilities in rotating cylinders, J. Fluid Mech. 476 (2003) 357–388
[10] P. Meunier, T. Leweke, Analysis and minimization of errors due to high gradients in particle image velocimetry, Exp. Fluids 35 (2003) 408–421
[11] P. Meunier, C. Eloy, R. Lagrange, F. Nadal, A rotating fluid cylinder subject to weak precession, J. Fluid Mech. 599 (2008) 405–440
[12] H. Greenspan, The theory of rotating fluids, Cambridge University Press, 1968
[13] R. Gans, On the precession of a resonant cylinder, J. Fluid Mech. 41 (1970) 865–872
[14] R. Lagrange, Instability of a fluid inside a precessing cylinder, Physics of Fluids. 20 (2008) 081701
[15] M. Kudlick, On the transient motions in a contained rotating fluid, P.h.D. Thesis, MIT, 1966
[16] Y. Fukumoto, The three-dimensional instability of a strained vortex tube revisited, J. Fluid Mech. 493 (2003) 287318

B. THÉORIE VISQUEUSE NON RÉSONNANTE SUR LA STABILITÉ D'UN FLUIDE DANS UN GYROSCOPE

Dans cette annexe, la publication parue dans la revue *Journal of Fluid Mechanics*, sous le titre "Non resonant viscous theory for the stability of a fluid-filled gyroscope" est reproduite.

Non-resonant viscous theory for the stability of a fluid-filled gyroscope

By Jean-Pierre Lambelin, François Nadal, Romain Lagrange† and Arthur Sarthou‡

Commissariat à l'Energie Atomique, CESTA, 33114 Le Barp, France

† IRPHE, CNRS, Université Aix Marseille I & II, 49 rue Joliot-Curie, 13013 Marseille, France

‡ Université Bordeaux I, TREFLE-ENSCPB, UMR CNRS 8508, 16 avenue Pey-Berland, 33607 Pessac Cedex, France

(Received 07 July 2008)

In the case of a gyroscope including a cylindrical fluid-filled cavity, the classic Poinsot's coning motion can become unstable. For certain values of the solid inertia ratio, the coning angle opens under the effect of the hydrodynamic torque. The coupled dynamics of such a non solid system is ruled by four dimensionless numbers : the small viscous parameter $\epsilon = Re^{-1/2}$ (where Re notes the Reynolds number), the fluid-solid inertia ratio κ which quantifies the proportion of liquid relative to the total mass of the gyroscope, the solid inertia ratio σ, and the aspect ratio h of the cylindrical cavity. The calculation of the hydrodynamic torque on the solid part of the gyroscope requires the preliminary evaluation of the possibly resonant flow inside the cavity. The hydrodynamic scaling used to derive such a flow essentially depends on the relative values of κ and ϵ. For small values of the ratio $\sqrt{\kappa}/\epsilon$ (compared to 1), Gans derived an expression of the growth rate of the coning angle. The principles of Gans' approach are briefly recalled but the details of the whole calculation are not given. At the opposite limit, that is for large values of $\sqrt{\kappa}/\epsilon$, the dominating flow is given by a linear inviscid theory. In order to take account of viscous effects, we propose a direct method involving an exhaustive calculation of the flow at order ϵ. We show that the deviations from Stewartson's inviscid theory do not originate from the viscous shear at the walls but rather from the bulk pressure at order ϵ related to the Ekman suction. Physical contents of Wedemeyer's heuristic theory are analysed in the view of our analytical results. The latter are tested numerically in a large range of parameters. Complete Navier-Stokes equations are solved in the cavity. The hydrodynamic torque obtained by numerical integration of the stress is used as a forcing term in the coupled fluid-solid equations. Numerical results and analytical predictions show a fairly good quantitative agreement.

1. Introduction

The behaviour of an isolated precessing tank is very dependent on the hydrodynamics of the fluid contained and approaches by *energy dissipation evaluation* (Garg (1986), Vanyo (1993)), although very useful, can be insufficient. An accurate prediction of a pos-

sible destabilization of the coupled fluid-structure system implies a good understanding of the flow forced by the precessional motion of the container.

Initial theoretical work on rotating fluids can be attributed to Sir W. Thomson (1880), who suggested that the linear inviscid flow of a disturbed rotating fluid could be written as a sum of so-called *Kelvin modes*. Using Lord Kelvin's approach, Greenhill (1880) calculated the inviscid flow in a rotating ellipsoidal cavity. As shown later by Kudlick (1966) and Greenspan (1968) for sufficiently high Reynolds numbers, viscous effects can be taken in account as corrections to Kelvin's inviscid approach. Experiments performed later (Fultz (1959), McEwan (1970), Kerswell (1995), Meunier (2008)) confirmed not only the values of the resonant eigen frequencies but also the times of viscous decay predicted by these linear theories. A theoretical expression of the viscously saturated amplitude at the resonance was established by Gans (1970). Meunier (2008) confirmed Gans' prediction and gave a more complete expression for the amplitude of the resonant mode, taking in account both viscous and non-linear terms in Navier-Stokes equations. However, further exprimental work performed at sufficiently high Reynolds numbers (McEwan (1970), Thomson (1970), Manasseh (1992,1994,1996), Mahalov (1993)) showed a systematic destabilization of the resonant flow into a fine-scale turbulent flow. This so-called *resonant collapse*, probably resulting from a triad mechanism (Lagrange (2008)), was explored by Kerswell (1999). In the present work, we do not take into account non linear effects such as triadic coupling senario of destabilization, since only very small coning angles are considered.

Pioneering theoretical work on the stability of a fluid-filled gyroscope was performed by Milne (1940), who applied Greenhill's inviscid solution for an ellipsoidal cavity to a completely liquid-filled spinning projectile, and exhibited a stability criterion in the form of a diagram (the so-called Milne's graph). Two decades later, Stewartson (1958) extended Milne's approach to the case of a partially or completely filled cylindrical cavity (Stewartson's theory was also based on the assumption that the inside liquid had zero viscosity). Milne-Stewartson's theory revealed the existence of unstable ranges of solid inertia ratio, for which the coning motion of the gyroscope forces a Kelvin mode close to one of its resonances. However, the discrepancies between these theories and the experiments performed by Ward (1959) were confirmed by further experimental data presented by Karpov (1962, 1965), Scott (1973) and D'Amico (1977, 1981). Indeed, the observed resonant frequency of the fluid-filled gyroscope was slightly (but systematically) shifted compared to the inviscid resonant frequency predicted by Stewartson (by *resonant frequency*, we mean here the frequency at which the growth rate of the coning angle is maximum). Besides, the growth rate of the coning angle was not strictly zero outside the range of unstable solid inertia ratios predicted by Stewartson.

Wedemeyer (1965, 1966) gave the first interpretation of these observations, invoking a change in the effective aspect ratio of the cylindrical cavity due to the thickness of the viscous boundary layers. Wedemeyer's theory, which is valid at high Reynolds numbers, is based on the following equivalence : the viscous system of aspect ratio H/R_c (H and R_c denote the height and radius of the cylindrical cavity) behaves as an inviscid system of aspect ratio $(H-\delta H)/(R_c-\delta R_c)$, where δH and δR_c are the thicknesses of the viscous

boundary layers on the top and lateral walls of the cylinder, respectively. At sufficiently high Reynolds numbers, the thicknesses of both boundary layers are proportional to ϵ. Consequently, since the value of the inviscid resonant frequency only depends on the aspect ratio, Wedemeyer's approach leads to a shift proportional to ϵ at leading order. In principle, Wedemeyer's work, as an extension of Stewartson's inviscid theory, does not hold in a close vicinity of any hydrodynamic resonance.

Gans (1984) derived an expression of the growth rate of the coning angle which is valid close to the resonance by applying the saturated viscous solution proposed by Gans (1970) himself to the dynamics of a near-resonant fluid-filled gyroscope. Instead of considering the main contribution of the flow as inviscid, the author calculates the viscously saturated amplitude of the main resonant Kelvin mode. This amplitude, which is $O(\epsilon^{-1})$, is determined by a solvability condition for the problem at the next order.

The main objective of the paper is to extend in a rigorous way Stewartson's inviscid theory to the case of a viscous fluid. Unlike Wedemeyer, whose method is heuristic, we adopt a perturbative approach that allows for an exhaustive calculation of the different viscous contributions to the total hydrodynamic torque. This method guarantees that all the contributions of same order are taken into account. The second objective is to perform an identification of Wedemeyer's physical ingredients, which are not clear due to the intuitive nature of the work.

The paper is organized as follows. In section 2, we first present a reminder of Stewartson's approach. We propose a simple criterion which defines the limit of validity of the theory presented in section 3. The main steps of the theory are given in the body of the article, while the tedious details of the calculations are gathered in the appendices. Precisions concerning the regime of applicability of Wedemeyer's theory are given at the end of section 3. In section 4, theoretical results are tested for a large range of physical parameters (Reynolds number Re, fluid-solid inertia ratio κ) by means of numerical simulations. Discrepancies between the numerical results and the present theory are discussed at the end of the section.

2. Presentation of the problem

2.1. *Definition of the frame of reference - Kinematics*

A cylindrical cavity full of fluid (viscosity μ, density ρ, kinematic viscosity $\nu = \mu/\rho$) is included in an axisymmetrical solid rigid body. Both solid and fluid parts of the gyroscope have the same axis of symmetry $\hat{\mathbf{k}}$. The centre of gravity of the whole system is supposed to be located at the centroid of the cylindrical cavity and we assume the mass of fluid is relatively small compared to that of the solid. $\mathcal{R}_0$ denotes the inertial reference frame.

Two sets of non inertial frames are then introduced, depending on whether we are interested in the hydrodynamics of the contained liquid or in the fluid-structure coupled dynamics. Unitary vectors related to a given reference frame are refered to as $\hat{\mathbf{x}}$, $\hat{\mathbf{y}}$ and $\hat{\mathbf{z}}$ with the appropriate subscript. The first set of reference frames ($\mathcal{R}_\psi$, $\mathcal{R}_\theta$, $\mathcal{R}_\phi$), suitable for the hydrodynamics, corresponds to the classic Euler's coordinates (ψ, θ, ϕ), as shown on

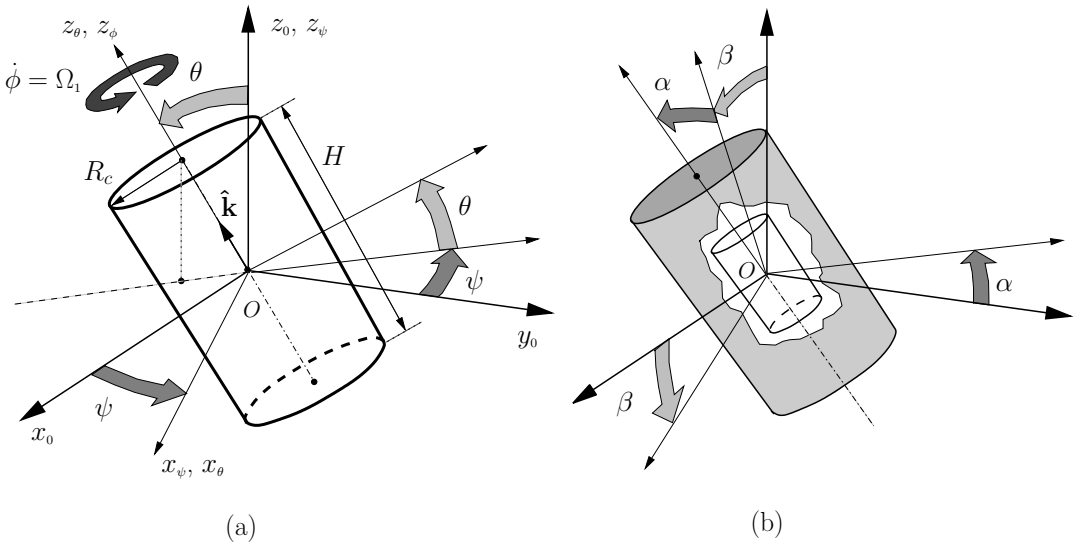

FIGURE 1. Definition of the frames of reference. (a) Euler's angles suitable for hydrodynamics. (b) Cardan's angles suitable for coupled fluid-structure dynamics.

Fig. 1(a). In the reference frame of the cylinder $\mathcal{R}_\phi$, the position of any point is defined by its polar coordinates $(R,\, \varphi,\, Z)$. Integrality of the theoretical analysis for hydrodynamics is achieved in $\mathcal{R}_\phi$. In the remainder of the text, spin angular velocity $\dot\phi$ and precessional velocity $\dot\psi$ are refered to as Ω_1 and Ω_2 respectively. $\mathbf{\Omega}$ is the time-dependent rotation vector of the whole system.

The second set $(\mathcal{R}_\alpha, \mathcal{R}_\beta)$, suitable for the study of the coupled fluid-structure dynamics, corresponds the the Cardan's coordinates $(\alpha,\, \beta)$ as depicted in Fig. 1(b). Actually, $\mathcal{R}_\alpha$ and $\mathcal{R}_\beta$ are the natural reference frames for classic experimental gyroscopes.

2.2. *Formulation of hydrodynamics*

The Navier-Stokes equations, written in the non-Galilean frame of reference $\mathcal{R}_\phi$ take on the following form

$$\frac{\partial \mathbf{U}}{\partial T} + (\mathbf{U}\cdot\boldsymbol{\nabla})\,\mathbf{U} + 2\,\mathbf{\Omega}\times\mathbf{U} + \frac{\mathrm{d}\mathbf{\Omega}}{\mathrm{d}T}\times\mathbf{R} + \mathbf{\Omega}\times(\mathbf{\Omega}\times\mathbf{R}) = -\frac{1}{\rho}\,\boldsymbol{\nabla}P + \nu\boldsymbol{\Delta}\mathbf{U} \qquad (2.1a)$$

and

$$\boldsymbol{\nabla}\cdot\mathbf{U} = \mathbf{0}, \qquad (2.1b)$$

with the boundary condition $\mathbf{U} = \mathbf{0}$ at the walls. In equation (2.1a), $\mathbf{R}$, $\mathbf{U}$ and P refer to the radius vector, fluid velocity and pressure respectively. The last three inertial terms of the left member are the Coriolis acceleration, the acceleration due to the non stationarity of $\mathbf{\Omega}$ and to centrifugal acceleration. As we consider the case $O' = O$, the term coming from the acceleration of the centre of gravity vanishes (otherwise, it could be incorporated in the pressure gradient). To specify the relative position of $\mathcal{R}_\phi$ and $\mathcal{R}_\theta$ at $T = 0$, we write

$$\mathbf{\Omega} = \Omega\,[\hat{\mathbf{k}} + \varepsilon\,\boldsymbol{\eta}(T)], \qquad (2.2)$$

with $\Omega = \mathbf{\Omega} \cdot \hat{\mathbf{k}} = \Omega_1 + \Omega_2 \cos\theta$, $\varepsilon = \Omega_2 \sin\theta/\Omega$ and $\boldsymbol{\eta}(T) = \cos(\Omega_1 T)\,\hat{\mathbf{x}}_\phi - \sin(\Omega_1 T)\,\hat{\mathbf{y}}_\phi$. Equation (2.1$a$) can be made dimensionless by choosing $\varepsilon\Omega R_c$, Ω^{-1} and R_c as typical scales for velocity, time and distance respectively. Using lowercase letters for dimensionless quantities and neglecting the non linear terms (proportional to ε^2), we obtain the linear dimensionless form of (2.1a)

$$\frac{\partial \mathbf{u}}{\partial t} + 2\,\hat{\mathbf{k}} \times \mathbf{u} + \boldsymbol{\nabla} p = -2\omega r \cos(\omega t + \varphi)\,\hat{\mathbf{k}} + \epsilon^2\,\boldsymbol{\Delta}\mathbf{u}, \tag{2.3}$$

where $\epsilon = (\Omega R_c^2/\nu)^{-1/2} = Re^{-1/2}$ is the small viscous parameter and $\omega = \Omega_1/\Omega$. The dimensionless pressure, which includes every potential terms, is

$$p = \frac{P}{\rho\varepsilon\Omega^2 R_c^2} - \frac{1}{2}\frac{r^2}{\varepsilon} + (1-\omega) r z \cos(\omega t + \varphi). \tag{2.4}$$

Further comments must be made on the hypothesis of linearization of equation (2.1a). For the non linear effects to be negligible in comparison with the viscous ones, the ratio ϵ^2/ε must be greater than 1. This condition can be rewritten $\theta < |1-\omega|^{-1} Re^{-1}$. As the forcing frequency and the Reynolds number are known in each case, the limit angle beyond which the non linear effects intervene is fixed (at least in order of magnitude).

In the remainder of the paper, (u, v, w) are the dimensionless cylindrical components of $\mathbf{u}$ in the reference frame $\mathcal{R}_\phi$ and, for the sake of concision in the notations, $\mathbf{v} = (\mathbf{u},\, p)$ designates the velocity-pressure field.

Let us give now the expression of the complex solution to the inviscid form ($\epsilon = 0$) of equation (2.3). The inviscid flow $\mathbf{v}^{(0)}$ in a forced precessing cylinder has been calculated by several authors (cf. Greenspan (1968) for example). It can be sought in the form of a particular solution $\mathbf{v}_{\text{part.}}$ completed by an infinite sum of Kelvin modes

$$\mathbf{v}^{(0)} = \mathbf{v}_{\text{part.}} + \sum_{i=1}^{\infty} a_i^{(0)} \mathbf{v}_i^{(0)}\, \mathrm{e}^{\mathrm{i}(\omega t + \varphi)}. \tag{2.5}$$

In the previous expression, $\mathbf{v}_i^{(0)} \mathrm{e}^{\mathrm{i}(\omega t+\varphi)}$ is the Kelvin mode of axial wavenumber $k_i^{(0)}$, radial wave number $\delta_i^{(0)}$ and frequency ω with

$$\mathbf{v}_i^{(0)} = \begin{pmatrix} \mathrm{i}\dfrac{\omega r \delta_i^{(0)} J_1'(\delta_i^{(0)} r) + 2 J_1(\delta_i^{(0)} r)}{r(\omega^2 - 4)} \sin(k_i^{(0)} z) \\ -\dfrac{2 r \delta_i^{(0)} J_1'(\delta_i^{(0)} r) + \omega J_1(\delta_i^{(0)} r)}{r(\omega^2 - 4)} \sin(k_i^{(0)} z) \\ \mathrm{i}\dfrac{k_i^{(0)}}{\omega} J_1(\delta_i^{(0)} r) \cos(k_i^{(0)} z) \\ J_1(\delta_i^{(0)} r) \sin(k_i^{(0)} z) \end{pmatrix}, \tag{2.6}$$

and the particular solution is

$$\mathbf{v}_{\text{part.}} = (0,\, 0,\, 2\mathrm{i}r\mathrm{e}^{\mathrm{i}(\omega t+\varphi)},\, 0). \tag{2.7}$$

In the following, $u_i^{(0)}$, $v_i^{(0)}$, $w_i^{(0)}$, and $p_i^{(0)}$ denote the four components of $\mathbf{v}_i^{(0)}$. The amplitude

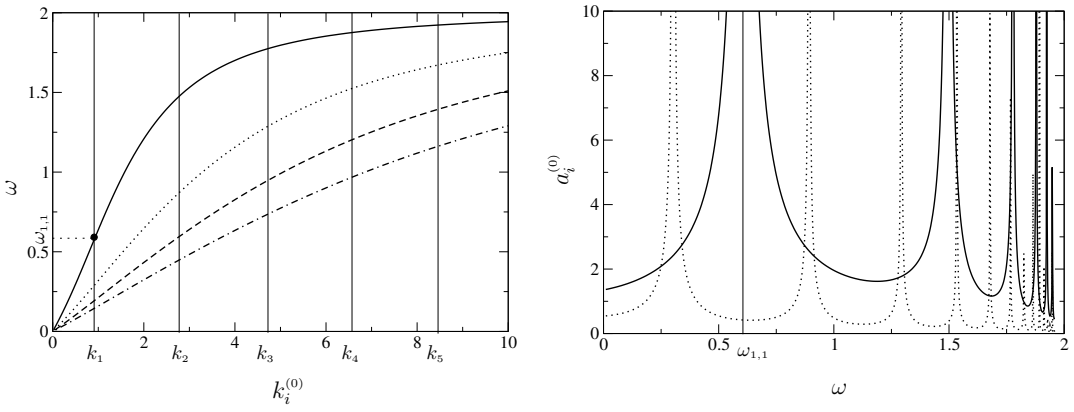

FIGURE 2. Inviscid theory for a precessing cylinder full of fluid ($R_c = 0.33$ m, $H = 0.1$ m). (a) Kelvin's relation of dispersion. Only the first four branches are plotted. $i = 1$ (solid), $i = 2$ (dotted), $i = 3$ (dashed), $i = 4$ (dot-dashed). (b) Amplitude of the first two Kelvin modes given by the inviscid theory. $i = 1$ (solid), $i = 2$ (dotted). Numerical simulations presented in section 4 are performed around the first resonance of the first mode $\omega_{1,1} = 0.605$.

$a_i^{(0)}$ of each Kelvin mode is given by

$$a_i^{(0)} = \frac{4\omega^2}{(\omega - 2)({k_i^{(0)}}^2 + 1)k_i^{(0)} J_1(\delta_i^{(0)}) \cos(k_i^{(0)} h)}, \tag{2.8}$$

where $h = H/2R_c$. The radial wavenumber $\delta_i^{(0)}$ satisfies the Kelvin's relation

$$\omega \delta_i^{(0)} J_1'(\delta_i^{(0)}) + 2J_1(\delta_i^{(0)}) = 0, \quad \text{with } |\omega| < 2 \tag{2.9}$$

and the axial wavenumber $k_i^{(0)}$ the constitutive relation

$${\delta_i^{(0)}}^2 = \frac{4 - \omega^2}{\omega^2} {k_i^{(0)}}^2. \tag{2.10}$$

The first four Kelvin branches corresponding to the dispersion relation (2.9-2.10) are plotted in Fig. 2(a). As shown by the expression (2.8), the amplitude $a_i^{(0)}$ of each Kelvin mode diverges (see Fig. 2(b)) for an infinity of wavenumbers $k_n = \pi(2n - 1)/2h$ (with n a non zero integer) for which the quantity $\cos(k_i^{(0)} h) = 0$. Thus, in the range $]-2, 2[$, a double infinity of resonant frequencies $\omega_{i,n}$ is obtained by considering on each branch the frequencies for which $k_i^{(0)} = k_n$. Note that the expression (2.8) does not hold any longer for ω in a close vicinity of any $\omega_{i,n}$, where Gans' expression of viscously saturated amplitude proved to be more relevant.

2.3. *Coupled dynamics formulation and Milne-Stewartson's theory*

Since the only torque acting on the solid part of the gyroscope comes from the hydrodynamic stress, one can write

$$\frac{d\,\mathcal{J}\boldsymbol{\Omega}}{dt} = \boldsymbol{M}, \tag{2.11}$$

where $\boldsymbol{\mathcal{J}}$ is the inertial tensor (which is diagonal in $\mathcal{R}_{phi}$), and $\boldsymbol{M}$ the hydrodynamic torque resulting from the integration of hydrodynamic constraints on the cavity walls. In (2.11), the time derivative is considered in $\mathcal{R}_0$. Projecting equation (2.11) on the x_α and y_α axis leads to the system

$$A\,\ddot{\alpha} + C\,\Omega\,\dot{\beta} = M_{x_\alpha}, \tag{2.12a}$$

$$A\,\ddot{\beta} - C\,\Omega\,\dot{\alpha} = M_{y_\alpha}, \tag{2.12b}$$

where A and C respectively denote the transverse and lengthwise inertia momenta of the solid part of the gyroscope ($\boldsymbol{\mathcal{J}} = [A,\, A,\, C]$ in $\mathcal{R}_{phi}$). (2.12) is equivalent to the more convenient form

$$A\ddot{\zeta} - \mathrm{i}C\Omega\dot{\zeta} = M_{y_\alpha} - \mathrm{i}M_{x_\alpha}, \tag{2.13}$$

where $\zeta = \beta - \mathrm{i}\alpha$ is the complex angular variable. In the linearized equations (2.12) and (2.13), quadratic terms involving α, β and their time derivatives are neglected owing to the assumption $\alpha,\, \beta \ll 1$, which is required for consistency with the earlier assumption of small coning angles. For an empty cavity ($\boldsymbol{M} = \boldsymbol{0}$), the solid describes the classic precessional Poinsot's motion for which the axis $\hat{\mathbf{k}}$ generates a cone of a fixed half-angle θ at the angular velocity $\Omega_2 = (C/A)\,\Omega$. In this case $\zeta = \theta\,\exp(\mathrm{i}\,\Omega_2\,T)$, Ω_2 being a real number. In the general case of a fluid-filled cavity, ζ is to be sought in the same form, but with Ω_2 in the complex domain. The characteristic time of aperture of the coning angle then equals $[\mathrm{Im}(\Omega_2)]^{-1}$.

Following Stewartson, we first consider in $\boldsymbol{M}$ the only contribution $\boldsymbol{M}^{(0)}$ of the inviscid flow (2.5). $\boldsymbol{M}^{(0)}$, which results from the integration of $p^{(0)}$ over the cavity walls, can be written in the reference frame $\mathcal{R}_\alpha$ as a function of ω and the dimensionless precession frequency $s = \Omega_2/\Omega$. We obtain

$$\boldsymbol{M}^{(0)} = \rho\varepsilon\Omega^2 R_c^5 \left[m^{(0)} + 2\pi h\,(1-\omega)\left(\frac{h^2}{3} - \frac{1}{4}\right)\right]\,\mathrm{e}^{\mathrm{i}\,st}\,[\hat{\mathbf{y}}_\alpha + \mathrm{i}\,\hat{\mathbf{x}}_\alpha], \tag{2.14}$$

where

$$m^{(0)} = 2\pi\,\sum_{i=1}^{\infty} a_i^{(0)}\left[\frac{J_2(\delta_i^{(0)})}{\delta_i^{(0)}}\sin(k_i^{(0)}h) - \frac{J_1(\delta_i^{(0)})}{{k_i^{(0)}}^2}[\sin(k_i^{(0)}h) - (k_i^{(0)}h)\cos(k_i^{(0)}h)]\right] \tag{2.15}$$

is $O(1)$. Let us now consider a unique resonant frequency ω_0 among the double infinity of $\omega_{i,n}$. We assume ω_0 is far enough from any other main hydrodynamic resonance. The relevance of this assumption is partially ensured by the viscous criterion of viability established by Gans (1970). Gans' inequality $\delta_i^{(0)} < Re^{1/7}$ stipulates that for a given Reynolds number, the Kelvin modes of high radial wave numbers cannot be forced, due to the viscous effects. For sufficiently low Reynolds numbers, this condition is likely to drastically reduce the density of resonances in the vicinity of ω_0. Considering the values of Re used in the present paper, the resonance $\omega_0 = \omega_{1,1}$ (which is examined further) will be regarded as isolated, but such a verification must be performed in each particular case.

So, the main diverging term is therefore kept in the Laurent's expansion of the involved

Kelvin mode, namely

$$m^{(0)} \simeq \frac{D^{(0)}}{\omega_0 - \omega}. \tag{2.16}$$

The expression of $D^{(0)}$ is given in appendix A. Using the previous expression of $m^{(0)}$ and the general form $\zeta = \theta \exp(\mathrm{i}\, st)$ in equation (2.13), we can rewrite the latter as a polynomial equation of variable s

$$-s + \sigma = \kappa \frac{D^{(0)}}{s - s_0}, \tag{2.17}$$

where

$$\sigma = C/A', \;\; \kappa = \rho R_c^5/A', \;\; s_0 = 1 - \omega_0 \;\text{ and }\; A' = A + 2\pi \left(\frac{h^2}{3} - \frac{1}{4}\right). \tag{2.18}$$

To derive equation (2.17), it is recalled that the case of small coning angles is considered, for which the approximations $s \simeq 1 - \omega$ and $\varepsilon \simeq \theta\, s$ are valid. Moreover, the assumption of quasi-staticity of the coning angle θ is supposed to be satisfied, namely $\dot{\theta} \ll \theta\Omega_2$ at any time. Actually, in the coupled situation, the part of the term $d\mathbf{\Omega}/dT$ in (2.1a) coming from the variation of the nutation angle θ (recal that $\dot{\theta} = 0$ in the forced regime), must be negligible compared to the one coming from the precession. This condition, that can be rewritten $\mathrm{Im}(s)/\mathrm{Re}(s) \ll 1$, defines the limit of use of the flow (2.5) in a situation in which θ is free to evolve. In other words, the equation (2.17) is valid for complex values of s, as long as $\mathrm{Im}(s) \ll \mathrm{Re}(s)$.

The physically acceptable solution to equation (2.17) depends on the range in which the inertia ratio σ lies

$$s = \frac{1}{2}\left[(\sigma + s_0) - \mathrm{i}[4\kappa D^{(0)} - (\sigma - s_0)^2]^{1/2}\right] \quad \text{for} \;\; |\sigma - s_0| < 2\sqrt{\kappa D^{(0)}} \tag{2.19a}$$

$$s = \frac{1}{2}\left[(\sigma + s_0) - [(\sigma - s_0)^2 - 4\kappa D^{(0)}]^{1/2}\right] \quad \text{for} \;\; \sigma < s_0 - 2\sqrt{\kappa D^{(0)}} \tag{2.19b}$$

$$s = \frac{1}{2}\left[(\sigma + s_0) + [(\sigma - s_0)^2 - 4\kappa D^{(0)}]^{1/2}\right] \quad \text{for} \;\; \sigma > s_0 + 2\sqrt{\kappa D^{(0)}} \tag{2.19c}$$

All the previous results have been established by Milne (1940) and Stewartson (1958), for the case of spheroidal and cylindrical cavities respectively. The reduced growth rate $\mathrm{Im}(s)$ is plotted as a function of the inertia ratio σ in Fig. 3(a). As shown in the plot, inertial effects at $Re = \infty$ make the fluid-filled gyroscope unstable in a range of width $4\sqrt{\kappa D^{(0)}}$ around s_0. The maximum rate of divergence is $\sqrt{\kappa D^{(0)}}$.

2.4. *Criterion of applicability for corrected Stewartson's theories*

As the main objective of the paper is to extend rigorously Stewartson's inviscid theory to the case of a viscous liquid, we have to figure out in which case (that is for which set of physical parameters) such an approach can be adopted (rather than Gans' approach).

First, the point is to evaluate the width $\Delta\omega$ of the Gans' "window", that is to say the range of forcing frequency in which the amplitude of the main flow is saturated by the viscous effects. Based on Meunier's modified Gans' theory (2008), one can show that the inviscid solution (2.5) is not valid anymore, as soon as the forcing frequency lies in a

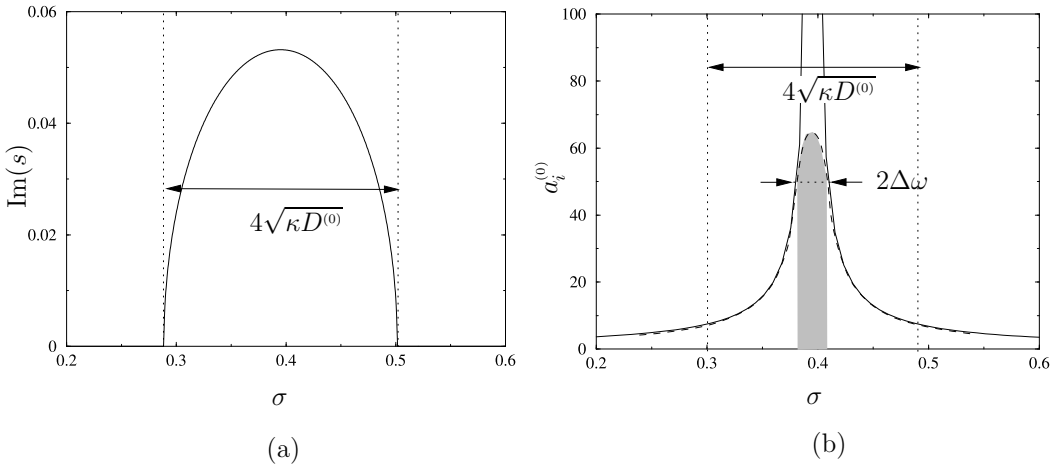

FIGURE 3. Criterion of validity for corrected Stewartson's theories. In these plots, we used $\kappa = 0.003$, $D^{(0)} = 0.9493$ and $\epsilon = 0.009$. (a) Imaginary part of s as a function of the inertial ratio σ. (b) inviscid (solid) and viscous (dashed) amplitudes of the Kelvin mode. The criterion of applicability (2.21) characterizes the width of the inviscid unstable domain (Stewartson's theory for the coupled problem) compared to the width of the hydrodynamic viscous domain.

domain of width

$$\Delta\omega \sim \epsilon\, \overline{a}^{(0)} f^{-1} \max[|\mu|, \epsilon\nu] \tag{2.20}$$

around the resonance. Details of the derivation of the previous expression are given in appendix B. In (2.20) , μ, ν and f are the surface and volume viscous parameters and the forcing parameter derived by Meunier (2008), the expressions of which are also reminded in appendix B. The expression of $\overline{a}^{(0)}$ is given in appendix A (the i-subscript has been removed since there is no ambiguity about the resonance).

Thus, for a forcing frequency of width $\Delta\omega$ around ω_0, the inviscid solution is diverging, which makes any corrective approach irrelevant. It therefore appears natural to expect any Stewarton's corrected approach to be of interest provided the inviscid unstable domain (of width $\sim \sqrt{\kappa D^{(0)}}$) is wider than the range of viscous saturation $\Delta\omega$, namely (see Fig. 3)

$$\sqrt{\kappa} > \epsilon \frac{\overline{a}^{(0)}}{2\sqrt{D^{(0)} f}} \max[|\mu|, \epsilon\nu]. \tag{2.21}$$

Inequation (2.21) constitutes a (sufficient) criterion of applicability of the theory presented in the next section. In other words, (2.21) tells us if there is or not a domain where Stewartson's corrected theories are relevant. However, (2.21) does not tell us in which domain of forcing frequency these theories can be used. Actually, for the theory presented in the next section to apply, the forcing frequency ω must stand outside the Gans' window, namely

$$|\omega - \omega_0| > \Delta\omega. \tag{2.22}$$

The previous inequality can be rewritten using the inertia parameter $\sigma = C/A'$ and

considering that $\sigma \simeq \mathrm{Re}(s) \simeq 1 - \omega$

$$|1 - \sigma - \omega_0| > \Delta\omega. \tag{2.23}$$

This previous criterion of validity characterizes the *corrected inertial regime*, that is to say the domain of forcing frequency in which the Stewartson's corrected theories apply.

3. Treatment of viscous effects in the corrected inertial regime

The pressure torque calculated from the inviscid solution becomes destabilizing in a domain of frequency of width $4\sqrt{\kappa D^{(0)}}$ around ω_0. Nonetheless, experiments performed by Karpov (1962, 1965) with real liquids clearly show a non zero growth rate outside the inviscid unstable domain. Unlike Wedemeyer, we present in the next section a direct calculation of the viscous corrections responsible for instance of such a broadening of the unstable region. The connection with Wedemeyer's theoretical results is made afterwards.

In the inertial coupling limit, the global velocity-pressure field is sought in the form of a double ϵ-expansion $\mathbf{v} = \mathbf{v}_{\mathrm{out}} + \mathbf{v}_{\mathrm{in}}$ with

$$\mathbf{v}_{\mathrm{out}} = \mathbf{v}^{(0)} + \epsilon\,\mathbf{v}^{(1)} + O(\epsilon^2) \ \text{ in the bulk,} \tag{3.1a}$$

$$\mathbf{v}_{\mathrm{in}} = \widetilde{\mathbf{v}}^{(0)} + \epsilon\,\widetilde{\mathbf{v}}^{(1)} + O(\epsilon^2) \ \text{ inside the boundary layer.} \tag{3.1b}$$

In addition, the condition $\mathbf{v}_{\mathrm{in}} = \mathbf{0}$ outside the boundary layer is required.

3.1. *Viscous and pressure torques*

Before going further, the relative orders of magnitude of the torques must be discussed. Quantities with dimension are therefore considered to the end of this paragraph. A hydrodynamic torque corresponds to each term of the previous expansions. Thus, $\boldsymbol{M}^{(0)}$, which intervenes in Stewartson's theory, results from the integration of the pressure at leading order in bulk over the cavity walls. In the following, $\widetilde{\boldsymbol{M}}^{(0)}$ notes the torque due to the viscous shear at leading order, $\boldsymbol{M}^{(1)}$ and $\widetilde{\boldsymbol{M}}^{(1)}$ designate the torques resulting from integration of the pressures at order ϵ outside and inside the boundary layer respectively. Note that the torque resulting from the pressure at leading order in the boundary layer is always zero (see appendix C).

As shown by (2.14), $\boldsymbol{M}^{(0)}$ is of the same order of magnitude as the scaling factor $\rho\varepsilon\Omega^2 R_c^5$ whereas $\widetilde{\boldsymbol{M}}^{(0)}$ proves to be one order greater in ϵ, that is $\widetilde{\boldsymbol{M}}^{(0)} \sim \epsilon\boldsymbol{M}^{(0)}$. Indeed, as the viscous constraint at leading order is of order $\mu\epsilon^{-1}\varepsilon\Omega$, the order of magnitude of the corresponding torque is $\mu\epsilon^{-1}\varepsilon\Omega R_c^3 = \rho\varepsilon\epsilon\Omega^2 R_c^5$. Generally, it can be shown that the shear torque $\widetilde{\boldsymbol{M}}^{(q)}$ calculated at a given order ϵ^q in velocity is of the order $\epsilon\boldsymbol{M}^{(q)}$, where $\boldsymbol{M}^{(q)}$ is the torque calculated at the same order ϵ^q in pressure. Consequently, taking account only of the torque $\widetilde{\boldsymbol{M}}^{(0)}$ for the coupling as Murphy (1982) is altogether questionable, the pressure torques $\boldsymbol{M}^{(1)}$ and $\widetilde{\boldsymbol{M}}^{(1)}$ beeing of the same order. This also means that the pressures at order ϵ inside and outside the boundary layer must be derived explicitely. As shown in paragraph 3.4, the main contribution of the viscous destabilization comes from the torque $\boldsymbol{M}^{(1)}$.

3.2. *Flows at leading order and order ϵ*

In principle, a direct integration of the N.-S. equations could lead to the expression of the flow at order ϵ in bulk. However, to avoid such a tedious pathway, it can be seen that both flows at leading order and at order ϵ satisfy the same inviscid N.-S. equations in bulk (if we forget the forcing term). This suggests seeking $\mathbf{v}^{(1)}$ by expanding the radial and lengthwise wavenumbers $\delta_i = \delta_i^{(0)} + \epsilon\delta_i^{(1)}$ and $k_i = k_i^{(0)} + \epsilon k_i^{(1)}$ in a global field $\mathbf{v}_{\rm out}$ of the same shape as the inviscid solution $\mathbf{v}^{(0)}$.

As we'll see further, this is not sufficient to satisfy the boundary conditions at order ϵ on top and bottom walls. The solution is to complete the ϵ-expanded flow by an additional flow "parallel" to $\mathbf{v}^{(0)}$ (same shape, same wave numbers $\delta_i^{(0)}$ and $k_i^{(0)}$, but different amplitudes a_i^+ of the Kelvin modes). Note that doing this is equivalent to expanding the amplitude in the flow $\mathbf{v}_{\rm out}$. This extra flow does not disturb the boundary condition on the lateral wall but permits the normal velocity at order ϵ to equal the Ekman pumping on the top and bottom wall.

Consequently the flow in the bulk $\mathbf{v}_{\rm out}$ can be written

$$\mathbf{v}_{\rm out} = \mathbf{v}^{(0)} + \epsilon \sum_{i=1}^{\infty} \left[a_i^+ \mathbf{v}_i^{(0)} + a_i^{(0)} \left(\delta_i^{(1)} \frac{\partial \mathbf{v}_i^{(0)}}{\partial \delta_i} + k_i^{(1)} \frac{\partial \mathbf{v}_i^{(0)}}{\partial k_i} \right) \right] \mathrm{e}^{\mathrm{i}(\omega t + \varphi)} + O(\epsilon^2), \tag{3.2}$$

where all the partial derivatives are considered at $(\delta_i^{(0)},\, k_i^{(0)})$. The amplitudes $a_i^{(0)}$ are still unknown at this stage.

The shape of the velocity-pressure field is fixed by the previous equation in which the unknown quantities $\delta_i^{(1)}$ and $k_i^{(1)}$ must be determined in order to satisfy the boundary conditions at order ϵ. In practice, the normal component of the velocity at order ϵ in bulk must equal the Ekman pumping at the wall, which results from the non homogeneity of the corrective viscous flow in the boundary layer (see e.g. Waleffe (1989)).

Leading order

We shall not revert to the resolution of the inviscid flow $\mathbf{v}^{(0)}$ given in §2.2. At this stage, the amplitudes $a_i^{(0)}$ are fixed by the inviscid boundary condition of tangential velocity at the walls. The classical derivation of the corrective viscous flow $\widetilde{\mathbf{v}}^{(0)}$ is given in appendix C.

Order ϵ

The expressions of the normal Ekman components $u_i^{\perp}\mathrm{e}^{\mathrm{i}(\omega t+\varphi)}$ (on the lateral wall) and $w_i^{\perp}\mathrm{e}^{\mathrm{i}(\omega t+\varphi)}$ (on the top and bottom walls) arising from the $i^{\rm th}$ Kelvin mode are also given in appendix C. The boundary condition at order ϵ applied to the flow given by (3.2) for a unique Kelvin mode

$$a_i^{(0)} \delta_i^{(1)} \frac{\partial u_i^{(0)}}{\partial \delta_i} = u_i^{\perp} \quad \text{at } r = 1 \tag{3.3}$$

leads to the expression of $\delta_i^{(1)}$ (see again appendix C for details)

$$\delta_i^{(1)} = \frac{1-\mathrm{i}}{\sqrt{2\omega}}\, \delta_i^{(0)}. \tag{3.4}$$

Once the expression of $\delta_i^{(1)}$ has been established, the correction to the lenghtwise wavenumber $k_i^{(1)}$ is fixed by the constituting relation (2.10) (which is also valid at order ϵ) and can not be freely choosen to satisfy the boundary conditions at order ϵ on top and bottom walls. Indeed, as the global field $\mathbf{v}_{\text{out}}$ is a solution of the inviscid N.-S. equation, the quantities $\delta_i^{(0)} + \epsilon\delta_i^{(1)}$ and $k_i^{(0)} + \epsilon k_i^{(1)}$ are connected by the constituting relation

$$[\delta_i^{(0)} + \epsilon\delta_i^{(1)}]^2 = \frac{4-\omega^2}{\omega^2}\,[k_i^{(0)} + \epsilon k_i^{(1)}]^2, \tag{3.5}$$

which involves

$$\delta_i^{(1)\,2} = \frac{4-\omega^2}{\omega^2}\,k_i^{(1)\,2}. \tag{3.6}$$

Due to this lack of available "degree of freedom", the introduction of the extra flows $a_i^+\mathbf{v}_i^{(0)}$ turns to be indispensable in order to properly compensate the Ekman pumping on top and bottom walls.

So, at the top and bottom walls, we have

$$a_i^{(0)}\left[\delta_i^{(1)}\frac{\partial w_i^{(0)}}{\partial \delta_i} + k_i^{(1)}\frac{\partial w_i^{(0)}}{\partial k_i}\right] + a_i^+\,w_i^{(0)} = w_i^\perp \quad \text{for } z = \pm h. \tag{3.7}$$

The calculation of the amplitudes a_i^+ of the Kelvin modes in the additional flow is exhaustively presented in appendix D. Thus, the boundary conditions at every wall are satisfied, and we finally get the pressure related to the flow in the bulk at order ϵ

$$p^{(1)} = \sum_{i=1}^{\infty} a_i^{(0)}\left[\delta_i^{(1)}\frac{\partial p_i^{(0)}}{\partial \delta_i} + k_i^{(1)}\frac{\partial p_i^{(0)}}{\partial k_i}\right]\,\mathrm{e}^{\mathrm{i}(\omega t+\varphi)} + \sum_{i=1}^{\infty} a_i^+\,p_i^{(0)}\,\mathrm{e}^{\mathrm{i}(\omega t+\varphi)}. \tag{3.8}$$

The pressure $\widetilde{p}^{(1)}$ in the boundary layer can be directly obtained by integrating the systems of equations (C 1*a*) and (C 1*b*) given in appendix C. The expression of $\widetilde{p}^{(1)}$ is given in appendix E.

3.3. *Coupled dynamics*

The new equation of coupling takes the following form

$$-s + \sigma = \kappa\,[m^{(0)} + \epsilon(\widetilde{m}^{(0)} + m^{(1)} + \widetilde{m}^{(1)})]\,. \tag{3.9}$$

The expressions of the complex torques $m^{(1)}$, $\widetilde{m}^{(1)}$ and $\widetilde{m}^{(0)}$ are collated in appendix E. As specified above, these torques result from the integration of $p^{(1)}$, $\widetilde{p}^{(1)}$ and the viscous stress related to $\widetilde{\mathbf{u}}^{(0)}$ respectively.

Following again Stewartson (inviscid coupling), each torque can be replaced by its Laurent's expansion. In this case, expansions are truncated after the last diverging term. For instance, the torques $\widetilde{m}^{(0)}$ and $\widetilde{m}^{(1)}$ which only contain poles of order 1, can be written

$$\widetilde{m}^{(0)} = \frac{\widetilde{D}_R^{(0)}}{s-s_0} + \mathrm{i}\,\frac{\widetilde{D}_I^{(0)}}{s-s_0}, \tag{3.10a}$$

$$\widetilde{m}^{(1)} = \frac{\widetilde{D}_R^{(1)}}{s-s_0} + \mathrm{i}\,\frac{\widetilde{D}_I^{(1)}}{s-s_0}. \tag{3.10b}$$

Expressions of the real quantities $\widetilde{D}_R^{(0)}$, $\widetilde{D}_I^{(0)}$, $\widetilde{D}_R^{(1)}$ and $\widetilde{D}_I^{(1)}$ are collated in appendix E.

(i,n)	$\omega_{i,n}$	$\widetilde{D}_R^{(0)}$	$\widetilde{D}_I^{(0)}$	$\widetilde{D}_R^{(1)}$	$\widetilde{D}_I^{(1)}$	$C_R^{(1)}$	$C_I^{(1)}$	$D_R^{(1)}$	$D_I^{(1)}$
(1, 1)	0.6047	-1.6326	1.3488	5.0075	5.0075	0.2676	1.2304	-4.7988	-1.6445
(1, 2)	1.4961	-0.7388	1.3982	0.0616	0.0616	0.01	-0.1489	1.0049	3.4896
(2, 1)	0.3026	-0.1572	0.1166	1.4323	1.4323	0.0368	0.1481	-1.6148	-1.1687
(2, 2)	0.8922	-0.0497	0.1944	0.0227	0.0277	0.0005	0.0031	0.1867	0.5526

TABLE 1. Coefficients of Laurent's expansion of the torques at order ϵ evaluated at the first two resonances modes of the first two Kelvin modes $i = 1$ and $i = 2$, for a cylinder of aspect ratio $h = 1.65$.

As for the torque $m^{(1)}$, which contains poles of order 1 and 2, it can be written in the form

$$m^{(1)} = \left[\frac{C_R^{(1)}}{(s-s_0)^2} + \frac{D_R^{(1)}}{s-s_0}\right] + \mathrm{i}\left[\frac{C_I^{(1)}}{(s-s_0)^2} + \frac{D_I^{(1)}}{s-s_0}\right]. \tag{3.11}$$

Expressions of the real quantities $C_R^{(1)}$, $C_I^{(1)}$ are also given in appendix E. Tedious expressions of the real quantities $D_R^{(1)}$ and $D_I^{(1)}$ are not given exhaustively in the paper, but their values for the first two resonances of the Kelvin modes $i = 1$ and $i = 2$ for a cylinder of aspect ratio $h = 1.65$ are given in table 1.

At order ϵ, equation (3.9) is equivalent to

$$-s + \sigma = \kappa\left[\frac{D^{(0)} + \epsilon\,(D_R + \mathrm{i}D_I)}{s - [s_0 + \epsilon(s_R + \mathrm{i}\,s_I)]}\right], \tag{3.12}$$

where

$$D_R = \widetilde{D}_R^{(0)} + \widetilde{D}_R^{(1)} + D_R^{(1)}, \tag{3.13a}$$

$$D_I = \widetilde{D}_I^{(0)} + \widetilde{D}_I^{(1)} + D_I^{(1)}, \tag{3.13b}$$

$$s_R = C_R^{(1)}/D^{(0)}, \tag{3.13c}$$

$$s_I = C_I^{(1)}/D^{(0)}. \tag{3.13d}$$

3.4. *Comparison with Wedemeyer's approach*

Equation (3.12) makes the connection with Wedemeyer's theory. Indeed, Wedemeyer's characteristic equation of coupling (given for example in Whiting (1981)) is formally almost identical to (3.12) where D_R and D_I are set to zero. The difference comes from the important fact that Wedemeyer's method only takes into account the effects linked to the Ekman pumping, namely the quantities s_R and s_I in (3.12). The viscous shear torque $\widetilde{m}^{(0)}$, the pressure torque $\widetilde{m}^{(1)}$ are not considered in Wedemeyer's approach. Thus, if the contribution $\epsilon(D_R + \mathrm{i}D_I)$ is small compared to $D^{(0)}$, Wedemeyer's and the present theory are very close to each other, as shown in Fig. 4(a). They are completely superimposed if this quantity is neglected. When not negligible with respect to $D^{(0)}$, the quantity $\epsilon(D_R + \mathrm{i}D_I)$ is responsible for a possible asymmetry of the viscous tails.

Fig. 4(b) plots the inviscid coupling coefficient $D^{(0)}$ as a function of the aspect ratio h,

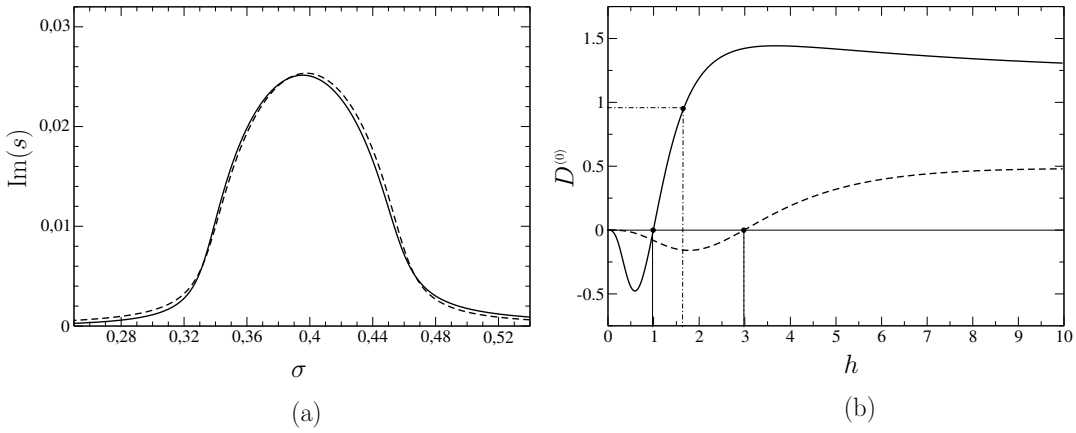

FIGURE 4. (a) Comparison of the present theory (solid line) with Wedemeyer's (dashed line) for the case II presented in the numerical section. Wedemeyer's and uncomplete present theory (obtained by taking D_R, $D_I = 0$) are superimposed. (b) $D^{(0)}$ plotted as a function of the aspect ratio h for the first (solid line) and second (dashed line) of the first Kelvin mode. For the first (resp. second) resonance, $D^{(0)} = 0$ at $h = 0.995$ (resp. $h = 2.985$).

for the first and second resonance of the first Kelvin mode, namely $\omega_{1,1}$ and $\omega_{1,2}$. For each resonance, $D^{(0)}$ cancels out at a given aspect ratio ($h = 0.995$ for the first resonance and $h = 2.985$ for the second resonance). For such aspect ratios, the respective weights of $D^{(0)}$ and $\epsilon(D_R + \mathrm{i}D_I)$ are inverted and Wedemeyer's theory is no longer suitable. Moreover, in a really close vicinity of these singular values, Laurent's expansions are not strictly valid either and must be taken one order further. Such a marginal treatment will be presented in a forthcoming communication. Note that most of the experimental studies for full cavities without an internal rod (see e.g. D'Amico (1977, 1981) and Whiting (1981)) have been performed for $h = 1$ and $h = 3$.

4. Numerical study

In this section, we present numerical studies performed in order to check the validity of the theoretical results reported in the previous section. The first part adresses the general features of the fluid dynamics code that is used in this study. In this part, the numerical coupling between the N.-S. equations and the container dynamics is briefly presented. The second part deals with the numerical results. We first present results related to the hydrodynamic flow in a forced regime (for which the kinematics of the container are fixed). Numerical results for the fluid-structure coupled dynamics are detailed afterwards. Numerical studies in forced and coupled regimes are made for a cavity of fixed aspect ratio $h = 1.65$ (heigth $H = 0.33$ m and radius $R_c = 0.1$ m). Ω is equal to 2π rad s^{-1} and the viscosity is varied to change the Reynolds number. The lengthwise inertia A is varied to change the fluid/solid inertia ratio. We focus on the first resonance of the first mode ($\omega_{1,1} = 0.605$) for which the criterion of applicability can be written in the simpler form $\sqrt{\kappa}/\epsilon < 1$, the rest of the right member of (2.21) being of order 1 in this case.

4.1. *Numerical schemes and parameters*

4.1.1. *Hydrodynamics*

N.-S. equations (2.1a) and (2.1b) are solved by means of an augmented Lagrangian method (Fortin (1982), Vincent (2000)). Equations of motion for the fluid are discretized with a finite volumes method on fixed staggered orthogonal cylindrical grids of type Maker And Cells (Harlow (1965)). To discretize the differential form (2.1a), a second order Euler scheme is used for the time derivative. The viscous and augmented Lagrangian terms are discretized thanks to a second order centered scheme. The resulting linear systems are solved using a Bi-CGSTAB II iterative method (van der Vorst (1992)), preconditioned under a Modified and Incomplete LU algorithm. A fully implicit order two integration scheme is used to perform time integration. A space and time convergence analysis guarantees the quality of the results. An example of numerical velocity field is presented in Fig. 5.

4.1.2. *Fluid-structure coupling*

In the numerical calculations, the Navier-Stokes equations (2.1) are solved without any simplification. Calculation of complementary inertial terms shown in (2.1a) requires the evaluation of $\mathbf{\Omega}$, the cartesian coordinates of which are Ω_{x_ϕ}, Ω_{y_ϕ}, and Ω_{z_ϕ}, in the reference frame $\mathcal{R}_\phi$. The rotation vector is obtained by numerical integration of the equations of motion for the solid. As the latter undergoes the hydrodynamic torque only, the evolution of its angular momentum takes the following form

$$\dot{\Omega}_{x_\phi} = (1 - C/A)\,\Omega_{y_\phi}\Omega_{z_\phi} + M_{x_\phi}/A, \tag{4.1a}$$

$$\dot{\Omega}_{y_\phi} = (C/A - 1)\,\Omega_{z_\phi}\Omega_{x_\phi} + M_{y_\phi}/A, \tag{4.1b}$$

$$\dot{\Omega}_{z_\phi} = M_{z_\phi}/C. \tag{4.1c}$$

The coupled problem is thus ruled by the equations (2.1) and (4.1). The coupling between the N.-S. equations and the equations of motion of the solid is performed thanks to a time splitting method : at the current time step, the N.-S. equations are solved using the coordinates of $\mathbf{\Omega}$ obtained at the previous step. The hydrodynamic torque $\boldsymbol{M}$ is computed by numerical integration of pressure and shear stress evaluated at the walls of the container. An Adams-Bashforth integration method of order four is used to perform the time integration of equations (4.1). This integration allows the update of $\mathbf{\Omega}$ and complementary acceleration terms in equation (2.1a) for the next step and so on.

4.2. *Numerical results and comparison with theory*

4.2.1. *Convergence analysis and forced regime*

The purpose of the studies in a forced regime is firstly to make a time and space convergence analysis, secondly to compare the amplitudes of the torque $\boldsymbol{M}^{(1)}$ with the theoretical prediction. It is in fact known that this quantity rules the process of destabilization far from the hydrodynamic resonance.

Only the space convergence analysis performed for a Reynolds number $Re = 12566$ is presented, that is for the following fluid parameters $\rho = 10^3$ kg m^{-3} and $\mu = 0.005$

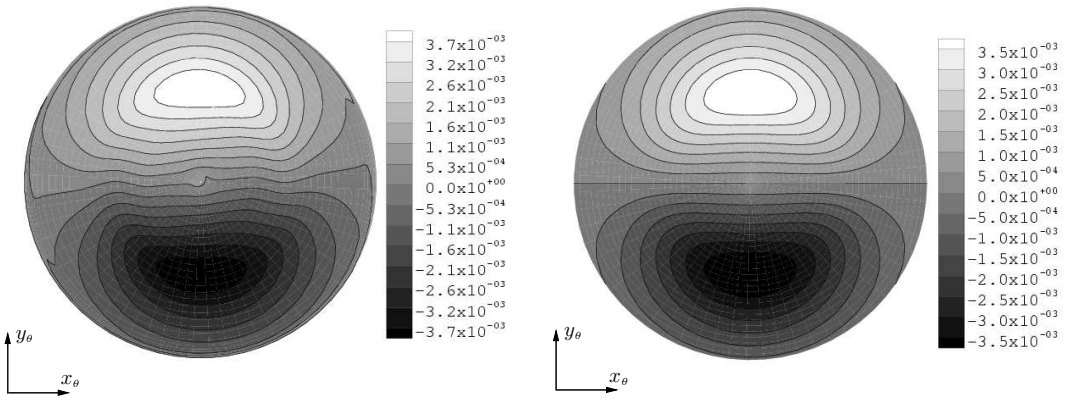

(a) (b)

FIGURE 5. Axial component of the real velocity field on a horizontal plane located at $z_\phi = 0$ in forced regime. Numerical values of the legend are given in m s^{-1}. The velocity field presented above corresponds to the following physical parameters : $\Omega = 2\pi$ rad s^{-1}, $\Omega_2 = 3.016$ rad s^{-1}, $R = 0.1$ m, $H = 0.33$ m, $\mu = 5\,10^{-3}$ Pa s and $\rho = 10^3$ kg m^{-3}. The dimensionless frequency, the Reynolds number and the non linear parameter are respectively $\omega = 0.520$, $Re = 12566$ and $\varepsilon = 1.6\,10^{-3}$. (a) Numerical field given at time $T = 40$ s. The transient stage is almost finished and lateral boundary layers are visible. (b) Analytical inviscid solution.

Pa s. The precession velocity choosen to make the analysis is $\Omega_2 = 1.508$ rad s^{-1}. The corresponding dimensionless forcing frequency $\omega = 0.520$ is located far from the resonance $\omega_{1,1} = 0.605$. As the main point of interest (regarding stability) is the component of the hydrodynamic torque M_{y_θ}, This quantity is used as the performance parameter in convergence analysis. Initially, the system is supposed to be in rigid rotation around the z_0 axis ($\theta = 0$). At $T = 0$, the system is instantaneously tilted towards a fixed coning angle $\theta = 0.1°$ and the flow slowly relaxes to a stationary state in the reference frame $\mathcal{R}_\theta$. To accurately take account of viscous effects, the boundary layers are meshed with cells of exponentially increasing size. A constant radial size is used to mesh the bulk. The characteristics of each mesh are given below in the form *number of radial divisions* × *number of azimutal division* × *number of lengthwise divisions* (*number of cells in the boundary layers*). The four main grids used in the convergence study at $Re = 12566$ are the following : $62 \times 80 \times 132\,(8)$, $50 \times 64 \times 104\,(8)$, $40 \times 50 \times 82\,(6)$, $32 \times 40 \times 64\,(5)$. When meshing, the characteristic size $(2\nu/\Omega)^{1/2}$ is considered to be representative of the boundary layer thickness, which is not entirely relevant since there are two different characteristic lengths for the top and bottom boundary layers (see expressions (C 8)). Besides, the number of cells in the boudary layer may appear insufficient to accurately capture the corrective flow but the comparison of analytic and numerical shear stresses shows a good agreement even with only five cells in the thickness. For this sole study, a time step of $2\,10^{-3}$ s is used. Nevertheless, as the calculations are very time consuming, the stationary state has to be estimated before the extinction of the transient stage. To

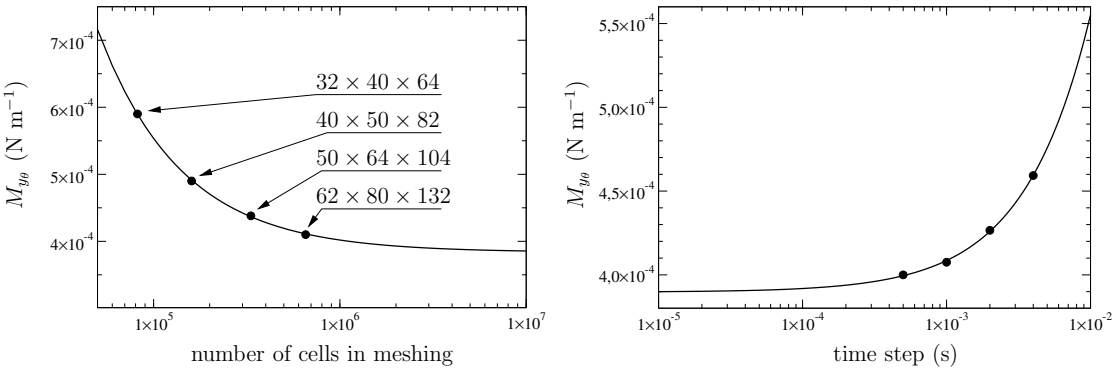

FIGURE 6. Convergence study in forced regime. (a) Space convergence : y_θ-component of the hydrodynamic torque (after stabilization) as a function of the number of cells. (b) Time convergence : y_θ-component of the hydrodynamic torque (after stabilization) as a function of the time step. Richardson's extrapolation is plotted in solid line. Numerical values are plotted in solid circles.

do so, we exploit the fact that the behaviour of the perturbed state is an exponentially damped sinus superimposed on a linear component. A convergence curve in space is presented in Fig. 6(a) in log-lin coordinates. The fit used to make the extrapolation to the smallest time steps is obtained by a Richardson's method.

In the time convergence analysis, the mesh $50\times64\times104(8)$ is selected and the same set of physical parameters as in the space convergence analysis presented above are used. A first computation is performed with a rough time step of $4\,10^{-3}$ s until a nearly stationary regime in $\mathcal{R}_\theta$ is reached. Then, a computation is made with smaller time steps until new converged values are obtained and so on. A time convergence curve is presented in Fig. 6(b) in lin-log coordinates. A power law is used for the extrapolation to the smallest time steps.

The conclusions related to the time and space convergence analysis are as follows : for low viscosities ($\mu = 0.001$ Pa s) a grid $50 \times 64 \times 104\,(8)$ is adopted ; for intermediate ($\mu = 0.005$ Pa s) and high viscosities ($\mu = 0.01$ Pa s), a coarser $50 \times 64 \times 64\,(6)$ grid is used. All studies are performed with a time step of 10^{-3} s, which seems to be a good compromise between precision and CPU calculation time.

The hydrodynamic torque at order ϵ must now be adressed. Numerical experiments enable to make the distinction between pressure and shear contributions to the hydrodynamic torque. These contributions are noted $\boldsymbol{M}^{\text{press}}$ and $\boldsymbol{M}^{\text{visc}}$ respectively. The configuration chosen (meshing and physical parameters) is the same as that used for the time convergence study. The y_θ-component of the pressure torque as a function of the forcing frequency ω is presented in Fig. 7(a) and both components of the shear torque are presented in Fig. 7(b). The forcing pulsation ω lies in the range [0.4, 0.8] which corresponds to the domain explored in the free coupling study (§4.2.2). Agreement between numerics and theory is good for the x_θ-components of the viscous torques. In the y_θ-direction, the

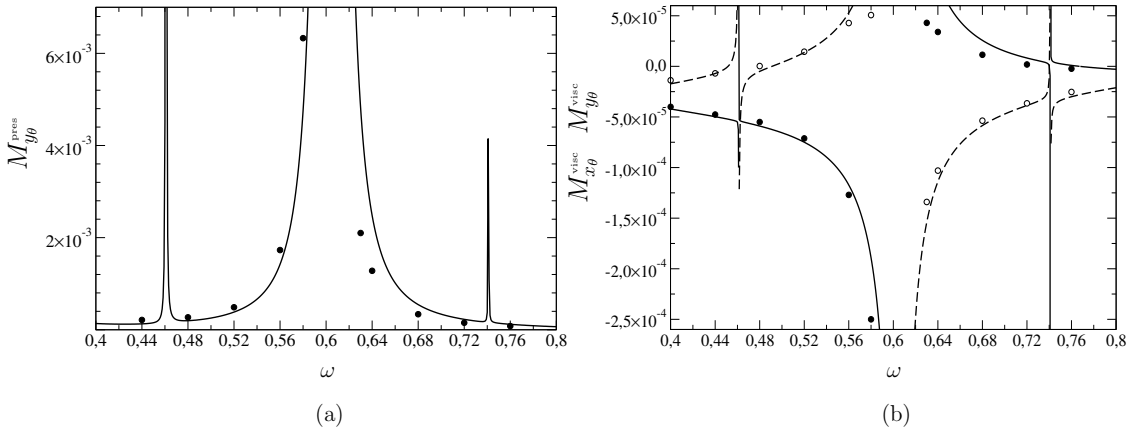

FIGURE 7. Hydrodynamic torque at order ϵ. (a) y_θ-component of the numerical pressure torque (closed circle). Component of the theoretical torque $\widetilde{\boldsymbol{M}}^{(1)} + \boldsymbol{M}^{(1)}$ in the y_θ-direction is plotted in solid line. (b) Components of the numerical shear torque in the x_θ-direction (open circles) and y_θ-direction (closed circles). Corresponding theoretical components $\widetilde{M}^{(0)}_{x\theta}$ and $\widetilde{M}^{(0)}_{y\theta}$ are plotted in dashed and solid lines respectiveley. Mesh and physical parameters are the same as in the time convergence study (see text).

case	$\boldsymbol{A}$ **(kg m²)**	$\boldsymbol{\rho}$ **(kg m⁻³)**	$\boldsymbol{\mu}$ **(Pa s)**	$\boldsymbol{Re}$	$\boldsymbol{\kappa}$	$\boldsymbol{\sqrt{\kappa}/\epsilon}$
I	5	1500	10^{-3}	94247	$3.0\,10^{-3}$	16.8
II	10	1000	$5.0\,10^{-3}$	12566	$9.36\,10^{-4}$	3.40
III	100	1000	10^{-2}	6280	10^{-4}	0.79

TABLE 2. Physical parameters for each case. κ and Re are given for information.

discrepancies for both pressure and viscous torques are greater on the right side of the resonance than on the left. This observation remains unexplained for the moment.

4.2.2. *Coupled regime*

Three numerical experiments (noted I, II, III) located in the corrected inertial regime are presented below. Initial conditions are the same as in the forced regime but the coning angle is free to evolve under the influence of the hydrodynamic torque. As stated in the first lines of the section, the geometry of the container and the value of $\Omega = 2\pi$ rad s^{-1} is the same for every case. The parameters varying from a case to another are collated in table 2. The ratio $\sqrt{\kappa}/\epsilon$, which is supposed to be greater than 1 for the present theory to be usable, is given in the last column. We notice that the third case stands at the edge of the domain of applicability of the present theory.

The configuration I is located in the inertial field since $\sqrt{\kappa}/\epsilon \gg 1$. In principle, the growth rate of the coning angle $\mathrm{Im}(s)$ (plotted as a function of ω in Fig. 9, 10 and 11) should have been obtained from numerical calculations by a simple estimation of the

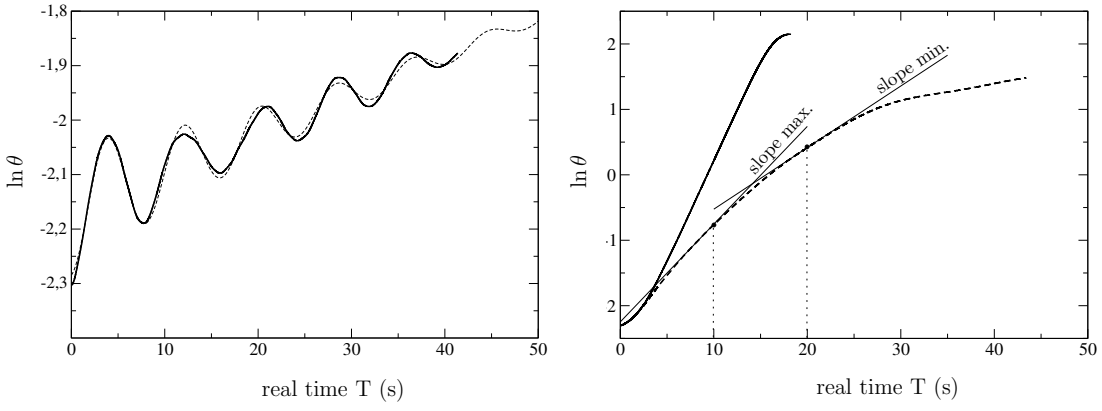

FIGURE 8. Coning angle (in degrees) as a function of the real time T for case I. (a) Outside the inviscid unstable domain, initial flow relaxes through damped oscillations. The solid line corresponds to $\sigma = 0.56$. The fitting curve is plotted in dashed line. (b) Non oscillating relaxation of the transcient stage. For $\sigma = 0.40$ (solid line), the evolution of the coning angle is exponential from 0.1° to about 5° and the growth rate can be evaluated without further interpretation. For $\sigma = 0.3$ (dashed line) the evolution is not straightforwardly exponential.

quantity $d\ln[\theta(T)]/dT$ in the very first seconds of destabilization. Unfortunately, the transient stage evolves through either oscillating or non oscillating decay, as illustrated in Fig. 8. Decaying oscillations correspond to situations in which the viscous effects are predominant (outside the inviscid unstable regime). In this case, estimation of the growth rate is given by assuming that the shape of $\ln[\theta(T)]$ results from the superposition of a linear term and an exponentially damped cosine. Such an identification process provides an accurate value of the growth rate $\mathrm{Im}(s)$. As we leave the viscously dominated region to enter the inviscid unstable domain, the identification of any possible linear regime proves to be difficult. The value chosen for $\mathrm{Im}(s)$ is given by the the slope of $\ln[\theta(T)]$ averaged over the period [$T = 10$ s, $T = 20$ s]. Uncertainty on the growth rate is then given by the minimum and maximum values of the slope encountered on the same interval of time. As we move closer to the region for which $\mathrm{Im}(s)$ plotted as a function of σ is the stiffest (see Fig. 9(a)), a characteristic linear evolution can be clearly identified as shown in Fig. 8(b). For large coning angles ($\theta \sim 5^\circ$), temporal evolution of $\ln[\theta(T)]$ is no longer linear. This kind of behaviour, which could be the indirect signature of non linear phenomena such as Lagrange's triadic instability (Lagrange (2008)), has been observed in Karpov's experimental data (Karpov (1965)). In Fig. 9(a), the agreement between numerical and theoretical growth rates is good. The bell-shaped curve corresponding to the present theory is fairly close to the numerical data. As for the quantity $\max[\mathrm{Im}(s)]$, the decay as well as the shift in σ observed for the numerical results (in comparison with the inviscid case) are properly calculated. Moreover, the viscous broadening observed on the numerical results outside the inviscid unstable domain of σ (i.e. the appearance of right and left viscous tails on the stability curve) is well predicted. However a zoom

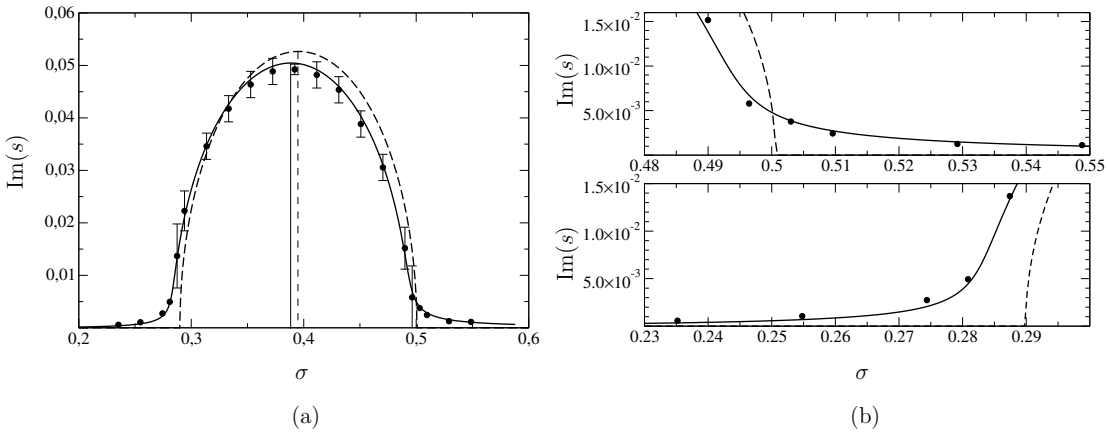

FIGURE 9. Stability curve for case I - $\kappa = 3.0\ 10^{-3}$, $Re = 94247$. (a) The present viscous theory is plotted in solid line. The dashed line corresponds to the inviscid Stewartson's theory. The numerical results are plotted in closed circles. (b) Details of the stability curve in the domain where the viscous effects are predominant.

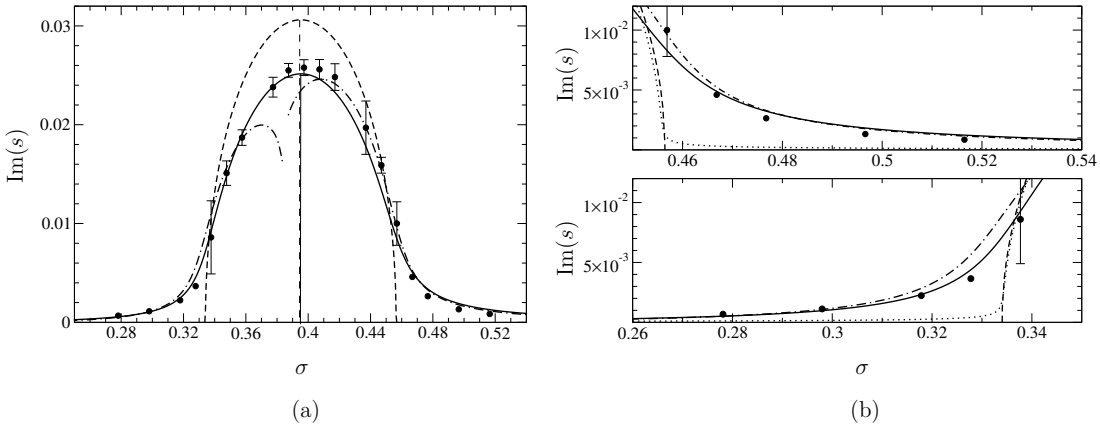

FIGURE 10. Stability curve - case II, $\kappa = 9.36\ 10^{-4}$, $Re = 12566$. (a) The viscous theory (equation (3.12)) is plotted in solid line. The dashed line corresponds to Stewartson's inviscid theory. The dot-dashed line has been obtained by solving directly the third order characteristic equation (3.9). The numerical results are plotted in solid circles. (b) Detailed vues of the stability curve in the domains where the viscous effects are predominant. On these views the dotted curve has been obtained by selecting only the shear torque $\widetilde{m}^{(0)}$ in the derivation of the theoretical stability curve.

performed on the right (resp. left) viscous tail of the stability curve (Fig. 9(b)) highlights a slight but systematic underestimation (resp. overestimation) of the numerical growth rate. As shown below, this tendency is also noticeable for cases II and III.

The configuration II is also located in the inertial regime since $\sqrt{\kappa}/\epsilon = 3.4$. Most of the comments related to the first case are still valid. The stability curves are presented in

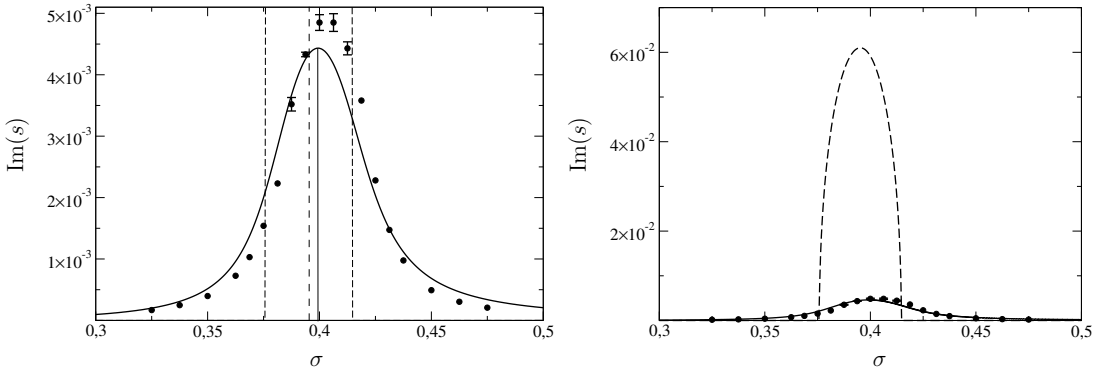

FIGURE 11. Stability curve - case III, $\kappa = 10^{-4}$, $Re = 6280$. (a) The present viscous theory (equation (3.12)) is plotted in solid line. The viscous effects lead to a decrease and a shift of the maximum growth rate compared to the inviscid theory (dashed line). The numerical results are plotted in closed circles. (b) rescaled view of (a) that points out the difference between the amplitudes of inviscid and viscous theories.

view 10(a) : as in the previous case, the agreement between the present theory and the numerical results is satisfactory. The physically acceptable solutions of the third order polynomial equation (3.9) are also plotted in Fig. 10(a). The comparison of the latter with the solutions of the second order polynomial equation (3.12) illustrates the order of magnitude of the error made by approximating (3.9) by (3.12). As shown in Fig. 10(a), the third order equation does not permit a precise determination of the shift of max[Im(s)] since ϵ-expansions no longer hold in the vicinity of the hydrodynamic resonance. In Fig. 10(a), the identification of max[Im(s)] (and the corresponding σ) becomes possible due to the "smoothing" of the approximate form (3.12). This means that the value of the resonant inertial ratio (given by $s_0 + \epsilon s_R$) must be considered cautiously. The situation is different in configuration I, for which both approaches give almost the same results. In Fig. 9(a), the corresponding curves would be superimposed. Note that the value of max[Im(s)] is slightly underestimated by 3-4%.

In Fig. 10(b), the dotted curve has been obtained by selecting only the viscous shear torque $\widetilde{m}^{(0)}$ for the calculation of the stability curve. The destabilization effects obtained outside the inviscid unstable domain are one order of magnitude smaller than the effects obtained by numerical calculation. This latter observation stresses the fact that, insofar as the dimensionless torque $m^{(1)}$ is predominant in the destabilization process, taking account only of the viscous torque $\widetilde{m}^{(0)}$ does not lead to a reasonable value of the growth rate.

The third configuration, noted III, corresponds to an intermediate situation, between the corrected inertial regime and the saturated viscous regime ($\sqrt{\kappa}/\epsilon = 0.79$). The results for case III are collated in Fig. 11. Altough this last case is located at the edge of the domain of validity of our theoretical results, the agreement between theory and numerics remains quite good. The maximum value of the growth rate is reasonably captured : the

theoretical and numerical growth rates agree within 10%. However, some discrepancies are more pronounced than in cases I and II. For instance, the shift of the maximum value of the growth rate is underestimated by a factor of 2. This shortcoming is also slightly visible in Fig. 10(a) and can be explained as follow : on coming closer to the viscous regime ($\sqrt{\kappa}/\epsilon \to 1$), the estimation of the resonance shift deteriorates, since the hydrodynamics are ruled by Gans' approach in a wider domain. In the right-hand viscous tail of the stability curve, the growth rate is overestimated of about 20-40% in the considered range of σ, depending on the distance from the resonance. Once again, this tendency, although it is less obvious, can be observed for case I and II. Fig. 10(b) illustrates the amplitude drop, which is about one order of magnitude, when taking account of the viscous effects.

5. Discussion and conclusion

The problem of a completely fluid-filled gyroscope, in the particular case of a simple cylindrical cavity, has been addressed. The whole work is valid at small coning angles, where the non linear effects are negligible. The Reynolds number is supposed to be high enough to allow for the boundary layer corrections. Moreover, the hydrodynamic resonance of interest is supposed to be sufficiently distant from any other resonance. This condition is satisfied as far as the Reynolds number is not too high, the threshold being fixed by Gans' criterion of viability $\delta_i^{(0)} < Re^{1/7}$.

Firstly, Milne-Stewartson's theory has been rewritten in a more convenient set of reference frames. By comparing the width of the inviscid unstable domain provided by Stewartson's approach to the width of the saturated viscous regime of the hydrodynamic flow studied by Gans (1970), a criterion is proposed for the present theory to be relevant. The corrected inertial regime, which corresponds to high values of κ, is treated theoretically and numerically. It has been shown that a direct calculation of the flows at order ϵ (inside and outside the boundary layer) enabled the evaluation of the destabilizing pressure torques $\widetilde{\boldsymbol{M}}^{(1)}$ and $\boldsymbol{M}^{(1)}$. In the vicinity of the resonant frequency, the latter behaves as a pole of order 2 (which is the leading term of its Laurent's expansion). It has also been shown that, when neglecting every other corrections other than the pole of order 2 in $\boldsymbol{M}^{(1)}$, the growth rate of the coning angle obtained plotted as a function of the inertia ratio σ is exactly superimposed on Wedemeyer's result. This finding highlights the fact that the viscously induced destabilization principally originates from the flow at order ϵ in bulk (namely the flow in volume corresponding to the Ekman pumping), rather than from the viscous shear at walls. In most cases, the latter only intervenes as a correction that eventually induces a slight asymmetry on the plots of $\mathrm{Im}(s)$ vs. σ. The marginal situations in which the viscous shear torque becomes predominant are not treated in the present article.

Numerical calculations were performed for a cylindrical cavity of aspect ratio $h = 1.65$. We focused on the first resonance of the first mode ($i = 1$, $n = 1$) for which the criterion of regime separation can be written in the simplified form $\sqrt{\kappa} > \epsilon$. We explored a relatively wide range of physical parameters, since for the three numerical cases treated, the ratio $\sqrt{\kappa}/\epsilon$ varies from 0.79 to 16.8. Use of numerical studies avoids

certain experimental problems as bearing frictions and aerodynamic torques. Theoretical prediction and numerical calculations of the maximum growth rate agree to within 5-10% depending on the case. As expected, agreement between numerics and theory deteriorates as the ratio $\sqrt{\kappa}/\epsilon$ diminishes. The main problem concerns the restitution of the shift of $\max[\mathrm{Im}(s)]$ compared to the inviscid Stewartson's value. For $\sqrt{\kappa}/\epsilon$ close to 1, this quantity is underestimated by a factor of almost two. This discrepancy is to be attributed to the irrelevance of the present theory in a very close vicinity of the resonance.

One restriction on the applicability of the present theory is that the resonance considered must not be close to the value $\omega = 1$. In this case, the value of the inviscid quantity $D^{(0)}$ becomes very small and the constant term in the Laurent's expansion of $m^{(0)}$ can no longer be omitted. In other words, for a given aspect ratio h, the resonances for which $D^{(0)}$ is close to zero cannot be treated by the present theory and require certain refinements. The treatment of such singular resonances is still incompleted and will be presented in a forthcoming communication. Most of the experimental work has been performed in a close vicinity of singular resonances. For instance, D'Amico's experiments presented in Whiting's paper (Whiting (1981)) are made at the second resonance of the first mode, which is singular for the considered aspect ratio $h \sim 3$. We expect that a better understanding of such marginal situations could lead to improvements in the interpretation of several experimental results already published.

Appendix A. Laurent's expansion of the inviscid torque

Let us consider the expression (2.15) of $m^{(0)}$. The leading term in Laurent's expansion of the latter is obtained by seaking the leading term in Laurent's expansion of $a_i^{(0)}$, the term in brackets beeing considered at $\omega = \omega_0$.

Laurent's ω-expansion of $a_i^{(0)}$ truncated after the first (and only) diverging term is

$$a_i^{(0)} \simeq \frac{\overline{a}_i^{(0)}}{\omega_0 - \omega}, \tag{A 1}$$

where

$$\overline{a}_i^{(0)} = \frac{4\omega_0^2}{(\omega_0 - 2)({k_i^{(0)}}^2 + 1)k_i^{(0)} J_1(\delta_i^{(0)})\, h\, \sin(k_i^{(0)} h)\, dk_i^{(0)}/d\omega}. \tag{A 2}$$

In (A 2), the wavenumbers $\delta_i^{(0)}$, $k_i^{(0)}$ and the derivative $dk_i^{(0)}/d\omega$ are considered at $\omega = \omega_0$, with

$$\frac{dk_i^{(0)}}{d\omega} = \frac{\omega_0}{k_i^{(0)}(4 - \omega_0^2)} \left[{\delta_i^{(0)}}^2 + {k_i^{(0)}}^2 + \delta_i^{(0)} \omega_0 \frac{d\delta_i^{(0)}}{d\omega} \right] \tag{A 3}$$

and

$$\frac{d\delta_i^{(0)}}{d\omega} = -\frac{\delta_i^{(0)} J_1'(\delta_i^{(0)})}{(\omega_0 + 2) J_1'(\delta_i^{(0)}) + \omega_0 \delta_i^{(0)} J_1''(\delta_i^{(0)})}. \tag{A 4}$$

Coming back to the Laurent's expansion of $m^{(0)}$, and knowing that $\cos(k_i^{(0)} h) = 0$ at $\omega = \omega_0$, we finally get

$$m^{(0)} \simeq \frac{D^{(0)}}{\omega_0 - \omega}, \tag{A 5}$$

with

$$D^{(0)} = 2\pi\overline{a}_i^{(0)}[J_2(\delta_i^{(0)})/\delta_i^{(0)} - J_1(\delta_i^{(0)})/{k_i^{(0)}}^2] \tag{A 6}$$

$$= \frac{8\pi\omega_0^2\,[J_2(\delta_i^{(0)})/\delta_i^{(0)} - J_1(\delta_i^{(0)})/{k_i^{(0)}}^2]}{(\omega_0-2)({k_i^{(0)}}^2+1)k_i^{(0)}J_1(\delta_i^{(0)})\,h\,dk_i^{(0)}/d\omega}. \tag{A 7}$$

Appendix B. Width of the Gans' window - Viscous and forcing parameters

From Meunier (2008), Gans' solvability condition yields to the following equation for the (viscously saturated) amplitude A of a Kelvin mode forced close to its resonance

$$(\mu+\epsilon\nu)\,A = \mathrm{i}f\left(1-\frac{\epsilon\,A}{a_i^{(0)}}\right). \tag{B 1}$$

In equation (B 1), expressions of the viscous and forcing parameters μ, ν and f calculated by Meunier (2008) are

$$\mu = -\frac{\pi}{N}J_1^2(\delta_i^{(0)})\big\{\alpha_i[2h-\sin(k_i^{(0)}h)/k_i^{(0)}] + 2\beta_i\sin^2(k_i^{(0)}h)[({\delta_i^{(0)}}^2-1)\omega_0^2+4]/(\delta_i^{(0)}\omega)^2\big\}, \tag{B 2}$$

$$\nu = {\delta_i^{(0)}}^2 + {k_i^{(0)}}^2, \tag{B 3}$$

and

$$f = \frac{4\pi}{N}\frac{\omega_0+2}{\omega_0}\sin(k_i^{(0)}h)J_1(\delta_i^{(0)})/{\delta_i^{(0)}}^2, \tag{B 4}$$

where

$$\alpha_i = \frac{1+\mathrm{i}}{\sqrt{2}}\frac{({\delta_i^{(0)}}^2-1)\omega_0^2+4}{(4-\omega_0^2)\omega^{3/2}}, \tag{B 5}$$

$$\beta_i = \frac{1-\mathrm{i}}{2\sqrt{2}}{\delta_i^{(0)}}^2\left[\frac{1}{(2-\omega_0)^{3/2}}+\frac{\mathrm{i}}{(2+\omega_0)^{3/2}}\right] \tag{B 6}$$

and

$$N = \pi J_1^2(\delta_i^{(0)})[2h+\sin(k_i^{(0)}h)/k_i^{(0)}]\frac{\omega_0^2(\omega_0+2\delta_i^2-2)-4\omega_0+8}{\omega_0^2(4-\omega_0^2)^2}. \tag{B 7}$$

From (B 1), the real part the viscously saturated amplitude can be calcultated and one gets

$$\mathrm{Re}(A) = f\frac{\epsilon f/a_i^{(0)}+\mu''}{(\epsilon f/a_i^{(0)}+\mu'')^2+(\mu'+\epsilon\nu)^2}. \tag{B 8}$$

This quantity is supposed to become equal to the inviscid amplitude $a_i^{(0)}$ as ω goes away from the resonant frequency ω_0. Thus, from (B 8), it appears that A can be considered as equal to $a_i^{(0)}$ provided that the second term of the denominator is small compared to the first one. By using the Laurent's expansion (A 1) of $a_i^{(0)}$ given in appendix A, we finally obtain an order of magnitude for the width $\Delta\omega$ for the Gans' window

$$\Delta\omega \sim \epsilon\,\overline{a}^{(0)}f^{-1}\max[|\mu|,\,\epsilon\nu]. \tag{B 9}$$

Appendix C. Corrections to the inviscid wavenumbers

C.1. *Rescaled N.-S. equations*

Corrective flow at order 1 on the lateral wall obtained by performing viscous rescaling $\widetilde{r} = (1-r)/\epsilon$ in the complete linear N.-S. equations (2.1a). Equivalent rescaling for the top wall is $\widetilde{z} = (h-z)/\epsilon$. This couple of transformations leads to the following systems

$$\text{lateral wall}\begin{cases} -2\widetilde{v}^{\,(0)} = \dfrac{\partial \widetilde{p}^{\,(1)}}{\partial \widetilde{r}} \\ \dfrac{\partial \widetilde{v}^{\,(0)}}{\partial t} - \dfrac{\partial^2 \widetilde{v}^{\,(0)}}{\partial \widetilde{r}} = 0 \\ \dfrac{\partial \widetilde{w}^{\,(0)}}{\partial t} - \dfrac{\partial^2 \widetilde{w}^{\,(0)}}{\partial^2 \widetilde{r}} = 0 \\ \dfrac{\partial \widetilde{u}^{\,(1)}}{\partial \widetilde{r}} = \dfrac{\partial \widetilde{v}^{\,(0)}}{\partial \zeta} + \dfrac{\partial \widetilde{w}^{\,(0)}}{\partial z} \end{cases} \qquad \text{upper wall}\begin{cases} \dfrac{\partial \widetilde{u}^{\,(0)}}{\partial t} - \dfrac{\partial^2 \widetilde{u}^{\,(0)}}{\partial \widetilde{z}^2} - 2\widetilde{v}^{\,(0)} = 0 \\ \dfrac{\partial \widetilde{v}^{\,(0)}}{\partial t} - \dfrac{\partial^2 \widetilde{v}^{\,(0)}}{\partial \widetilde{z}^2} + 2\widetilde{u}^{\,(0)} = 0 \\ \dfrac{\partial \widetilde{p}^{\,(1)}}{\partial z} = 0 \\ \dfrac{\partial \widetilde{w}^{\,(1)}}{\partial \widetilde{z}} = \dfrac{\partial \widetilde{u}^{\,(0)}}{\partial r} + \dfrac{\widetilde{u}^{\,(0)}}{r} + \dfrac{1}{r}\dfrac{\partial \widetilde{v}^{\,(0)}}{\partial \zeta} \end{cases} \qquad (\mathrm{C}\,1a,b)$$

C.2. *Corrective flow at order* 1 *(boundary layer)*

Normal corrective velocity $\widetilde{u}^{(0)}$ and pressure $\widetilde{p}^{(0)}$ are zero. The two tangential components of $\widetilde{\mathbf{v}}^{(0)}$, obtained from system (C 1a), are given by

$$\widetilde{v}^{\,(0)} = -\sum_{i=1}^{\infty} a_i^{(0)} v_i^{(0)}(1,\, z)\, \mathrm{e}^{\,\kappa_l\, \widetilde{r}}\, \mathrm{e}^{\,\mathrm{i}(\omega t+\varphi)}, \qquad (\mathrm{C}\,2a)$$

$$\widetilde{w}^{\,(0)} = \mathrm{i}\left[\sum_{i=1}^{\infty} a_i^{(0)} w_i^{(0)}(1,\, z)\, -2\right] \mathrm{e}^{\,\kappa_l\, \widetilde{r}}\, \mathrm{e}^{\,\mathrm{i}(\omega t+\varphi)}, \qquad (\mathrm{C}\,2b)$$

where

$$\kappa_l = \frac{1+\mathrm{i}}{\sqrt{2}}\sqrt{\omega}. \qquad (\mathrm{C}\,3)$$

Integration of the rescaled continuity equation at order 1 provides the Ekman pumping component at the lateral wall (which is of order ϵ)

$$u^{\perp} = \sum_{i=1}^{\infty} a_i^{(0)} u_i^{\perp} \mathrm{e}^{\,\mathrm{i}(\omega t+\varphi)}, \qquad (\mathrm{C}\,4)$$

where

$$u_i^{\perp} = -\frac{1+\mathrm{i}}{\sqrt{2}} \frac{1}{\omega^{3/2}(4-\omega^2)} J_1(\delta_i^{(0)}) \left[\omega^2({\delta_i^{(0)}}^2 - 1) + 4\right] \sin(k_i^{(0)} z). \qquad (\mathrm{C}\,5)$$

Corresponding expressions to (C 2) for the upper wall come from the integration of the system (C 1b). In this case

$$\widetilde{u}^{\,(0)} = \frac{\mathrm{i}}{2} \sum_{i=1}^{\infty} a_i^{(0)} \left[S_i^{+}(r) \mathrm{e}^{\,\kappa_s\, \widetilde{z}} + D_i^{+}(r) \mathrm{e}^{\,\kappa_d\, \widetilde{z}}\right] \mathrm{e}^{\,\mathrm{i}(\omega t+\varphi)}, \qquad (\mathrm{C}\,6a)$$

$$\widetilde{v}^{\,(0)} = \frac{1}{2} \sum_{i=1}^{\infty} a_i^{(0)} \left[S_i^{+}(r) \mathrm{e}^{\,\kappa_s\, \widetilde{z}} - D_i^{+}(r) \mathrm{e}^{\,\kappa_d\, \widetilde{z}}\right] \mathrm{e}^{\,\mathrm{i}(\omega t+\varphi)}, \qquad (\mathrm{C}\,6b)$$

where

$$S_i^{+}(r) = u_i^{(0)}(r,\, h) - v_i^{(0)}(r,\, h) \quad , \quad D_i^{+}(r) = u_i^{(0)}(r,\, h) + v_i^{(0)}(r,\, h) \qquad (\mathrm{C}\,7)$$

and

$$\kappa_s = -(1+\mathrm{i})\sqrt{\frac{2+\omega}{2}} \quad \text{and} \quad \kappa_d = -(1-\mathrm{i})\sqrt{\frac{2-\omega}{2}} \tag{C 8a,b}$$

Likewise, integration of the rescaled continuity equation at order 1 provides the Ekman pumping component at the upper wall

$$w^{\perp} = \sum_{i=1}^{\infty} a_i^{(0)} w_i^{\perp} \mathrm{e}^{\,\mathrm{i}(\omega t+\varphi)}, \tag{C 9}$$

with

$$w_i^{\perp} = -\frac{1+\mathrm{i}}{2\sqrt{2}} {\delta_i^{(0)}}^2 J_1(\delta_i^{(0)} r)\left[\frac{1}{(2+\omega)^{3/2}} - \frac{\mathrm{i}}{(2-\omega)^{3/2}}\right] \tag{C 10}$$

C.3. *Boundary condition at order ϵ on the lateral wall*

The flow at order ϵ coming from ϵ-expansion of the wave numbers in the inviscid flow (term in brackets in (3.2)) is supposed to compensate the Ekman pumping given by (C 4) and (C 5). Use of Kelvin's relation of dispersion enables a simplification of the derivatives of the normal velocity at $r = 1$

$$\frac{\partial u_i^{(0)}}{\partial \delta_i} = -\frac{\mathrm{i}}{4-\omega^2}[2J_1'(\delta_i^{(0)}) + \omega[\delta_i^{(0)} - (1/\delta_i^{(0)})]J_1(\delta_i^{(0)})]\sin(k_i^{(0)} z), \tag{C 11a}$$

$$\frac{\partial u_i^{(0)}}{\partial k_i} = 0. \tag{C 11b}$$

The condition (3.3) then leads to the expression (3.4) of $\delta_i^{(1)}$. Given the constitutive relation (3.6), the correction to the lengthwise wavenumber can be written

$$k_i^{(1)} = \frac{1-\mathrm{i}}{\sqrt{2}}\sqrt{\frac{\omega}{4-\omega^2}}\,\delta_i^{(0)}. \tag{C 12}$$

Appendix D. Amplitude of the additional flow

The amplitude $a_i^{(0)}$ is determined by means of the boundary condition (3.7) at $z = +h$. Using the derivatives of $w_i^{(0)}$ with respect to δ_i and k_i at $r = 1$, and replacing in (3.7) each term by its expression, we obtain

$$\begin{aligned}\mathrm{i}\sum_i a_i^{(0)}\frac{1}{\omega}\left[\delta_i^{(1)} k_i^{(0)} r J_1'(\delta_i^{(0)} r)\cos(k_i^{(0)} h) + k_i^{(1)} J_1(\delta_i^{(0)} r)[\cos(k_i^{(0)} h) - k_i^{(0)} h\,\sin(k_i^{(0)} h)]\right] \\ + \mathrm{i}\sum_i a_i^{+}\,\frac{k_i^{(0)} J_1(\delta_i^{(0)} r)}{\omega}\cos(k_i^{(0)} h) = \\ + \frac{1+\mathrm{i}}{2\sqrt{2}}\sum_i a_i^{(0)} {\delta_i^{(0)}}^2 J(\delta_i^{(0)} r)\sin(k_i^{(0)} h)\left[\frac{1}{(2+\omega)^{3/2}} - \frac{\mathrm{i}}{(2-\omega)^{3/2}}\right]\end{aligned} \tag{D 1}$$

In order to derive the expression of the a_i^{+}, one has to express the quantity $rJ_1'(\delta_i^{(0)} r)$ as a function of the $J_1(\delta_i^{(0)} r)$. The Dini's expansion of $rJ_1'(\delta_i^{(0)} r)$ can be obtained by means of the formula in Watson's book (Watson (1952), pages 580 and 581), giving

$$rJ_1'(\delta_i^{(0)} r) = 2\sum_{m=1}^{\infty}\frac{{\delta_m^{(0)}}^2 S_{im}}{({\delta_m^{(0)}}^2 - 1)\,[J_1(\delta_i^{(0)})]^2 + {\delta_m^{(0)}}^2\,[J_1'(\delta_i^{(0)})]^2} J_1(\delta_i^{(0)} r), \tag{D 2}$$

where

$$S_{im} = \int_0^1 u^2 J_1'(\delta_m^{(0)} u)\, J_1(\delta_i^{(0)} u)\, du. \tag{D 3}$$

The integrated expression of S_{im} is as follows

$$S_{im} = \frac{1}{{\delta_i^{(0)}}^2} J_0(\delta_i^{(0)}) J_1(\delta_i^{(0)}) - \frac{1}{2\delta_i^{(0)}} J_0^2(\delta_i^{(0)}) \quad \text{for } i = m, \tag{D 4}$$

$$\begin{aligned} S_{im} = {} & \frac{1}{\delta_m^{(0)}} \frac{\delta_i^{(0)} J_1(\delta_i^{(0)}) J_0(\delta_m^{(0)}) - \delta_m^{(0)} J_0(\delta_i^{(0)}) J_1(\delta_m^{(0)})}{{\delta_m^{(0)}}^2 - {\delta_i^{(0)}}^2} \\ & \frac{1}{{\delta_m^{(0)}}^2 - {\delta_i^{(0)}}^2} \Bigg\{ \delta_i^{(0)} J_0(\delta_i^{(0)}) J_0(\delta_m^{(0)}) \\ & + \frac{2\delta_i^{(0)}}{{\delta_m^{(0)}}^2 - {\delta_i^{(0)}}^2} [\delta_i^{(0)} J_1(\delta_i^{(0)}) J_0(\delta_m^{(0)}) - \delta_m^{(0)} J_0(\delta_i^{(0)}) J_1(\delta_m^{(0)})] \\ & + \delta_m^{(0)} J_1(\delta_i^{(0)}) J_1(\delta_m^{(0)}) \Bigg\} \quad \text{for } i \neq m \end{aligned} \tag{D 5}$$

A linear identification in (D 1) leads to the expression of a_i^+

$$\begin{aligned} a_i^+ = {} & -\frac{1-\mathrm{i}}{\sqrt{2}} \Bigg\{ \frac{\delta_i^{(0)}}{k_i^{(0)}} a_i^{(0)} \left(\frac{\omega}{4-\omega^2} \right)^{1/2} \\ & + \frac{2{\delta_i^{(0)}}^2 \sum_m a_m^{(0)} k_m^{(0)} \delta_m^{(0)} \cos(k_m^{(0)} h) S_{mi}}{\omega^{1/2} k_i^{(0)} \cos(k_i^{(0)} h) [({\delta_i^{(0)}}^2 - 1)\, [J_1(\delta_i^{(0)})]^2 + {\delta_i^{(0)}}^2\, [J_1'(\delta_i^{(0)})]^2]} \Bigg\} \\ & + \frac{1-\mathrm{i}}{\sqrt{2}} a_i^{(0)} \delta_i^{(0)} \tan(k_i^{(0)} h) \left\{ \frac{(2-\omega)^{1/2}}{2(2+\omega)} + h \left[\frac{\omega}{4-\omega^2} \right]^{1/2} \right\} \\ & - \frac{1+\mathrm{i}}{2\sqrt{2}} a_i^{(0)} \delta_i^{(0)} \tan(k_i^{(0)} h) \frac{(2+\omega)^{1/2}}{(2-\omega)} \end{aligned} \tag{D 6}$$

Appendix E. Expressions of the corrective complex torques

E.1. *Expression of* $\widetilde{m}^{(0)}$

The viscous shear complex torque results from the integration of the shear constraint on the lateral wall, giving

$$\begin{aligned} \widetilde{m}^{(0)} = -\pi\sqrt{2\omega}(1+\mathrm{i}) \Bigg\{ & \sum_{i=1}^{\infty} a_i^{(0)} \Bigg[\frac{2\delta_i^{(0)} J_1'(\delta_i^{(0)}) + \omega J_1(\delta_i^{(0)})}{4-\omega^2} \frac{\sin(k_i^{(0)} h) - k_i^{(0)} h \cos(k_i^{(0)} h)}{{k_i^{(0)}}^2} \\ & + \frac{J_1(\delta_i^{(0)})}{\omega} \sin(k_i^{(0)} h) \Bigg] + 2h \Bigg\} \\ & + \pi\sqrt{2} h (1-\mathrm{i}) \frac{1}{(2-\omega)^{1/2}} \sum_{i=1}^{\infty} a_i^{(0)} \sin(k_i^{(0)} h) J_1(\delta_i^{(0)}) \end{aligned} \tag{E 1}$$

At the resonant frequency ω_0, coefficients of Laurent's expansion (3.10a) of $\widetilde{m}^{(0)}$ are

$$\widetilde{D}_{R}^{(0)} = \pi\sqrt{2}\frac{4\omega_0^2}{(\omega_0-2)({k_i^{(0)}}^2+1)k_i^{(0)}J_1(\delta_i^{(0)})\ h\ dk_i^{(0)}/d\omega}\left\{\frac{hJ_1(\delta_i^{(0)})}{(2-\omega_0)^{1/2}}\right.$$
$$\left.-\omega_0^{1/2}\left[\frac{2\delta_i^{(0)}J_1'(\delta_i^{(0)})+\omega_0 J_1(\delta_i^{(0)})}{(4-\omega_0^2){k_i^{(0)}}^2}+\frac{J_1(\delta_i^{(0)})}{\omega_0}\right]\right\} \tag{E 2}$$

$$\widetilde{D}_{I}^{(0)} = -\pi\sqrt{2}\frac{4\omega_0^2}{(\omega_0-2)({k_i^{(0)}}^2+1)k_i^{(0)}J_1(\delta_i^{(0)})\ h\ dk_i^{(0)}/d\omega}\left\{\frac{hJ_1(\delta_i^{(0)})}{(2-\omega_0)^{1/2}}\right.$$
$$\left.+\omega_0^{1/2}\left[\frac{2\delta_i^{(0)}J_1'(\delta_i^{(0)})+\omega_0 J_1(\delta_i^{(0)})}{(4-\omega_0^2){k_i^{(0)}}^2}+\frac{J_1(\delta_i^{(0)})}{\omega_0}\right]\right\} \tag{E 3}$$

In the previous expressions, $\delta_i^{(0)}$, $k_i^{(0)}$ and the derivative $dk_i^{(0)}/d\omega$ are considered at $\omega=\omega_0$.

E.2. *Expression of* $\widetilde{m}^{(1)}$

Corrected pressure at order 1 in the lateral boundary layer results from the integration of the first equation of the system (C 1a).

$$\widetilde{p}^{(1)} = -\frac{2}{\sqrt{\omega}}\frac{1-\mathrm{i}}{\sqrt{2}}\sum_{i=1}^{\infty}a_i^{(0)}\frac{2\delta_i^{(0)}J_1'(\delta_i^{(0)})+\omega J_1(\delta_i^{(0)})}{4-\omega^2}\sin(k_i^{(0)}z)\mathrm{e}^{\kappa\widetilde{r}}\mathrm{e}^{\mathrm{i}(\omega t+\phi)}. \tag{E 4}$$

The equivalent quantity for the upper wall is zero. Integration of the previous expression leads to the complex torque $\widetilde{m}^{(1)}$

$$\widetilde{m}^{(1)} = \frac{2\sqrt{2}}{\sqrt{\omega}}\pi(1+\mathrm{i})\sum_{i=1}^{\infty}a_i^{(0)}\frac{2\delta_i^{(0)}J_1'(\delta_i^{(0)})+\omega J_1(\delta_i^{(0)})}{4-\omega^2}\frac{1}{{k_i^{(0)}}^2}[\sin(k_i^{(0)}h)-$$
$$k_i^{(0)}h\cos(k_i^{(0)}h)] \tag{E 5}$$

At the resonant frequency ω_0, the associated coefficients in Laurent's expansion (3.10b) of $\widetilde{m}^{(1)}$ are

$$\widetilde{D}_{R}^{(1)} = \frac{2\sqrt{2}\pi}{\sqrt{\omega_0}}\frac{4\omega_0^2}{(\omega_0-2)({k_i^{(0)}}^2+1)k_i^{(0)}J_1(\delta_i^{(0)})\ h\ dk_i^{(0)}/d\omega}\frac{2\delta_i^{(0)}J_1'(\delta_i^{(0)})+\omega_0 J_1(\delta_i^{(0)})}{(4-\omega_0^2){k_i^{(0)}}^2} \tag{E 6}$$

and

$$\widetilde{D}_{I}^{(1)} = \widetilde{D}_{R}^{(1)} \tag{E 7}$$

In the previous expressions, $\delta_i^{(0)}$, $k_i^{(0)}$ and the derivative $dk_i^{(0)}/d\omega$ are considered at $\omega=\omega_0$.

E.3. *Expression of* $m^{(1)}$

$$m^{(1)} = -\pi\sqrt{2}\sum_{i=1}^{\infty}\left[(d_i - e_i + c_i) + \mathrm{i}(d_i + e_i + c_i)\right]\left[\frac{J_1(\delta_i^{(0)})}{{k_i^{(0)}}^2}[\sin(k_i^{(0)}h) - k_i^{(0)}h\cos(k_i^{(0)}h)] - \frac{J_2}{\delta_i^{(0)}}\sin(k_i^{(0)}h)\right]$$
$$+\pi\sqrt{2}(1+\mathrm{i})\left(\frac{\omega}{4-\omega^2}\right)^{1/2}\sum_{i=1}^{\infty}a_i^{(0)}\delta_i^{(0)}\left[\frac{J_2(\delta_i^{(0)})}{\delta_i^{(0)}}h\cos(k_i^{(0)}h) - \frac{J_1}{{k_i^{(0)}}^3}[{k_i^{(0)}}^2h^2\sin(k_i^{(0)}h) - 2\sin(k_i^{(0)}h) + 2k_i^{(0)}h\cos(k_i^{(0)}h)]\right]$$
$$-\pi\sqrt{2}(1+\mathrm{i})\omega^{-1/2}\sum_{i=1}^{\infty}a_i^{(0)}\delta_i^{(0)}\left[\frac{J_1'(\delta_i^{(0)})}{{k_i^{(0)}}^2}[\sin(k_i^{(0)}h) - k_i^{(0)}h\cos(k_i^{(0)}h)] - \sin(k_i^{(0)}h)\left[\frac{J_1(\delta_i^{(0)})}{\delta_i^{(0)}} - 3\frac{J_2(\delta_i^{(0)})}{{\delta_i^{(0)}}^2}\right]\right] \tag{E 8}$$

with

$$c_i = -\frac{2{\delta_i^{(0)}}^2\sum_m a_m^{(0)}k_m^{(0)}\delta_m^{(0)}\cos(k_m^{(0)}h)S_{mi}}{\omega^{1/2}k_i^{(0)}\cos(k_i^{(0)}h)[({\delta_i^{(0)}}^2-1)\,[J_1(\delta_i^{(0)})]^2 + {\delta_i^{(0)}}^2\,[J_1'(\delta_i^{(0)})]^2]} - a_i^{(0)}\frac{\delta_i^{(0)}}{k_i^{(0)}}\left(\frac{\omega}{4-\omega^2}\right)^{1/2}, \tag{E 9}$$

$$d_i = a_i^{(0)}\delta_i^{(0)}\tan(k_i^{(0)}h)\left[\frac{1}{2}\frac{(2-\omega)^{1/2}}{(2+\omega)} + h\left(\frac{\omega}{4-\omega^2}\right)^{1/2}\right], \tag{E 10}$$

$$\text{and}\quad e_i = a_i^{(0)}\delta_i^{(0)}\tan(k_i^{(0)}h)\frac{1}{2}\frac{(2+\omega)^{1/2}}{(2-\omega)} \tag{E 11}$$

The coefficients of poles of order 2 in Laurent's expansion (3.11) of $m^{(1)}$ are given by

$$C_R^{(1)} = \sqrt{2}\pi\frac{4\omega_0^2\delta_i^{(0)}}{(\omega_0-2)({k_i^{(0)}}^2+1)k_i^{(0)}J_1(\delta_i^{(0)})(h\,dk_i^{(0)}/d\omega)^2}\left[\frac{J_2(\delta_i^{(0)})}{\delta_i^{(0)}} - \frac{J_1(\delta_i^{(0)})}{{k_i^{(0)}}^2}\right]\left[h\left(\frac{\omega_0}{4-\omega_0^2}\right)^{1/2} + \frac{1}{2}\frac{(1-\omega_0)^{1/2}}{2+\omega_0} - \frac{1}{2}\frac{(1+\omega_0)^{1/2}}{2-\omega_0}\right] \tag{E 12}$$

$$C_I^{(1)} = \sqrt{2}\pi\frac{4\omega_0^2\delta_i^{(0)}}{(\omega_0-2)({k_i^{(0)}}^2+1)k_i^{(0)}J_1(\delta_i^{(0)})(h\,dk_i^{(0)}/d\omega)^2}\left[\frac{J_2(\delta_i^{(0)})}{\delta_i^{(0)}} - \frac{J_1(\delta_i^{(0)})}{{k_i^{(0)}}^2}\right]\left[h\left(\frac{\omega_0}{4-\omega_0^2}\right)^{1/2} + \frac{1}{2}\frac{(1-\omega_0)^{1/2}}{2+\omega_0} + \frac{1}{2}\frac{(1+\omega_0)^{1/2}}{2-\omega_0}\right] \tag{E 13}$$

As usually $\delta_i^{(0)}$, $k_i^{(0)}$ and the derivative $dk_i^{(0)}/d\omega$ are considered at the resonant frequency $\omega = \omega_0$. The coefficients $D_R^{(1)}$ and $D_I^{(1)}$ of the pole of order 1 in $m^{(1)}$ Laurent's expansion are not given as their expressions are too lengthy. They can be easily obtained by using a formal calculation software.

REFERENCES

D'Amico, W.P. 1977 Inertial Mode Corrections for the Large Amplitude Motion of a Liquid-Filled Gyroscope. PhD Thesis, University of Delaware, Newark, Delaware, June 1977.

D'Amico, W.P. & Rogers, T.H. 1981 Yaw Instabilities Produced by Rapidly Rotating, Highly Viscous Liquids. *AIAA paper 81-0224*

Fortin, M. & Glowinski, R. 1982 Méthodes de Lagrangien augmenté. Application à la résolution numérique de problèmes aux limites. Paris, Dunod

Fultz 1959 A note on overstability and elastoid-inertia oscillations of Kelvin, Solberg and Bjerknes. *J. Meteorol.* **16**, 199–208

Gans, R.F. 1970 On the precession of a resonant cylinder. *J. Fluid Mech.* **476**, 865–872

Gans, R.F. 1984 Dynamics of a Near-Resonant Fluid-Filled Gyroscope. *AIAA Journal* **22**, 1465–1471

Garg, S.C., Furunoto, N. & Vanyo, J.P. 1986 Spacecraft Nutational Instability Prediction by Energy Dissipation Measurements. *J. Guidance* **9** (3), 357–361

Greenhill, A.G. 1880 Proc. Camb. Phil. Soc. 4 (4).

Greenspan, H.P. 1968 *The theory of rotating fluids.* Cambridge University Press.

Harlow, F.H & Welsh, J.E. 1965 Numerical calculation of time dependant viscous incompressible flows. *The Physics of Fluids*, **8**, 2182–2189

Karpov, B.G. 1962 Experimental Observations of the Dynamic Behaviour of Liquid-Filled Shell. *BRL Report 1171.* Aberdeen Provig Ground, Md.

Karpov, B.G. 1965 The Effect of Reynolds Number on Resonance. *BRL Report 1302.* Aberdeen Provig Ground, Md.

Kerswell, R.R. & Barenghi, C.F. 1995 On the viscous decay rates of inertial waves in a rotating circular cylinder *J. Fluid Mech.* **285**, 203–214

Kerswell, R.R. 1999 Secondary instabilities in rapidly rotating fluids: inertial wave breakdown. *J. Fluid Mech.* **382**, 283–306

Kobine, J.J. 1995 Inertial wave dynamics in a rotating and precessing cylinder. *J. Fluid Mech.* **303**, 233–352

Kobine, J.J. 1996 Azimuthal flow associated with inertial wave resonance in a precessing cylinder. *J. Fluid Mech.* **319**, 387–406

Kudlick, M. 1966 On the transient motions in a contained rotating fluid. PhD thesis, Massachussets Institute ofe Technology.

Lagrange, R. 2008 Instability of a fluid inside a precessing cylinder. *Phys. of Fluids.* accepted

Mahalov, A. 1993 The instability of rotating fluid columns subjected to a weak external Coriolis force. *Phys. Fluids A*, **5** (4), 891–900

Manasseh, R. 1992 Breakdown regimes of inertia waves in precessing cylinder. *J. Fluid Mech.* **243**, 261–296

Manasseh, R. 1994 Distortions of inertia waves in a rotating fluid cylinder forced near its fundamental mode resonance. *J. Fluid Mech.* **265**, 345–370

Manasseh, R. 1996 Nonlinear behaviour of contained inertia waves. *J. Fluid Mech.* **315**, 151–173

McEwan, A.D. 1970 Inertial oscillations in a rotating fluid cylinder. *J. Fluid Mech.* **40**, 603–640

Meunier, P., Eloy, C., Lagrange, R. & Nadal, F. 2008 Rotating fluid cylinder subject to weak precession. *J. Fluid Mech.* **599**, 405—440

Milne, E.A. 1940 On the Stability of a Liquid-Filled Shell (U). *EBD report No. 6*

Murphy, C.H. 1982 Angular Motion of a Spinning Projectile with a Viscous Payload. *ARBRL-TR-02422*

Scott, W.E. & D'Amico, W.P. 1973 Amplitude-Dependent Behavior of a Liquid-Filled Gyroscope. *Fluid Mech.* **60**, 751–758

Stewartson, K. 1958 On the stability of a spinning top containing liquid. *Fluid Mech.* **5**, 577–592

Sir W. Thomson 1880 Vibrations of a columnar vortex. *Phil. Mag.* **10**, 155–168

Thomson, R. 1970 Diurnal tides and shear instabilities in a rotating cylinder. *J. Fluid Mech.* **40**, 737–751

van der Vorst, H.A. 1992 Bi-CGSTAB: a fast and smoothly converging variant of Bi-CG for the solution of nonsymmetric linear system. *SIAM-Journal on Scientific and Statistical Computing.* **13**, 631–644

Vanyo, J.P. 1993 *Rotating fluids in Engineering and Science*. Dover.

Vincent, S. & Caltagirone J.-P. 2000 A One-Cell Local Multigrid method for solving unsteady incompresible multiphase flow. *Journal of Computational Physics*. **163**, 172–215

Waleffe, F. 1989 The 3D instability of a strained vortex and its relation to turbulence. PhD thesis, Massachussets Institute of Technology

Ward, G.N. 1959 Appendix to K. Stewartson "On the stability of a spinning top containing liquid". *J. Fluid Mech.* **5**, 577–592

Watson, G.N. 1952 *Theory of Bessel functions*. Cambridge University Press.

Wedemeyer, E.H. 1965 Dynamics of a Liquid-Filled Shell : Theory of Viscous Corrections to Stewartson's Stability Problem. *BRL Report N° 1287*. U.S. Army Ballistic Research Laboratory. Aberdeen Proving Ground, Maryland

Wedemeyer, E.H. 1966 Viscous Corrections to Stewartson's Stability Criterion. *BRL Report N° 1325*. U.S. Army Ballistic Research Laboratory. Aberdeen Proving Ground, Maryland

Whiting, R.D. & Gerber, N. 1981 Dynamics of a Liquid-Filled Gyroscope : Update of Theory and Experiment. *ARBRL-TR-02221*

BIBLIOGRAPHIE

Afanasyev, Y. D. 2002 Experiments on instability of columnar vortex pairs in rotating fluid. *Geophys. Astrophys. Fluid Dyn.* **96(1)**, 31–48.

Agrawal, B. N. 1993 Dynamics characteristics of liquid motion in partially filled tanks of a spinning spacecraft. *J. Guid. Control Dynam.* **16** (4), 636–640.

Bao, G. W. & Pascal, M. 1997 Stability of a spinning liquid filled spacecraft. *Appl. Mech.* **67**, 407–421.

Bayly, B. J. 1986 Three-dimensional instability of elliptical flow. *Phys. Rev. Lett.* **57**, 2160–2163.

Beardsley, R. 1970 An experimental study of inertial waves in a closed cone. *Stud. Appl. Math.* **49**, 187.

Bondi, H. 1953 The effect of precession on the motion of the liquid core. *Proc. Camb. Phil. Soc.* **49**, 498–515.

Bullard, E. C. 1949 The magnetic field within the earth. *Proc. R. Soc. London, Ser. A* **197**, 433.

Busse, F. 1968 Steady fluid flow in a precessing spheroidal shell. *J. Fluid Mech.* **33**, 739–752.

Chandrasekhar, S. 1961 *Hydrodynamic and hydromagnetic stability*. Clarendon Press, Oxford.

Chossat, P. & Iooss, G. 1994 *The Couette-Taylor Problem*. Applied Math Science 102, Springer, New-York.

Craik, A. D. D. & Criminale, W. O. 1986 Evolution of wavelike disturbances in shear flows : a class of exact solutions of the navier-stokes equations. *Proc. R. Soc. London Ser. A* **406**, 13–26.

Drazin, P. G. & Reid, W. H. 1981 *Hydrodynamic stability*. Cambridge University Press.

Eloy, C. 2000 Instabilité multipolaire de tourbillons. PhD thesis, Université Aix-Marseille II.

Eloy, C. & Le Dizès, S. 1999 Three-dimensional instability of burgers and lamb–oseen vortices in a strain field. *J. Fluid Mech.* **378**, 145–166.

Eloy, C., Le Gal, P. & Le Dizès, S. 2000 Experimental study of the multipolar vortex instability. *Phys. Rev. Lett.* **85**, 3400–3403.

Eloy, C., Le Gal, P. & Le Dizès, S. 2003 Elliptic and triangular instabilities in rotating cylinders. *J. Fluid Mech.* **476**, 357–388.

Fabre, D., Sipp, D. & Jacquin, L. 2006 Kelvin waves and the singular modes of the lamb-oseen vortex. *J. Fluid Mech.* **551**, 235–274.

Fenstermacher, P. R., Swinney, H. L. & Gollub, J. P. 1979 Dynamical instabilities and the transition to chaotic taylor vortex flow. *J. Fluid Mech.* **94**, 103–128.

Fotheringham, P. & Hollerbach, R. 1998 Inertial oscillations in a spherical shell. *Geophys. Astrophys. Fluid Dyn.* **89**, 23.

Fukumoto, Y. 2003 The three dimensional instability of a strained vortex tube revisited. *J. Fluid Mech.* **493**, 287–318.

Fultz, D. 1959 A note on overstability and elastoid-inertia oscillations of kelvin, solberg and bjerknes. *J. Meteorol.* **16**, 199–208.

Gailitis, A., Lielaussis, O., Platacis, E., Stefani, F. & Gerbeth, G. 2002 Laboratory experiments on hydromagnetic dynamos. *Rev. Mod. Phys.* **74**, 973.

Gans, R. F. 1970*a* On hydromagnetic precession in a cylinder. *J. Fluid Mech.* **45**, 111.

Gans, R. F. 1970*b* On the precession of a resonant cylinder. *J. Fluid Mech.* **476**, 865–872.

Gans, R. F. 1984 Dynamics of a near-resonant fluid-filled gyroscope. *AIAA J.* **22**, 1465–1471.

Garg, S. C., Furunoto, N. & Vanyo, J. P. 1986 Spacecraft nutational instability prediction by energy dissipation measurments. *J. Guid.* **9** (3), 357–361.

Gauthier, G., Gondret, P. & Rabaud, M. 1998 Motions of anisotropic particules : Application to visualization of three-dimensional flows. *Phys. Fluids* **10** (9), 2147–2154.

Glatzmaier, G. A. & Roberts, P. H. 1996 Rotation and magnetism of earth's inner core. *Science* **274**, 1887–1891.

Gledzer, E. B. & Ponomarev, V. M. 1992 Instability of bounded flows with elliptical streamlines. *J. Fluid Mech.* **240**, 1–30.

Goldsmith, H. L. & Mason, S. G. 1962 Particle motions in sheared suspensions. 13. the spin and rotation of disks. *J. Fluid Mech.* **12**, 88–96.

Goto, S., Ishii, N., Kida, S. & Nishioka, M. 2007 Turbulence generator using a precessing sphere. *Phys. Fluids* **19**, 061705.

GREENSPAN, H. P. 1968 *The theory of rotating fluids*. Cambridge University Press.

GREENSPAN, H. P. 1969 On the non-linear interaction of inertial modes. *J. Fluid Mech.* **36** (2), 257–264.

GROTE, F. & BUSSE, H. 2001 Dynamics of convection and dynamos in rotating spherical fluid shells. *Fluid Dyn. Res.* **28**, 349–368.

GROTE, F., BUSSE, H. & TILGNER, A. 1999 Convection driven quadrupolar dynamos in rotating spherical shells. *Phys. Rev. E* **60**, R5025.

GROTE, F., BUSSE, H. & TILGNER, A. 2000 Regular and chaotic spherical dynamos. *Phys. Earth Planet. Inter.* **117**, 259.

GÖRTLER, H. 1944 Einige bemerkungen über strömungen in rotierenden flüssigkeiten. *Z. angew. Math. Mech.* **24**, 210–14. <p. 10.>.

GÖRTLER, H. 1957 On forced oscillations in rotating fluids. *5th Midwestern Conf. on Fluid Mech.* pp. 1–10. <pp. 3, 10, 192, 202.>.

GUYON, E., HULIN, J. P. & PETIT, L. 2001 *Hydrodynamique Physique*. Edp Sciences.

HENDERSON, G. A. & ALDRIDGE, K. D. 1992 A finite-element method for inertial waves in a frustrum. *J. Fluid Mech.* **234**, 317–327.

HERBERT, T. 1986 Viscous fluid motion in a spinning and nutating cylinder. *J. Fluid Mech.* **167**, 181–198.

HOLLERBACH, R. & KERSWELL, R. 1995 Oscillatory internal shear layers in rotating and precessing flows. *J. Fluid Mech.* **298**, 327.

KARPOV, B. G. 1965 *Ballistic Research Labs. Maryland, U. S., Report BRL R 1302* .

KELVIN, L. 1880 Vibrations of a columnar vortex. *Phil. Mag.* **10**, 155–168.

KERSWELL, R. R. 1993 The instability of precessing flow. *Geophys. Astrophys. Fluid Dyn.* **72**, 107–144.

KERSWELL, R. R. 1995 On the internal shear layers spawned by the critical regions in oscillatory ekman boudary layers. *J. Fluid Mech.* **298**, 311–325.

KERSWELL, R. R. 1996 Upper bounds on the energy dissipation in turbulent precession,. *J. Fluid Mech.* **321**, 335–370.

KERSWELL, R. R. 1999 Secondary instabilities in rapidly rotating fluids : inertial wave breakdown. *J. Fluid Mech.* **382**, 283–306.

KERSWELL, R. R. 2002 Elliptical instability. *Ann. Rev. Fluid Mech.* **34**, 83–113.

KERSWELL, R. R. & BARENGHI, C. F. 1995 On the viscous decay rates of inertial waves in a rotating cylinder. *J. Fluid Mech.* **285**, 203–214.

Kerswell, R. R. & Malkus, W. V. R. 1998 Tidal instability as the source for io's magnetic signature. *Geophys. Res. Lett.* **25**, 107–144.

Kobine, J. J. 1995 Inertial wave dynamics in a rotating and precessing cylinder. *J. Fluid Mech.* **303**, 233–252.

Kobine, J. J. 1996 Azimuthal flow associated with inertial wave resonance in a precessing cylinder. *J. Fluid Mech.* **319**, 387–406.

Koschmieder, E. L. 1993 *Benard Cells and Taylor Vortices*. Cambridge University Press.

Kudlick, M. 1966 On the transient motions in a contained rotating fluid. PhD thesis, Massachussets Institute of Technology.

Lacaze, L., Le Gal, P. & Le Dizès, S. 2004 Elliptical instability in a rotating spheroid. *J. Fluid Mech.* **505**, 1–22.

Lagrange, R., Eloy, C., Nadal, F. & Meunier, P. 2008 Instability of a fluid inside a precessing cylinder. *Physics of Fluids.* **20(8)**, 081701.

Lambelin, J. P., Nadal, F., Lagrange, R. & Sarthou, A. 2009 Non-resonant viscous theory for the stability of a fluid-filled gyroscope. *J. Fluid Mech.* pp. 08–S–0525.R2.

Laporte, F. & Corjon, A. 2000 Direct numerical simulations of the elliptic instability of a vortex pair. *Phys. Fluids* **12**, 1016–1031.

Leweke, T. & Williamson, C. H. K. 1998*a* Cooperative elliptic instability of a vortex pair. *J. Fluid Mech.* **360**, 85–119.

Leweke, T. & Williamson, C. H. K. 1998*b* Three-dimensional instabilities in wake transition. *Eur. J. Mech.* B/*Fluids* **17**, 571–586.

Lifschitz, A. & Hameiri, E. 1991 Local stability conditions in fluid dynamics. *Phys. Fluids* A **3** (11), 2644–2651.

Loper, D. E. 1975 Torque balance and energy budget for the precesionally driven dynamo. *Phys. Earth Planet. Inter.* **43**, 43.

Lorenzani, S. & Tilgner, A. 2001 Fluid instabilities in precessing spheroidal cavities. *J. Fluid Mech.* **447**, 111–128.

Lorenzani, S. & Tilgner, A. 2003 Inertial instabilities of fluid flow in precessing spheroidal shells. *J. Fluid Mech.* **492**, 363.

Lubow, S. H., Pringle, J. E. & Kerswell, R. R. 1993 Tidal instability of accretion disks. *Astrophysical Journal* **419**, 758.

Mahalov, A. 1993 The instability of rotating fluid columns subjected to a weak external coriolis-force. *Phys. Fluids A* **5** (4), 891–900.

Malkus, W. V. R. 1968 Precession of the earth as the cause of geomagnetism. *Science* **160**, 259–264.

Malkus, W. V. R. 1989 An experimental study of global instabilities due to tidal (elliptical) distortion of a rotating elastic cylinder. *Geophys. Astrophys. Fluid Dynamics* **48**, 123–134.

Malkus, W. V. R. 1994 Energy sources for planetary dynamos. *In M. R. E. Proctor ans A. D. Gilbert, editors, Lectures on Solar and Planetary Dynamos, Publications of the Newton Institute. Cambridge University Press* **2**, 161–279.

Manasseh, R. 1992 Breakdown regimes of inertia waves in a precessing cylinder. *J. Fluid Mech.* **243**, 261–296.

Manasseh, R. 1994 Distorsions of inertia waves in a precessing cylinder forced near its fundamental mode resonance. *J. Fluid Mech.* **265**, 345–370.

Manasseh, R. 1996 Nonlinear behaviour of contained inertia waves. *J. Fluid Mech.* **315**, 151–173.

Mason, D. M. & Kerswell, R. R. 1999 Nonlinear evolution of the elliptical instability : an example of inertial breakdown. *J. Fluid Mech.* **396**, 73–108.

McEwan, A. D. 1970 Inertial oscillations in a rotating fluid cylinder. *J. Fluid Mech.* **40** (3), 603–640.

Meunier, P., Eloy, C., Lagrange, R. & Nadal, F. 2008 A rotating fluid cylinder subject to weak precession. *J. Fluid Mech.* **599**, 405–440.

Meunier, P. & Leweke, T. 2003 Analysis and minimization of errors due to high gradients in particule image velocimetry. Exp. Fluids.

Moore, D. W. & Saffman, P. G. 1971 Structure of a line vortex in an imposed strain. In *Aircraft wake turbulence and its detection* (ed. J. H. Olsen, A. Golburg & M. Rogers), pp. 339–354. Plenum, New York.

Moore, D. W. & Saffman, P. G. 1975 The instability of a straight vortex filament in a strain field. *Proc. R. Soc. London Ser. A* **346**, 413–425.

Noir, J. 2000 Écoulement d'un fluide dans une cavité en précession : approches numérique et expérimentale. *Ph.D. thesis, Université Joseph Fourier, Grenoble 1* .

Noir, J., Brito, D., Aldridge, K. & Cardin, P. 2001*a* Experimental evidence of inertial waves in a precessing spheroidal cavity. *Geophys. Res. Lett.* **38**, 3785–3788.

Noir, J., Cardin, P., Jault, D. & Masson, J. P. 2003 Experimental evidence of nonlinear resonance effects between retrograde precession and the tilt-over mode within a spheroid. *Geophys. J. Int.* **154**, 407–416.

Noir, J., Jault, D. & Cardin, P. 2001*b* Numerical study of the motions within a slowly precessing sphere at low Ekman number. *J. Fluid Mech.* **437**, 283–29.

Oser, H. 1958 Experimentelle untersuchung uber harmonische schwingungen in rotierenden flussigkeiten. *Z. angew. Math. Mech.* **38**, 386–91. <pp. 3, 10, 192.>.

Pais, M. A. 1999 Sur quelques mouvements animant le noyau terrestre. *Thèse de l'Institut de Physique du Gloge de Paris,IPGP* .

Pedlosky, J. 1987 *Geophysical fluid dynamics*. 2nd edn. Springer, New York.

Phillips, O. M. P. 1953 Energy transfer in rotating fluids by reflection of inertial waves. *Phys. Fluids* **49**.

Pierrehumbert, R. T. 1986 Universal short-wave instability of two-dimensional eddies in an inviscid fluid. *Phys. Rev. Lett.* **57**, 2157–2160.

Pocha, J. J. 1987 An experimental investigation of spacecraft sloshing. *Space Commun. Broadcasting* **5**, 323–332.

Poincaré, H. 1910 Sur la précession des corps déformables. *Bull. Astro.* **27**, 257–264.

Racz, J.-P. & Scott, J. F. 2007 Parametric instability in a rotating cylinder of gas subject to sinusoidal axial compression. part2. weakly nonlinear theory. *J. Fluid Mech.* **595**, 291–321.

Rayleigh, L. 1916 On the dynamics of revolving fluids. *Proc. R. Soc. London Ser. A* **93**, 148–154.

Rieutord, M. 1997 *Une introduction à la dynamique des fluides*. Masson.

Rieutord, M. & Valdetarro, L. 1997 Inertial waves in a rotating spherical shell. *J. Fluid Mech.* **341**, 77–99.

Roberts, P. H. & Gubbins, D. 1987 Origin of the main field : Kinematics. *Geomagnetism, Ed. J. A. Jacobs, Academic Press* **2**, 185–249.

Robinson, A. C. & Saffman, P. G. 1984 Three-dimensional stability of an elliptical vortex in a straining field. *J. Fluid Mech.* **142**, 452–466.

Rochester, M. G., Jacobs, J. A., Smylie, D. E. & Chong, K. F. 1975 Can precession power the geomagnetic dynamo ? *Geophys. J. R. Astron. Soc.* **43**, 661.

Saffman, P. G. 1992 *Vortex dynamics*. Cambridge University Press.

Sipp, D. 2000 Weakly nonlinear saturation of short-wave instabilities in a strained lamb-oseen vortex. *Phys. Fluids* **12**, 1715–1729.

Sipp, D. & Jacquin, L. 1998 Elliptic instability in 2-D flattened Taylor-Green vortices. *Phys. Fluids* **10**, 839–849.

Sloudsky, T. 1895 De la rotation de la terre supposée fluide à son intérieur. *Bulletin de la Société Impériale des Naturalistes* **9**, 285.

STEWARTSON, K. 1958 On the stability of a spinning top containing liquid. *J. Fluid Mech.* **5**, 577–592.

STEWARTSON, K. & ROBERTS, P. H. 1963 On the motion of a liquid in a spheroidal cavity of a precessing rigid body. *J. Fluid Mech.* **17**, 1–20.

SYNGE, J. L. 1933 The stability of heterogenous liquids. *Trans. R. Soc. Canada* **27**, 1–18.

TAYLOR, G. I. 1923 Stability of a viscous liquid contained between two rotating cylinders. *Philos. Trans. R. Soc. London Ser. A* **223**, 289–343.

THOMAS, P. J. & AUERBACH, D. 1994 The observation of the simultaneous development of a long- and a short- wave instability mode on a vortex pair. *J. Fluid Mech.* **265**, 289–302.

THOMPSON, R. 1970 Diurnal tides and shear instabiliies in a rotating cylinder. *J. Fluid Mech.* **40**, 737–751.

TILGNER, A. 1999*a* Driven inertial oscillations in spherical shells. *Phys. Rev. E* **59**, 1789.

TILGNER, A. 1999*b* Magnetohydrodynamic flow in precessing spherical shells. *J. Fluid Mech.* **379**, 303–318.

TILGNER, A. 1999*c* Non-axisymmetric shear layers in precessing fluid ellipsoidal shells. *Geophys. J. Int.* **136**, 629–636.

TILGNER, A. 2000*a* Oscillatory shear layer in source driven flows in an unbounded rotating fluid. *Phys. Fluids* **12**, 1101–1111.

TILGNER, A. 2000*b* Towards experimental fluid dynamos. *Phys. Earth Planet. Inter.* **117**, 171.

TILGNER, A. 2005 Precession driven dynamos. *Phys. Fluids* **17**, 034104.

TILGNER, A. & BUSSE, F. H. 2001 Fluid flows in precessing spherical shells. *J. Fluid Mech.* **426**, 387.

TSAI, C.-Y. & WIDNALL, S. E. 1976 The stability of short waves on a straight vortex filament in a weak externally imposed strain field. *J. Fluid Mech.* **73** (4), 721–733.

VANYO, J. P. 1991 A geodynamo powered by luni-solar precession. *Astrophys. Fluid Dyn.* **59**, 209.

VANYO, J. P. 1993 *Rotating fluids in engineering and science*. Dover, New York.

VANYO, J. P. & LIKINS, P. W. 1971 Measurement of energy dissipation in a liquid-filled, precessing, spherical cavity. *ASME Trans. J. Appl. Mech.* **38**, 674.

VANYO, J. P., WILDE, P. & CARDIN, P. 1995 Experiments on precessing flows in the earth's liquid core. *Geophys. J. Int.* **121**, 136–142.

WALEFFE, F. 1989 The 3d instability of a strained vortex and its relation to turbulence. PhD thesis, Massachusetts Institute of Technology.

WALEFFE, F. 1990 On the three-dimensional instability of strained vortices. *Phys. Fluids* A **2** (1), 76–80.

WALTON, I. 1975 Viscous shear layers in an oscillating rotating fluid. *Proc. R. Soc. London, Ser. A* **344**, 101.

WIDNALL, S. E., BLISS, D. & TSAI, C.-Y. 1974 The instability of short waves on a vortex ring. *J. Fluid Mech.* **66** (1), 35–47.

WOOD, W. W. 1965 Properties of inviscid, recirculating flows. *J. Fluid Mech.* **22** (2), 337–346.

WOOD, W. W. 1966 An oscillatory disturbance of rigidly rotating fluid. *Proc. Roy. Soc. Lond.* **293**, 181–212.

Dynamics of a fluid inside a precessing cylinder

Abstract

This thesis deals with the theoretical and experimental study of the dynamics of a fluid inside a precessing cylinder. It is a rotating flow problem which has many applications in aeronautics (precession of a flying object with a propellant liquid) and in geophysics (influence of the Earth precession on the dynamics of the Earth liquid core).

At moderate Reynolds numbers, the precessing flow is the sum of a solid body rotation and waves called Kelvin modes. These waves are resonant when their eigenfrequency equals the precessing frequency. In order to predict the amplitude of a resonant Kelvin mode, a viscous and weakly nonlinear theory has been carried out and confirmed experimentally.

When the Reynolds number is increased, the base flow becomes unstable. PIV measurements have shown that this instability is due to an interaction between the Kelvin mode forced by precession and two free Kelvin modes. A linear analysis of stability based on a mechanism of triadic resonance between Kelvin modes predicts correctly the threshold and the growth rate of the instability.

This instability is saturated by a geostrophic mode due to the nonlinear and viscous interaction of the free Kelvin modes with themselves. In agreement with experiments, a weakly nonlinear theory shows that the Kelvin modes amplitudes are stationary or oscillating (cycles of intermittency) depending on the Reynolds number. Finally, the fixed point of the nonlinear equations (dynamical system with four degrees of freedom) predicts fairly well the mean flow inside the cylinder, even for very high Reynolds numbers (i.e. $Re > 50000$).

Keywords : Rotating flow, hydrodynamics instability, transition to turbulence, precession, Kelvin mode, triadic resonance

---

Résumé

Cette thèse est une étude théorique et expérimentale de l'écoulement d'un fluide dans un cylindre en précession. Elle s'inscrit dans le domaine des écoulements tournants et trouve de nombreuses applications en aéronautique (précession des objets volants avec carburant liquide) et géophysique (influence de la précession terrestre sur la dynamique du noyau externe).

Pour des nombres de Reynolds modérés, l'écoulement d'un fluide en précession est une rotation solide à laquelle se superposent des ondes appelées modes de Kelvin. Ces ondes deviennent résonnantes lorsque leur fréquence propre est égale à la fréquence de précession. Afin de prédire l'amplitude d'un mode de Kelvin résonnant, une théorie visqueuse et faiblement non-linéaire a été développée puis confirmée expérimentalement.

Lorsque le nombre de Reynolds augmente, l'écoulement de base devient instable. Des mesures PIV ont montré que cette instabilité est due à une interaction entre le mode forcé par la précession et deux modes de Kelvin libres. Une analyse linéaire de stabilité basée sur un mécanisme de résonance triadique entre modes de Kelvin permet de prédire correctement le seuil et le taux de croissance de l'instabilité.

Cette instabilité est saturée par un mode géostrophique créé par l'interaction non-linéaire et visqueuse des modes de Kelvin libres avec eux même. En accord avec les expériences, une théorie faiblement non-linéaire montre que les amplitudes des modes de Kelvin sont stationnaires ou oscillantes (cycles intermittents) en fonction du nombre de Reynolds. Finalement, le point fixe des équations non-linéaires (système dynamique à quatre degrés de liberté) prédit correctement l'écoulement moyen à l'intérieur du cylindre, même pour des très grands nombres de Reynolds (i.e. $Re > 50000$).

Discipline : Mécanique, Physique des Fluides

Mots Clés : Écoulement tournant, instabilité hydrodynamique, transition à la turbulence, précession, mode de Kelvin, résonance triadique

---

Laboratoire : Institut de Recherche sur les Phénomènes Hors Équilibre
CNRS UMR 6594, Aix-Marseille Université
49, rue Frederic Joliot-Curie, B.P. 146
F-13384 Marseille Cedex 13, France